DOCTOR OF PHILOSOPHY

Mathematical Modelling of Mechanisms for Biofilm Expansion

Li, Laoshen

Award date:
2014

Mathematical Modelling of Mechanisms for Biofilm Expansion

By

Laoshen Li

A Thesis submitted for the degree of Doctor of Philosophy

Division of Mathematics

University of Dundee

Dundee

November 2014

Contents

List of figures

List of tables

Acknowledgements

Firstly, I would like to express sincere gratitude to my supervisor, Dr. Fordyce Davidson. Always on hand for discussions throughout my PhD, his thoughtful insight, knowledge and patient guidance have simply made this thesis possible. I have learned a great deal from him and his enthusiasm for understanding the observed biological phenomenon as well as the mathematics that is used for this purpose has continually encouraged me to persevere and kept me on the right track.

I'm very much indebted to all those in the Molecular Microbiology group at the University of Dundee for educating me in the ways of the lab. Particular thanks to Dr. Nicola Stanley-Wall, Dr. Laura Hobley and Mr. Michael Porter for all their help with experiment preparation and general good ideas over the years.

I would also like to thank Dr. Joao B. Xavier at the Memorial Sloan Kettering Cancer Center in New York, U.S.A for kindly providing me the Java code used to in Chapter 4.

I'm also very much appreciative to all of the staff in the Division of Mathematics at Dundee for many helpful discussions and for generally making my time here enjoyable.

Last, but not least, a big thank you to all of my friends and family, especially my fiancee, who has supported me, had faith in me, proofread for me, and encouraged

me constantly during the more difficult times by reminding me that I am capable to achieve what I wish for. Without all of you, I'm absolutely sure that I would not have been able to complete this thesis. It certainly hasn't gone unappreciated.

Declaration

I declare that the following thesis is my own composition and that it has not been submitted before in application for a higher degree.

Laoshen Li

Certification

This is to certify that Laoshen Li has complied with all the requirements for the submission of this Doctor of Philosophy thesis to the University of Dundee.

Dr. Fordyce Davidson

Abstract

Biofilms are multi-cellular communities of microorganisms attached to surfaces. It has been estimated that about 99% of all bacteria exist in biofilm. Thus to understand the critical role bacteria play in natural and man-made ecosystems, requires a better knowledge of these multi-cellular communities.

Biofilms are complex structures comprising cells embedded in a sticky material composed of extracellular polymeric substances (EPS) produced by the cells themselves. The physical structure of the biofilm has been shown to be important to its evolutionary success. EPS is involved in maintaining structural integrity of the biofilm and protects the embedded bacterial cells from adverse elements in the environment. It is known that the morphology and growth rate of biofilms are controlled by a number of factors including environmental conditions and the expression of particular genes.

The aim of this thesis was to better understand the links between physical and genetic mechanisms that underpin the function of the EPS matrix.

In this thesis, we investigate role of EPS in the structure and development of the biofilm. We do this by adopting an interdisciplinary approach that combines mathematical modelling and analysis, numerical simulation and laboratory experiments. First, we investigate cross-diffusion processes between the cells and the EPS matrix to establish whether structure is mediated in this manner. Then, we study the hypothesis

that the cells dominate the growth dynamics in the biofilm, i.e. expansion and structure is determined by cell growth and division. Next, we investigate the hypothesis that the matrix dominates and biofilm expansion is determined by water uptake. Finally, we compare these results to our experimental observations.

Chapter 1

Introduction

1.1 Biological Background

1.1.1 Biofilms

A microorganism is a living organism that is too small to be seen with naked eye but visible under a microscope [81], including all the bacteria and archaea and almost all the protozoa. Microorganisms live everywhere including in soil, hot springs, on the ocean floor, high in the atmosphere and deep inside rocks. Prokaryotes, including bacteria and archaea, are estimated to make up approximately half of the total biomass [134]. Microorganisms are important in many ways. They are vital to the environment, as they participate in the Earth's element cycles such as the carbon and nitrogen cycles. In addition, they also play important roles in virtually all ecosystems, such as recycling remains and waste products through decomposition [53]. Microorganisms, in particular bacteria are also essential for the correct functions of humans as they play a key role in digestion and other functions. Microorganism are also responsible for plant, animal and human diseases.

Compared to the plant and animal kingdoms, the diversity of microbial life is considerably less well explored and less deeply understood [71]. Recent studies have shown that microorganisms are capable of complex differentiation and have different behaviours. Thus, a set of guiding principles is needed to better understand the distribution, diversity and function of microorganisms.

In this thesis, we will focus on bacteria as a special microorganism. It is believed that much of the bacterial biomass is located in close-knit communities, designated biofilms. The precise definition of a biofilm varies depending on the different aspects of a biofilm being studied. However, all definitions contain the same essential aspects. First of all, biofilms are communities of bacteria that are able to grow adhered to surfaces. These surfaces can be solid-liquid surfaces, air-liquid surfaces. The liquid-air surfaces includes living tissues, indwelling medical devices, industrial or portable water system piping and natural aquatic systems. Secondly, in biofilms, bacteria produce an extracellular matrix and bacterial cells are encased in this matrix [19, 58, 86]. Thirdly, biofilms can comprise a single microbial species or multiple species depending on the environmental parameters [29, 98]. Biofilms that are composed of multiple species can be found in most environments, while biofilms that are formed by single species exist in particular infections and on the surface of medical implants [1, 6, 33, 98]. Finally, most biofilms have been found to exhibit heterogeneity to some extent [29, 39, 83]. Instead of being a continuous homogeneous layer, biofilms contain microcolonies of bacterial cells separated from other microcolonies by interstitial voids (water channels). Examples of biofilms formed by different species are shown in Figure 1.1 and Figure 1.2.

The development of biofilms is often characterised as a multi-stage process as shown in Figure 1.3. In the first stage, isolated microbes that are in the planktonic state attach to a surface. Once attached to a surface, microbes such as bacteria sense certain environmental parameters that trigger the transition from the planktonic state to the

Figure 1.1: Legionella biofilm that has colonised plastic pipework. Image reproduced from [151].

biofilm state [29, 71, 99]. At the biofilm state, the microbes start to divide and produce and secrete the extracellular matrix material to anchor themselves to the surface. Next, microcolonies are formed and join the new community leading to the growth of the biofilm. Finally, the fully mature biofilm reaches a quasi-steady state where growth of the microbes is balanced by the loss through a variety of actions, such as erosion and detachment due to mechanical stress, self-induced dispersal and cell death.

1.1.2 Characteristics of Biofilms

Biofilms are composed primarily of microbial cells and the surrounding extracellular matrix material that they secrete themselves. This matrix is composed of a mixture of components such as extracellular polymeric substance (EPS), protein, nucleic acids and other substances. The most studied component is the EPS, which accounts for 50% to 90% of the total biofilm [47]. The production of EPS involves a significant

Figure 1.2: Biofilm found on cobbles of a stream in High Ore Creek, Montana. The biofilm is shown in the greenish-brown slime. Image reproduced from [132].

investment of carbon and energy by the microorganisms. This must be beneficial in order to have evolved as a growth strategy. Next, we will discuss some of the benefits that are typically attributed to EPS.

First of all, EPS is involved in maintaining the structural integrity of biofilms and therefore the overall stability of the biofilm structure. This is because there exist certain polymer sequences in the EPS and when these sequences are present, the polymers tend to be much more rigid in structure and less deformable [123].

Secondly, EPS protects the embedded bacteria from adverse environmental effects. Bacteria are sheltered and remain at a steady state to a certain extent when residing within a biofilm. This role of EPS is fulfilled either by acting as an ion exchanger, thereby restricting diffusion of compounds from the surrounding area into the biofilm [31, 123] or by effectively reducing the concentration of the antimicrobial agents [123].

Thirdly, the EPS matrix is also suggested to be one way by which microorganisms can

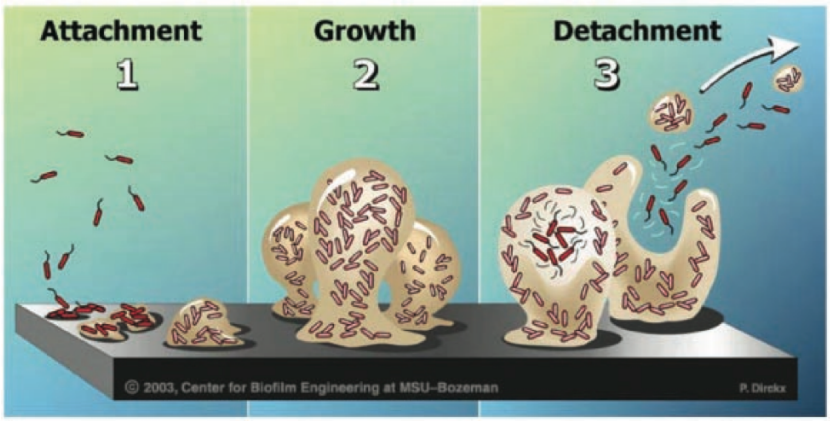

Figure 1.3: Stages of the biofilm life cycle. Image reproduced from [151]

ensure that they survive in environments where nutrient availability is low. That is, EPS acts as a nutrient reservoir to store carbon and energy for the long-term.

Fourthly, the EPS matrix has been proposed to affect the motility of bacteria embedded in the biofilm and therefore the expansion of the biofilm due to both its physical and its properties related genetic control. EPS are mostly composed of polysaccharides and proteins, which are all highly-weighted molecules. In addition, the EPS is a highly visco-elastic and sticky material. Thus, it is expected to hinder the movement/ spreading of bacteria embedded inside [19, 46, 142] by physical interaction. Moreover, for some certain species of bacteria, such as *Bacillus subtilis*, it has been shown that the loss of flagella-mediated motility is genetically coupled to the production of extracellular matrix [20, 59, 69]. This is because both motility and EPS production are dominated by a gene called *sinR*. *sinR* is inhibited when EPS is produced, which leads to the loss of flagella-mediated motility. This switch results in a slow type of surface motility that allows the biofilm to spread outwards on the substrate. This genetic switch between motility and matrix production is presented in [20].

Despite the above, it has been shown [20, 21, 116, 135] that mutants lacking the EPS component show a greatly reduced surface motility compared to the wild-type biofilm,

despite the cell growth rate of EPS mutants following a similar growth curve as the wild-type [18, 70]. It is clear that the EPS matrix plays a key role on determining the expansion of the biofilm. Hence, it is necessary to understand the mechanisms behind biofilm expansion and therefore the possible functional effect of the EPS matrix.

Apart from EPS, another important component of the biofilm, BslA protein, has attracted recent attention from researchers. Genetic and biochemical analyses showed that the self-polymerization activity of BslA was essential for its ability to localize to the biofilm matrix, and confocal laser scanning microscopy showed that BslA formed a hydrophobic layer on the biofilm surface [64, 73]. This protein has been identified as a major contributor to the surface repellency of *B.subtilis* biofilms. The existence of the hydrophobic layer formed by the BslA has been proposed to be the reason why the *B.subtilis* biofilms display persistent resistance to liquid wetting and gas penetration.

Another significant characteristic of the biofilm is that cells can communicate with each other using chemical signalling molecules. Initially, cells constantly produce and release a small amount of chemical signalling molecules. A class of signalling molecules that are used for communication between cells are called autoinducers. The quantity of the autoinducers produced is related to the population density. Cells are able to measure the concentration of the autoinducers and when a critical concentration is reached, changes in gene expression will arise. This type of gene regulation is known as quorum sensing (QS) [48, 71]. In planktonic populations of the same kinds of cells, chemical signalling molecules produced by the cells are simply not concentrated enough to cause changes in gene expression. However, in biofilms, since cells are glued together by the EPS matrix, it allows the concentration of these molecules to build up to threshold level. Hence, as one would expect, cells in the biofilm have a very different behaviour to those in the planktonic state.

In this thesis, we develop generic models for biofilm growth. Moreover, we will present

our experimental work in which we study the growth and development of the biofilm formed by a particular Gram-positive bacterium *Bacillus subtilis*. *B.subtilis* is an endospore forming bacteria that is naturally found in soil. There are several uses for *B. subtilis* such as creating proteases and amylase enzymes, converting dangerous explosives into compounds of nitrogen, carbon dioxide and water, and as a soil inoculant. More recently, *B.subtilis* has become the model agent in laboratory research because of its easy genetic manipulation. It has been used to understand the signalling processes that control multicellular behaviour exhibited by single-celled bacteria, as well as the molecular mechanism of biofilm formation.

B. subtilis can divide symmetrically to make two daughter cells, or asymmetrically to produce a single endospore that can remain viable for decades and is resistant to unfavourable environmental conditions. When cells are in an active state, they use their flagella for a swarming motility. This motility occurs on surfaces and it is switched off once cells start to secrete the EPS matrix, as discussed before. *B. subtilis* bacteria are aerobic, meaning that they require oxygen to grow. Therefore, this type of bacterium is usually found on air-solid or air-liquid surfaces.

1.1.3 Biofilm Pattern Formation

As mentioned before, most biofilms exhibit heterogeneity to some extent. With a variety of experiments, it has been shown that numerous strains of bacteria, in the form of colony rather than the form of biofilm, aggregate to form macroscopic patterns under certain conditions. These patterns are of surprising complexity but also show regularity. For example, *Paenibacillus dendritiformis* exhibits the well-known branching pattern when it grows on an agar surface (see Figure 1.4), and *B. subtilis* presents a wrinkling pattern when it grows on an agar surface (see Figure 1.5).

Figure 1.4: Example of branching pattern of *Paenibacillus dendritiformis*. Image reproduced from [55] with kindly permission.

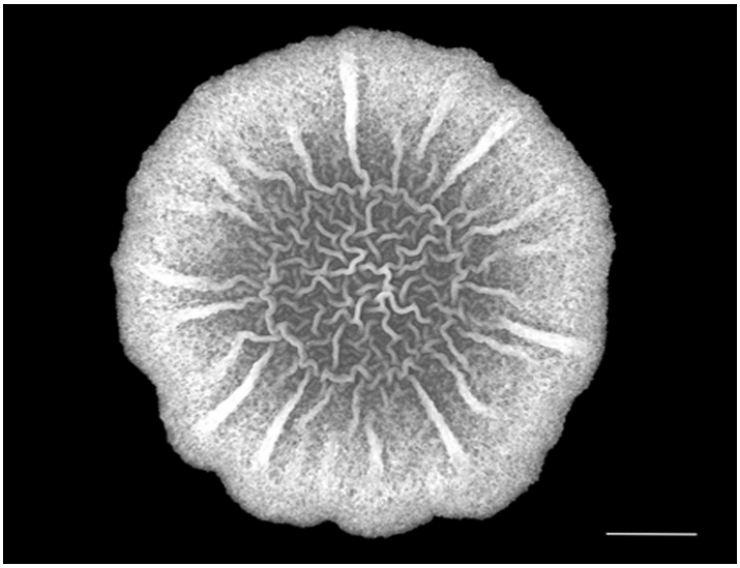

Figure 1.5: Example of wrinkling pattern of *Bacillus subtilis*. The detail of how the image is obtained can be referred to in Chapter 6.

Spatial patterns of biofilms are of significant importance. It has been shown that a rich structure of ecological, spatial-heterogeneity induced niches exist in biofilms [31]. These niches provide the biofilm with considerable flexibility and allow water to flow through. The water channels are essentially the lifeline of the system since they provide another way of circulating nutrients as well as exchanging metabolic products with the outside environment.

Hence, without any doubt, understanding how biofilm spatial patterns form, and determining whether or not there is any general patterning principle that is shared by different strains, will allow us to learn more about biofilms and how they grow and develop. However, the problem of how the patterns form is strongly connected with how the cells move within the biofilm. In the last three decades, a number of hypotheses regarding the mechanisms for the cell movement have been proposed. Next, we will summarise the most commonly held understading.

Cell swimming mediated by flagella is one of the widely studied mechanisms for cell movement [55, 95, 109]. In the modelling context, this mechanism is also often referred to as cell diffusion. Cells move nearly straight forward but the movements are separated by obvious tumblings. Cell swimming can only occur when there exists a suitably thick fluid layer.

The other mechanism for cell movement is called gliding. This is the surface translocation displayed by non-flagella bacteria that is mediated by expansive forces in a growing culture. This kind of movement can occur when the cells are growing on a solid but lubricated surface. Dockery and Klapper [37] proposed that cell growth and division within a biofilm increase the mechanical pressure locally and this pressure causes expansion of the biofilm.

More recently, Seminara et al. [116] conducted experiments to investigate the difference in the colony expansion of the *B.subtilis* biofilm between wild-type and the *eps*

mutant which is not capable of producing EPS matrix. Experimentally, they found that the *eps* mutant showed a reduced expansion compared to that of the wild-type. Hence, they suggested that the production of EPS was crucial for biofilm spreading. Therefore, they proposed that the spreading of the biofilm is primarily driven by osmotic stresses generated collectively by the secretion of EPS in the biofilm. Based on the experiments, Seminara et al. hypothesised that the EPS matrix causes an increase in the osmotic pressure, causing swelling of the biofilm, through uptake of water from the agar.

In this thesis, we will consider each of the above mechanisms in turn.

1.2 Mathematical Background

Biofilm formation is a complicated dynamical process which is determined by a combination of different physical and biochemical mechanisms. The development of a biofilm heavily depends on both the environmental conditions and the species of bacteria that form the biofilm. Therefore, a biofilm constitutes a very complex biological system.

The diverse range of outcomes ensures that it is not easy to explain either the spatial patterns or the expansion of biofilms observed using experimental methods above. However, these phenomena can be further investigated with the use of mathematical models.

Mathematical modelling of biofilms has been a popular method in the study of biofilms during the last three decades, in which the focus ranges from the microscopic to the macroscopic scale. Models have been developed at the cellular level and aimed at

investigating the function of certain generic networks that contribute to the important characteristics of a biofilm [65, 84, 96, 108, 131, 150]. Another popular topic in the biofilm modelling is pattern formation. The main motivation of these models has been to investigate how spatial patterns form by considering the interaction between environmental conditions and the biomass [43, 48, 55, 90, 95, 128, 129]. Another area of biofilm modelling combined biofilm formation with physical mechanisms, such as fluid low, osmotic pressure and physical properties of the biofilm itself [30, 37, 40, 45, 72, 102, 103, 104, 110, 116, 121, 122, 138, 152].

In this section, we will give a review of biofilm models developed in the past 30 years. All of them consider either biofilm pattern formation or the physical and chemical mechanisms behind the biofilm development. We classify the models into three categories based on the way in which the biofilm is treated: discrete models, discrete-continuum models, and continuum models.

1.2.1 Discrete Modelling Approach

Transport of particular components that comprise a biofilm occurs due to bacterial growth or decay. The movement of these components can be represented in various ways. Discrete modelling approaches have been widely used to study biofilm development. In models with a discrete description of particulate components, individual cells and particles are displaced according to empirical rules that mimic advective or diffusive flux [10, 76, 101, 104, 105].

One of the typical discrete models used is the individual-based modelling (IbM) which was first proposed by Kreft et al. [76] and later on, a number of models based on this paper [77, 101, 133, 146, 148, 149]. In [76], each cell is represented as a sphere that has a volume as variable. Each cell grows by consuming the substrate and divides when

a critical volume of cell is reached. Cell movement is determined by displacement of cells to minimise overlap between cells. The substrate concentration is governed by a reaction-diffusion equation. The IbM is confluent and rounded due to the steady, deterministic and directionally unconstrained spreading of cells, although this type of modelling approach relies heavily on computational simulation.

Another typical discrete model used is the diffusion-limited aggregation (DLA) model, which was first proposed in [144] and studied extensively in [49, 50, 91]. The process of the DLA model is as follows. The domain is divided into a lattice. Firstly, a seed particle is chosen as the origin of the lattice. Then another particle is released far away from the origin and is allowed to move randomly within the domain. Once the particle arrives at the nearest site to the origin, it will stop moving and stick to the site. Both particles together constitute a cluster. Next, another particle is released and is allowed to move until it gets to the nearest site to the cluster. After repeating the same process for a certain amount of particles, a cluster that shows the branching morphology will be obtained. The DLA model has been widely studied and used to describe the branching morphology exhibited by *B. subtilis* although it also depends very heavily on the nature of the computational simulation.

A further widely studied discrete model is the cellular automaton (CA). CA models for the biofilm pattern formation capture various biofilm patterns observed in the experiments by incorporating biological rules that govern processes such as the cell growth and movement, interaction between cells and the substrate concentration. A cellular automaton consists of a regular grid of cells and each cell is assigned by a finite number of states, such as active and inactive for the bacterial cells. After an initial setup of the state of the cells, new generation (advancing t by 1) is created according to the rules set in the model. For example, in [15], the substrate concentration as well as the current state of the cells are used to determine the state of each cell at the next time point. CA models suggest that the biofilm structure is determined by the substrate concentration

and by varying the concentration of the substrate, CA models can reproduce biofilm structures such as penetrated water-channel biofilm, heterogeneous mosaic biofilm and dense confluent biofilm [141]. CA models are more widely used in discrete-continuum approaches.

1.2.2 Discrete-Continuum Models

Discrete-continuum modelling approaches have been used to incorporate the flow over the irregular biofilm's surfaces, convective and diffusive mass transfer of substrate, bacterial growth and biomass spreading [10, 102, 103]. In these models, the biomass growth and spreading is modelled by a discrete CA model, the mass balance of the substrate is modelled by a continuity equation, and the flow field is governed by momentum balance (Navier-Stokes) equations. In this manner, the fluid flow is found to affect the biofilm's growth by regulating the substrate concentration at the biofilm-fluid interface, and shearing the surface of the biofilm. In [34, 35], a completely different discrete-continuum biofilm model was proposed, based on the Immersed Boundary Method. In the model, the cells are treated as discrete while the bulk flow and the substrate are presented as continuum. The formation of the biofilm is achieved by a cell-cell aggregation which is described to an appropriate binding force.

The discrete-continuum biofilm model was a full quantitative model incorporating many physical, chemical and biological processes affecting the development of biofilms. This approach is capable to produce simulation results in good agreement with experimental data.

1.2.3 Continuous Models

A continuous approach is the traditional way to model biological phenomenon. All the mathematical models used in this thesis are continuous models. In continuous models, the microorganisms are represented by their 2-D density and a differential equation of this density is used to describe the time evolution of the microorganisms. Next, we will classify the continuous biofilm models into ODE models and PDE models.

1.2.3.1 ODE Approach

An ODE approach has been widely used in the biofilm modelling to investigate the growth of the cell density over time, particularly used for studies of how bacterial cells respond to antibiotics or other environmental changes [25, 27, 62]. Predictions which can be obtained in these models can be used to fit the experimental data of cell growth. In the case of ODE approach, the quantities of interest, such as the cell density, substrate concentration, are modelled as a function of time only. In [27], an ODE system was proposed to investigate the resistance mechanism to antimicrobial for the bacterial biofilms. In this model, it was hypothesised that there is a phenotype-switch between normal cells and 'persister' cells which are extremely tolerant of the antimicrobials. Numerical simulation and analysis of a simplified model of [27] indicate that the relative dose times are important in determining the effectiveness of a dosing treatment.

ODE approaches are also widely used in the study of cell-cell signalling processes. The first class of ODE models regarding cell-cell signalling processes are related to chemotaxis [3, 7, 54, 61, 94, 107, 108, 115]. These models have been made to predict adaptation mechanisms of the rotational orientation of flagella in response to changes in concentrations of external substances. The other class of ODE models regarding cell-cell signalling processes are related to quorum sensing [16, 36, 56, 66, 114, 137].

In [137], Ward et al. proposed a model to describe bacterial population growth and quorum sensing in a well mixed system. They viewed the population of bacteria as consisting of down-regulated and up-regulated sub-populations where quorum sensing molecules were produced at a faster rate by the up-regulated cells. The other cell-cell signalling process which involves a number of ODE models is sporulation. There is a number of previous models concerning sporulation in *B. subtilis* [65, 67, 68, 136]. In [65], a system of deterministic ODEs was used to cover almost the fullly known network responsible for detecting sporulation-related signals. The model included signals related to nutrient levels, DNA damage age, population size and the products of the competence genes, and was able to capture a variety of signal types including environmental and metabolic ones.

1.2.3.2 PDE Approach

In the mathematical modelling for biofilm development, such as pattern formation and the interaction between cells and environmental elements, a PDE approach has been widely used.

Reaction diffusion approach One of the most commonly used PDE approaches is to use reaction diffusion systems to study the interaction between cells and substrate concentration.The evolution equation of the density is coupled to the other reaction-diffusion equations for the chemical fields. The general form of such a model is given in (1.1). The first two terms on the right of the equation include the diffusion and

advection of the component.

$$\begin{pmatrix}\text{Net rate of}\\ \text{accumulation}\\ \text{of mass}\end{pmatrix} = \begin{pmatrix}\text{Mass flow}\\ \text{of the}\\ \text{component}\\ \text{coming in}\end{pmatrix} - \begin{pmatrix}\text{Mass flow}\\ \text{of the}\\ \text{component}\\ \text{going out}\end{pmatrix} + \begin{pmatrix}\text{Rate of}\\ \text{production}\\ \text{of the}\\ \text{component}\end{pmatrix} - \begin{pmatrix}\text{Rate of}\\ \text{consumption}\\ \text{of the}\\ \text{component}\end{pmatrix}. \tag{1.1}$$

Ben-Jacob et al. [11, 12, 13, 14, 15, 55, 127], Mimura et al. [92, 95, 124], proposed mathematical models which used reaction-diffusion models to study the mechanisms behind the pattern formation of bacterial colony, i.e. branching morphology. Especially, Kozlovsky et al. [75] proposed that the cell movement is enhanced by a lubricant, i.e. the EPS matrix. The model consists of four coupled equations describing the spatio-temporal evolution of the active cell density, substrate concentration, the lubricant concentration and the inactive cell density. Using numerical simulations, they found that this model is able to capture all of the dense circular colony, branching pattern and a DLA-like pattern by varying the initial nutrient concentration

Reaction-diffusion systems have also been used to investigate the quorum sensing in bacteria and spatial distribution of cells due to quorum sensing [5, 26, 36, 48, 138]. In [48], Frederick et al. presented a mathematical model that described the quorum sensing phenomenon in bacterial biofilms, consisting of a nonlinear reaction system. The model includes production and spatial spreading of biomass, conversion of down-regulated biomass into up-regulated biomass as a consequence of the quorum sensing signalling molecule concentration. They found that at sufficiently high bulk flow rates, biofilm growth and signalling molecule production is enhanced.

More recently, Asalley et al. [8] employed a reaction diffusion system to study the effect of cell death on both the spatial pattern formation of biofilm and cell distribution in the biofilm. Experimentally they discovered a pattern of localised cell death that

spatially focuses mechanical forces, and thereby initiates wrinkle formation. Guided by these findings, they proposed a mathematical model which incorporated the cell death with the mechanical forces. The model was able to generate artificial wrinkle patterns within biofilms.

Conservation approach Along with the reaction diffusion approach, another widely used PDE approach is to apply the energy or mass conservation law to model the mechanisms, in particular physical mechanisms, that are responsible for the biofilm development. This approach is used to study the interaction between bacterial cells and environmental effects. In [10, 40, 44, 45, 48, 72, 152], the hydrodynamics of the bulk flow was taken into account to study the structure of biofilms through both the convection of the nutrient and the detachment of the biomass.

Dockery and Klapper [37] suggested that the spreading of the colony is attributed to biomass growth. They developed a continuum model of a single substrate limited biofilm growing into a static aqueous environment. In the model, cell movement is no longer modelled by diffusion. Instead, Darcy's law is used to model the biofilm expansion attributed to biomass growth. Xavier et al. [147] extended this idea to model the cell distribution when multi-species exist in the biofilm. They found that when different genotypes meet and compete, natural selection favours energetically costly spreading strategies, like polymer secretion, that simultaneously reduce productivity and disrupt the spatial patterns.

Energy conservation laws are also widely used in the biofilm study. In [116], Seminara et al. hypothesised that the EPS matrix secreted by the biofilm is able to absorb water from the agar. Therefore, the EPS concentration causes an increase in the osmotic pressure, causing the swelling of the biofilm. They developed a model that treats the biofilm as a two-component system consisting of biomass and water. The movement of

the biomass was modelled by modified Darcy's law which takes the osmotic pressure into consideration. The modified Darcy's law can be derived from conservation of energy in the biomass-water system. They found out that there are two stages of biofilm expansion. During the initial expansion, the height of the biofilm increases with the radius of it remaining a constant. At the onset of the second stage, the radius of the biofilm starts to expand. Similar models can be found in [4, 72, 143, 152].

1.3 Thesis Outline

As mentioned in the previous section, there have been a number of modelling approaches proposed to investigate how biofilms expand and how the heterogeneous structure of biofilms occurs. The aim of this thesis is to investigate different hypotheses regarding mechanisms that cause the biofilm to expand and generate a heterogeneous structure. To accomplish this aim, we will consider biofilms from different view points. We will first study the planar growth of biofilms, as is illustrated in Figure 1.5, and investigate the overall morphology and radial expansion speed. Then, we will change our focus to the cross-section aspect (Figure 1.3), so we may study the morphology of the biofilm interface, the expansion speed in the radial direction and the expansion speed of the biofilm height. The structure of this thesis is as follows.

In Chapter 2, we will investigate the functional effects of the EPS matrix secreted by the biofilm on both the observed pattern formation and the biofilm expansion. We present the construction of the general form of the reaction-diffusion system we will use, which considers cross-diffusion effects between the cells and the EPS molecules. The system comprises two partial differential equations that describe the spatio-temporal evolution of cell density, $b(\mathbf{x},t)$, and the EPS concentration, $m(\mathbf{x},t)$. The mathematical

model is given in dimensional form by

$$\begin{aligned}\frac{\partial b}{\partial t} &= \nabla \cdot [d_1(b,m)\nabla b + d_2(b,m)\nabla m] + f_1(b) - f_2(b),\\ \frac{\partial m}{\partial t} &= \nabla [d_3(b,m)\nabla b + d_4(b,m)\nabla m] + g_1(b) - g_2(b,m).\end{aligned} \tag{1.2}$$

We apply travelling wave analysis in the radial direction to study what determines the expansion speed of the wild-type biofilm. An expression for the traveling wave speed is derived and we state the effect of the EPS matrix on the expansion speed of the biofilm. Subsequently, we specify the possible expressions for the terms in the model and use a numerical simulation to show a typical travelling wave profile. We also compare the theoretical travelling wave speed with the simulated one.

We then apply stability analysis in the angular direction to investigate what component in the system is responsible for pattern formation. We further investigate two common hypotheses that are used to explain the possible role that the EPS matrix plays in the biofilm system. According to these different hypotheses, we specify the terms in the system and use a numerical simulation to show possible patterns.

In Chapter 3, we investigate cell growth as the mechanism that may be responsible for the expansion of the biofilm. This piece of work is an extension of the model proposed by Dockery and Klapper [37]. We first give a detailed construction of the model including appropriate assumptions that are not explicitly mentioned in the original paper. Using the nondimensionalisation process, we reduce the model to a quasi-steady state problem. We then show an alternative way to the method used in [37] of looking for planar solutions by introducing a new variable $a = z - h(t)$ to track the biofilm interface $h(t)$. This analysis is performed for the general form of model for which the biofilm is assumed to be infinitely thick. We investigate the existence of the 1-D planar solution by using a phase plane argument. An important result of the biofilm interface evolution is stated. Then, we consider the stability of the 1-D planar solution. The conditions

for linear instability of the 1-D planar solution are stated in terms of the general form of the reaction terms. Then, we apply the analysis to the specific model that is given in [37] and give the specific conditions that are required for the linear instability. We then extend the original model to a domain with finite depth and add a death rate to the cell growth term. The new system for substrate S and pressure P is given in (1.3) and (1.4).

$$\begin{cases} \nabla^2 S - GS = 0; \\ \\ \nabla^2 P = -S + \mu; \end{cases} \qquad 0 < z < h(x,t) \tag{1.3}$$

$$\nabla^2 S = 0, \qquad h(x,t) < z < h(x,t) + L, \tag{1.4}$$

for some constant L. We look for a 1-D planar solution to this extended model and derive the evolution equation of the biofilm height. Important results concerning the biofilm height will also be shown. Next, we investigate the stability of the planar solution, where we derive a dispersion relation for the extended model. We will state the effect of the cell death on the linear instability and the important role of the cell death in generating different patterns.

In Chapter 4, we study the 2-D solutions of model (1.3) - (1.4). The model is solved numerically using the level set method. We first show a simple example in order to motivate how the level set method is used to generate solutions. Then, we give a brief re-derivation of the equations used in level set method. Next, we briefly state the numerical scheme that is used to solve the level set equation before studying the 2-D numerical solution of the model. Numerical simulations of system (1.3)-(1.4) are presented for a variety of parameter values and different wave numbers.

In Chapter 5, we investigate the function of a special component in the biofilm, i.e. the hydrophobic layer around the biofilm surface. We adapt an existing mathematical model proposed by Seminara et al. [116], with a different, but appropriate boundary

condition. We first present the general idea of the model set up, as well as the hypotheses that we will investigate with the use of this model. Subsequently, we simplify the model by applying the thin-film approximation. With the simplified model, we are able to solve the model analytically and obtain a relationship to describe how the height of the biofilm changes over time. Finally, we give our interpretation of the function of the hydrophobic layer and therefore further discuss the possible treatment for the biofilm.

In Chapter 6, we outline the materials, method and results for all our laboratory experiments. Our experiments are based on experimental observations reported by Seminara et al. in [116] on the expansion of both the wild-type of *B. subtilis* and the correspondingly *eps* mutant, where the radius and height of colonies are measured within 18 hours. Our experiments also consider the development of the *bslA* mutant and the time scale in our experiment is extended to 48 hours. We describe the new method which we have developed to measure the height of the biofilm. We report our observations concerning the radius and height development for these three strains over time and compare the results.

Finally in Chapter 7 we present and summarize key results and discuss the possible implications of our work to understand the development of the biofilm. A discussion of possible future directions for mathematical modelling and experimental work is also given.

Chapter 2

Expansion of Biofilm Driven By Cell Diffusion

2.1 Introduction

Experimentally, it has been shown that the wild-type biofilm presents a complex spatial pattern, while the *eps* mutant, which lacks the gene that is responsible for the secretion of a component of EPS matrix, presents a flat biofilm without any spatial pattern (Figure 6.1 in Chapter 6). Moreover, the wild-type biofilm expands faster in the radial direction than the *eps* mutant does. Due to the significant difference on the pattern formation and expansion speed between the wild-type biofilm and the *eps* mutant, we are interested in the functional effect of the EPS matrix secreted by the biofilm on both the observed pattern formation and the biofilm expansion.

In this chapter, we will adapt the well-studied reaction-diffusion approach to study the effect of the EPS matrix. We first construct the general form of the reaction-diffusion system we will use, which considers cross-diffusion effects between the cells and the

EPS molecules. Then, we will apply travelling wave analysis in the radial direction to study what determines the expansion speed of the wild-type biofilm. Later, we will apply stability analysis in the angular direction to study what component in the system is responsible for the pattern formation. We will further investigate two common hypotheses that are used to explain the possible role that the EPS matrix plays on the biofilm system.

2.2 Model Set Up

As mentioned in Chapter 1, the biofilm pattern formation has been broadly studied by the reaction-diffusion approach [55, 75, 95]. As our first attempt at studying the development of the biofilm, we will adapt the reaction-diffusion approach to study the effect of the EPS matrix on the biofilm pattern formation and the biofilm spreading.

The biofilm we consider in this chapter grows on the surface of agar and the agar is attached to the petri dish. Within our consideration, the biofilm will never grow big enough to touch the boundary of the petri dish. Hence, although the petri dish is of a round shape in reality, we choose a square domain with side of length L as the computational domain for computational convenience, on which substrate is maintained at a sufficiently high level to allow biofilm growth. We view the biofilm from above. Initially, the cells are spotted in the centre of the petri dish. The geometry of the model is shown in Figure 2.1. The origin of the coordinates is set to be the centre of the square domain.

The key components in our system are the cell density $b(\mathbf{x},t)$ and the EPS concentration $m(\mathbf{x},t)$. Following the standard reaction-diffusion approach, the general form of

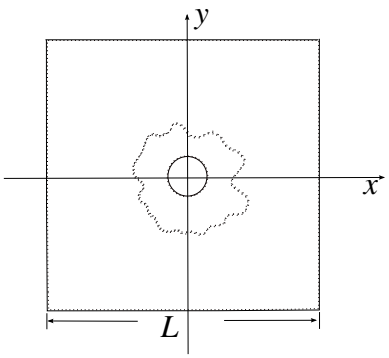

Figure 2.1: Schematic of the biofilm geometry which is studied in this chapter. The circle in the centre indicates the initial inoculation and the dashed curve represents the typical biofilm morphology after a certain time.

such a model for these two components in $\Omega = [-\frac{L}{2}, \frac{L}{2}] \times [-\frac{L}{2}, \frac{L}{2}]$ is as follows :

$$\frac{\partial b}{\partial t} = -\nabla \cdot \mathbf{J}_b + f_1(b) - f_2(b); \tag{2.1a}$$

$$\frac{\partial m}{\partial t} = -\nabla \cdot \mathbf{J}_m + g_1(b) - g_2(b,m), \tag{2.1b}$$

where $\mathbf{J}_b$ and $\mathbf{J}_m$ are the diffusion flux of cells and EPS molecules respectively, $f_1(b)$ and $f_2(b)$ represent the cell proliferation and cell death respectively. It has been shown that during *Bacillus substilis* biofilm formation, a subpopulation of cells differentiates into a specialized population that synthesizes the exopolysaccharide of the extracellular matrix and breaks it down [24, 89]. In the model, we use $g_1(b)$ to represent the production of exopolysaccharide and $g_2(b,m)$ to represent the decay of it.

We assume that the flux of cells and the flux of EPS molecules are not only induced by the gradient of themselves but also induced by the gradient of each other. Accordingly, the diffusion flux of cells is modelled by $\mathbf{J}_b = -d_1(b,m)\nabla b - d_2(b,m)\nabla m$ and the diffusion flux of the EPS concentration is modelled by $\mathbf{J}_m = -d_3(b,m)\nabla b - d_4(b,m)\nabla m$.

In this way, system (2.1) becomes:

$$\frac{\partial b}{\partial t} = \nabla \cdot [d_1(b,m)\nabla b + d_2(b,m)\nabla m] + f_1(b) - f_2(b); \tag{2.2a}$$

$$\frac{\partial m}{\partial t} = \nabla \cdot [d_3(b,m)\nabla b + d_4(b,m)\nabla m] + g_1(b) - g_2(b,m). \tag{2.2b}$$

Notice here, in order to consider the most general form of the diffusion, we assume that the flux coefficients d_i where $i = 1,2,3,4$ are functions of both the cell density and the EPS concentration.

Next, we will specify the form of the cross-diffusion flux for system (2.2) according to the biological information. We assume that for the cross-diffusion we have

$$d_2(0,m) = d_3(b,0) = 0. \tag{2.3}$$

This is a reasonable assumption because when there is no cells in the system, the diffusion flux of the cells due to the gradient of the EPS matrix reduces to zero since no cells can be carried by the EPS matrix. Similar reasoning applies to the diffusion flux of the EPS matrix due to the gradient of the cell density.

Also, some restrictions need to be set for the reaction terms in system (2.2). As a summary, all the assumptions used in this Chapter are as follows:

A1: $f_1(0) = f_2(0) = g_1(0) = g_2(0,m) = g_2(b,0) = 0$: If no cells exist in the system, then neither cells nor EPS will be produced and there is no death for cells and no consumption of EPS. Additionally, if there is no EPS in the system, then cells can not consume EPS.

A2: $f_1 > 0, f_2 > 0, g_1 > 0, g_2 > 0$ for $b > 0, m > 0$: All the production / loss activities are ongoing as long as cells and EPS exist in the system;

A3: There exists a non-zero steady state of (2.2): $(b,m) = (b^*, m^*)$;

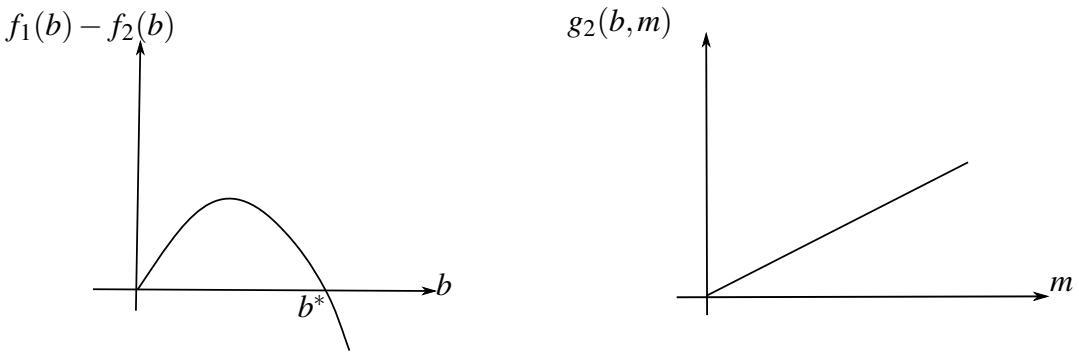

Figure 2.2: Schematic plot of the desired form of the reaction terms in system (2.1).

A4: $f_1(b) > f_2(b)$ for $b < b^*$ and $f_1(b) < f_2(b)$ for $b > b^*$: Cell proliferation is dominating when there is not enough cells in the system, while cell death should dominate when the cell population is too large to be sustainable by the available space.

A5: $f_1'(b) > f_2'(b)$ as $b \to 0$ and $f_1'(b) < f_2'(b)$ as $b \to b^*$.

A6: $g_{2,m}(b,m) > 0$: The more exopolysaccharide is in the system, the faster the subpopulation of cells can break it down.

Based on the assumptions above, the desired form of the reaction terms $f_1(b) - f_2(b)$ and $g_2(b,m)$ are schematically plotted in Figure 2.2.

Next, we will specify the boundary conditions as well as the initial conditions to complete the model. At the boundary of the petri dish, we assume that neither the cells nor the EPS molecules can escape the petri dish. Therefore, we apply no flux boundary condition to the system, i.e.

$$\mathbf{J}_b = \mathbf{J}_m = 0, \quad \text{on} \quad x = -\frac{L}{2}, \frac{L}{2} \quad \text{and} \quad y = -\frac{L}{2}, \frac{L}{2}. \tag{2.4}$$

As mentioned at the beginning, initially the cells are spotted in the centre of the petri dish and form a circular shape. Therefore, the initial condition for system (2.2) is given

as follows:

$$b(\mathbf{x},0) = \begin{cases} b_0 \quad \text{for} \quad |\mathbf{x}| \leq h; \\ 0 \quad \text{for} \quad |\mathbf{x}| > h \end{cases} \tag{2.5}$$

and

$$m(\mathbf{x},0) = 0 \quad \text{in} \quad \Omega. \tag{2.6}$$

where h is the initial radius of the inoculation.

Equations (2.2) along with the boundary conditions (2.4) and the initial conditions (2.5)-(2.6) constitute the mathematical model that we will use to study the cross-diffusion between cell density and the EPS molecules.

As usual, before analysing the model, we will rewrite system (2.2) and the boundary conditions (2.4) along with the initial conditions (2.5)-(2.6) in dimensionless form in order to reduce the number of parameters. Assume the typical length of biofilm to be $\omega = \frac{L}{100}$, the standard Fickian diffusion coefficient for the cells is D_b, and the typical EPS concentration to be m_0. By introducing the non-dimensional variables

$$u = \frac{b}{b_0}, \quad v = \frac{m}{m_0}, \quad \mathbf{x}' = \frac{\mathbf{x}}{\omega}, \quad \tau = \frac{D_b}{\omega^2}t,$$

system (2.2) can be rewritten as

$$\frac{\partial u}{\partial \tau} = \nabla(D_1(u,v)\nabla u + D_2(u,v)\nabla v) + F_1(u) - F_2(u), \tag{2.7a}$$

$$\frac{\partial v}{\partial \tau} = \nabla(D_3(u,v)\nabla u + D_4(u,v)\nabla v) + G_1(u) - G_2(u,v), \tag{2.7b}$$

where

$$F_i(u) = \frac{\omega^2}{b_0 D_b} f_i(b), \quad G_1(u) = \frac{\omega^2}{m_0 D_b} g_1(b), \quad G_2(u,v) = \frac{\omega^2}{m_0 D_b} g_2(b,m)$$

are dimensionless reaction terms, and

$$D_{1,4}(u,v)=\frac{d_{1,4}(b,m)}{D_b},\quad D_2(u,v)=\frac{m_0 d_2(b,m)}{b_0 D_b},\quad D_3(u,v)=\frac{b_0 d_3(b,m)}{m_0 D_b},$$

are the dimensionless flux functions.

Similarly, with the dimensionless variables, the boundary conditions (2.4) can be rewritten as: on $x=-50,50$ and $y=-50,50$,

$$D_1(u,v)\nabla u+D_2(u,v)\nabla v=0\quad\text{and}\quad D_3(u,v)\nabla u+D_4(u,v)\nabla v=0; \tag{2.8}$$

and the initial conditions given in (2.5) and (2.6) can be rewritten as

$$u(\mathbf{x},0)=\begin{cases}1, & \text{for}\quad |\mathbf{x}|\le H\\ 0, & \text{for}\quad |\mathbf{x}|>H\end{cases} \tag{2.9}$$

where $H=\frac{h}{\omega}$, and

$$v(\mathbf{x},0)=0\quad\text{for}\quad \mathbf{x}\in[-50,50]\times[-50,50]. \tag{2.10}$$

after dropping the $'$ of $\mathbf{x}'$.

System (2.7) along with the boundary conditions (2.8) and the initial conditions (2.9)-(2.10) constitute the dimensionless form of mathematical model we will study.

It can be seen from the experimental image of the wild-type biofilm (Figure 6.1 in Chapter 6), the wrinkling pattern of the wild-type biofilm happens along the angular direction when the radius is large, and the expansion of the biofilm happen along the radial direction. Therefore, we will analyse system (2.7) in the polar coordinates by setting $x=r\cos(\theta), y=r\sin(\theta)$. In polar coordinates, the cross diffusion terms under

the Cartesian coordinate can be rewritten as:

$$\nabla \cdot (D_{1,3}(u,v)\nabla u) = [D_{1,3}(u,v)u_r]_r + \frac{1}{r}D_{1,3}(u,v)u_r + \frac{1}{r^2}[D_{1,3}(u,v)u_\theta]_\theta;$$
$$\nabla \cdot (D_{2,4}(u,v)\nabla v) = [D_{2,4}(u,v)v_r]_r + \frac{1}{r}D_{2,4}(u,v)v_r + \frac{1}{r^2}[D_{2,4}(u,v)v_\theta]_\theta.$$

Substituting the above expressions into (2.7) yields:

$$\begin{aligned}\frac{\partial u}{\partial \tau} =& [D_1(u,v)u_r]_r + \frac{1}{r}D_1(u,v)u_r + \frac{1}{r^2}[D_1(u,v)u_\theta]_\theta \\ &+ [D_2(u,v)v_r]_r + \frac{1}{r}D_2(u,v)v_r + \frac{1}{r^2}[D_2(u,v)v_\theta]_\theta + F_1(u) - F_2(u), \qquad (2.11a)\\ \frac{\partial v}{\partial \tau} =& [D_3(u,v)u_r]_r + \frac{1}{r}D_3(u,v)u_r + \frac{1}{r^2}[D_3(u,v)u_\theta]_\theta \\ &+ [D_4(u,v)v_r]_r + \frac{1}{r}D_4(u,v)v_r + \frac{1}{r^2}[D_4(u,v)v_\theta]_\theta + G_1(u) - G_2(u,v). \qquad (2.11b)\end{aligned}$$

System (2.11) is the alternative form of system (2.7) in the polar coordinates. This system will be analysed in depth in the following section.

2.3 Travelling Wave Analysis of the Reaction-Diffusion System with Cross-Diffusion

As the first attempt, we wish to understand what determines the expansion speed in the biofilm and whether the presence of the EPS matrix will affect the biofilm expansion or not. It can be seen in Figure 6.1 in Chapter 6 that the biofilm expands radially and symmetrically. Therefore, we will look for travelling wave solutions of system (2.11) along the r direction.

2.3.1 Travelling Wave Analysis

We assume that all the variables in system (2.11) are radially symmetric, i.e. functions of r only. In order to simplify the system, we also assume that r is sufficiently large. Therefore, system (2.11) can be approximated by:

$$\frac{\partial u}{\partial \tau} = [D_1(u,v)u_r + D_2(u,v)v_r]_r + F_1(u) - F_2(u); \tag{2.12a}$$

$$\frac{\partial v}{\partial \tau} = [D_3(u,v)u_r + D_4(u,v)v_r]_r + G_1(u) - G_2(u,v). \tag{2.12b}$$

We seek solutions in terms of the travelling wave coordinate $z = r - c\tau$, where c is the propagation speed which has to be determined. By writing $u(r,\tau) \equiv U(z), v(r,\tau) \equiv V(z)$, we obtain the travelling waveforms of the equations:

$$\begin{aligned} -cU' =& D_1U'' + D_{1,U}(U')^2 + D_{1,V}U'V' \\ &+ D_2V'' + D_{2,U}U'V' + D_{2,V}(V')^2 + F_1(U) - F_2(U); \end{aligned} \tag{2.13a}$$

$$\begin{aligned} -cV' =& D_3U'' + D_{3,U}(U')^2 + D_{3,V}U'V' \\ &+ D_4V'' + D_{4,U}U'V' + D_{4,V}(V')^2 + G_1(U) - G_2(U,V), \end{aligned} \tag{2.13b}$$

where prime denotes differentiation with respect to z. By denoting $S(z) \equiv U'(z)$ and $W(z) \equiv V'(z)$, system (2.13) can be rewritten as follows:

$$\begin{aligned} -cS =& D_1S' + D_{1,U}S^2 + D_{1,V}SW \\ &+ D_2W' + D_{2,U}SW + D_{2,V}W^2 + F_1(U) - F_2(U); \end{aligned} \tag{2.14a}$$

$$\begin{aligned} -cW =& D_3S' + D_{3,U}S^2 + D_{3,V}SW \\ &+ D_4W' + D_{4,U}SW + D_{4,V}W^2 + G_1(U) - G_2(U,V). \end{aligned} \tag{2.14b}$$

From system (2.14), S' and W' can be expressed in terms of U,V,S,W only. Therefore, system (2.14) can be rewritten as a first-order ODE system of four equations for U,V,S,W as follows:

$$U' = S; \tag{2.15a}$$

$$\begin{aligned} -(D_1D_4 - D_2D_3)S' =& (D_4D_{1,U} - D_2D_{3,U})S^2 + (D_4D_{2,V} - D_2D_{4,V})W^2 \\ &+ (D_4D_{1,V} - D_2D_{3,V} + D_4D_{2,U} - D_2D_{4,U})SW \\ &+ D_4(F_1 - F_2) - D_2(G_1 - G_2) - c(D_2W - D_4S); \end{aligned} \tag{2.15b}$$

$$V' = W; \tag{2.15c}$$

$$\begin{aligned} (D_1D_4 - D_2D_3)W' =& (D_3D_{1,U})S^2 + (D_3D_{2,V} - D_1D_{4,V})W^2 \\ &+ (D_3D_{1,V} - D_1D_{3,V} + D_3D_{2,U} - D_1D_{4,U})SW \\ &+ D_3(F_1 - F_2) - D_1(G_1 - G_2) - c(D_1W - D_3S). \end{aligned} \tag{2.15d}$$

It is clear from the restrictions A1 and A3, detailed in Section 2.2, that there are two steady states of system (2.15), i.e.:

$$(U_s,S_s,V_s,W_s) = (0,0,V^*,0) \quad \text{and} \quad (U_s,S_s,V_s,W_s) = (U^*,0,V^*,0).$$

For the first steady state, the reaction term in (2.13b) implies that V cannot grow significantly large compared to U. Therefore, the first steady state with $V^* > 0$ is not relevant for the given initial conditions. Hence, we consider only the case where $V^* = 0$ for the first steady state.

The U,V components of solutions must be non-negative and bounded to guarantee their biological relevance. Therefore, we require the eigenvalues of the Jacobian matrix at the trivial steady state to be real, so that as we approach the trivial steady state, there will be no oscillations in the solution.

Next, we will linearise the ODE system (2.15) around the trivial steady state and solve for the eigenvalues in the usual way. We assume that the solution to system (2.15) has the following form:

$$U(z) = U_s + U_1(z), \quad S(z) = S_s + S_1(z), \quad V(z) = V_s + V_1(z), \quad W(z) = W_s + W_1(z),$$

where $|U_1| \ll 1, |S_1| \ll 1, |V_1| \ll 1, |W_1| \ll 1$ are small perturbations, and $(U_s, S_s, V_s, W_s) = (0,0,0,0)$. Substituting the assumed form of solutions into system (2.15) gives the equations that the small perturbations satisfy:

$$U_1' = S_1; \tag{2.16a}$$

$$\begin{aligned} -(D_1^* D_4^* - D_2^* D_3^*) S_1' =& D_4^*(F_1'^* - F_2'^*) U_1 - D_2^*(G_1'^* - G_{2,U}^*) U_1 + D_2^* G_{2,V}^* V_1 \\ & - cD_2^* W_1 + cD_4^* S_1; \end{aligned} \tag{2.16b}$$

$$V_1' = W_1; \tag{2.16c}$$

$$\begin{aligned} (D_1^* D_4^* - D_2^* D_3^*) W_1' =& D_3^*(F_1'^* - F_2'^*) U_1 - D_1^*(G_1'^* - G_{2,U}^*) U_1 + D_1^* G_{2,V}^* V_1 \\ & - cD_1^* W_1 + cD_3^* S_1, \end{aligned} \tag{2.16d}$$

where the superscript * indicates the evaluation of the function at the trivial steady state. Denoting $A = D_1^* D_4^* - D_2^* D_3^*$ for simplicity, the corresponding Jacobian matrix is given by

$$J = \begin{pmatrix} 0 & 1 & 0 & 0 \\ -\frac{D_4^*(F_1'^* - F_2'^*) - D_2^*(G_1'^* - G_{2,U}^*)}{A} & -\frac{cD_4^*}{A} & -\frac{D_2^* G_{2,V}^*}{A} & \frac{cD_2^*}{A} \\ 0 & 0 & 0 & 1 \\ \frac{D_3^*(F_1'^* - F_2'^*) - D_1^*(G_1'^* - G_{2,U}^*)}{A} & \frac{cD_3^*}{A} & \frac{D_1^* G_{2,V}^*}{A} & -\frac{cD_1^*}{A} \end{pmatrix},$$

and the associated characteristic equation for the eigenvalues is as follows:

$$\lambda^2\left[\left(\lambda+\frac{D_4^*}{A}c\right)\left(\lambda+\frac{D_1^*}{A}c-\frac{D_2^*D_3^*}{A^2}c^2\right)\right]+\lambda\left[-\left(\lambda+\frac{D_4^*}{A}c\right)\frac{D_1^*}{A}G_{2,V}^*+\frac{D_2^*D_3^*}{A^2}G_{2,V}^*c\right]$$
$$+\lambda\left[\left(\lambda+\frac{D_1^*}{A}c\right)\frac{D_4^*(F_1'^*-F_2'^*)-D_2^*(G_1'^*-G_{2,U}^*)}{A}-\frac{D_3^*(F_1'^*-F_2'^*)-D_1^*(G_1'^*-G_{2,U}^*)}{A^2}D_2^*c\right]$$
$$-\frac{D_4^*(F_1'^*-F_2'^*)-D_2^*(G_1'^*-G_{2,U}^*)}{A^2}D_1^*G_{2,V}^*+\frac{D_3^*(F_1'^*-F_2'^*)-D_1^*(G_1'^*-G_{2,U}^*)}{A^2}D_2^*G_{2,V}^*=0. \tag{2.17}$$

According to (2.3), we have $D_2^*=D_3^*=0$ where the superscript * indicates the evaluation at $(U,V)=(0,0)$. Therefore, $A=D_1^*D_4^*$ and equation (2.17) can be simplified further to

$$\lambda^2\left(\lambda+\frac{c}{D_1^*}\right)\left(\lambda+\frac{c}{D_4^*}\right)-\lambda\left(\lambda+\frac{c}{D_1^*}\right)\frac{G_{2,V}^*}{D_4^*}+\lambda\left(\lambda+\frac{c}{D_4^*}\right)\frac{F_1'^*-F_2'^*}{D_1^*}-\frac{F_1'^*-F_2'^*}{D_1^*D_4^*}G_{2,V}^*=0,$$

which leads to

$$\left(\lambda^2+\frac{c}{D_1^*}\lambda+\frac{F_1'^*-F_2'^*}{D_1^*}\right)\left(\lambda^2+\frac{c}{D_4^*}\lambda-\frac{G_{2,V}^*}{D_4^*}\right)=0. \tag{2.18}$$

It is reasonable to assume that $D_1^*\geq 0$ and $D_4^*\geq 0$. This is because the self-diffusion exists in the absence of the interaction between the cells and the EPS matrix. Hence, it is clear from the restriction A6 that the second bracket in (2.18) has two real solutions. In order to guarantee that all the solutions of (2.18) are real, we require that the roots of the first bracket in (2.18) to be real. Hence, the necessary condition for this is:

$$c\geq c_{min}=2\sqrt{D_1^*(F_1'^*-F_2'^*)}, \tag{2.19}$$

where $F_1'^*-F_2'^*>0$ from restriction A5.

The expression of c_{min} in (2.19) indicates that the minimum speed of the spreading of leading edge of the biofilm depends on the self-diffusion of cells and the net cell growth rate at the leading edge. It is noticeable that c_{min} is independent of variable V, which is the EPS concentration, and the EPS net production function $G_1 - G_2$. It is purely the kinetics of the self-diffusing and proliferating cells that determine the travelling wave speed. We discuss this conclusion in more detail later.

2.3.2 Numerical Simulation of Specific Model

Next, we will present numerical simulations of model (2.12) after specifying the expressions for $D_i(u,v)$ where $i = 1,2,3,4$ and the reaction terms F_1, F_2, G_1 and G_2, in order to illustrate and explore further the theoretical results we have obtained from the travelling wave analysis. Similar results can also be obtained for other combination of $D_i(u,v)$ and F_1, F_2, G_1, G_2.

We assume that the self diffusions of cells and EPS molecules follow the Fickian diffusion. Therefore, flux D_1 and D_4 are chosen to be constants. We specify $D_2(u,v) = D_2 u$, which is consistent with the assumption (2.3). As for $D_3(u,v)$, we assume that the EPS molecules, which are pushed around by the cells, is proportional to the EPS concentration, i.e. $D_3(u,v) = D_3 v$ to satisfy assumption (2.3).

From the modelling point of view, logistic population growth has been widely used to represent the source term of cell dynamics. Therefore, we specify the cell growth and death term in the dimensionless form to be $F_1 - F_2 = \rho u(\delta - u)$, where ρ and δ represent the birth rate and carrying capacity of the environment respectively. This form of reaction term satisfies the assumptions A1 to A5. As for the reaction term for the EPS concentration, it is reasonable to assume that the consumption of EPS is proportional to both the cell density and the EPS concentration. Therefore, we assume

that $G_2(u,v) = \eta uv$. This expression satisfies assumption A6. The amount of EPS produced is related to the cell density and the more cells exist, the more EPS is produced. Therefore, we choose $G_1(u) = \beta u^2$. Combining the specific expressions of $G_1(u)$ and $G_2(u,v)$ together, it implies that the EPS produced is limited by the amount of cells. It can be shown that η can be rescaled into the non-dimensional form of v, so without loss of generality, we consider $\eta = 1$. Hence, system (2.12) becomes:

$$\frac{\partial u}{\partial \tau} = [D_1 u_r + D_2 u v_r]_r + \rho u(\delta - u), \tag{2.20a}$$

$$\frac{\partial v}{\partial \tau} = [D_3 v u_r + D_4 v_r]_r + \beta u^2 - uv. \tag{2.20b}$$

We apply the no-flux boundary conditions for system (2.20). The initial conditions for system (2.20) are given by

$$u(r,0) = \begin{cases} 1, & \text{for} \quad |r| \leq H \\ 0, & \text{for} \quad |r| > H \end{cases} \tag{2.21}$$

and

$$v(r,0) = 0 \quad \text{for} \quad |r| \in [0,50]. \tag{2.22}$$

Following [129, 130], the default parameter values are chosen to be: $\delta = 20, \rho = 0.01$, $\beta = 0.2$ and $H = 5$.

System (2.20) has steady states: $(u_s, v_s) = (0, v^*)$ where v^* is any constant, and $(u_s, v_s) = (\delta, \beta\delta)$. However, the reaction term in (2.20b) implies that v cannot grow significantly large compared to u. Therefore, the steady state $(u_s, v_s) = (0, v^*)$ with $v^* > 0$ is not relevant for the given initial conditions. Hence, we consider only $(u_s, v_s) = (0,0)$ and $(u_s, v_s) = (\delta, \beta\delta)$.

System (2.20) can be solved numerically by using the MATLAB PDEPE package. The

script used for solving this system is given in Appendix 8.2. In the simulation, we took 21 snapshots of profile of the cell density from time 0 to 100. Figure 2.3 shows the numerical solutions of the system (2.20) with the default parameter values. Initially, the cell density increases both up and along the r axis, and it tends monotonically to the non-trivial steady state value of $u = \delta$. Eventually, the cell density profile appears fixed and moves along at an apparent constant speed.

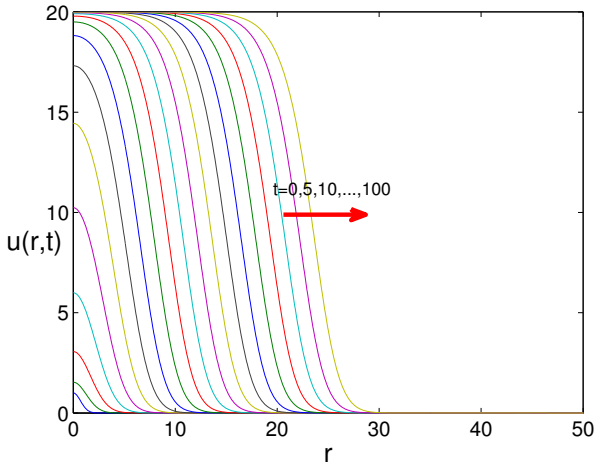

Figure 2.3: Time evolution of the cell density $u(r,t)$ of system (2.20) with the default parameter values in r direction. The cross-diffusion coefficients are chosen to be $D_1 = 0.1, D_3 = 0.1, D_2 = 0.005$ and $D_4 = 0.5$, and other parameters are chosen as: $\delta = 20, \rho = 0.01$, $\beta = 0.2$ and $H = 5$.

From the travelling wave analysis we found that the wave speed is determined by (2.19). Substituting the specific form of the reaction terms and the cross-diffusion terms of system (2.20) into (2.19) yields the theoretical travelling wave speed which is given as follows:

$$c \geq c_{min} = 2\sqrt{D_1 \rho \delta}. \tag{2.23}$$

Next, we will investigate from the numerical solutions of (2.20) how the simulated travelling wave speed changes with parameters ρ, δ and D_1 and how the simulated travelling wave speed compares to the theoretical one.

First of all, we will give the idea of how the simulated travelling wave speed was calculated. The corresponding script can be found in Appendix 8.2. It is clear from (2.23) that the minimum travelling wave speed is independent of D_2 and D_3. It will be shown in the next section that the non-trivial steady state of system (2.20) is stable when $D_2^* = 0$, in which case the solution of (2.20) presents a compact support that is of the form as shown in Figure 2.3. Hence, in order to simplify the problem, we will consider the case where $D_2^* = 0$, i.e. $D_2 = 0$ in system (2.20). We numerically solved system (2.20) with the given parameter values, one of which varied for each simulation. Then for each time point, we looked for the r coordinate of the solution of u that becomes zero at the first time as r increases. We stored these r coordinates for each time point in a vector as $\vec{R} = (r(t_1), r(t_2), ..., r(t_n))$, and finally computed the speed of the travelling wave by

$$c_{computed} = \frac{1}{n-2} \sum_{i=2}^{i=n} \frac{r(t_i) - r(t_{i-1})}{\Delta t}.$$

Figure 2.4(a) shows the wave speed of the cell density when ρ varies from the default value $\rho = 0.01$ to $\rho = 0.03$. It can be seen from the figure that the simulated wave speed, shown in blue, increases with ρ in the similar manner as the expression of c_{min} in (2.23). Figure 2.4(b) shows the simulated wave speed of the cell density when δ increases from $\delta = 10$ to the default value $\delta = 20$. Similarly, the simulated wave speed increases with δ in the similar manner as the expression of c_{min} in (2.23). Figure 2.4(c) shows the simulated wave speed of the cell density when D_1 varies from $D_1 = 0.1$ to $D_1 = 5$. It can be seen from Figure 2.4(c) that the simulated wave speed also increases with D_1 in the similar manner as the expression of c_{min} in (2.23). Figure 2.4(d) shows that the wave speed remains constant when β increases. It is also clear from Figure 2.4 that the wave speed calculated from the numerical solutions of (2.20) is larger but very close to the theoretical minimum wave speed c_{min} which is given by (2.23).

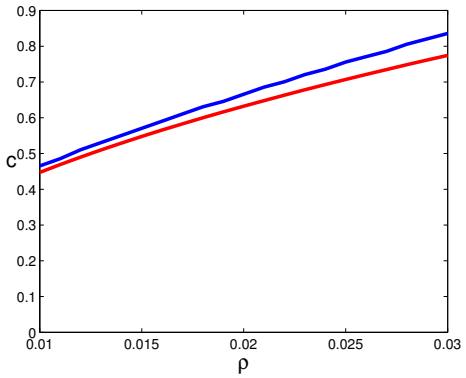

(a) Travelling wave speed changes with ρ.

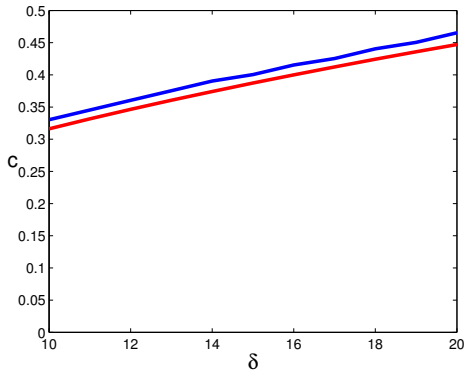

(b) Travelling wave speed changes with δ.

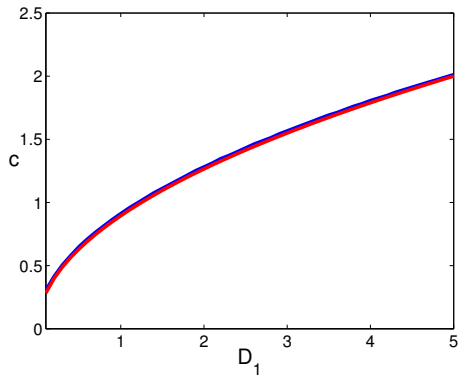

(c) Travelling wave speed changes with D_1.

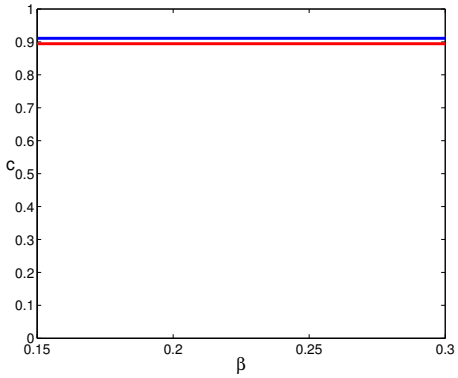

(d) Travelling wave speed changes with β.

Figure 2.4: Comparison of the theoretical minimum travelling wave speed (red) and the simulated travelling wave speed (blue) of system (2.20) and all the other parameters are the same as used in Figure 2.3.

2.4 Instability Conditions for the Reaction-Diffusion System with Cross-Diffusion

It can be seen from the experimental images of the wild-type biofilm and the *eps* mutant biofilm shown in Figure 6.1 in Chapter 6 that the wild-type biofilm exhibits the wrinkling pattern formation in the angular direction in the region where the radius is large after 24 hours, whilst the *eps* mutant biofilm exhibits a flat biofilm over time. The experimental observations suggest that the EPS matrix in the biofilm may play a significant role on the angular pattern formation. Therefore, in this section, we will

investigate how the EPS matrix affects the angular pattern formation of the biofilm.

2.4.1 Instability Analysis

By assuming that all variables depend on θ only, i.e. assuming $r = R$, for some constant and sufficiently large R, system (2.11) becomes

$$\frac{\partial u}{\partial \tau} = \frac{1}{R^2}[D_1(u,v)u_\theta]_\theta + \frac{1}{R^2}[D_2(u,v)v_\theta]_\theta + F_1(u) - F_2(u), \tag{2.24a}$$

$$\frac{\partial v}{\partial \tau} = \frac{1}{R^2}[D_3(u,v)u_\theta]_\theta + \frac{1}{R^2}[D_4(u,v)v_\theta]_\theta + G_1(u) - G_2(u,v). \tag{2.24b}$$

It is clear from the restrictions A1 and A3 placed on the reaction terms that there is a non-zero steady state $(u^*, v^*) = (u_s, v_s)$ and a trivial steady state $(u^*, v^*) = (0,0)$ of (2.24). Assuming that the full solution to system (2.24) is of the form

$$u(\theta,\tau) = u^* + u_1(\theta,\tau), \quad v(\theta,\tau) = v^* + v_1(\theta,\tau), \tag{2.25}$$

where $|u_1| \ll 1, |v_1| \ll 1$, system (2.24) can be linearised around the steady state and the equations for the small perturbations are as follows:

$$u_{1,\tau} = \frac{D_1^*}{R^2}u_{1,\theta\theta} + \frac{D_2^*}{R^2}v_{1,\theta\theta} + \left(F_1'^* - F_2'^*\right)u_1, \tag{2.26a}$$

$$v_{1,\tau} = \frac{D_3^*}{R^2}u_{1,\theta\theta} + \frac{D_4^*}{R^2}v_{1,\theta\theta} + \left(G_1'^* - G_{2,u}^*\right)u_1 - G_{2,v}^* v_1. \tag{2.26b}$$

Here the superscript * denotes the evaluation at the steady state. Since we wish to study the stability of the steady states to perturbations that vary in the angular direction, it is reasonable to assume that the perturbations in (2.25) have the following form: $u_1(\theta,\tau) = u_1(\tau)\cos(k\theta)$ and $v_1(\theta,\tau) = v_1(\tau)\cos(k\theta)$, where k is the wavenumber of the perturbations in the angular direction. Substituting this assumed form into system

(2.26) gives

$$u_1' = \left(-\frac{D_1^*}{R^2}k^2 + F_1'^* - F_2'^*\right)u_1 - \frac{D_2^*}{R^2}k^2 v_1, \tag{2.27a}$$

$$v_1' = \left(-\frac{D_3^*}{R^2}k^2 + G_1'^* - G_{2,u}^*\right)u_1 - \left(\frac{D_4^*}{R^2}k^2 + G_{2,v}^*\right)v_1. \tag{2.27b}$$

The associated Jacobian matrix is given by

$$J = \begin{pmatrix} -\frac{D_1^*}{R^2}k^2 + F_1'^* - F_2'^* & -\frac{D_2^*}{R^2}k^2 \\ -\frac{D_3^*}{R^2}k^2 + G_1'^* - G_{2,u}^* & -\left(\frac{D_4^*}{R^2}k^2 + G_{2,v}^*\right) \end{pmatrix},$$

and corresponding characteristic polynomial

$$\begin{aligned} \lambda^2 + \left(\frac{D_1^*}{R^2}k^2 - F_1'^* + F_2'^* + \frac{D_4^*}{R^2}k^2 + G_{2,v}^*\right)\lambda \\ + \left(\frac{D_1^*}{R^2}k^2 - F_1'^* + F_2'^*\right)\left(\frac{D_1^*}{R^2}k^2 + G_{2,v}^*\right) - \frac{D_2^*}{R^2}k^2\left(\frac{D_3^*}{R^2}k^2 - G_1'^* + G_{2,u}^*\right) = 0. \end{aligned} \tag{2.28}$$

Assuming that the solutions of (2.28) are λ_1 and λ_2, from (2.28) we have

$$\mathscr{R}(\lambda_1) + \mathscr{R}(\lambda_2) = g(k^2) = -\left(\frac{D_1^*}{R^2}k^2 - F_1'^* + F_2'^* + \frac{D_4^*}{R^2}k^2 + G_{2,v}^*\right); \tag{2.29a}$$

$$\begin{aligned} \mathscr{R}(\lambda_1)\mathscr{R}(\lambda_2) &= h(k^2) \\ &= \left(\frac{D_1^*}{R^2}k^2 - F_1'^* + F_2'^*\right)\left(\frac{D_1^*}{R^2}k^2 + G_{2,v}^*\right) - \frac{D_2^*}{R^2}k^2\left(\frac{D_3^*}{R^2}k^2 - G_1'^* + G_{2,u}^*\right). \end{aligned} \tag{2.29b}$$

When $k = 0$, we have $g(0) = (F_1'^* - F_2'^* - G_{2,v}^*)$ and $h(0) = -(F_1'^* - F_2'^*)G_{2,v}^*$. At the trivial steady state, according to the restrictions A5 and A6, we have $h(0) < 0$. This indicates that the solutions of (2.28) are real and of different signs given $k = 0$ at the trivial steady state. Therefore, we can further deduce that the trivial steady state of

system (2.24) is unstable without the angular effect. At the non-trivial steady state, according to the restrictions A5 and A6, we have $h(0) > 0$ and $g(0) < 0$. This result implies that both of the real parts of the solutions of (2.28) are negative. Hence, without the angular effect, the non-trivial steady state of system (2.24) is stable.

We wish to investigate whether the angular effect will destabilise a steady state of system (2.24). Therefore, we will focus on the non-trivial steady state in the following analysis, i.e. from now on, the superscript * is the evaluation of the function at the non-trivial steady state. In order for the instability to occur, we require the real part of at least one of the solutions of (2.28) to be positive.

When $k \neq 0$, the functions $g(k^2)$ and $h(k^2)$ can be rewritten as functions of $m = \frac{k^2}{R^2}$ as follows:

$$g(m) = -(D_1^* + D_4^*)m + F_1'^* - F_2'^* - G_{2,v}^*; \tag{2.30a}$$

$$h(m) = (D_1^* D_4^* - D_2^* D_3^*)m^2 + \left[D_1^* G_{2,v}^* + D_4^*(F_2'^* - F_1'^*) + D_2^*(G_1'^* - G_{2,u}^*)\right] m + G_{2,v}^*(F_2'^* - F_1'^*). \tag{2.30b}$$

We first consider the assumption that $D_1^* > 0$ and $D_4^* > 0$. It is clear from the restrictions A5, A6 that $g(m) < 0$. This result implies that at least one of $\mathscr{R}(\lambda_1)$ and $\mathscr{R}(\lambda_2)$ is negative. In order for the instability to arise, we require only one of $\mathscr{R}(\lambda_1)$ and $\mathscr{R}(\lambda_2)$ to be negative, i.e. $h(m) = \mathscr{R}(\lambda_1)\mathscr{R}(\lambda_2) < 0$ for some $m > 0$. Notice that $h(m)$ is a quadratic in m of the form $h(m) = am^2 + bm + c$. We will derive the condition for the instability to occur in two cases: $D_1^* D_4^* - D_2^* D_3^* > 0$ and $D_1^* D_4^* - D_2^* D_3^* < 0$.

In the case where $D_1^* D_4^* - D_2^* D_3^* > 0$, in order to have $h(m) < 0$ for some $m > 0$, we require $b < 0$ and $b^2 - 4ac > 0$. Therefore, substituting the expression of a, b, c from

(2.30b) into these two inequalities yields:

$$D_1^* G_{2,v}^* + D_4^*(F_2'^* - F_1'^*) + D_2^*(G_1'^* - G_{2,u}^*) < 0 \tag{2.31a}$$

$$\left[D_1^* G_{2,v}^* + D_4^*(F_2'^* - F_1'^*) + D_2^*(G_1'^* - G_{2,u}^*)\right]^2 > 4(D_1^* D_4^* - D_2^* D_3^*) G_{2,v}^*(F_2'^* - F_1'^*) \tag{2.31b}$$

Inequalities (2.31) are the conditions for the instability to occur in the case where $D_1^* D_4^* - D_2^* D_3^* > 0$. In the case where $D_1^* D_4^* - D_2^* D_3^* < 0$, it is clear that $h(m) < 0$ for large values of m.

Next, we will consider a special combination of D_i, which will be discussed later in the next section. In this case, we assume that $D_1^* = 0, D_2^* < 0, D_3^* > 0$ and $D_4^* < 0$. The biological assumptions implied in this situation will be explained later in this chapter. It is clear from (2.30a) that in this case, $g(m) > 0$ for large wavenumber m. Hence, at least one of the real part of the eigenvalues is positive. Accordingly, this result implies that the non-trivial steady state is unstable for large wavenumber m.

Clearly from the discussion above, the stability of the non-trivial steady state to small spatial perturbations depends on values of D_i, where $i = 1, 2, 3, 4$. We will consider the stability of the non-trivial steady state of system (2.24) with different combinations of the values of D_i. Biologically, the EPS molecules are 'pushed' away by the cells. Therefore, it is reasonable to assume that $D_3 \geq 0$. Next, we will give the result of the stability of the non-trivial steady state to small spatial perturbations given likely combination of $D_i, i = 1, 2, 3, 4$. The result is shown in Table 2.1. It can be seen from Table 2.1 that the spatial pattern can only occur under the situation where either $D_2^* D_3^* > 0$ or $D_2^* < 0$.

Case	D_1^*	D_2^*	D_3^*	D_4^*	Pattern
1	$+$	$+$	$+$	$+$	$D_1^*D_4^* - D_2^*D_3^* > 0$: No pattern $D_1^*D_4^* - D_2^*D_3^* < 0$: Pattern occurs when m is large
2	$+$	$+$	$+$	0	Pattern occurs when m is large
3	$+$	$+$	0	$+$	No pattern
4	$+$	$+$	0	0	No pattern
5	$+$	0	$+$	$+$	No pattern
6	$+$	0	$+$	0	No pattern
7	$+$	0	0	$+$	No pattern
8	$+$	0	0	0	No pattern
9	$+$	$-$	$+$	$+$	Pattern for a range of m if (2.31) are satisfied
10	$+$	$-$	$+$	0	Pattern for a range of m if (2.31) are satisfied
11	$+$	$-$	0	$+$	Pattern for a range of m if (2.31) are satisfied
12	$+$	$-$	0	0	$D_1^*G_{2,v}^* + D_2^*(G_1'^* - G_{2,u}^*) > 0$: No pattern $D_1^*G_{2,v}^* + D_2^*(G_1'^* - G_{2,u}^*) < 0$: Pattern occurs when m is large
13	0	$-$	$+$	$-$	Pattern for a range of m

Table 2.1: Likely combination of D_i and the corresponding pattern formation

2.4.2 1-D Numerical Simulations of Two Specific Models

In this section, we will simulate system (2.24) in the θ direction with specified terms to illustrate the stability of the system. However, similar results can be obtained for other models. The reaction terms used in this section are the same as the ones used in system (2.20). Hence, the general form of the model that will be solved numerically in the θ direction is given as follow:

$$\frac{\partial u}{\partial \tau} = \frac{1}{R^2}[D_1(u,v)u_\theta]_\theta + \frac{1}{R^2}[D_2(u,v)v_\theta]_\theta + \rho u(\delta - u), \tag{2.32a}$$

$$\frac{\partial v}{\partial \tau} = \frac{1}{R^2}[D_3(u,v)u_\theta]_\theta + \frac{1}{R^2}[D_4(u,v)v_\theta]_\theta + \beta u^2 - uv, \tag{2.32b}$$

where R is the radius of interest and is set to be a constant. It is clear that system (2.32) has one trivial steady state and one non-trivial steady state which is given by $(u^*, v^*) = (\delta, \beta\delta)$. We will specify the diffusion terms in (2.32) according to the hypotheses of how the EPS matrix affects the cell movement later in this section.

System (2.32) is solved numerically with COMSOL 4.2 along the θ direction $\theta \in [0, 2\pi]$. As can be seen from the experimental images in Figure 6.1 in Chapter 6, initially, the biofilm represents a circular shape, which implies that the cell density is uniform in the θ direction. In order to instigate instability, we also require some randomness for the initial condition. Therefore, the initial cell density is chosen to be a uniform distribution with mean of 1 and $u(\theta, 0) \in [0.5, 1.5]$. Initially, we assume that there is no EPS in the system. As a summary, the initial conditions we use in the simulations are given by:

$$u(\theta, 0) = u^*(\theta), \quad \text{where} \quad u^* \in [0.5, 1.5]; \tag{2.33a}$$

$$v(\theta, 0) = 0. \tag{2.33b}$$

To be realistic, the boundary conditions are chosen to be periodic, i.e.

$$u(0, \tau) = u(2\pi, \tau), v(0, \tau) = v(2\pi, \tau). \tag{2.34}$$

Following [129, 130], the default parameter values are chosen to be:

$$\delta = 20, \rho = 0.01, \beta = 0.2. \tag{2.35}$$

Hypothesis 1: Haptotaxis

We first hypothesise that cells move towards higher EPS concentration by haptotaxis, and the more EPS there is, the stronger the haptotaxis force is. Therefore, we assume that cells move towards the higher EPS concentration. Mathematically, this hypothesis can be modelled by the cross-diffusion $D_2(u, v)$. In addition, we assume that $D_2(u, v)$ is a linear function of cell density, i.e. $D_2(u, v) = -D_2 u$. Furthermore, we assume that at the early development of the biofilm, cells can diffuse according to Fick's law, i.e.

$D_1(u,v) = D_1$. Since the EPS molecules are of high weight and are sticky enough, we assume that EPS molecules are so sticky that they cannot diffuse, i.e. $D_4 = 0$. However, the EPS molecules can be 'pushed' away by the diffusion of cells, and this movement is a linear function of the EPS concentration, i.e. $D_3(u,v) = D_3 v$. In this way, the system we will solve numerically is given as:

$$\frac{\partial u}{\partial \tau} = \frac{1}{R^2}[D_1 u_\theta]_\theta - \frac{1}{R^2}[D_2 u v_\theta]_\theta + \rho u(\delta - u), \tag{2.36a}$$

$$\frac{\partial v}{\partial \tau} = \frac{1}{R^2}[D_3 v u_\theta]_\theta + \beta u^2 - uv, \tag{2.36b}$$

where R is the radius of interest and is set to be a constant. The boundary conditions are stated in (2.34) and the initial conditions used in the numerical simulations are shown in (2.33).

This model corresponds to case 10 in Table 2.1. Therefore, according to the stability result given in Table 2.1, the non-trivial steady state should be unstable in the θ direction if (2.31) are satisfied, or stable otherwise.

System (2.36) was solved with COMSOL 4.2 in 1-D where R was from $R = 5$ to $R = 30$. Figure 2.5(a) shows the numerical simulation of the cell density of system (2.36) at $\tau = 0, 10, 20, 30$ when $R = 5$. It is clear that initially, the cell density increases almost uniformly along the θ direction. Later on, the cell density aggregates at certain angles.

Then for each value of R we took the solution as a function of θ only at the fixed time point $\tau = 60$. Then we mapped $u(\theta)$ back to Cartesian coordinates by $x = R\cos\theta, y = R\sin\theta$ and $u(x,y) \equiv u(\theta)$. Then we plotted the points (x,y) red where $u(x,y) < 20$ and we plotted the points blue where $u(x,y) > 20$. Here, the threshold $u(x,y) = 20$ is chosen to be the steady state of the cell density. This plot is shown in Figure 2.5(b). As can be seen, the radial pattern formation is generated in this simulation, which

resembles the outer region of the wild-type biofilm shown in Figure 6.1 in Chapter 6. We also notice that as we increase the radius, more radial pattern is formed.

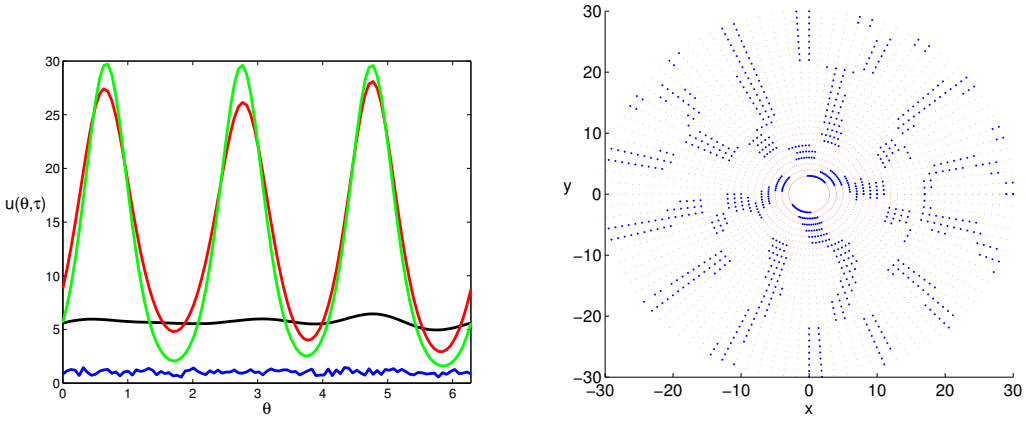

(a) $u(\theta,\tau)$ at $\tau = 0, 10, 20, 30$.

(b) $u(\theta, 60)$ for varied radius plotted in Cartesian coordinate.

Figure 2.5: Numerical simulation of system (2.36) with the default parameter values (2.35) and $D_1 = 0.25$, $D_2 = -1$ and $D_3 = 1$. Figure 2.5(a) is the 1-D solution of cell density u at time $\tau = 0$(blue), 10(black), 20(red) and 30(green). Figure 2.5(b) is the corresponding 2-D profile with different radius plotted in the (x, y) plane. The red dots indicate $u(\theta, 60) < 20$ and the blue dots indicate $u(\theta, 60) > 20$.

Hypothesis 2: Contraction

In this part, we will discuss the other possible function of the EPS matrix which may result in the spatial pattern formation. In experiments, it is clear that both the agar plate and the biofilm that is growing on the surface of the agar plate dry out at the later stage of the biofilm development. Accordingly, we hypothesise that the EPS matrix contracts due to the drying of agar in a well developed biofilm. Next, we will specify the diffusion terms for this hypothesis according to the biological information.

Biologically, it has been shown that the secretion of EPS molecules and the cell motility are controlled by the same protein called *SinR*. This protein promotes the cell motility but inhibits the EPS secretion. Once cells start to produce EPS molecules, less *SinR* protein is produced and therefore the cell motility is inhibited [20]. According to this

information, it is reasonable to assume that $D_1 = 0$ for the well developed biofilm. To model the contracting effect of EPS matrix on the biofilm development, we assume that both the cells and the EPS molecules will move towards the location where the EPS matrix is of higher concentration, i.e. $D_2(u,v) < 0, D_4(u,v) < 0$. In addition, we assume that D_2 is a linear function of cell density and D_4 is a linear function of the EPS concentration, i.e. $D_2(u,v) = -D_2 u, D_4(u,v) = -D_4 v$, where $D_2 > 0, D_4 > 0$. Similar as in the first hypothesis, we assume that the EPS molecules can be 'pushed' away by the cells and this movement is a linear function of the EPS concentration, i.e. $D_3(u,v) = D_3 v$, where $D_3 > 0$. In this way, the system we will solve numerically is given by:

$$\frac{\partial u}{\partial \tau} = -\frac{1}{R^2}[D_2 u v_\theta]_\theta + \rho u(\delta - u), \tag{2.37a}$$

$$\frac{\partial v}{\partial \tau} = \frac{1}{R^2}[D_3 v u_\theta]_\theta - \frac{1}{R^2}[D_4 u v_\theta]_\theta + \beta u^2 - uv, \tag{2.37b}$$

where R is the radius of interest and is set to be a constant. The boundary conditions are stated in (2.34) and the initial conditions used in the numerical simulations are shown in (2.33).

This model corresponds to case 13 in Table 2.1. Therefore, according to the stability result given in Table 2.1, the non-trivial steady state should be unstable in the θ direction when the wavenumber is large.

System (2.37) was solved with COMSOL 4.2 in 1-D where R was from $R = 5$ to $R = 30$, excluding $R = 6, 11, 19, 26, 27$, all of which cause difficulty in the numerical simulation. Figure 2.6(a) shows the numerical simulation of the cell density of system (2.37) at $\tau = 0, 10, 20, 30$ when $R = 5$. Same as the previous model, initially the cell density increases almost uniformly along the θ direction. Later on, the cell density aggregates at certain angles.

Then for each value of R, we took the solution as a function of θ only at the fixed time point $\tau = 30$. Here we chose $\tau = 30$ because at later time point, the solution is unstable for large wavenumber that causes difficulty in the numerical simulation. Then we mapped $u(\theta)$ back to Cartesian coordinates by $x = R\cos\theta$, $y = R\sin\theta$ and $u(x,y) \equiv u(\theta)$. Then we plotted the points (x,y) red where $u(x,y) < 20$ and we plotted the points blue where $u(x,y) > 20$. Here, the threshold $u(x,y) = 20$ is chosen to be the steady state of the cell density. This plot is shown in Figure 2.6(b). Similar to the numerical result of system (2.36), as can be seen, the radial pattern formation is generated in this simulation too. This resembles the outer region of the wild-type biofilm shown in Figure 6.1 in Chapter 6. We also notice that as we increase the radius, more radial pattern is formed.

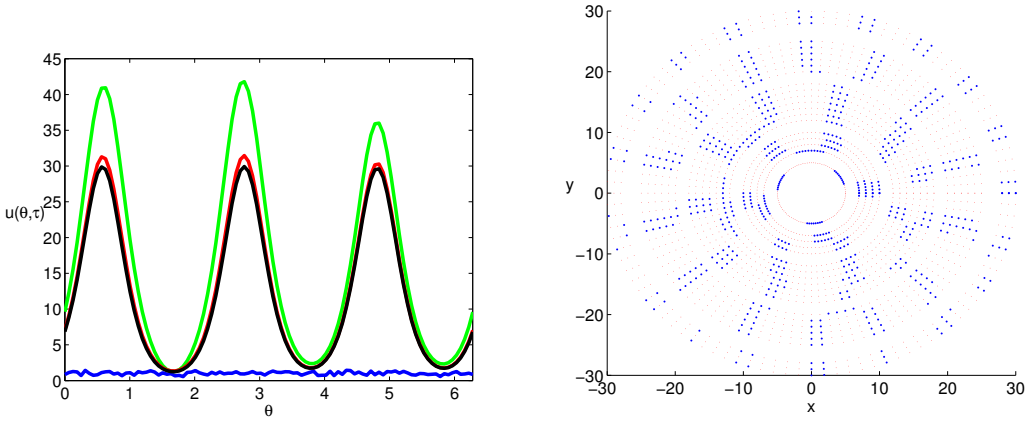

(a) $u(\theta,\tau)$ at $\tau = 0, 10, 20, 30$.

(b) $u(\theta, 30)$ for varied radius plotted in Cartesian coordinate.

Figure 2.6: Numerical simulation of system (2.37) with the default parameter values (2.35) and $D_1 = 0$, $D_2 = -1$, $D_3 = 1$ and $D_4 = -1$. Figure 2.6(a) is the 1-D solution of cell density u at time $\tau = 0$(blue), 10(black), 20(red) and 30(green). Figure 2.6(b) is the corresponding 2-D profile with different radius plotted in the (x,y) plane. The red dots indicate $u(\theta,30) < 20$ and the blue dots indicate $u(\theta,30) > 20$.

From these two hypotheses and the stability result shown in Table 2.1, it can be concluded that the spatial pattern can occur under both hypotheses. Therefore, we can

further conclude that cells in the biofilm may move towards the higher EPS concentration by haptotaxis or the EPS matrix may be able to contract the biofilm due to its stickiness when the agar dries out.

2.5 Conclusion

In this chapter, we constructed a general form of reaction-diffusion system that considered the cross-diffusion effect between the cells and the EPS matrix. We used this model to investigate the function of the EPS matrix on both the observed pattern formation and the biofilm expansion.

We conducted the travelling wave analysis in the radial direction to study what determines expansion speed of the biofilm. We found that the minimum travelling wave speed is determined solely by the self-diffusion of cells and the net cell growth rate at the leading edge. This minimum travelling wave speed is independent on any information of the EPS concentration in the system. However, this contradicts the experimental observation in Figure 6.1. Experimentally, the *eps* mutant which is defected with the EPS matrix expands much more slowly than the wild-type. We suggest that the reaction-diffusion approach between the cells and the EPS matrix may not be sufficiently enough to explain this phenomena.

Experimentally, we found that the *eps* mutant does not exhibit the spatial pattern that can be observed in the wild-type biofilm. In this chapter, we applied stability analysis in the angular direction to study this. We considered two different hypotheses regarding possible effects of the EPS matrix on the cell movement: the first hypothesis was that the cells move towards the higher EPS concentration by haptotaxis and the second hypothesis was that the EPS matrix contracts the biofilm system when the agar dries out. We found that a spatial pattern can occur under both of these two hypotheses. The

first hypothesis suggests that the cells might move towards the higher EPS concentration by haptotaxis. However, there is no literature that supports this hypothesis. The second hypothesis suggests that the EPS matrix might contribute to the contraction of the biofilm when the agar dries out at the later stage of the biofilm development. However, this hypothesis requires more experimental result to support.

Since the result of the travelling wave analysis contradicts to the experimental observation and there is no evidence to support the two hypotheses we proposed for the spatial pattern formation, we can conclude that the cross-diffusion effect between the cells and the EPS molecules may not be the essential cause for the biofilm expansion and the spatial pattern formation. In the remaining of this thesis, we will adapt other approaches to study the reason of the difference on the biofilm expansion between the wild-type and the *eps* mutant as well as the spatial pattern formation.

Chapter 3

Expansion of Biofilms Driven by Growth Pressure

3.1 Introduction

In the previous chapter, with a general form of reaction-diffusion approach, we found out that the EPS matrix does not affect the spreading speed of the biofilm, and the EPS matrix might be the key component for the spatial pattern formation. In this chapter, we will investigate the cell 'pushing' effect as the mechanism that may be responsible for the expansion of the biofilm.

This piece of work is an extension of the model proposed by Dockery and Klapper [37]. We first give the detailed construction of model with appropriate assumptions. We then show an alternative way of looking for the 1-D planar solution of the model when the biofilm is assumed to be infinitely thick to the method used in [37]. Then, we consider the stability of the 1-D planar solution.

Later in the chapter, we extend the model to a domain with finite depth. Then we will

show the 1-D planar solution of the system and finally consider the stability of the 1-D planar solution.

Following the model with a domain with finite depth, we add a death rate to the cell growth term. Again, we look for the 1-D planar solution and derive the evolution equation of the biofilm height. Next, we investigate the stability of the planar solution, where we derive a dispersion relation. We finally investigate the effect of the cell death on the linear instability and the important role of the cell death in generating different patterns.

3.2 Model Set Up

3.2.1 Model Construction

Recent improvements in microscopy and imaging techniques have resulted in the realisation that most biofilms are of complex structures. The complex structure of biofilms has been one of the most important areas in biofilm research. De Beer *et al.* [32] have shown that there are interstitial voids extending from the the surface of the biofilm to its base. The voids facilitated oxygen transport from the bulk liquid through the biofilm. Later on, Stoodley *et al.* [121] demonstrated that water can flow through these voids.

It has been of great concern about the cause of the heterogeneity. Dockery and Klapper [37] presented a simple model of a single substrate limited biofilm growing into a static aqueous environment. They found out that the biofilm interface is shown to be linearly unstable to fingering instabilities under certain conditions. Our work in this Chapter will follow the work done by Dockery and Klapper.

The mathematical model proposed in [37] describes a growing biofilm community

in a narrow conduit, mimicking the conditions that occur in soil pores, oil pipes or plant/blood vessels. Normally, the width of biofilms is much larger compared to the height [116, 138]. Therefore, it is assumed that the biofilm is of infinite width. It is observed that biofilms are not of uniform thickness [55, 63]. We wish to understand the processes that cause biofilms to develop such a heterogeneous structure. To study the basic differences between homogeneous and heterogeneous biofilms thickness, we consider the biofilm thickness to be dependent on only the x direction. In addition, the mathematical model is constructed on the mesoscopic scale. Therefore, the computational domain is chosen to be an open subdomain with length w, existing within a longer conduit. In order to eliminate any thin-film effect, it is reasonable to choose w to be of the same order of the height of the conduit.

The model focuses on the second stage of biofilm growth after a sufficiently high cell density is reached. Hence, the bacterial cell density inside the biofilm is considered to be constant throughout this chapter. Two regions are distinguished by the biofilm height $h(x,t) > 0$ which is shown in Figure 3.1: the biofilm region $z_0 < z < h(x,t)$ and the aqueous region $z > h(x,t)$. The coordinate of biofilm-substratum interface, z_0 can take either infinite or a finite value (in this case scaled to 0) for different situations being considered.

The aqueous region is assumed to be static and consists of dissolved substrate. The substrate diffuses within this aqueous region in a standard Fickian manner. Thus, the substrate concentration $s(x,z,t)$ in the aqueous region is governed by

$$s_t = D_1 \nabla^2 s. \tag{3.1}$$

It is reasonably assumed that the substrate concentration far away from the interface does not have any significant effect on biofilm growth. Therefore, far away from the interface, the substrate concentration can be assumed to be a constant. The height

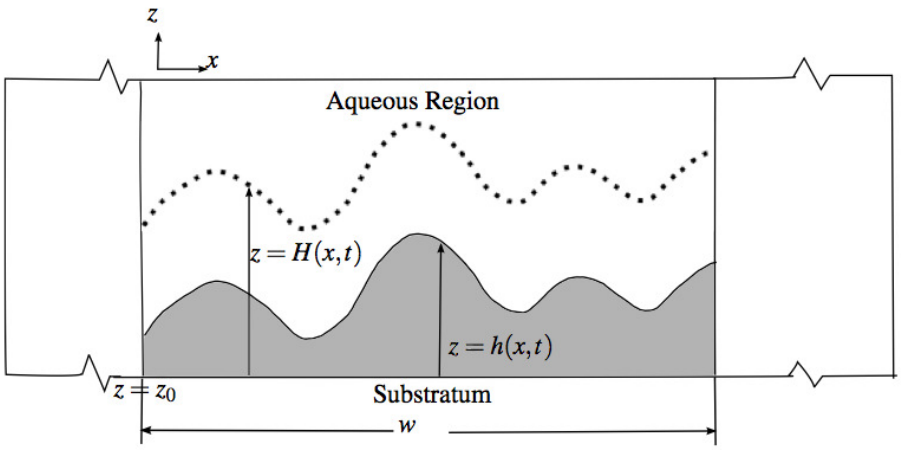

Figure 3.1: Schematic of biofilm, indicating the orientation of axes, with infinite width. The biofilm is defined to be in the region $z_0 < z < h(x,t)$.

above which substrate can be treated as a constant is denoted by $H(x,t) \equiv h(x,t) + L$, where L is a constant.

In the biofilm region, the biofilm expands due to cell growth which is coupled to the availability of the dissolved substrate. Substrate is degraded in the biofilm by the cell growth. Because of the void structure of biofilms, which allows water to flow through, it is reasonable to assume biofilm to be a porous medium from the macroscopical point of view. It is further assumed that cells are in a planktonic state freely swimming within the voids. Under these assumptions, a constitutive relationship exists that relates the velocity of bacterium movement $\mathbf{u} \equiv (u,v)$ and the pressure gradient $\nabla p(x,z,t)$: Darcy's law

$$\mathbf{u} = -\lambda \nabla p, \tag{3.2}$$

where λ is the coefficient defined as the ratio of permeability of the biofilm over the product of medium viscosity and porosity.

By definition, the bacterial mass flux is described as $\mathbf{J} = \rho \mathbf{u}$, where ρ is the bacterial

density which is assumed to be a constant. It is also known from the mass conservation law that

$$\nabla \cdot \mathbf{J} + \frac{\partial \rho}{\partial t} = g, \tag{3.3}$$

where g is the net production of bacteria per unit volume per unit time. Generally speaking, the growth function g is related to both bacterial density and availability of substrate. A further assumption of linear growth is made, which yields

$$g \equiv g(s)\rho. \tag{3.4}$$

From (3.3) and (3.4), the equation for the dynamics of bacterial density is given as follows:

$$\nabla \cdot (\rho \mathbf{u}) + \frac{\partial \rho}{\partial t} = g(s)\rho. \tag{3.5}$$

By setting ρ to be a constant, (3.5) becomes

$$\nabla \cdot \mathbf{u} = g(s) \tag{3.6}$$

for some prescribed net growth function $g(s)$. Hence, combining equations (3.2) and (3.6) yields:

$$-\lambda \nabla^2 p = g(s). \tag{3.7}$$

Equation (3.7) suggests that the pressure gradient in the biofilm is caused by the net growth of bacterial cells. As the bacterial cells grow and divide, cells push each other to expand and therefore causes the movement of the biofilm interface. The net growth approach is viewed as an alternative to the mechanism of random walks as a driving force of cell movement.

In the biofilm region where the fluid is treated as static, the dissolved substrate is transported by the concentration difference rather than the pressure difference. Therefore,

it is assumed that the substrate is transported by Fickian diffusion. However, the effective diffusion coefficient, which describes diffusion through the pore space of porous medium is estimated as [41, 139]:

$$D_2 = \phi_{poro} D_1. \tag{3.8}$$

The parameter ϕ_{poro} is the porosity available for the transport, which is defined as the ratio of the volume of void space over the total volume of the porous medium. Thus, $D_2 < D_1$ always holds.

The substrate is also consumed in the biofilm by cell growth. Usually the substrate consumption is of the form $f(s,\rho)$. However here the cell density is assumed to be a constant, therefore, the substrate consumption rate is denoted as $f(s)$. Therefore, the rate of change of substrate concentration $s(x,z,t)$ with respect to time is given by

$$s_t = D_2 \nabla^2 s - f(s). \tag{3.9}$$

The substrate consumption is necessary for cell growth to occur, and the rate of growth is closely related to the rate at which substrate is consumed. Hence, the net cell growth rate $g(s)$ in (3.4) will be taken to be a function of the substrate consumption rate f, i.e. $g(s) \equiv g(f(s))$.

The differential mass balance equations for the dependent variables $s(x,z,t)$ and $p(x,z,t)$ in both biofilm and aqueous regions can be summarised as:

$$s_t = D_1 \nabla^2 s; \quad h(x,t) < z < H(x,t) \tag{3.10}$$

$$\begin{cases} s_t = D_2 \nabla^2 s - f(s); \\ -\lambda \nabla^2 p = g(f(s)); \end{cases} \quad z_0 < z < h(x,t) \tag{3.11}$$

where $x \in [0, w], z \in [z_0, H(x,t))$.

Next we shall construct the boundary conditions for the system. The computational domain is chosen to be a subdomain of the conduit with infinite width. This is shown by imposing the periodic condition for both pressure $p(x,z,t)$ and substrate concentration $s(x,z,t)$ at $x = 0$ and $x = w$.

The biofilm-substratum interface is impermeable to the biofilm, and therefore the vertical velocity of cell movement is set to be 0. From (3.2), the vertical velocity of cell movement satisfies $v = -\lambda p_z$. Hence, the boundary condition for the growth driven pressure $p(x,z,t)$ at the biofilm-substratum interface is given by

$$p_z(z = z_0) = 0.$$

For the same reason, the flux of substrate $s(x,z,t)$ across the boundary is set to be 0 at the biofilm-substratum interface, i.e.

$$s_z(z = z_0) = 0.$$

The biofilm interface is the solution $z = h(x,t)$ to the zero growth driven pressure, i.e. $p(z = h) = 0$. Therefore, at the biofilm interface, we apply boundary condition $p(z = h) = 0$ to the growth driven pressure. The substrate concentration should change continuously across the biofilm-aqua interface. This requires that the substrate concentration close to the interface in both regions must match, i.e. $s(z = h^+) = s(z = h^-)$. Here, $h^\pm$ refers to z approaching h from above $(+)$ or below $(-)$. In addition, the substrate flux leaving the aqueous region from the biofilm-aqua interface is assumed to enter into the biofilm region directly through the interface. The Robin boundary

condition applied to the diffusive substrate concentration is given by

$$-D_i \nabla s \cdot \mathbf{n} = \text{flux leaving the boundary},$$

where $\mathbf{n}$ is the unit upward normal. Hence, the substrate concentration close to the biofilm-aqua interface approaching from both regions satisfies

$$D_1 \nabla s(z = h^+) \cdot \mathbf{n} = D_2 \nabla s(z = h^-) \cdot \mathbf{n}.$$

The substrate concentration is assumed to remain constant for $z > H(x,t)$. Hence, $s(z = H) \equiv s_\infty$ is defined at the top boundary of the aqueous region.

As a summary, the boundary conditions imposed on the domain are as follow:

$$p(z = h) = 0; p_z(z = z_0) = 0; \tag{3.12a}$$

$$s(z = H) = s_\infty, s_z(z = z_0) = 0; \tag{3.12b}$$

$$s(z = h^+) = s(z = h^-); \tag{3.12c}$$

$$D_1 \nabla s(z = h^+) \cdot \mathbf{n} = D_2 \nabla s(z = h^-) \cdot \mathbf{n}, \tag{3.12d}$$

and periodic in $p(x,z,t)$ and $s(x,z,t)$ at $x = 0$ and $x = w$.

Since the model considers a slab with infinite width, only the changes in the biofilm height will be investigated. At the biofilm interface, i.e. $z = h(x,t)$, if we define an auxiliary function $\Phi = z - h(x,t) = 0$, then we have

$$\Phi_t = \mathbf{u} \cdot \nabla h - h_t = 0,$$

where $\mathbf{u}$ is the velocity of the biofilm interface. With the definition $\mathbf{n} = \frac{\nabla h}{|\nabla h|}$, the above

equation can be rewritten as

$$h_t = |\nabla h| \mathbf{u} \cdot \mathbf{n}.$$

It can be shown that $|\nabla h| = \sqrt{h_x^2 + 1}$. Hence, with the assumption that $h_x \ll 1$, we have $|\nabla h| \approx 1$, i.e. $h_t \approx \mathbf{n} \cdot \mathbf{u}|_{z=h^-}$.

Using (3.2), the normal velocity of the cells at the interface $(x, h(x,t))$ is given by:

$$\mathbf{n} \cdot \mathbf{u}|_{z=h^-} = -\mathbf{n} \cdot \lambda \nabla p|_{z=h^-},$$

then since the velocity of the interface equals the velocity of the cells at the interface

$$\frac{\partial h(x,t)}{\partial t} = -\mathbf{n} \cdot \lambda \nabla p|_{z=h^-}. \tag{3.13}$$

Equations (3.10) and (3.11), together with their boundary conditions (3.12) and the equation for the interface velocity given by (3.13) comprise the biofilm model to be studied in this chapter.

3.2.2 Non-Dimensionalization

Equations (3.10) - (3.11) includes a moving boundary, which makes the system difficult to study. Therefore, we introduce some scaling factors to simplify the model. Dockery and Klapper [37] introduced the system time scale, T, measuring the time scale for the biofilm to increase in height by an $O(w)$. By setting

$$\bar{x} = \frac{x}{w}, \bar{z} = \frac{z}{w}, \bar{h} = \frac{h}{w}, \bar{H} = \frac{H}{w}, \bar{t} = \frac{t}{T}, S = \frac{s}{s_\infty},$$

$$\bar{f}(s) = \frac{f(s)}{f(s_\infty)}, \bar{g}(\bar{f}(s)) = g(f(s)) \frac{s_\infty}{f(s_\infty)}, P = \frac{p}{A}$$

and substituting into the biofilm model (3.10)-(3.11), the nondimensional system can be obtained after dropping bars for simplicity:

$$\begin{aligned}
&\frac{w^2}{D_1 T} S_t - \nabla^2 S = 0; && h(x,t) < z < H(x,t) \\
&\frac{w^2}{D_2 T} S_t - \nabla^2 S = -\frac{w^2}{s_\infty D_2} f(s_\infty) f(s_\infty S); && z_0 < z < h(x,t) \\
&\nabla^2 P = -\frac{w^2}{\lambda A} g(f(s_\infty S)) \frac{f(s_\infty)}{s_\infty}; && z_0 < z < h(x,t)
\end{aligned}$$

with interface evolution equation

$$\frac{w}{T}\frac{\partial h}{\partial t} = -\frac{A\lambda}{w} \mathbf{n} \cdot \nabla P|_{z=h^-}.$$

Letting $A = \frac{w^2}{\lambda T}, G = \frac{w^2}{s_\infty D_2} f(s_\infty)$, and $\varepsilon_i = \frac{w^2}{D_i T}$ yields the nondimensional system as follow:

$$\varepsilon_1 S_t - \nabla^2 S = 0, \qquad h(x,t) < z < H(x,t) \tag{3.14}$$

$$\begin{cases} \varepsilon_2 S_t - \nabla^2 S = -G f(S); \\ \nabla^2 P = -g[f(S)]; \end{cases} \qquad z_0 < z < h(x,t) \tag{3.15}$$

where we have rewritten $f(s_\infty S) = f(S)$. The interface evolution equation is given by

$$\frac{\partial h}{\partial t} = -\mathbf{n} \cdot \nabla P|_{z=h^-}. \tag{3.16}$$

Substituting the desired forms of non-dimensional variables into the boundary conditions (3.12) yields the corresponding dimensionless boundary conditions:

$$P(z=h)=0, P_z(z=z_0)=0; \tag{3.17a}$$

$$S(z=H)=1, S_z(z=z_0)=0; \tag{3.17b}$$

$$S(z=h^+)=S(z=h^-); \tag{3.17c}$$

$$K\nabla S\cdot\mathbf{n}(z=h^+)=\nabla S\cdot\mathbf{n}(z=h^-), \tag{3.17d}$$

where $K=D_1/D_2$. From (3.8), we have $K=1/\phi_{poro}$. Parameter ϕ_{poro} is defined as the ratio of the volume of void space over the total volume of the porous media, and the void space is related to how much EPS there is in the biofilm, i.e. the more EPS matrix, the less the void space is in the biofilm. Hence, K can be viewed as the indicator of how much EPS there is in the biofilm. It can be deduced that $D_2 < D_1$ from the estimation of diffusion coefficient in a porous media. Hence, parameter K is always chosen to be greater than 1 throughout this chapter.

In the process of non-dimensionalisation, G and ε_i are dimensionless parameters. The parameter G is the ratio of the time for the substrate to diffuse in the biofilm over the time needed for the substrate to be consumed at its maximum consumption rate. This is often referred as the *Thiele number* [4, 10, 45, 103], which gives the a measurement of the relative strengths of reaction and diffusion. Usually, a system with a Thiele number $\ll 1$ suggests a reaction limited regime while the system with a Thiele number $\gg 1$ indicates a diffusion limited regime. In the model considered in this chapter, the system is assumed to be diffusion limited. Therefore, $G \gg 1$ will be used throughout the chapter. The non-dimensional parameters $\varepsilon_1.\varepsilon_2$ are numbers comparing the substrate diffusion time in both aqueous region and biofilm region respectively to the biofilm evolution time. Estimating $D_i \approx 10^{-9} m^2/s$ and conservatively, the time for the biofilm evolution $T = 10^5 s$ [57], ε_i can be considered small for biofilm length scales up to

$10^4 \mu m$, which is well within observable level [37]. Hence, by setting $\varepsilon_1 = \varepsilon_2 = 0$ yields the quasi-static description of equations (3.14) and (3.15):

$$\nabla^2 S = 0; \qquad h(x,t) < z < H(x,t) \tag{3.18}$$

$$\begin{cases} \nabla^2 S = Gf(S); \\ \nabla^2 P = -g[f(S)]; \end{cases} \qquad z_0 < z < h(x,t) \tag{3.19}$$

In order to make the system well-posed, some restrictions need to be put on to the form of $f(S)$. First of all, from a biological point of view, when there is no substrate in the biofilm, bacteria growth should stop, whilst in the presence of substrate cells should grow at a positive rate (degeneration is ignored at this stage). Therefore, $f(0) = 0$ and $f(S) > 0$ for $S > 0$. Secondly, $f'(S) \geq 0$ is assumed in this system as the more substrate there is, the faster cells will grow until saturation occurs.

To summarise, equations (3.18) and (3.19), together with the interface dynamic (3.16) and the boundary conditions (3.17) constitute the dimensionless form of biofilm model studied in this chapter.

3.3 Growth and Stability of Deep Biofilms

The original model (3.10) - (3.11) has been reduced to a quasi-static problem after rescaling. However, the interface that separates the biofilm and aqueous regions varies with time. Therefore, both substrate concentration and growth driven pressure are essentially implicit functions of time.

In this section, we will consider an infinite domain with $z_0 = -\infty$ to investigate the existence of solutions to system (3.18) - (3.19). We will start by seeking a solution

with a special structure.

3.3.1 Planar Growth

Dockery and Klapper [37] have shown that there exists a unique solution to system (3.18) - (3.19), with the corresponding boundary conditions (3.17), if the solution is assumed to be uniform in the x direction. This solution is referred to as a planar solution. However, they did not specify whether the planar solution is dependent on the biofilm height or not. By tracking the wave front, we will present an alternative way of finding the planar front solution. By doing this, we are able to derive a dispersion relation that does not depend on the prior knowledge of the biofilm depth. At this stage, we discount the spatial variable x.

We introduce a new variable $a = z - h(t)$ to track the biofilm interface. Hence, the aqueous region is redefined as $0 < a < L$ and the biofilm region becomes $a < 0$, and $a = 0$ defines the biofilm-aqua interface. Writing $S(z,t) = S(a), P(z,t) = P(a)$ in system (3.18) - (3.19) yields:

$$S_{aa} = 0; \qquad 0 < a < L \tag{3.20}$$

$$\begin{cases} S_{aa} = Gf(S); \\ P_{aa} = -g[f(S)], \end{cases} \qquad a < 0 \tag{3.21}$$

The interface evolution equation (3.16) becomes

$$h'(t) = -P_a|_{a=0^-}, \tag{3.22}$$

Notice here, although we have eliminated the biofilm height $h(t)$ in our system, we keep using $h(t)$ as a notation for the purpose of calculating the interface velocity. The

boundary conditions (3.17) become

$$P(a=0)=0, P_a(a=-\infty)=0; \tag{3.23a}$$

$$S(a=L)=1, S_a(a=-\infty)=0; \tag{3.23b}$$

$$S(a=0^+)=S(a=0^-); \tag{3.23c}$$

$$KS_a(a=0^+)=S_a(a=0^-). \tag{3.23d}$$

System (3.20) - (3.21) constitutes an ODE system that can be solved with boundary conditions (3.23). First of all, solving the substrate equation in the aqueous region (3.20) gives $S(a)=Aa+B$ where constants A and B are to be determined by the boundary conditions. With $S(L)=1$, A and B must satisfy $AL+B=1$. Hence, the solution for the substrate concentration in the aqueous region has the following form:

$$S(a)=A(a-L)+1 \qquad 0<a<L. \tag{3.24}$$

It is difficult to find a general explicit solution to the substrate concentration in the biofilm region, since it depends on the choice of $f(S)$. However, as a first step, we can check if a solution $S(a)$ exists with the given boundary conditions. By manipulating the matching conditions (3.23c) - (3.23d), we have $1-AL=S(0^-)$ and $KA=S_a(0^-)$. Eliminating A gives $S(0^-)+K^{-1}LS_a(0^-)=1$. Therefore, it becomes apparent that for $a<0$ we need to solve for

$$S_{aa}=Gf(S); \tag{3.25a}$$

$$S_a(-\infty)=0; \tag{3.25b}$$

$$S(0^-)+K^{-1}LS_a(0^-)=1. \tag{3.25c}$$

Next we study (3.25) in the phase plane of the variables $S(a)$ and $Q(a):=S_a(a)$ in

order to investigate the behaviour of the solution. Writing $S' := S_a$ and $Q' := Q_a$ we have that $S(a)$ and $Q(a)$ satisfy the system

$$S' = Q; \tag{3.26a}$$

$$Q' = Gf(S); \tag{3.26b}$$

$$Q(-\infty) = 0; \tag{3.26c}$$

$$S(0^-) + K^{-1}LQ(0^-) = 1. \tag{3.26d}$$

Equations (3.26c) and (3.26d) imply that the solution trajectory in the phase plane has to intersect with the straight lines $Q = 0$ and $S + K^{-1}LQ = 1$.

From the restrictions that were stated at the end of last section, we have $f(0) = 0$, so $(S,Q) = (0,0)$ is a steady state of system (3.26a)-(3.26b). Furthermore, the corresponding Jacobian matrix to (3.26a) - (3.26b) can be obtained:

$$J = \begin{pmatrix} 0 & 1 \\ Gf'(S) & 0 \end{pmatrix}.$$

Substituting the trivial steady state into this Jacobian matrix yields the related characteristic polynomial $\lambda^2 - Gf'(0) = 0$. From the second restriction placed on $f(S)$, $f'(S) \geq 0$ for $S \geq 0$. As a consequence, the steady state $(0,0)$ is a saddle point. It is easy to show that an eigenvector corresponding to the positive eigenvalue $\lambda = \sqrt{Gf'(0)}$ is $(1, \sqrt{Gf'(0)})$ and therefore one half of the unstable manifold points into the first quadrant.

On the S-axis, $Q = 0$ and therefore (3.26a) - (3.26b) simplifies to $S' = 0, Q' = Gf'(S)S$. For $S \geq 0$, we have $f'(S) \geq 0$, and hence $Q' \geq 0$. Similarly on the Q-axis, we have $S' = Q, Q' = 0$. This information about possible trajectory directions is shown in Figure 3.2. From these results it follows that there is a unique trajectory coming from

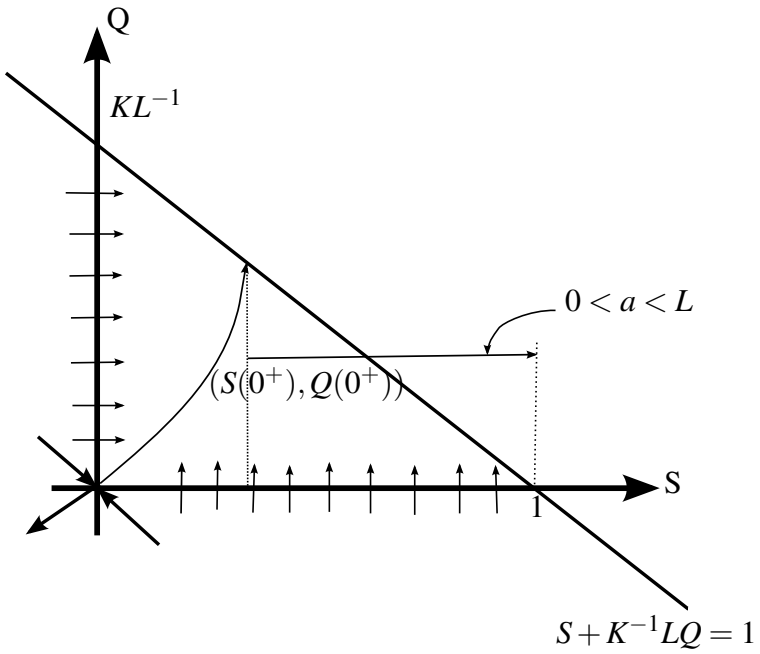

Figure 3.2: Phase plane of system (3.26) and equation (3.24).

$(0,0)$ towards the line $S+K^{-1}LQ=1$. The intersection of this trajectory with the line $S+K^{-1}LQ=1$ corresponds to the solution of substrate concentration at the biofilm interface. From (3.24), we have $Q(a)=S'(a)=A$ for $0<a<L$. Therefore, the phase plane of (S,Q) for $0<a<L$ is a straight line parallel to the S-axis, and the starting point of the straight line is the solution at the interface approaching from the aqueous region. From (3.23c), the solution of S approaching from both the biofilm and aqueous regions are the same. However, from (3.23d), we have $Q(0^+)<Q(0^-)$, because $K>1$. This discontinuity is shown in Figure 3.2.

To summarise, we have shown the existence of a substrate concentration solution in the biofilm region which satisfies $S(a=-\infty)=0$ and $S(a=0^-)=1-AL$. We have also found that in the aqueous region $S(a)=A(a-L)+1$.

Given a solution, $S(a)$, to the substrate equation in the biofilm region, from (3.21), the pressure field can be solved, therefore the interface evolution equation in (3.22)

becomes

$$\begin{aligned} h'(t) &= -P_a(a=0^-) \\ &= \int_{-\infty}^{0^-} g[f(S(a))]da \end{aligned}$$

Notice here, the biofilm interface changes at a rate equal to the volume of net bacteria growth. Also, the integral is independent of time. So the model predicts that deep biofilms will increase in height at a uniform rate.

3.3.2 Non-Planar Growth: A Linear Stability Analysis

So far, we have proved that there exists a unique solution that is uniform in the x direction to system (3.20) - (3.21) with the boundary conditions (3.23). However, the thickness of a biofilm is not necessarily uniform [4, 122, 140]. In order to study the non-uniform surface profile of biofilms, we wish to find out whether the planar solutions are sensitive to small changes that are heterogeneous in x, i.e. the stability of the planar solutions to such perturbations. Dockery and Klapper [37] showed that the planar front solutions of (3.18)-(3.19) are linearly unstable to perturbations that vary in the x direction under certain circumstances. They also claimed that this instability arises as a consequence of the difference between two quantities. These two quantities are the small changes in the biofilm height, which is referred to as fingering process, and the small change in the growth driven pressure from below. We perform a similar stability analysis here, however we analyse system (3.20)-(3.21). Our analysis also shows that the instability of this system is independent of the planar height of the biofilm.

We will look for solutions in (x,z) when we study the stability to spatial perturbations. Therefore, we will return to system (3.18)-(3.19) but keep using the coordinate

transformation $a = z - h_0(t)$ for the purpose of front tracking. Note here, $h_0(t)$ is the planar height solution obtained in the previous section. Writing $S(x,z,t) = S(x,a,t)$, $P(x,z,t) = P(x,a,t)$ in (3.18)-(3.19) yields

$$S_{xx} + S_{aa} = 0; \qquad h(x,t) - h_0(t) < a < L \tag{3.27}$$

$$\begin{cases} S_{xx} + S_{aa} = Gf(S); \\ P_{xx} + P_{aa} = -g[f(S)], \end{cases} \qquad a < h(x,t) - h_0(t) \tag{3.28}$$

For simplicity, we ignore the impact of the small difference between the height of the interface and its planar height on the top boundary of the aqueous region, i.e $L + h(x,t) - h_0(t) \approx L$.

In order to investigate the stability of the planar solutions to small perturbations in space, we will linearise system (3.27)-(3.28) about the planar solutions by writing

$$\begin{aligned} S(x,a,t) &= S_0(a) + S_1(x,a,t) \\ P(x,a,t) &= P_0(a) + P_1(x,a,t) \\ h(x,t) &= h_0(t) + h_1(x,t) \end{aligned} \tag{3.29}$$

where $S_0(a), P_0(a), h_0(t)$ are the planar front solutions we have obtained before. $S_1(x,a,t), P_1(x,a,t)$ and $h_1(x,t)$ are perturbations on substrate, pressure and biofilm height respectively. As usual, the perturbations are assumed to be sufficiently small, i.e. $||S_1||, ||P_1||, ||h_1|| \ll 1$ in the sense that both the function values and the first derivations of these functions are small.

For any point on the biofilm-aqua interface, the coordinate is given by $(x, h(x,t))$. Hence

$$\text{slope of tangent line} = \lim_{\delta x \to 0} \frac{h(x+\delta x,t) - h(x,t)}{\delta x}.$$

Substituting the expression for $h(x,t)$ given in (3.29) into this expression and letting $\delta x \to 0$ yields

$$\text{slope of tangent line} = \frac{\partial h_1(x,t)}{\partial x}.$$

Thus, the corresponding normal at this point is

$$\mathbf{n} = \left(\frac{-\partial h_1(x,t)}{\partial x}, 1 \right). \tag{3.30}$$

This is referred to as a perturbed upward normal on the biofilm-aqua interface.

Using the current definition of a, $a = z - h_0(t)$, along with the definition of the interface $z = h(x,t)$, we obtain that the interface is defined in terms of the wave front coordinate by $a = h(x,t) - h_0(t) = h_1(x,t)$. Hence, the boundary conditions for the full system are given as:

$$P(a = h_1(x,t)) = 0, P_a(a = -\infty) = 0; \tag{3.31a}$$

$$S(a = L) = 1, S_a(a = -\infty) = 0; \tag{3.31b}$$

$$S(a = 0^+ + h_1(x,t)) = S(a = 0^- + h_1(x,t)); \tag{3.31c}$$

$$K(S_x, S_a) \cdot \mathbf{n}|_{a=h_1(x,t)} = (S_x, S_a) \cdot \mathbf{n}|_{a=h_1(x,t)} \tag{3.31d}$$

The interface evolution equation (3.16) becomes

$$\frac{\partial h(x,t)}{\partial t} = -(P_x, P_a) \cdot \mathbf{n}|_{a=h_1(x,t)}, \tag{3.32}$$

where $\mathbf{n}$ is the perturbed upward normal on the biofilm-aqua interface, which is given by (3.30).

Substituting the expressions in (3.29) into (3.27) - (3.28) and retaining the first order

in S_1, P_1 gives

$$S_{1,aa} + S_{1,xx} = 0; \qquad h_1(x,t) < a < L \tag{3.33}$$

$$\begin{cases} S_{1,aa} + S_{1,xx} = Gf'(S_0)S_1; \\ P_{1,aa} + P_{1,xx} = -g'(f(S_0))f'(S_0)S_1; \end{cases} \qquad a < h_1(x,t) \tag{3.34}$$

using (3.20) - (3.21). Notice that system (3.34) includes S_0 which is dependent on the variable a.

Next, we derive the boundary conditions for the first order perturbations. Substituting the expression (3.29) into (3.31a) gives

$$\begin{aligned} P(x,h_1(x,t)) =& P_0(h_1(x,t)) + P_1(x,h_1(x,t),t) \\ \approx& P_0(0) + h_1(x,t)P_{0,a}(0) + [P_1(x,0,t) + h_1(x,t)P_{1,a}(x,0,t)] \\ =& 0. \end{aligned}$$

From (3.23a) we have $P_0(0) = 0$. Therefore, dropping the last term since $||h_1|| \ll 1$ and $||P_{1,a}|| \ll 1$, we obtain

$$h_1(x,t)P_{0,a}(0) + P_1(x,0,t) = 0. \tag{3.35}$$

Similarly, (3.31a) gives another boundary condition for the perturbation of growth driven pressure at the biofilm-substratum interface, i.e.

$$P_{1,a}(x,-\infty,t) = 0. \tag{3.36}$$

Applying the same technique to (3.31b) yields

$$S_0(L) + S_1(x,L,t) = 1 \text{ and } S_{0,a}(-\infty) + S_{1,a}(x,-\infty,t) = 0.$$

Again using the boundary conditions for the planar solutions (3.23b), we can obtain:

$$S_1(x,L,t) = 0, S_{1,a}(x,-\infty,t) = 0. \tag{3.37}$$

Furthermore, substituting (3.29) into both sides of (3.31c) separately and discounting products of 'small' quantities gives:

$$\begin{aligned} S(x,0^+ + h_1(x,t),t) &= S_0(0^+ + h_1(x,t)) + S_1(x,0^+ + h_1(x,t),t) \\ &\approx S_0(0^+) + S_{0,a}(0^+)h_1(x,t) + S_1(x,0^+,t) + S_{1,a}(x,0^+,t)h_1(x,t) \\ &\approx S_0(0^+) + S_{0,a}(0^+)h_1(x,t) + S_1(x,0^+,t). \end{aligned}$$

Similarly,

$$S(x,0^- + h_1(x,t),t) \approx S_0(0^-) + S_{0,a}(0^-)h_1(x,t) + S_1(x,0^-,t).$$

Therefore, from (3.31c) and (3.23c), we have:

$$S_{0,a}(0^+)h_1(x,t) + S_1(x,0^+,t) = S_{0,a}(0^-)h_1(x,t) + S_1(x,0^-,t). \tag{3.38}$$

Substituting (3.29) and the perturbed upward normal (3.30) into both sides of (3.31d) separately results in

$$\begin{aligned} (S_x,S_a)\cdot\mathbf{n}|_{(0^+ + h_1(x,t))} &= (S_x,S_a)\cdot\left(\frac{-\partial h_1(x,t)}{\partial x},1\right)|_{0^+ + h_1(x,t)} \\ &= \left(\frac{\partial S_1(x,a,t)}{\partial x}, S_{0,a} + S_{1,a}(x,a,t)\right)\cdot\left(\frac{-\partial h_1(x,t)}{\partial x},1\right)|_{0^+ + h_1(x,t)} \\ &\approx S_{0,a}(0^+ + h_1(x,t)) + S_{1,a}(x,0^+ + h_1(x,t),t) \\ &\approx S_{0,a}(0^+) + S_{0,aa}(0^+)h_1(x,t) + S_{1,a}(x,0^+,t). \end{aligned}$$

Similarly,

$$(S_x, S_a)\cdot \mathbf{n}|_{(0^- + h_1(x,t))} \approx S_{0,a}(0^-) + S_{0,aa}(0^-)h_1(x,t) + S_{1,a}(x,0^-,t).$$

Hence on substituting into (3.31d) and applying (3.23d), we have:

$$K[S_{0,aa}(0^+)h_1(x,t) + S_{1,a}(x,0^+,t)] = S_{0,aa}(0^-)h_1(x,t) + S_{1,a}(x,0^-,t). \tag{3.39}$$

Finally, from the interface evolution equation (3.32), we have

$$\begin{aligned} h_0' + \frac{\partial h_1(x,t)}{\partial t} &= -(P_x, P_a)\cdot\left(\frac{-\partial h_1(x,t)}{\partial x}, 1\right)|_{a=h_1(x,t)} \\ &= -(P_{1,x}(x,a,t), P_{0,a} + P_{1,a}(x,a,t))\cdot\left(\frac{-\partial h_1(x,t)}{\partial x}, 1\right)|_{a=h_1(x,t)} \\ &\approx -[P_{0,a}(h_1(x,t)) + P_{1,a}(x,h_1(x,t),t)] \\ &\approx -[P_{0,a}(0) + P_{0,aa}(0)h_1(x,t) + P_{1,a}(x,0,t)]. \end{aligned}$$

Hence, on using (3.22), the perturbed biofilm height h_1 satisfies

$$\frac{\partial h_1(x,t)}{\partial t} = -h_1(x,t)P_{0,aa}(0) - P_{1,a}(x,0,t).$$

Furthermore, from (3.21) we have $P_{0,aa}(a) = -g[f(S_0(a))]$, and therefore the previous equation has an alternative form:

$$\frac{\partial h_1(x,t)}{\partial t} = h_1(x,t)g[f(S_0(0^-))] - P_{1,a}(x,0,t). \tag{3.40}$$

Since we wish to study the stability of the planar solutions, it is reasonable to assume that the perturbations in (3.29) have the following form: $S_1(x,a,t) = S_1(a,t)\cos(kx)$, $P_1(x,a,t) = P_1(a,t)\cos(kx)$ and $h_1(x,t) = h_1(t)\cos(kx)$, where k is the wavenumber of

the perturbations. Thus, system (3.33)-(3.34) can be rewritten as

$$S_{1,aa} - k^2 S_1 = 0; \qquad h_1(t)\cos(kx) < a < L \tag{3.41}$$

$$\begin{cases} S_{1,aa} - (k^2 + Gf'(S_0))S_1 = 0; \\ P_{1,aa} - k^2 P_1 = -g'(f(S_0))f'(S_0)S_1; \end{cases} \quad a < h_1(t)\cos(kx) \tag{3.42}$$

the boundary conditions (3.35)-(3.39) can be rewritten as

$$h_1(t)P_{0,a}(0) + P_1(0,t) = 0; \tag{3.43a}$$

$$P_{1,a}(-\infty,t) = 0; \tag{3.43b}$$

$$S_1(L,t) = 0, S_{1,a}(-\infty,t) = 0; \tag{3.43c}$$

$$S_{0,a}(0^+)h_1(t) + S_1(0^+,t) = S_{0,a}(0^-)h_1(t) + S_1(0^-,t); \tag{3.43d}$$

$$K\left[S_{0,aa}(0^+)h_1(t) + S_{1,a}(0^+,t)\right] = S_{0,aa}(0^-)h_1(t) + S_{1,a}(0^-,t). \tag{3.43e}$$

The interface evolution equation (3.40) becomes

$$h_1'(t) = h_1(t)g[f(S_0(0^-))] - P_{1,a}(0,t). \tag{3.44}$$

Therefore, system (3.41) - (3.42), together with the perturbed interface evolution equation (3.44) and the boundary conditions (3.43a) - (3.43e) constitute a full system for the first order perturbations to the planar solutions that will be studied to investigate the stability of the planar solutions.

For simplicity, we assume that the substrate consumption rate $f(S)$ is a linear function of S and the net growth function $g(f(S))$ is a linear function of the substrate consumption $f(S)$. In this way, both $f'(S_0)$ and $g'(f(S_0))$ are reduced to constants so that system (3.41) and (3.42) can be solved analytically.

Solving (3.41) gives the general solution

$$S_1(a,t) = \tilde{A}e^{ka} + \tilde{B}e^{-ka},$$

where $\tilde{A}$ and $\tilde{B}$ are independent of a and need to be determined by the boundary conditions. Note here, $\tilde{A}$ and $\tilde{B}$ can be functions of time because the aqueous region itself changes with time. Applying (3.43c) to this solution yields $\tilde{B} = -\tilde{A}e^{2kL}$. Hence and on writing $A^* = 2\tilde{A}e^{kL}$ yields

$$S_1(a,t) = A^* \sinh(k(L-a)), \qquad h_1(t)\cos(kx) < a < L \tag{3.45}$$

and correspondingly, $S_{1,a}(a,t) = -A^* \cosh(k(L-a))$.

Similarly, solving (3.42) gives

$$S_1(a,t) = B^* e^{ma} + C^* e^{-ma},$$

where $m^2 = k^2 + Gf'(S_0)$. Hence,

$$S_{1,a}(a,t) = mB^* e^{ma} - mC^* e^{-ma} \quad a < h_1(t)\cos(kx). \tag{3.46}$$

Note here, we have assumed that $f(S)$ is a linear function of S. Substituting the lower boundary condition for perturbed substrate concentration in the biofilm region (3.43c) into (3.46) gives $C^* = 0$ and therefore for $a < h_1(t)\cos(kx)$ we have

$$S_1(a,t) = B^* e^{ma}. \tag{3.47}$$

Substituting (3.45) and (3.47) into (3.43d) and using (3.23d) to eliminate $S_{0,a}(0^+)$

yields

$$K^{-1}S_{0,a}(0^-)h_1 + A^* \sinh(kL) = h_1 S_{0,a}(0^-) + B^*.$$

Therefore, A^* can be expressed in terms of S_0 as

$$A^* = h_1 \frac{S_{0,a}(0^-) + B^*/h_1 - K^{-1}S_{0,a}(0^-)}{\sinh(kL)}.$$

From (3.24) we have $S_{0,aa} = 0$ for $a > h_1(t)\cos(kx)$, and from (3.21) we know $S_{0,aa} = Gf(S_0(a))$ for $a < h_1(t)\cos(kx)$. Differentiating (3.45) and (3.47) and substituting into (3.43e) and using these properties of $S_{0,aa}$ yields

$$-KA^*k\cosh(kL) = h_1 Gf(S_0(0^-)) + mB^*.$$

Combining the previous two equations and eliminating A^*, it follows

$$B^* + (kK)^{-1}\tanh(kL)mB^* = -h_1[(1-K^{-1})S_{0,a}(0^-) + (kK)^{-1}\tanh(kL)Gf(S_0(0^-))].$$

Hence, we can obtain an expression for $B^*(t)$ in terms of the known solution S_0,

$$B^* = -h_1 \frac{(1-K^{-1})S_{0,a}(0^-) + (kK)^{-1}\tanh(kL)Gf(S_0(0^-))}{1 + (kK)^{-1}\tanh(kL)m}. \tag{3.48}$$

Notice that since A^* and B^* are linear function of h_1, it follows from (3.45) and (3.47) that $S_1(a,t)$ are linear functions of perturbed biofilm height $h_1(t)$, for both $a < h_1(t)\cos(kx)$ and $h_1(t)\cos(kx) < a < L$.

Next, we will solve for $P_1(a,t)$. Since we have assumed that the substrate consumption rate $f(S)$ is a linear function of S, and the net growth rate $g(f(S))$ is a linear function in $f(S)$, and we know $S_1(a,t)$ for $a < h_1(t)\cos(kx)$ from (3.47), we can solve (3.42)

for P_1 which gives an expression of the form

$$P_1(a,t) = E^* e^{ka} + F^* e^{-ka} + \bar{C} e^{ma}.$$

Substituting this expression into (3.42) and equating coefficients yields $\bar{C} = -\frac{g'(f(S_0(a)))}{G} B^*$. The boundary condition (3.43b) implies that $F^* = 0$. From the second equation in (3.21), it can be shown that

$$P_{0,a}(0) = -\int_{-\infty}^{0} g[f(S_0(a))]da,$$

and combining this with (3.43a) gives

$$E^* = h_1 \int_{-\infty}^{0} g[f(S_0(a))]da + \frac{g'(f(S_0(a)))}{G} B^*,$$

where B^* is given in (3.48). Hence, the solution for the perturbation to the growth driven pressure is given by

$$P_1(a,t) = \left(h_1 \int_{-\infty}^{0} g[f(S_0(a))]da + \frac{g'(f(S_0(a)))}{G} B^* \right) e^{ka} - \frac{g'(f(S_0(a)))}{G} B^* e^{ma}.$$

Since $g'(f(S_0(a)))$ is a constant, we have

$$P_{1,a}(0,t) = k \left(h_1 \int_{-\infty}^{0} g[f(S_0(a))]da + \frac{g'(f(S_0(0)))}{G} B^* \right) - \frac{g'(f(S_0(0)))}{G} m B^*. \quad (3.49)$$

Next, we will investigate whether the perturbations at the biofilm interface grow or decay with time for any given wave number. Substituting (3.49) into (3.44) yields the following equation for the perturbation of the biofilm height, $h_1(t)$,

$$h_1'(t) = h_1 g[f(S_0(0^-))] - k h_1 \int_{-\infty}^{0} g[f(S_0(a))]da + \frac{g'(f(S_0(0)))}{G} B^*(m-k).$$

From (3.48), B^* is a linear function of h_1, and hence $h_1'(t)$ in the above equation can be rewritten as $h_1'(t) = \omega(k)h_1(t)$, where

$$\begin{aligned}\omega(k) =& g[f(S_0(0^-))] - k\int_{-\infty}^{0} g[f(S_0(a))]da \\ & - f'(S_0)\frac{g'(f(S_0(0^-)))}{m+k}\frac{(1-K^{-1})S_{0,a}(0^-) + (kK)^{-1}\tanh(kL)Gf(S_0(0^-))}{1+(kK)^{-1}\tanh(kL)m}.\end{aligned} \tag{3.50}$$

Therefore, $h_1(t) \propto e^{\omega(k)t}$ and the sign of $\omega(k)$ determines the long term behaviour of h_1. If $\omega(k) > 0$, then $h_1(t)$ grows exponentially with time and therefore the planar interface solution $h_0(t)$ is stable to perturbation with the corresponding wave numbers k. Thus, $\omega(k)$ can be thought of as the 'dispersion relation' for the perturbation.

3.3.3 An Instructive Example

As a particular example, the simplest form of the linear functions $f(S)$ and $g[f(S)]$ will be used, which are the functions

$$f(S) = S, \quad g[f(S)] = \alpha f(S) = \alpha S.$$

It can be shown that α can be rescaled into the non-dimensional form of pressure P, so without loss of generality, we consider $\alpha = 1$. Clearly, $f(S)$ satisfies the assumptions $f(0) = 0$ and $f(S) > 0$ for $S > 0$, $f'(S) = 1 > 0$ that were required to make the system well-posed.

Following the process above, we will solve for planar solutions first. Denoting the planar solutions, in terms of the front tracking variable a, to be $S_0(a), P_0(a)$ and $h_0(t)$,

and substituting $f(S)$ and $g[f(S)]$ into (3.20)-(3.21) gives

$$S_{0,aa} = 0; \qquad 0 < a < L$$

$$\begin{cases} S_{0,aa} = GS_0; \\ P_{0,aa} = -S_0, \end{cases} \qquad a < 0.$$

The interface evolution equation (3.22) and the boundary conditions (3.23) remain unchanged. Solving for $S_0(a)$ in both regions with boundary conditions (3.23b) yields

$$S_0(a) = \begin{cases} A^*(a-L)+1 & 0 < a < L; \\ C^* e^{\sqrt{G}a} & a < 0. \end{cases}$$

Applying (3.23c) - (3.23d) to the above solutions implies

$$A^* = \frac{\sqrt{G}}{K + L\sqrt{G}};$$
$$C^* = \frac{1}{K^{-1}\sqrt{G}L + 1}.$$

Thus, the planar substrate solution is

$$S_0(a) = \begin{cases} 1 + \dfrac{\sqrt{G}}{K + L\sqrt{G}}(a-L) & 0 < a < L, \\ \dfrac{1}{K^{-1}\sqrt{G}L + 1} e^{\sqrt{G}a} & a < 0. \end{cases} \tag{3.51}$$

Substituting the solution of $S_0(a)$ for $a < 0$ into $P_{0,aa} = S_0$, we have

$$P_{0,aa} = \frac{1}{K^{-1}\sqrt{G}L + 1} e^{\sqrt{G}a} \qquad a < 0.$$

Integrating the above equation twice with respect to a gives:

$$P_0(a) = -\frac{1}{G}\frac{1}{K^{-1}\sqrt{G}L+1}e^{\sqrt{G}a} + B^*a + D^*.$$

Applying the boundary conditions (3.23a) to the solution of $P_0(a)$, we obtain

$$P_0(a) = \frac{1}{1+K^{-1}L\sqrt{G}}\frac{1}{G}(1-e^{\sqrt{G}a}). \tag{3.52}$$

Thus, the interface evolution equation (3.22) becomes

$$h_0'(t) = \frac{1}{1+K^{-1}L\sqrt{G}}\frac{1}{\sqrt{G}}. \tag{3.53}$$

Note that the right hand side of the interface equation is a constant. Thus, this analysis predicts that the biofilm will increase in the planar height at a uniform rate. It is clear that $h_0'(t)$ decreases as G increases; G is the *Thiele number* that measures the balance between reaction and diffusion in the system [4, 10, 45, 103]. Therefore, it predicts that the planar height of biofilm will grow at a slower speed if the substrate uptake happens lot more faster than the diffusion. It is also clear that $h_0'(t)$ increases as K increases. We know that K can be viewed as the reciprocal of the amount of EPS in the biofilm. Hence, we can also deduce that the more viscous the biofilm is (smaller K), the slower the planar biofilm height grows.

Next, to investigate the stability of the planar solutions to perturbations in the x direction, we will linearise system (3.27)-(3.28) about the planar solutions by writing the solutions as (3.29) and consider perturbations of the form $S_1(a,t)\cos(kx)$, $P_1(a,t)\cos(kx)$ and $h_1(t)\cos(kx)$. Therefore the system for the perturbations $S_1(a,t)$, $P_1(a,t)$ is given by

$$S_{1,aa} - k^2 S_1 = 0; \qquad h_1(t)\cos(kx) < a < L$$

$$\begin{cases} S_{1,aa} - (k^2+G)S_1 = 0; \\ P_{1,aa} - k^2 P_1 = -S_1; \end{cases} \qquad a < h_1(t)\cos(kx)$$

and the equation for the height perturbation $h_1(t)$ in (3.44) becomes (to the first order):

$$h_1'(t) = S_0(0^-)h_1(t) - P_{1,a}(0). \tag{3.54}$$

The boundary conditions for the small perturbations are as in (3.43a)-(3.43e).

Solving for $S_1(a)$ in both regions with the boundary conditions (3.43c) yields:

$$S_1(a,t) = \begin{cases} A^* \sinh[k(a-L)], & h_1(t)\cos(kx) < a < L, \\ C^* e^{ma}, & a < h_1(t)\cos(kx), \end{cases}$$

where $m^2 = k^2 + G$. Applying the boundary conditions (3.43d)-(3.43e) to $S_1(a)$ with the substitution of (3.51), it follows:

$$\begin{aligned} A^* &= \frac{KG(K+\sqrt{G}L)^{-1}h_1 + \sqrt{k^2+G}\,C^*}{Kk\cosh(kL)}; \\ C^* &= \frac{\sqrt{G}h_1}{K^{-1}\sqrt{G}L+1}\frac{(K-1)+k^{-1}\sqrt{G}\tanh(kL)}{K+k^{-1}m\tanh(kL)}. \end{aligned}$$

Substituting the solution of $S_1(a,t)$ for $a < h_1(t)\cos(kx)$ into $P_{1,aa} - k^2 P_1 = -S_1$ allows us to solve for $P_1(a,t)$. With the boundary conditions (3.43a)-(3.43b), we obtain

$$P_1(a,t) = \left(\frac{h_1}{\sqrt{G}+K^{-1}LG}\frac{1}{\sqrt{G}} + \frac{C^*}{G}\right)e^{ka} - \frac{C^*}{G}e^{ma}.$$

Next, we will investigate whether the perturbation $h_1(t)$ of the biofilm height $h_0(t)$ grows or decays with time for any given wave number. Combining the solution of $S_0(a)$ for $a < h_1(t)\cos(kx)$ in (3.51) with the above solution of the pressure perturbation, and

substituting into (3.54) yields

$$h_1'(t) = h_1 \frac{1}{1+K^{-1}L\sqrt{G}} \left[1 - \frac{k}{\sqrt{G}} - \frac{\sqrt{G}}{m+k} \frac{k(K-1)+\sqrt{G}\tanh(kL)}{kK+m\tanh(kL)} \right]. \tag{3.55}$$

Defining $\bar{W} := (1+K^{-1}L\sqrt{G})^{-1}$, we can rewrite (3.54) as $h_1'(t) = \omega(k)h_1(t)$ with

$$\begin{aligned} \omega(k) =& \bar{W} \left[1 - \frac{k}{\sqrt{G}} - \frac{\sqrt{G}}{m+k} \frac{k(K-1)+\sqrt{G}\tanh(kL)}{kK+m\tanh(kL)} \right] \\ =& \bar{W}(\omega_1(k)+\omega_2(k)) \end{aligned}$$

where

$$\omega_1(k) := 1 - \frac{k}{\sqrt{G}} \quad \text{and} \quad \omega_2(k) := \frac{-\sqrt{G}[k(K-1)+\sqrt{G}\tanh(kL)]}{(m+k)[kK+m\tanh(kL)]}. \tag{3.56}$$

This is the same result as Klapper and Dockery [37] obtained in their linear stability analysis for the simple model. However, we have shown that the planar solutions given in (3.51) and (3.52) have a travelling wave profile, by tracking the biofilm interface. Note that the stability of the perturbations depend only on the frequency of the perturbations, and not on the functions that are being perturbed. In particular, the planar interface $h_0(t)$ does not influence the stability of the perturbation.

The above expression $\omega(k)$ is referred to as the *dispersion relation*. If $\omega(k) > 0$ then a small perturbation of the biofilm height will increase with time, thus instability can occur; while if $\omega(k) < 0$ then a small perturbation $h_1(t)$ will decrease with time and tend to 0, eventually tending to a uniformly moving interface $h(x,t) \approx h_0(t)$. Thus, the sign of ω influences the evolution of the perturbed biofilm interface. This indicates the stability of the planar solutions. Next, we will show that a spatial instability exists for some range of wavenumber k. We now study the sign of $\omega(k)$ by considering $\omega_1(k)$ and $\omega_2(k)$ separately.

Since as we noted previously $K > 1$, $\omega_2(k)$ is always negative. When the wavenumber k is chosen to be sufficiently small, $\tanh(kL) \approx kL$. Hence from (3.56) we have

$$\omega_2(k) \approx \frac{-\sqrt{G}[(K-1)+\sqrt{G}L]}{(m+k)(K+mL)}.$$

Therefore, using $m^2 = k^2 + G$ gives

$$\begin{aligned}
\lim_{k\to 0} \omega_2(k) &= \lim_{k\to 0} \frac{-\sqrt{G}[(K-1)+\sqrt{G}L]}{(m+k)(K+mL)} \\
&= \lim_{k\to 0} \frac{-\sqrt{G}(K-1+\sqrt{G}L)}{(\sqrt{k^2+G}+k)(K+\sqrt{k^2+G}L)} \\
&= -\frac{K-1+\sqrt{G}L}{K+\sqrt{G}L} \\
&= \frac{1}{K+\sqrt{G}L} - 1
\end{aligned}$$

Also, from (3.56) $\lim_{k\to 0} \omega_1(k) = 1$, hence

$$\lim_{k\to 0} \omega(k) = \bar{W}\left(1 + \frac{1}{K+\sqrt{G}L} - 1\right) = \frac{\bar{W}}{K+\sqrt{G}L}, \tag{3.57}$$

which is always positive.

On the other hand, when the wavenumber k is chosen to be sufficiently large, $\tanh(kL) \approx 1$. Hence, from (3.56), $\omega_2(k)$ can be approximated by

$$\omega_2(k) \approx \frac{-\sqrt{G}[k(K-1)+\sqrt{G}]}{(m+k)(kK+m)}.$$

Hence,

$$\begin{aligned}\lim_{k\to\infty}\omega_2(k) &= \lim_{k\to\infty}\frac{-\sqrt{G}[k(K-1)+\sqrt{G}]}{(m+k)(kK+m)}\\ &= \lim_{k\to\infty}\frac{-\sqrt{G}[k(K-1)+\sqrt{G}]}{(\sqrt{k^2+G}+k)(kK+\sqrt{k^2+G})}\\ &= \lim_{k\to\infty}\frac{-\sqrt{G}[(K-1)+\frac{\sqrt{G}}{k}]}{(\sqrt{k^2+G}+k)(K+\sqrt{1+\frac{G}{k^2}})}\\ &=0.\end{aligned}$$

From (3.56) $\lim_{k\to\infty}\omega_1(k) = -\infty$, therefore, we have

$$\lim_{k\to\infty}\omega(k) = -\infty.$$

The plots of $\omega_1(k), \omega_2(k)$ and $\omega(k)$ are shown in Figure3.3.

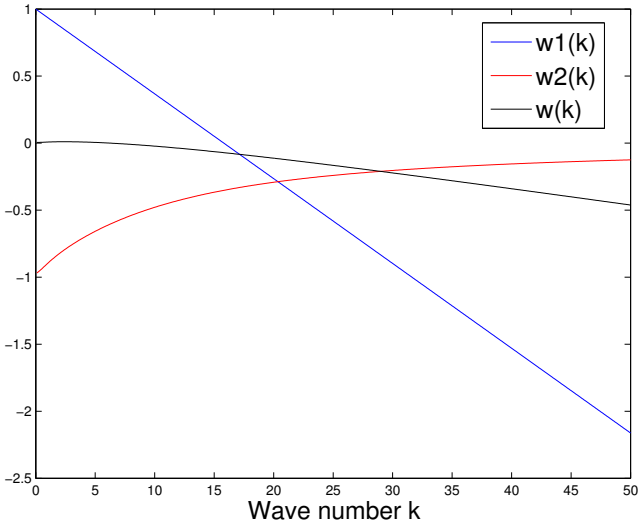

Figure 3.3: Plot of $\omega_1(k)$(blue line), $\omega_2(k)$(red curve) and the dispersion relation $\omega(k)$(black curve). Parameter values used are from Dockery and Klapper's work [37], $L = 2, G = 250, K = 8$.

Hence, the dispersion relation is always positive when k is sufficiently close to 0 but it negative when k is sufficiently large. Therefore, there must exist at least one critical

wavenumber k such that $\omega(k) = 0$. Denote the smallest value of $k > 0$ such that $\omega(k) = 0$ by k_{crit}. Notice that $\omega_1(\sqrt{G}) = 0$, and $\omega_2(k) < 0$ for all $k > 0$. Therefore, the critical wavenumber must have $k_{crit} < \sqrt{G}$. We have mentioned in the non-dimensionalisation section that $G \gg 1$ since the model is assumed to be diffusion limited. Therefore, from (3.56), it can be shown that $\omega(k)$ is dominated by G. Several dispersion curves are shown in Figure 3.4 for increasing values of G.

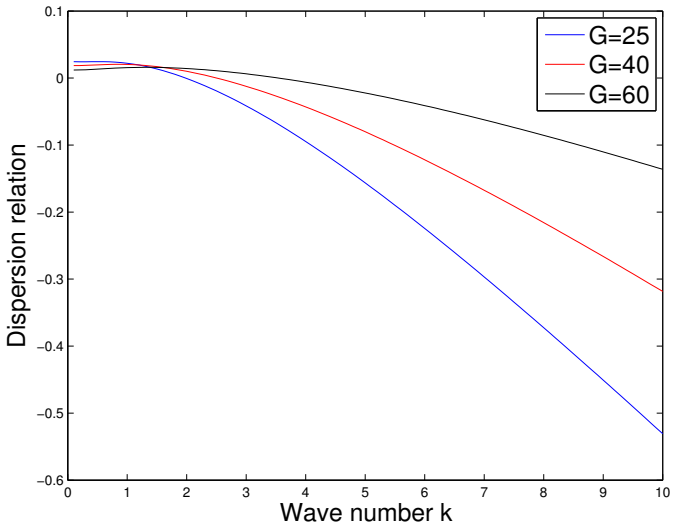

Figure 3.4: Plot of $\omega(k)$ for different values of G with parameter set $L = 2, K = 8$.

We have shown that the dispersion relation $\omega(k)$ can be positive, zero or negative for any given set of parameter values. Thus, we can conclude that for any given parameter values, the planar solutions can be stable or unstable to perturbations of the form $\cos(kx)$ by varying the wavenumber k.

Since both the planar height (3.53) and the perturbed height of the biofilm (3.55) grow with time, the comparison of which one grows faster will give us a clear insight into how the spatial pattern can emerge. We will only consider the case where spatial patterns will arise, i.e. when $\omega(k) > 0$.

The solution of (3.55) is:

$$h_1(t) = h_1(0)e^{\omega(k)t},$$

where $h_1(0)$ is the initial value of the perturbed height. Thus, the rate of change of the perturbed height is explicitly given by

$$h_1'(t) = h_1(0)\omega(k)e^{\omega(k)t}. \tag{3.58}$$

If we denote $\eta := h_0'(t) - h_1'(t)$, then we wish to study how the sign of η changes with time. From (3.53) and (3.58), η follows:

$$\eta = \frac{1}{\sqrt{G}(1+\sqrt{G}LK^{-1})} - h_1(0)\omega(k)e^{\omega(k)t}.$$

Therefore $\eta'(t) = -h_1(0)\omega(k)^2 e^{\omega(k)t}$, which is negative for all t. Hence, η is a decreasing function of time. Furthermore, it is obvious that $\eta \to -\infty$ as $t \to \infty$. This result shows that the growth of the perturbed biofilm height will eventually take over the planar height of biofilm and the spatial pattern will become more distinguishable.

The value of $\eta(0)$ turns out to be important in the way that it determines what the biofilm interface looks like at the beginning. Substituting $t = 0$ into η yields

$$\eta(0) = \frac{1}{\sqrt{G}(1+\sqrt{G}LK^{-1})} - h_1(0)\omega(k).$$

From the discussion above we know that $\omega(k)$ is a decreasing function in k. Therefore, using (3.57) we have

$$\begin{aligned}\eta(0) &> \frac{1}{\sqrt{G}(1+\sqrt{G}LK^{-1})} - h_1(0)\omega(0) \\ &= \frac{1}{1+\sqrt{G}LK^{-1}}\left[\frac{1}{\sqrt{G}} - \frac{\bar{W}h_1(0)}{K}\right].\end{aligned}$$

In addition, the initial perturbation height is always chosen to be small that gives $h_1(0) \ll 1$. Hence, as long as the initial perturbed height can be chosen as $h_1(0) < \frac{K}{\bar{W}\sqrt{G}}$, then we will have a biofilm that expands uniformly in the vertical direction at the beginning and the spatial pattern will be observable later. Otherwise, the spatial pattern will be observed from the beginning of biofilm growth.

3.4 Growth and Stability of Shallow Biofilms

In the previous section, the biofilm depth is assumed to be infinite, i.e. $z_0 = -\infty$. This is the case studied in [37]. This assumption is useful in that it allows for a richer mathematical analysis of the solution to system (3.18)-(3.19). Moreover, this can be used as a reasonable model for very deep biofilms. However, biofilms can be of varying depths. In this section, we will investigate how the biofilm depth can affect the stability of the system.

The mathematical model that will be studied in this section is (3.18)-(3.19) together with the interface dynamic (3.16) and the boundary conditions (3.17) with the assumption that the lower boundary of the biofilm region $z_0 = 0$. Furthermore, we will continue using the linear functions for cell growth and substrate consumption. Thus, the complete model studied in this section is given by:

$$\begin{cases} \nabla^2 S = GS \\ \\ \nabla^2 P = -S \end{cases} \qquad 0 < z < h(x,t); \tag{3.59}$$

$$\nabla^2 S = 0 \qquad h(x,t) < z < H(x,t), \tag{3.60}$$

with boundary conditions

$$P(z=h)=0, P_z(z=0)=0; \tag{3.61a}$$

$$S(z=H)=1, S_z(z=0)=0; \tag{3.61b}$$

$$S(z=h^+)=S(z=h^-); \tag{3.61c}$$

$$K\nabla S\cdot\mathbf{n}(z=h^+)=\nabla S\cdot\mathbf{n}(z=h^-). \tag{3.61d}$$

The interface evolution equation remains the same as (3.16). System (3.59)-(3.60), boundary conditions (3.61) and the interface evolution equation (3.16) constitute the mathematical model we will use to carry out the linear stability analysis in order to investigate the effect of biofilm depth on pattern formation.

3.4.1 Planar Growth

As before, we first obtain the planar solution of system (3.59) - (3.60). Denoting the planar solutions, in terms of z,t, to be $S_0(z,t), P_0(z,t)$ and $h_0(t)$ gives

$$\begin{cases} S_{0,zz}=GS_0 \\ P_{0,zz}=-S_0 \end{cases} \qquad 0<z<h_0(t); \tag{3.62}$$

$$S_{0,zz}=0 \qquad h_0(t)<z<h_0(t)+L. \tag{3.63}$$

with the corresponding boundary conditions:

$$P_0(z=h_0)=0, P_{0,z}(z=0)=0; \tag{3.64a}$$

$$S_0(z=H)=1, S_{0,z}(z=0)=0; \tag{3.64b}$$

$$S_0(z=h_0^+)=S_0(z=h_0^-); \tag{3.64c}$$

$$KS_{0,z}(z=h_0^+)=S_{0,z}(z=h_0^-). \tag{3.64d}$$

In this case, the interface evolution equation (3.16) is reduced to $h_0'(t) = -P_{0,z}(z = h_0)$.

Solving for $S_{0,zz} = 0$ with boundary condition $S_0(z = H) = 1$ yields

$$S_0(z,t) = A(t)(z - (h_0 + L)) + 1 \quad \text{for} \quad h_0(t) < z < h_0(t) + L,$$

where $A(t)$ is a constant of integration. Similarly, solving for $S_{0,zz} = GS_0$ with $S_{0,z}(z = 0) = 0$ gives

$$S_0(z,t) = B(t)\cosh(\sqrt{G}z) \quad \text{for} \quad 0 < z < h_0(t)$$

and again $B(t)$ is a constant of integration. Combining (3.64c) and (3.64d) yields:

$$\begin{cases} A(t) = & \dfrac{\sqrt{G}\tanh(\sqrt{G}h_0)}{K + \sqrt{G}L\tanh(\sqrt{G}h_0)}; \\ B(t) = & \dfrac{K}{K\cosh(\sqrt{G}h_0) + \sqrt{G}L\sinh(\sqrt{G}h_0)}. \end{cases}$$

Thus, the solution of substrate concentration in both regions is given by

$$S_0(z,t) = \begin{cases} \dfrac{\sqrt{G}\tanh(\sqrt{G}h_0)}{K + \sqrt{G}L\tanh(\sqrt{G}h_0)}(z - h_0 - L) + 1; & h_0 < z < h_0 + L \\ \dfrac{K\cosh(\sqrt{G}z)}{K\cosh(\sqrt{G}h_0) + \sqrt{G}L\sinh(\sqrt{G}h_0)}. & 0 < z < h_0 \end{cases} \tag{3.65}$$

Next, we use this solution for S_0 to solve for P_0. Substituting the expression valid for $0 < z < h_0$ from (3.65) into $P_{0,zz} = -S_0$ and integrating twice gives

$$P_0(z,t) = \frac{-B(t)}{G}\cosh(\sqrt{G}z) + C(t)z + D(t),$$

where $B(t)$ is as determined before and $C(t)$ and $D(t)$ are constants of integration. Substituting $P_0(z,t)$ into the boundary conditions $P_0(z = h_0) = 0, P_{0,z}(z = 0) = 0$ yields

$C(t) = 0$ and $D(t) = \frac{B(t)}{G}\cosh(\sqrt{G}h_0)$. Thus, we have

$$P_0(z,t) = \frac{B(t)}{G}[\cosh(\sqrt{G}h_0) - \cosh(\sqrt{G}z)]. \tag{3.66}$$

By substituting (3.66) into the interface evolution equation $h_0'(t) = -P_{0,z}(z = h_0)$, we are able to solve for $h_0(t)$, which is given by

$$h_0'(t) = \frac{1}{\sqrt{G}}\frac{K\tanh(\sqrt{G}h_0)}{K + \sqrt{G}L\tanh(\sqrt{G}h_0)}. \tag{3.67}$$

Comparing (3.67) to the the planar interface evolution equation for the system with infinite biofilm depth, (3.53), we note that the rate of change of the biofilm interface depends on the biofilm depth . Furthermore, when $h_0(t)$ is small, $\tanh(\sqrt{G}h_0) \approx \sqrt{G}h_0$ which leads to $h_0'(t) \approx \frac{Kh_0}{K + GLh_0}$. Hence, it can be shown that for small $h_0(t)$, $h_0'(t)$ is an increasing function of biofilm height. This can be understood in the following way: when the biofilm is sufficiently thin, the biofilm depth can be viewed as as approximation of the amount of bacteria. Therefore, the increase in the biofilm height h_0 (within a reasonably small range) is equivalent to an increase in the amount of bacteria. Thus, the increasing amount of bacteria pushes the interface to move faster.

When the biofilm is sufficiently thick, i.e. h_0 is sufficiently large, then $\tanh(\sqrt{G}h_0) \approx 1$. Hence, (3.67) simplifies to

$$h_0'(t) = \frac{1}{\sqrt{G}}\frac{K}{K + \sqrt{G}L}.$$

This is exactly the same expression as we obtained for the infinite domain (3.53). In other words, the problem in a channel with finite depth and sufficiently thick biofilm is equivalent to the problem where the channel is of infinite depth.

3.4.2 Non-Planar Growth: A Linear Stability Analysis

Next, to investigate the stability of the planar solutions to perturbations in the x direction, we will linearise system (3.59)-(3.60) about the planar solutions by writing the solutions as

$$\begin{aligned} S(x,z,t) &= S_0(z,t) + S_1(z,t)\cos(kx) \\ P(x,z,t) &= P_0(z,t) + P_1(z,t)\cos(kx) \\ h(x,t) &= h_0(t) + h_1(t)\cos(kx) \end{aligned} \tag{3.68}$$

Therefore, the system for the perturbations $S_1(z,t), P_1(z,t)$ is given by

$$S_{1,zz} - k^2 S_1 = 0; \qquad h(x,t) < z < h(x,t) + L \tag{3.69}$$

$$\begin{cases} S_{1,zz} - (k^2+G)S_1 = 0; \\ P_{1,zz} - k^2 P_1 = -S_1; \end{cases} \qquad 0 < z < h(x,t) \tag{3.70}$$

where k is the wavenumber in the x direction and the equation for the height perturbation $h_1(t)$ is given by

$$h_1'(t) = S_0(h_0^-)h_1(t) - P_{1,z}(h_0). \tag{3.71}$$

As before, the corresponding boundary conditions for the small perturbations can be derived from (3.61) and the planar solution as follow:

$$h_1 P_{0,z}(h_0) + P_1(h_0) = 0; P_{1,z}(0) = 0; \tag{3.72a}$$

$$S_1(h_0 + L) = 0, S_{1,z}(0) = 0; \tag{3.72b}$$

$$h_1 S_{0,z}(h_0^+) + S_1(h_0^+) = h_1 S_{0,z}(h_0^-) + S_1(h_0^-) \tag{3.72c}$$

$$K S_{1,z}(h_0^+) = S_{0,zz}(h_0^-)h_1 + S_{1,z}(h_0^-). \tag{3.72d}$$

Solving for $S_1(z,t)$ in both regions with the boundary conditions (3.72b) yields:

$$S_1(z,t) = \begin{cases} A^*(t)\sinh(k(h_0+L-z)); & h(x,t) < z < h(x,t)+L \\ C^*(t)\cosh(\sqrt{k^2+G}z); & 0 < z < h(x,t) \end{cases} \tag{3.73}$$

where $A^*(t)$ and $C^*(t)$ are constants of integration. Applying boundary conditions (3.72c)-(3.72d) to $S_1(z,t)$ gives

$$A^*(t) = \frac{h_1(1-K^{-1})S_{0,z}(h_0^-) + C^*(t)\cosh(\sqrt{k^2+G}h_0)}{\sinh(kL)};$$

$$C^*(t) = -h_1\cosh(\sqrt{k^2+G}h_0)^{-1}\left[1+\frac{N}{Kk}\sqrt{k^2+G}M(t)\right]^{-1} \times \left[\frac{(1-K^{-1})\sqrt{G}KQ(t)}{\sqrt{G}LQ(t)+K} + \frac{N}{k}\frac{G}{\sqrt{G}LQ(t)+K}\right],$$

where we denote $N \equiv \tanh(kL), M(t) \equiv \tanh(\sqrt{k^2+G}h_0), Q(t) \equiv \tanh(\sqrt{G}h_0)$.

Substituting the solution of $S_1(z,t)$ for $0 < z < h(x,t)$ into the equation for P_1 in (3.70) and solving for $P_1(z,t)$ gives

$$P_1(z,t) = E^*(t)e^{kz} + F^*(t)e^{-kz} - \frac{C^*(t)}{G}\cosh(\sqrt{k^2+G}z)$$

where $C^*(t)$ has been determined above, but $E^*(t)$ and $F^*(t)$ are undetermined constants of integration. Applying the boundary condition (3.72a) as well as the planar solution (3.66) to $P_1(z)$ gives

$$E(t) = F(t) = \frac{1}{2}\cosh^{-1}(kh_0)\left[\frac{C^*(t)}{G}\cosh(\sqrt{k^2+G}h_0) + h_1\frac{K}{\sqrt{G}}\frac{Q(t)}{\sqrt{G}LQ(t)+K}\right].$$

Finally, as before, we will investigate whether the perturbation of the biofilm height $h_1(t)$ increases or decays with time. On the substitution of $S_0(z,t)$ for $0 < z < h(x,t)$

in (3.65) and $P_1(z,t)$ to (3.71), $h_1(t)$ satisfies the following equation:

$$h_1' = \frac{K\cosh(\sqrt{G}h_0)}{K\cosh(\sqrt{G}h_0)+\sqrt{G}L\sinh(\sqrt{G}h_0)}h_1 \\ -Ek\sinh(kh_0)+\frac{C^*}{G}\sqrt{k^2+G}\sinh(\sqrt{k^2+G}h_0).$$

Substituting the expression for $C^*(t)$ into this equation and letting $R(t) \equiv \tanh(kh_0)$ yields

$$h_1'(t) = h_1 W\left[\left(1+\frac{kR}{\sqrt{G}}\hat{W}\right)-\left(\frac{kRQ}{\sqrt{G}}+\frac{\sqrt{k^2+G}}{\sqrt{G}}M\hat{W}\right)\right] \tag{3.74}$$

where

$$W = \frac{1}{\sqrt{G}LQ(t)K^{-1}+1} \quad \text{and} \quad \hat{W} = \frac{k(K-1)Q(t)+N}{1+\sqrt{k^2+G}NM(t)}. \tag{3.75}$$

Equation (3.74) is of the form $h_1'(t) = \omega(k,t)h_1(t)$, where $\omega(k,t)$ is the dispersion relation of system (3.59)-(3.60) about the planar solutions given by (3.65)-(3.66). In a similar way to the analysis of the dispersion relation (3.55) for the previous system for infinite depth biofilms, the sign of $\omega(k,t)$ varies depending on the choice of the wavenumber k as well as other parameter values. Thus, the planar height of system (3.59)-(3.60) can be stable or unstable to perturbation in x direction given different wave numbers.

The right hand side of (3.74) contains the planar height solution $h_0(t)$. Therefore, (3.67) and (3.74) form coupled system of non-linear ODEs for $h_0(t)$ and $h_1(t)$. This system is in general analytically intractable. However, it has been shown that both of the planar height (3.67) and the perturbed height (3.74) can be dramatically simplified with different categories of $h_0(t)$: h_0 is sufficiently small (thin film case) and h_0 is sufficiently large (thick film case).

When $h_0(t)$ is sufficiently large (thick film case), we have $Q(t) \approx 1, M(t) \approx 1$ and

$R(t) \approx 1$. Therefore, the expression of W and $\hat{W}$ given in (3.75) can be reduced to

$$W = \frac{1}{\sqrt{G}LK^{-1}+1};$$
$$\hat{W} = \frac{k(K-1)+N}{1+\sqrt{k^2+GN}},$$

and the dispersion relation of (3.74) can be simplified into

$$\omega(k) = W\left[1 - \frac{k}{\sqrt{G}} - \frac{\sqrt{G}}{m+k}\frac{k(K-1)+\sqrt{G}\tanh(kL)}{kK+m\tanh(kL)}\right].$$

This is exactly the same as the dispersion relation for the infinite domain (3.55) and it is independent of the planar height solution $h_0(t)$.

However, in the thin film case where $h_0(t)$ is small, $Q(t) \approx \sqrt{G}h_0, M(t) \approx \sqrt{k^2+G}h_0$ and $R(t) \approx kh_0$. So the dispersion relation of (3.74) can be simplified but still depends on the planar height. Since the planar solution $h_0(t)$ is a function of time, the right hand side of (3.74) is a complex expression in term of time. Therefore, (3.74) cannot be solved analytically by separation of variable. However, since h_0 is a function of time, $\omega(k,t)$ in (3.74) will change with time, so we expect that the stability dynamics in the thin film case is significantly different from the dynamics in the thick film case.

3.5 Model with Cell Death

In previous sections, we considered biofilm growth as the only mechanism responsible for pressure change. However, biofilm formation is clearly a more complicated process. It is well known that bacterial death occurs in the biofilm [8, 43, 113]. Therefore, it is more realistic to add on a death term to the net bacterial growth function $g(f(S))$. For simplicity, we will use the linear substrate consumption function $f(S) = S$ and a constant death rate in this section, i.e. $g(S) = S - \mu$ where μ is the constant death rate.

In the phase plane analysis, weak and realistic conditions have been placed on the growth function $g(S)$ in order to make the system well-posed. With $g(f(S))$ chosen to be $g(f(S)) = S - \mu$, after substituting $S_0(a)$ for $a < 0$ in (3.51) into $P_{0,aa} = -S_0 + \mu$ and integrating once we will have

$$P_{0,a}(a) = \frac{1}{\sqrt{G}} \frac{1}{1 + K^{-1} L \sqrt{G}} e^{\sqrt{G}a} - \mu a + \text{constant}.$$

It is not possible to choose the constant of integration to satisfy the boundary condition $P_{0,a}(-\infty) = 0$. This illustrates that in the infinite domain case, $g(f(S))$ can be of the form $S - \mu$ only if $\mu = 0$. In the finite domain case, we do not have this restriction. Therefore, the finite domain enables us to consider a more general model with $g(0) \neq 0$. Therefore, the system we are studying in this section is as follows:

$$\begin{cases} \nabla^2 S - GS = 0; \\ \nabla^2 P = -S + \mu; \end{cases} \qquad 0 < z < h(x,t) \tag{3.76}$$

$$\nabla^2 S = 0. \qquad h(x,t) < z < h(x,t) + L \tag{3.77}$$

The boundary conditions and the interface evolution equation remain the same as (3.61) and (3.16) respectively. In this section, we will follow the analysis process we used previously, to investigate the effect of the biofilm death on pattern formation.

3.5.1 Planar Growth

As before, we first obtain the planar solution of system (3.76)-(3.77). Denoting the planar solutions in terms of z,t to be $S_0(z,t), P_0(z,t)$ and $h_0(t)$ gives the system for the

planar solutions:

$$\begin{cases} S_{0,zz} = GS_0 \\ P_{0,zz} = -S_0 + \mu \end{cases} \qquad 0 < z < h_0(t);$$

$$S_{0,zz} = 0 \qquad h_0(t) < z < h_0(t) + L.$$

The boundary conditions for the planar solutions follow:

$$P_0(z = h_0) = 0, P_{0,z}(z = 0) = 0;$$

$$S_0(z = H) = 1, S_{0,z}(z = 0) = 0;$$

$$S_0(z = h_0^+) = S_0(z = h_0^-);$$

$$KS_{0,z}(z = h_0^+) = S_{0,z}(z = h_0^-).$$

The interface evolution equation is $h_0'(t) = -P_{0,z}(z = h_0)$.

Notice that both the equations and boundary conditions for the substrate concentration $S_0(z,t)$ are the same as the model in the previous section. Therefore, the solution for $S_0(z,t)$ is the same as (3.65). Substituting $S_0(z,t)$ for $0 < z < h_0(t)$ into $P_{0,zz} = -S_0 + \mu$ and integrating twice gives

$$P_0(z,t) = \frac{-B}{G}\cosh(\sqrt{G}z) + \frac{\mu}{2}z^2 + Cz + D,$$

where $B = \dfrac{K}{K\cosh(\sqrt{G}h_0) + \sqrt{G}L\sinh(\sqrt{G}h_0)}$ from (3.65).

Substituting $P_0(z,t)$ into the boundary conditions $P_0(z = h_0) = 0$ and $P_{0,z}(z = 0) = 0$ yields $C = 0$ and $D = \frac{B}{G}\cosh(\sqrt{G}h_0) - \frac{\mu}{2}h_0^2$. Thus, we have

$$P_0(z,t) = -\frac{K}{G}\frac{\cosh(\sqrt{G}z) - \cosh(\sqrt{G}h_0)}{\sqrt{G}L\sinh(\sqrt{G}h_0) + K\cosh(\sqrt{G}h_0)} + \frac{1}{2}\mu(z^2 - h_0^2). \tag{3.78}$$

Substituting (3.78) into the interface evolution equation

$$h_0'(t) = -P_{0,z}(z = h_0)$$

gives

$$h_0'(t) = \frac{K\tanh(\sqrt{G}h_0)}{GL\tanh(\sqrt{G}h_0) + \sqrt{G}K} - \mu h_0, \tag{3.79}$$

which allows us to solve for $h_0(t)$.

The first term of the above equation is exactly the same as (3.67). However, introducing the death rate, μ, gives the interface velocity an extra negative term, which is proportional to the depth of the biofilm planar layer. Hence, we first investigate the effect of the death rate, μ, on the growth of the planar biofilm height.

It can be shown that the first term of the right hand side of (3.79) increases as h_0 increases and it is bounded above by $\frac{K}{GL+\sqrt{G}K}$. Hence, this term exhibits a sigmoid shape. If μ is chosen to be sufficiently large, then h_0 will decrease with time initially. In order to have a growing biofilm, we require the death rate μ to be small enough to guarantee that $h_0'(t) > 0$. We note that, $\tanh(\sqrt{G}h_0) \approx \sqrt{G}h_0$ when h_0 is small while $\tanh(\sqrt{G}h_0) \approx 1$ when h_0 becomes large. We solve (3.79) numerically using the exact form of the right hand side and also with approximations of the right hand side using these two alternative approximations for tanh. Figure 3.5 shows the comparison of the exact solution to (3.79) with the approximate solutions using the two different approximations. The corresponding plots of the velocity of the planar height, $h_0'(t)$ are also shown.

From Figure 3.5, when the initial height is small, we can observe a transition time that separates biofilm growth into two stages, i.e. the velocity of the planar biofilm growth initially increases with time and later decreasing to 0, as shown in Figure 3.5(c). We refer the former stage as vertical expansion and the latter stage as vertical relaxation.

However, when we start with a larger initial height, the planar biofilm growth only exhibits as the vertical relaxation (shown in Figure 3.5(d)). Therefore, we will mainly focus on the case where the initial height is small since the larger time solution behaviour in this case is of the same form as the solution behaviour for the large initial height case.

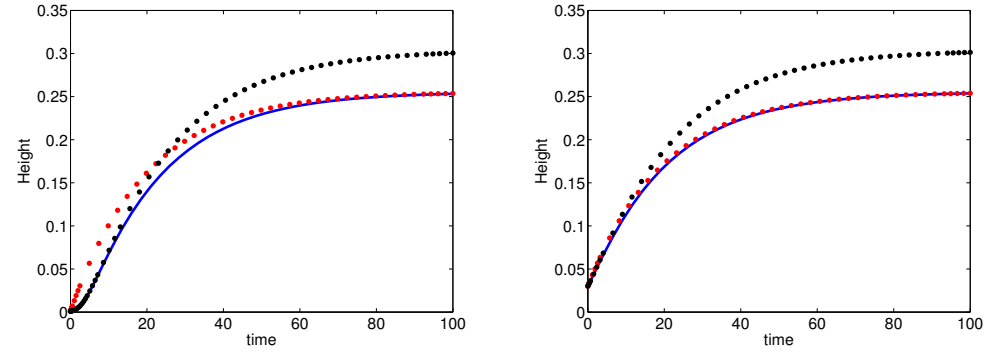

(a) Height plot with $h_0 = 0.001$.

(b) Height plot with $h_0 = 0.03$.

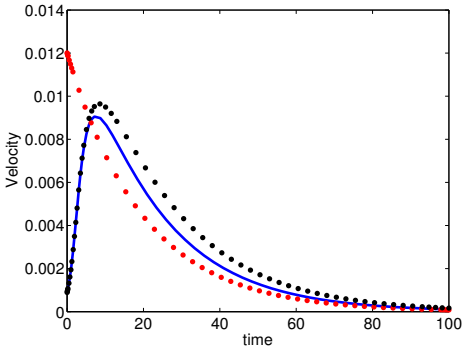

(c) Velocity plot with $h_0 = 0.001$.

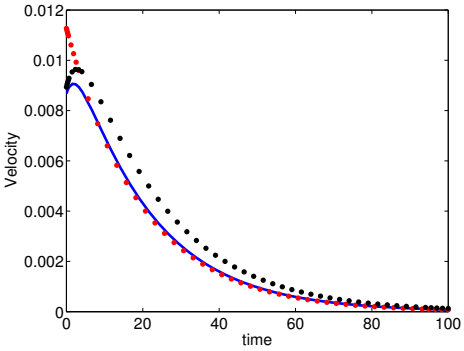

(d) Velocity plot with $h_0 = 0.03$.

Figure 3.5: Numerical solution to equation (3.79) with both 3.5(a)small initial height ($h(0) = 0.001$) and 3.5(a) large initial height ($h(0) = 0.03$). The corresponding velocities of each case are shown in 3.5(c) and 3.5(d). Parameter values are: $K = 8, G = 250, \mu = 0.05, L = 2$, which are given in [37]. The blue curve is the numerical solution to equation (3.79), the red dot line is the approximate solution where $\tanh(x) = 1$, and the black dot line is the approximate solution where $\tanh(x) = x$.

Next, we will use our two approximations for tanh to obtain an approximate solution of (3.79) and also to estimate the transition time between the two stages of planar growth. To complete the ODE equation (3.79), we set the initial condition $h_0(0) = h_{ini}$ and we

assume that h_{ini} is sufficiently small.

First, we will consider the case where $h_0(t)$ is small. Therefore, we use $\tanh(\sqrt{G}h_0) \approx \sqrt{G}h_0$. Substituting this approximation into (3.79) gives

$$h_0'(t) = \frac{Kh_0}{GLh_0 + K} - \mu h_0.$$

Given that h_0 is small, we can expand the right hand side of this equation with a Taylor expansion to give:

$$h_0'(t) \approx (1-\mu)h_0.$$

With the initial condition $h_0(0) = h_{ini}$, the above equation can be solved explicitly to give the following expression and the corresponding velocity, which is referred to as the inner velocity and denoted by $v_{in}(t)$

$$h_0(t) \approx h_{ini}e^{(1-\mu)t}, \tag{3.80a}$$

$$v_{in}(t) \approx (1-\mu)h_{ini}e^{(1-\mu)t}. \tag{3.80b}$$

Once $h_0(t)$ is sufficiently large, $\tanh(\sqrt{G}h_0) \approx 1$. Then (3.79) becomes

$$h_0'(t) = \frac{K}{GL + \sqrt{G}K} - \mu h_0. \tag{3.81}$$

Note here, since $h_0(t)$ is an increasing function, (3.81) is a good approximation of the long time behaviour of (3.79). Setting the right hand side of (3.81) equal to 0 gives the steady state of (3.81):

$$h_0^* = \frac{K}{\mu(GL + \sqrt{G}K)}. \tag{3.82}$$

It is easy to show that this steady state is stable.

From (3.82), we can conclude that the steady state of the planar solution decreases as

either the Thiele number or the death rate μ increases, but increases as the diffusivity ratio K increases. Recall $K = \frac{D_1}{D_2} = \phi_{poro}^{-1}$, where ϕ_{poro} is defined as the ratio of the volume of void space over the total volume of the porous media. Since EPS is responsible for the porous structure of biofilm, it is clear that the more EPS exists, the smaller ϕ_{poro} should be, and therefore, the bigger K becomes. Hence, our result suggests that the planar height of a biofilm with more EPS matrix should be higher than the planar height of a biofilm with less EPS matrix. More specifically, our result predicts that the height of the wild-type biofilm should be higher than that of the *eps* mutant biofilm. Hence, we conclude that the EPS concentration is positively correlated to the biofilm depth.

With the initial condition $h_0(0) = h_{ini}$, (3.81) can be solved to give $h_0(t)$ and the corresponding velocity, which is referred to as the outer velocity and denoted by $v_{out}(t)$ as follows:

$$h_0(t) = \frac{K}{\mu(GL + \sqrt{G}K)} + \beta e^{-\mu t},$$
$$v_{out}(t) = -\mu\beta e^{-\mu t},$$

where $\beta = h_{ini} - \dfrac{K}{\mu(GL + \sqrt{G}K)}$. Note here, since both of the death rate μ and the initial planar height h_{ini} are chosen to be small, β is negative in our case. In order to simplify the expression, we define a parameter group

$$U := \frac{1}{\sqrt{G}LK^{-1} + 1}. \tag{3.83}$$

Therefore, we have

$$h_0(t) = \frac{U}{\sqrt{G}\mu} + \beta e^{-\mu t}, \tag{3.84a}$$
$$v_{out}(t) = -\mu\beta e^{-\mu t}, \tag{3.84b}$$

and $\beta = h_{ini} - \dfrac{U}{\sqrt{G}\mu}$.

It is clear from (3.80b) that $v_{in}(t)$ is an increasing function in time, and from (3.84b) that $v_{out}(t)$ is a decreasing function. Therefore, our first approximation is most appropriate for the vertical expansion stage of the solution and our second approximation is most appropriate for the vertical relaxation stage. Hence, it is reasonable to approximate the transition time by the intersection of these two approximate solutions. Defining the approximate transition time as T and equating (3.80b) and (3.84b), we have

$$(1-\mu)h_{ini}e^{(1-\mu)T} = -\mu\beta e^{-\mu T}.$$

Solving this equation for e^T and substituting the expression for β and then substituting the expression for U yields:

$$e^T = \frac{1}{(\sqrt{G}LK^{-1}+1)\sqrt{G}(1-\mu)h_{ini}} - \frac{\mu}{1-\mu}. \tag{3.85}$$

Some conclusions can be drawn from (3.85). First of all, T decreases as the initial height h_{ini} increases. This is consistent with our observation of Figure3.5. Furthermore, T increases as K increases. The relationship between the approximate transition time and the diffusivity ratio, K, is plotted in Figure 3.6. Hence, our result predicts that a more viscous biofilm will stay in the vertical expansion stage for a longer period of time. In other words, biofilms with more EPS will tend to stay in the planar growth phase for longer.

3.5.2 Non-Planar Growth: A Linear Stability Analysis

Next, in order to investigate the stability of the planar solutions to perturbations in the x direction, and also to study the effect of bacterial death, we will linearise system

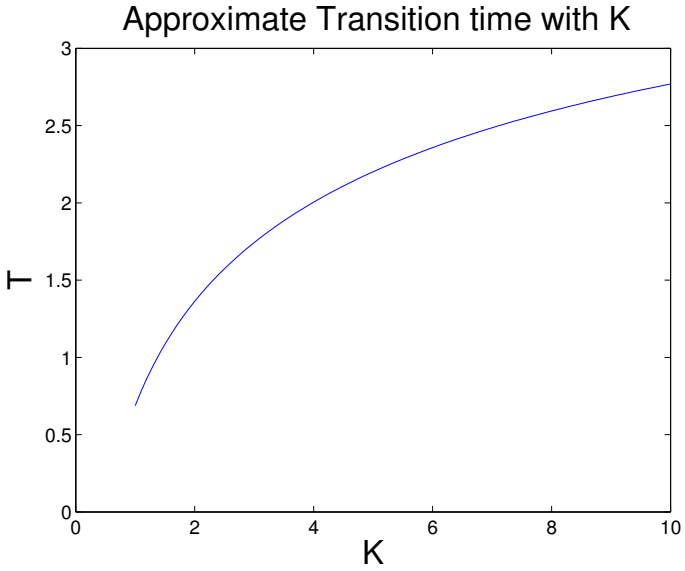

Figure 3.6: Relationship between T and the diffusivity ratio K from (3.85). Parameter values used are: $G = 250, \mu = 0.05, L = 2, h_{ini} = 0.001$.

(3.76)-(3.77) by writing the solutions as

$$S(x,z,t) = S_0(z,t) + S_1(z,t)\cos(kx)$$
$$P(x,z,t) = P_0(z,t) + P_1(z,t)\cos(kx)$$
$$h(x,t) = h_0(t) + h_1(t)\cos(kx),$$

where $|S_1| \ll 1, |S_{1,z}| \ll 1, |P_1| \ll 1, |P_{1,z}| \ll 1, |h_1| \ll 1, |h_1'(t)| \ll 1$ and where k is the wavenumber in the x direction. Therefore, the system for the perturbations $S_1(z,t), P_1(z,t)$ is given by

$$\begin{cases} S_{1,zz} - (k^2+G)S_1 = 0; \\ P_{1,zz} - k^2 P_1 = -S_1; \end{cases} \qquad 0 < z < h(x,t) \tag{3.86}$$

$$S_{1,zz} - k^2 S_1 = 0; \qquad h(x,t) < z < h(x,t) + L \tag{3.87}$$

and the height perturbation $h_1(t)$ is given by

$$h_1'(t) = (S_0(h_0^-) - \mu)h_1(t) - P_{1,z}(h_0). \tag{3.88}$$

As before, the corresponding boundary conditions for the small perturbations S_1, P_1, h_1 can be derived from (3.61) and the planar solutions obtained. Thus, we have

$$h_1 P_{0,z}(h_0) + P_1(h_0) = 0; P_{1,z}(0) = 0; \tag{3.89a}$$

$$S_1(h_0 + L) = 0, S_{1,z}(0) = 0; \tag{3.89b}$$

$$h_1 S_{0,z}(h_0^+) + S_1(h_0^+) = h_1 S_{0,z}(h_0^-) + S_1(h_0^-) \tag{3.89c}$$

$$K S_{1,z}(h_0^+) = S_{0,zz}(h_0^-) h_1 + S_{1,z}(h_0^-). \tag{3.89d}$$

System (3.86)-(3.89) constitutes the system for the small perturbations. Notice that the system (3.86)-(3.87) is the same as the system for perturbations when bacterial death is excluded, i.e. (3.69)-(3.70), and the boundary conditions in (3.89) are also the same as in (3.72). However, (3.86)-(3.87) and (3.89) all depend on the values of the planar solution and therefore these equations are affected by the bacterial death rate μ. Hence, the death rate indirectly changes the dynamics of the small perturbations.

Since (3.86)-(3.87) and (3.89) are the same as (3.69)-(3.70) and (3.72), and the planar solutions of $S_0(z,t)$ in both regions are the same as the result in (3.65), it follows that solutions of $S_1(z,t)$ in (3.86)-(3.87) are the same as (3.73), Hence, we can further obtain

$$P_1(z,t) = E^*(t) e^{kz} + F^*(t) e^{-kz} - \frac{C^*(t)}{G} \cosh(\sqrt{k^2 + G} z) \tag{3.90}$$

where

$$C^*(t) = -h_1 \cosh\left(\sqrt{k^2 + G} h_0\right)^{-1} \left[1 + \frac{N}{Kk} \sqrt{k^2 + G} M(t)\right]^{-1} \times \left[\frac{(1 - K^{-1}) \sqrt{G} K Q(t)}{\sqrt{G} L Q(t) + K} + \frac{N}{k} \frac{G}{\sqrt{G} L Q(t) + K}\right]$$

and $N := \tanh(kL), M(t) := \tanh(\sqrt{k^2+G}h_0), Q(t) := \tanh(\sqrt{G}h_0)$. Applying the boundary condition (3.89a) as well as the planar solution of $P_0(z,t)$ in (3.78) to $P_1(z,t)$ gives:

$$E^* = F^* = \frac{1}{2}\cosh^{-1}(kh_0)\left[C^*G^{-1}\cosh(\sqrt{k^2+G}h_0) + h_1\left(\frac{K}{\sqrt{G}}\frac{Q(t)}{\sqrt{G}LQ(t)+K} - \mu h_0\right)\right].$$

Finally, as before, we will study how the perturbation of the biofilm height $h_1(t)$ changes with time. On the substitution of the expression for $S_0(z,t)$ for $0 < z < h(x,t)$ given in (3.65) and $P_1(z,t)$ given in (3.90) into (3.88), we obtain

$$h_1'(t) = h_1\left[(kRh_0 - 1)\mu + U\left(1 + \frac{kR}{\sqrt{G}}\hat{U}\right) - U\left(\frac{kRQ}{\sqrt{G}} + \frac{\sqrt{k^2+G}}{\sqrt{G}}M\hat{U}\right)\right] \quad (3.91)$$

where $R := \tanh(kh_0)$, U is defined in (3.83) and $\hat{U}$ is

$$\hat{U} := \frac{k(K-1)+N}{1+N\sqrt{k^2+G}} \quad (3.92)$$

Note that (3.91) is of the form $h_1'(t) = \omega(k,t)h_1(t)$, where $\omega(k,t)$ is the dispersion relation of system (3.76)-(3.77) about the planar solutions. It is clear that the sign of $\omega(k,t)$ varies depending on the choice of the wavenumber k and other parameter values. Therefore, the planar height of system (3.76)-(3.77) can be stable or unstable to perturbations in the x direction given different wave numbers.

The term $(kRh_0 - 1)\mu$ in the dispersion relation $\omega(k,t)$ is the effect of the bacterial death. However, the sign of this term relies on the wavenumber and the planar height h_0. It is clear that when kh_0 is small enough, the introduction of μ gives an extra negative term in the dispersion relation. Therefore, we can predict that at the early stage of biofilm growth, where h_0 is small, bacterial death stabilises the planar height growth to heterogeneous perturbations. However, as h_0 increases, the sign of $(kRh_0 - 1)$ switches from negative to positive, whereby the introduction of cell death, $\mu > 0$,

provides an extra positive term in $\omega(k,t)$. Hence, at the mature stage of biofilm growth, bacterial death destabilises the planar height growth. This result suggests that bacterial death assists with spatial pattern formation in mature biofilms.

It is known that typically, spatial patterns arise in mature biofilms [8, 9]. Therefore, to consider the spatial pattern formation, it is reasonable to assume that the biofilm planar height is sufficiently large. Next, we will study the effect of bacterial death on the types of biofilm pattern formations by comparing the growing speed of the planar height (3.84) and the perturbation height (3.91).

In the earlier analysis of (3.84), we assumed that the death rate μ was sufficiently small to guarantee that $v_{out} > 0$. Then, $h_0(t)$ increased with time which corresponded to a growing biofilm. However, the constant β in (3.84b) increases as μ increases. Therefore, there must exist a critical value of the death rate, i.e. μ^*, such that for $\mu > \mu^*$, we have $\beta > 0$ and therefore $v_{out}(t) < 0$. The critical value of μ^* can be calculated by letting $\beta = 0$, i.e.

$$\mu^* = \frac{U}{\sqrt{G}h_{ini}}. \tag{3.93}$$

Hence, it is clear that the critical bacterial death rate μ^* separates the biofilm growth into two categories: growing planar height and decaying planar height, as shown in Figure 3.7.

Since we are more interested in the case where the biofilm is growing, we will focus on the case $\mu < \mu^*$ to gain some insight of the influence of death rate μ on the comparison between the planar height and the perturbed height. Following the assumption that h_0 is large enough, we have $R \approx 1, Q \approx 1, M \approx 1$. In this manner, (3.91) can be simplified as

$$h_1'(t) = h_1[(kh_0 - 1)\mu + U\bar{U}]$$

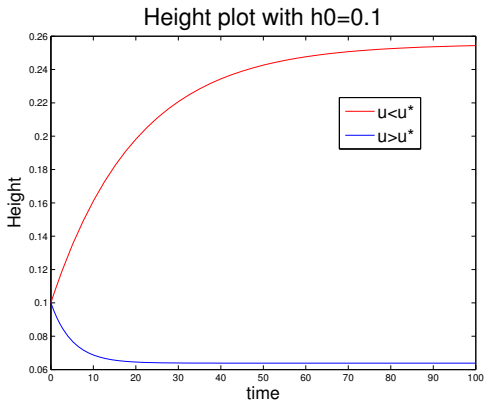

Figure 3.7: Plot of the biomass height in z direction with different values of μ. Parameter values used are: $G = 250, L = 2, K = 8, h_{init} = 0.1$ and $\mu = 0.05$ for the red line and $\mu = 0.2$ for the blue line. The critical death rate is $\mu^* = 0.1277$.

where $\bar{U} = 1 + \frac{k}{\sqrt{G}}\hat{U} - (\frac{k}{\sqrt{G}} + \frac{\sqrt{k^2+G}}{\sqrt{G}}\hat{U})$ and U and $\hat{U}$ are defined in (3.83) and (3.92).

Since we assume that h_1 is small, it is reasonable to set the initial value of h_1 also to be small, i.e. $h_1(0) = \varepsilon$. Substituting $h_0(t)$ in the case where h_0 is large (3.84a) into the previous equation gives

$$h_1'(t) = h_1 \left[\frac{k}{\sqrt{G}}U + U\bar{U} - \mu + (h_{ini} - \frac{U}{\sqrt{G\mu}})\mu k e^{-\mu t} \right]. \tag{3.94}$$

Using separation of variables to integrate yields

$$h_1(t) = C^* \exp \left[\left(\frac{k}{\sqrt{G}}U + U\bar{U} - \mu \right) t - k \left(h_{ini} - \frac{1}{\sqrt{G\mu}}U \right) e^{-\mu t} \right].$$

Applying the initial condition $h_1(0) = \varepsilon$ to this equation gives the expression of $h_1(t)$ and if we define the expression for $v_1(t)$, the speed of the perturbed height by $v_1(t) := h_1'(t)$,

then (3.94) gives:

$$h_1(t) = \varepsilon^* \exp\left[\left(\frac{k}{\sqrt{G}}U + U\bar{U} - \mu\right)t - ke^{-\mu t}\left(h_{ini} - \frac{U}{\sqrt{G}\mu}\right)\right], \tag{3.95a}$$

$$v_1(t) = h_1\left[\frac{k}{\sqrt{G}}U + U\bar{U} - \mu + \left(h_{ini} - \frac{U}{\sqrt{G}\mu}\right)\mu k e^{-\mu t}\right], \tag{3.95b}$$

where $\varepsilon^* = \varepsilon \exp\left[k\left(h_{ini} - \frac{U}{\sqrt{G}\mu}\right)\right]$. Noting that (3.94) has the form $v_1(t) = h_1'(t) = \omega(k,t)h_1$, where

$$\omega(k,t) = \left[\frac{k}{\sqrt{G}}U + U\bar{U} - \mu + (h_{ini} - \frac{U}{\sqrt{G}\mu})\mu k e^{-\mu t}\right], \tag{3.96}$$

then $\omega(k,t)$ is the dispersion relation. We are only interested in the case where spatial patterns arise, therefore we require the situation where $\omega(k,t) > 0$.

From (3.84b), it is clear that the planar height $h_0(t)$ grows with time. From (3.95b), provided that $\omega(k,t) > 0$, $h_1(t)$ will also grow with time. Next, we will follow the discussion in Section 3.3.3 by considering which height grows faster to provide a clear insight into how a spatial pattern can emerge. We will only consider the case where a spatial pattern can occur, i.e. $\omega(k,t) > 0$ for any $t > 0$. We summarise the conditions and assumptions that will be used in the following analysis:

A1: $\mu < \mu^* = \frac{U}{\sqrt{G}h_{ini}}$: This guarantees that the planar height $h_0(t)$ is growing over time;

A2: $\omega(k,t) > 0$ for any $t > 0$: This guarantees that the height perturbation $h_1(t)$ is growing over time;

A3: $kh_0(t)$ is sufficiently large so that $\tanh(kh_0(t)) \approx 1$. Therefore, the solution of $h_0(t)$ is given by (3.84a).

Our analysis will involve comparing the values of $h_0(t)$ and $h_1(t)$ at $t = 0$ and $t \to \infty$.

When $t = 0$, from (3.84b) and (3.95b), we have

$$v_{out}(0) = \frac{U}{\sqrt{G}} - \mu h_{ini}, \tag{3.97a}$$

$$v_1(0) = \varepsilon(k\mu h_{ini} + U\bar{U} - \mu). \tag{3.97b}$$

And when $t \to \infty$, we have

$$\lim_{t\to\infty} v_{out}(t) = 0, \tag{3.98a}$$

$$\lim_{t\to\infty} v_1(t) \sim \lim_{t\to\infty} h_1(t) \left(\frac{kU}{\sqrt{G}} + U\bar{U} - \mu \right). \tag{3.98b}$$

Letting $t \to \infty$ in (3.95a) gives

$$\lim_{t\to\infty} h_1(t) = \lim_{t\to\infty} \varepsilon^* \exp\left[\left(\frac{kU}{\sqrt{G}} + U\bar{U} - \mu \right) t \right]. \tag{3.99}$$

From A2, $\omega(k,t) > 0$ for any $t > 0$ and letting $t \to \infty$ in (3.96) gives

$$\lim_{t\to\infty} \omega(k,t) \sim \frac{kU}{\sqrt{G}} + U\bar{U} - \mu > 0. \tag{3.100}$$

Hence from (3.99) and (3.100) we have $\lim_{t\to\infty} h_1(t) \sim \infty$, and therefore from (3.98b) $\lim_{t\to\infty} v_1(t) \sim \infty$. Then combining this with (3.98a), we have that, for t sufficiently large, $v_1(t) > v_{out}(t)$, i.e. for large t, the velocity of the perturbed height will be the dominating element in the dynamic of biomass height. However, the dynamics are also affected by the comparison of v_{out} and v_1 at $t = 0$. Next, we will discuss the different possible dynamics in detail.

Case 1: $v_{out}(0) > v_1(0) > 0$ This case corresponds to the growth of the planar solution initially being larger than the growth of the perturbation. Substituting the expressions for $v_{out}(0)$ and $v_1(0)$ from (3.97) into this inequality gives:

$$\frac{U}{\sqrt{G}} - \mu h_{ini} > \varepsilon(k\mu h_{ini} + U\bar{U} - \mu).$$

Hence provided $\varepsilon \ll 1$ we have

$$\mu < \mu_1 := \frac{\frac{U}{\sqrt{G}} - \varepsilon U\bar{U}}{h_{ini} - \varepsilon(1 - kh_{ini})}, \tag{3.101}$$

which is a condition for the growth of the planar solutions to initially be larger than the growth of the perturbations.

From A1, we have

$$\mu < \mu^* = \frac{U}{\sqrt{G}h_{ini}}. \tag{3.102}$$

We now check that this behaviour at $t = 0$ can occur along with the planar solution growing over time. Therefore, we need to check if (3.101) and (3.102) can be satisfied at the same time. Consider

$$\begin{aligned}\mu^* - \mu_1 &= \frac{U}{\sqrt{G}h_{ini}} - \frac{\frac{U}{\sqrt{G}}\,\varepsilon U\bar{U}}{h_{ini} - \varepsilon(1 - kh_{ini})} \\ &= \frac{\varepsilon U\left(\sqrt{G}h_{ini}\bar{U} + kh_{ini} - 1\right)}{\sqrt{G}h_{ini}\left[h_{ini}\varepsilon(1 - kh_{ini})\right]}.\end{aligned}$$

From A3, kh_0 is sufficiently large such that $\tanh(kh_0(t)) \approx 1$ for all t, therefore $kh_0(t) > 1$ for all t, hence we have $kh_0(0) = kh_{ini} > 1$. Hence, it is clear that $\mu^* - \mu_1 > 0$ and therefore $\mu^* > \mu_1$, and therefore if the death rate $\mu < \mu_1$, then both (3.101) and (3.102) are satisfied and the biofilm height initially expands in a planar wave manner regardless of the perturbation. However, as time goes by, the perturbation grows faster than the planar height and eventually the spatial pattern emerges.

Case 2: $v_1(0) > v_{out}(0) > 0$ Similar calculations to case 1 give that for this inequality to hold for $\varepsilon \ll 1$, the death rate μ must satisfy $\mu > \mu_1$, i.e. for the perturbation growth to be dominant from $t = 0$, $\mu > \mu_1$. For the planar height to be growing over time, we already have the general result $\mu < \mu^*$. Combining these gives $\mu \in (\mu_1, \mu^*)$. i.e.

$$\frac{\frac{U}{\sqrt{G}} - \varepsilon U\bar{U}}{h_{ini} - \varepsilon(1 - kh_{ini})} < \mu < \frac{U}{\sqrt{G}h_{ini}}.$$

In this case, the growing velocity for the height perturbation is always faster than the one for the planar height. Therefore, spatial pattern occur immediately after the biofilm starts to grow.

As a conclusion, we can classify the different dynamics of the interface pattern in terms of the death rate, μ, and the initial biofilm height, using Figure 3.8. When the initial biofilm height h_{ini} is chosen in the dashed domain, by increasing the death rate μ, we can obtain three different patterns from 'expansion first and pattern later', to 'pattern occurs immediately', to 'decaying biofilm'.

3.6 Conclusion

In this chapter, we digressed to explore the mathematics of the model that hypothesised that the expansion of the biofilm is caused by the cell growth. Our aim was to investigate whether the heterogeneous structure of the biofilm would arise from the net cell growth only, without the influence of the cell diffusion and other external effects.

We first analysed the mathematical model that includes the cell growth without any loss of cells. This model was first proposed by Dockery and Klapper [37]. The analytical results showed that it is possible to obtain the heterogeneous structure on the biofilm interface.

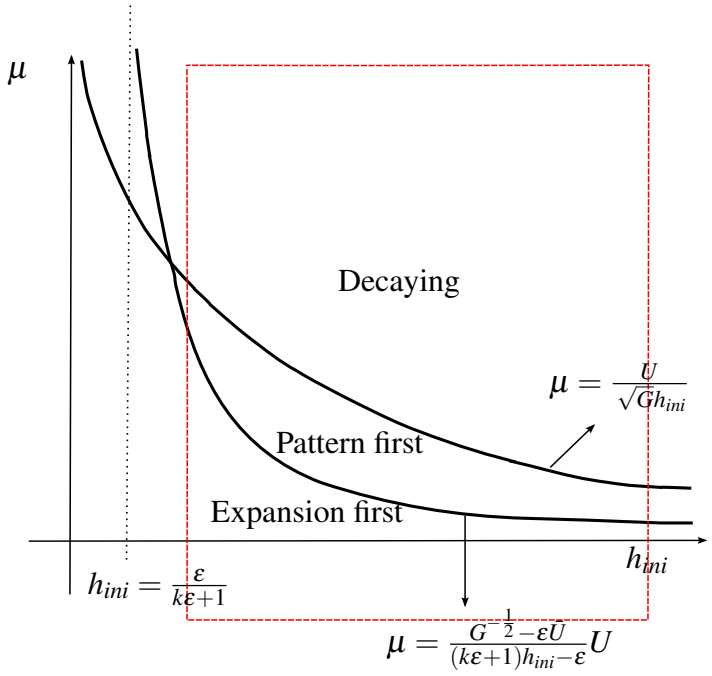

Figure 3.8: Schematic plot of which regions of the (h_{ini}, μ) plane correspond to different growth dynamics. The red dashed region is the region we are interested in.

Then we extended the original model to include the loss of cells in order to examine the effect of the cell loss on the structure of the biofilm. The 1-D planar solution analysis showed the factors which determine the average height of the biofilm and the time which is required before the interface heterogeneity starts to form. We conclude that average height of a more viscous biofilm should be higher than the average height of a less viscous biofilm. Also, the result of the 1-D planar solutions analysis predicted that a more viscous biofilm will spend longer time before the interface heterogeneity is possible to arise. Therefore we deduced that one of the role of the EPS matrix, which enables the viscous property of the biofilm, was to enhance the height of the biofilm and keep the biofilm staying in the planar growth phase for a longer period.

Results of the interface instability analysis showed that the term $(kRh_0 - 1)\mu$ in the dispersion relation was introduced by the cell death. Therefore, we predicted that at the early stage of biofilm growth, bacterial death stabilises the planar interface to

heterogeneous perturbations, however at the mature stage of biofilm growth, the cell death destabilises the planar interface. Hence, we suggest that the cell death assists with spatial pattern formation in mature biofilms. By comparing the velocity of the planar interface growth and that of the perturbed height, we were able to classify the different dynamics of the interface pattern in terms of the death rate μ. By increasing the death rate, we could obtain three different patterns from 'expansion first and pattern later', to 'pattern occurs immediately', to 'decaying biofilm'.

Chapter 4

Numerical Simulations

4.1 Introduction

In the previous chapter, we extended the mathematical model which assumed that the biofilm expansion is caused by the cell division to include the effect of the cell death. Theoretically, we found that cell death plays various and important roles on the biofilm development. The extended model captures more realistic features of biofilms. Furthermore, this model can be reduced to simpler special cases that have been studied in the previous chapter by setting the parameter values to some certain value. In this chapter, we will solve (3.76)-(3.77) numerically. It is clear from our previous analysis of this system that the biofilm interface, which separates the biofilm and aqueous regions, evolves with time. We employ the level set method in 2-D. We use a level set function $\Phi(x,z,t)$, by which the interface can be tracked implicitly [97].

4.2 Level Set Method

The level set method is a widely used numerical technique to represent an interface that separates two distinct regions or materials from one another [97, 117]. It has been applied to a wide range of areas including problems in the fluid mechanics [118], image processing [23, 88], and the shape of soap bubbles [26]. On an interface, if we know the dynamics of how the interface moves, the level set method allows us to compute the position of the interface at any given time. The level set method makes it very easy to follow interfaces that change topology, for example when an interface develops sharp corners, breaks apart, or when two interfaces merge together.

Before the introduction of the level set method, most numerical techniques relied on markers. The markers attempt to track the motion of the interface by breaking the interface into 'buoys' that are connected by pieces of 'rope'. In this method, each buoy moves with velocity V, but is always connected by the ropes [111]. However, this method fails in the case where the interface tries to break into two, or two interfaces merge together.

Instead of tracking the interface itself, the level set method constructs a surface, and the interface is defined by the intersection of this surface with a plane. In other words, the level set method first increases the dimension of the interface by 1 and then reduces the dimension back by intersecting with a plane. Figure 4.1 shows an illustration of the level set method.

4.2.1 Example of the Level Set Method

Next, we will use a 1-D example to illustrate this method. Suppose that we are tracking a point that is moving along the positive direction of the x-axis with speed v and the

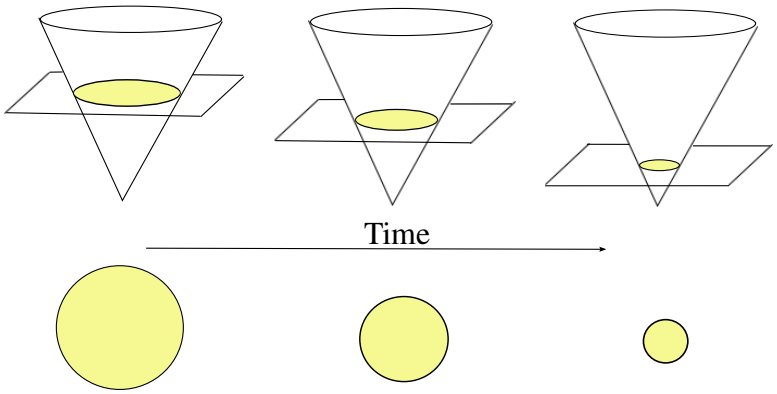

Figure 4.1: Level set method builds up a surface based on the interface. The interface is defined as the intersection of the surface and a plane. In the lower row we see the shape and above it is the corresponding surface.

position of the point at time t is denoted as $x^*(t)$, shown in Figure 4.2(a). The x axis is divided into two distinct regions by this point. The region $\Omega^- = (-\infty, x^*(t))$ is referred to as the inside domain while the region $\Omega^+ = (x^*(t), \infty)$ is referred to as the outside domain. Suppose that at $t = 0$, the point is located at $x^* = 1$, i.e. $x^*(0) = 1$, then it is clear that

$$x^*(t) = 1 + vt \quad \text{for} \quad t > 0. \tag{4.1}$$

This is the explicit representation of the position of the moving point.

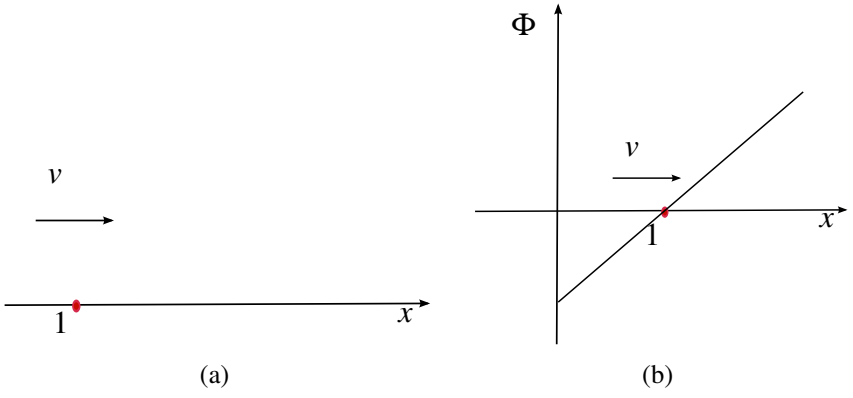

Figure 4.2: 1-D moving point (red) in 4.2(a) and the initial implicit function $\Phi(x(0), 0) = x(0) - 1$.

Alternatively, we can construct an implicit function $\Phi(x(t), t)$, where $x(t) \in (-\infty, \infty)$,

to track the point. In this way, the moving point can be represented by the isocontour of the implicit function. If we define the implicit function in our example to be of the form

$$y = \Phi(x(t),t), \tag{4.2}$$

then the moving point of interest $x^*(t)$ is implicitly given by $\Phi(x^*(t),t) = 0$, and $\Phi(x(t),t) > 0$ represents $x(t) \in \Omega^+$ while $\Phi(x(t),t) < 0$ represents $x(t) \in \Omega^-$. Initially, the implicit function is set to be the signed distance from the point of interest. Thus, for any point $x(t)$ on the x-axis, we have

$$\Phi(x(0),0) = x(0) - x^*(0) = x(0) - 1. \tag{4.3}$$

The initial value of the implicit function is shown in Figure 4.2(b).

Differentiating (4.2) on both sides with respect to t gives

$$0 = \Phi_t + x'(t)\Phi_x.$$

Since we know that the point of interest travels with speed v, i.e. $x'(t) = v$, the previous equation can be rewritten as

$$\Phi_t + v\Phi_x = 0. \tag{4.4}$$

Equation (4.4) is a simple 1-D convection equation, which has a travelling wave solution $\Phi(x(t),t) = \phi(x(t) - vt)$. Applying the initial condition (4.3) to this solution yields

$$\Phi(x(0),0) = \phi(x(0)) = x(0) - 1.$$

Hence, on replacing $x(0)$ by $x(t) - vt$ in the above solution gives

$$\Phi(x(t),t) = \phi(x(t) - vt) = x(t) - vt - 1. \tag{4.5}$$

By definition, the point of interest $x^*(t)$ is implicitly given by $\Phi(x^*(t),t) = 0$. Hence, it is clear that the position of the point of interest is given by

$$x^*(t) = 1 + vt.$$

This is the same as the explicit solution in (4.1).

4.2.2 Derivation of the Level Set Method

Motivated by the previous 1-D example, we will introduce the level set method mathematically. Given an interface $\Gamma(t)$ in 2-D which changes with time, bounding an open region Ω, we wish to compute the subsequent motion under a velocity field $\vec{v} \equiv (u,v)$. This velocity can depend on position, time and the external physics. The level set method represents the interface Γ using an auxiliary function $\Phi(\vec{X}(t),t)$, called the level set function, where $\vec{X}(t) \equiv (x(t),y(t))$. Instead of tracking the interface in 2-D directly, the level set method constructs a surface

$$z = \Phi(\vec{X}(t),t), \tag{4.6}$$

where the geometry is extended to 3-D. The level set function has the following properties:

$$\begin{aligned}
\Phi(\vec{X}(t),t) &< 0 \quad \text{for} \quad \vec{X}(t) \in \Omega \\
\Phi(\vec{X}(t),t) &> 0 \quad \text{for} \quad \vec{X}(t) \notin \Omega \\
\Phi(\vec{X}(t),t) &= 0 \quad \text{for} \quad \vec{X}(t) \in \Gamma(t).
\end{aligned}$$

Alternatively, it is also possible to define $\Phi(\vec{X}(t),t) > 0$ for $\vec{X}(t) \in \Omega$, $\Phi(\vec{X}(t),t) > 0$ for $\vec{X}(t) \notin \Omega$. Therefore, the interface is captured for all later time by locating $\Gamma(t)$ to

where $\Phi(\vec{X}(t),t) = 0$.

Initially, the level set function is set to be $\Phi(\vec{X}(0),0) = d$, where d is the signed distance from the point $\vec{X}(0)$ to the interface, such that $\Phi(\vec{X}(0),0) < 0$ in Ω and $\Phi(\vec{X}(0),0) > 0$ outside Ω. As the function $\Phi(\vec{X}(t),t)$ evolves with time, the interface evolves implicitly as well.

Next, we will derive the governing equation for the level set function $\Phi(\vec{X}(t),t)$. Suppose that $\vec{X}(t)$ describes the path of a point on the interface over time, i.e. $\Phi(\vec{X}(t),t) = 0$. Then differentiating this equation with respect to t and applying the chain rule yields

$$\Phi_t + \vec{v} \cdot \nabla\Phi = 0, \tag{4.7}$$

where $\vec{v} \equiv \vec{X}'(t)$ is the desired velocity on the interface, and is chosen arbitrarily elsewhere, and $\nabla \equiv \nabla_{\vec{X}}$ which is the spatial differentiation on the 2-D plane that the interface is sitting on. Let $\vec{n}$ be the outward directed normal to the interface, then $\vec{n}$ can be rewritten in terms of $\Phi(\vec{X}(t),t)$ as follows:

$$\vec{n} = \frac{\nabla\Phi}{|\nabla\Phi|}.$$

Thus we have $\nabla\Phi = \vec{n}|\nabla\Phi|$. Defining the normal component of $\vec{v}$ as $v_{norm} = \vec{v} \cdot \vec{n}$, we can rewrite (4.7) as

$$\Phi_t + v_{norm}|\nabla\Phi| = 0. \tag{4.8}$$

Both (4.7) and alternatively (4.8) are widely used as the governing equation for the level set function $\Phi(\vec{X}(t),t)$. Once the level set function is computed, the interface can be found by solving $\Phi(\vec{X}(t),t) = 0$.

4.2.3 Numerical Scheme

Equation (4.7) can be solved numerically using a finite difference scheme on a Cartesian grid. One of the best finite difference methods for (4.7) is the *upwind method* which uses the simple *forward Euler method* to discretise the time and uses either forward or backward Euler method, depending on the direction of the velocity, for the spatial discretization. Taking (4.7) in 1-D as an example for simplicity, the discretization of (4.7) at point (t_n, x_i) can be written as

$$\frac{\Phi_i^{n+1} - \Phi_i^n}{\triangle t} + V_i^n (\Phi_x)_i^n = 0,$$

where

$$\Phi_x = \begin{cases} \Phi_x^- = \frac{\Phi_i - \Phi_{i-1}}{\triangle x} & \text{when} \quad V_i < 0 \\ \Phi_x^+ = \frac{\Phi_{i+1} - \Phi_i}{\triangle x} & \text{when} \quad V_i > 0. \end{cases} \tag{4.9}$$

The upwind method is always consistent and stable in certain circumstances. However, the scheme can be improved by using a more accurate approximation for Φ_x^- and Φ_x^+ in order to achieve higher accuracy. Harten et al. [60] introduced the idea of essentially non-oscillatory (ENO) polynomial interpolation of data for the numerical solution of conservation laws. Using the 1-D version as an example, in the ENO method, they used Newton polynomial interpolation to approximate the smooth level set function Φ with the discrete data set (x_i, Φ_i), and then differentiated to get Φ_x. The Newton polynomial for $\Phi(x)$ is given by

$$\Phi(x) = \Phi(x_i) + A_1(x - x_i) + A_2(x - x_k)(x - x_{k+1}) + A_3(x - x_{k^*})(x - x_{k^*+1})(x - x_{k^*+2}) + O(x^4), \tag{4.10}$$

where $k = i - 1$ to find Φ_x^-, $k = i$ to find Φ_x^+, k^* can be chosen to be $k-1$ or k depending on certain conditions, and A_i, where $i = 1, 2, 3$, are the divided differences to i^{th} order.

After differentiating (4.10) and evaluating the derivative at $x = x_i$, Φ_x can be obtained in the following form

$$\Phi_x(x_i) = A_1 + O(x_i^2). \tag{4.11}$$

It can be shown that A_1 has the same form as the right hand side of (4.9) depending on the choice of k. In other words, the first-order accurate polynomial interpolation is exactly first-order unwinding. Improvements are obtained by including higher order terms of x_i.

In the ENO method, a subset of $\Phi_{i-3}, \Phi_{i-2}, \Phi_{i-1}, \Phi_i, \Phi_{i+1}, \Phi_{i+2}$ are used when calculating Φ_x^-. Liu et al. [85] pointed out that the ENO method overkills some stencils in smooth regions where the data are well behaved. They proposed a weighted ENO (WENO) which assigns different weight to each stencil. Hence, the governing formulae of the WENO method can be summarised as follow:

$$\Phi_x^-(x_i) = \omega_1\Phi_{i-3} + \omega_2\Phi_{i-2} + \omega_3\Phi_{i-1} + \omega_4\Phi_i + \omega_5\Phi_{i+1} + \omega_6\Phi_{i+2}. \tag{4.12}$$

Further details of the numerical schemes can be found in [119, 120]. In our numerical simulations, we choose to use the WENO method to solve for the level set function.

4.3 Numerical Results

In this section, we will show the results of numerical simulations of system (3.76)-(3.77). However, since the parameter values in their dimensional form are known in the literature, we chose to use the dimensional form of (3.76)-(3.77) as follows:

$$D_1\nabla^2 s = 0; \quad h(x,t) < z < H(x,t)$$

$$\begin{cases} D_2\nabla^2 s - \alpha s = 0; \\ -\lambda\nabla^2 p = \beta s - \mu; \end{cases} \qquad 0 < z < h(x,t)$$

where $x \in [0,w], z \in [0,H(x,t))$. There are 6 dimensional parameters in the system: α is the nutrient consumption rate; β is the bacterial growth rate; μ is the bacterial death rate; λ is the Darcy's law constant; and D_1 and D_2 are the substrate diffusion coefficient in the aqueous and biofilm region respectively.

To simulate this dimensional system, we rewrite the two region system into one governing system by introducing a new variable b to represent the biofilm density, which is defined as follows:

$$b = \begin{cases} b_0 \quad \text{for} \quad 0 < z < h(x,t); \\ 0 \quad \text{for} \quad h(x,t) < z < H(x,t). \end{cases}$$

In this way, by using b to indicate the region, we have

$$0 = D\nabla^2 s - \alpha s b; \tag{4.13}$$

$$-b\lambda\nabla^2 p = b(\beta s - \mu); \tag{4.14}$$

where $D = D_2 b + D_1(b_0 - b)$. The dimensional form of the interface evolution equation is given by

$$\vec{v} = \frac{\partial h(x,t)}{\partial t} = -\mathbf{n}\cdot\lambda\nabla p|_{z=h^-}. \tag{4.15}$$

Notation	Description	Value	Unit
D_1	Substrate diffusion coefficient in the aqueous region	10.41×10^6	$\mu m^2 h^{-1}$
D_2	Substrate diffusion coefficient in the biofilm region	8.33×10^6	$\mu m^2 h^{-1}$
b_0	Biofilm density	200	gL^{-1}
s_0	Initial substrate concentration	3×10^{-3}	gL^{-1}
α	Substrate consumption rate per cell	0.025	h^{-1}
$\frac{\beta}{\lambda}$	Bacterial growth rate over Darcy's coefficient	2.5	h^{-1}

Table 4.1: Dimensional parameter values from [147]

The boundary conditions of this system is given by

$$p(z=h)=0; p_z(z=0)=0; \tag{4.16a}$$

$$s(z=H)=s_\infty, s_z(z=0)=0; \tag{4.16b}$$

$$s(z=h^+)=s(z=h^-); \tag{4.16c}$$

$$D_1 \nabla s(z=h^+)\cdot \mathbf{n} = D_2 \nabla s(z=h^-)\cdot \mathbf{n}, \tag{4.16d}$$

along with periodic boundary conditions for $p(x,z,t), s(x,z,t)$ and $h(x,t)$ at $x=0$ and $x=w$.

System (4.13) - (4.16) was solved numerically on a domain of $100\mu m \times 100\mu m$. We used 128×128 grid points in the computational domain. The parameter values used in the simulations are shown in Table 4.1 which were taken from [147].

The numerical scheme used to study the dynamics of biofilm growth was a finite difference scheme. A central finite difference method was used to discretize the spatial derivative, and the level set method is used to update the biofilm interface after each time step. A multi-grid method was also used to accelerate the convergence of each iterate [126].

Next, we will introduce the general process of the simulations. The flow chart in Figure 4.3 shows the process for one iteration. As the first step, the biofilm is updated according to the value of the level set function $\Phi(x,z,t)$. The biofilm variable denoted by b is set to b_0 if the grid point is inside the biofilm region, i.e. $\Phi(x,z,t) < 0$, otherwise 0. Next, as the second step, the substrate concentration $s(x,z,t)$ is computed from (4.13). The numerical scheme used in this step is the finite difference discretisation in space and the full-approximation storage multi-grid method [106]. In step three, once the substrate concentration is computed, the biofilm growth rate in (4.14) is updated. Therefore, by using the central difference discretisation and the multi-grid solver, (4.14) is solved to give the pressure field for each grid point. In the fourth step, the interface velocity from (4.15) can be computed by using a central difference second order scheme. In the final step, with the velocity of the interface, the level set function given in (4.7) can be advanced using WENO method. In this method, in order to guarantee the stability of the numerical method, Courant-Friedreichs-Lewy condition (CFL condition) is checked after each iteration. Since we fixed the spatial step size ∇x, to guarantee the stability, we modify the time step size ∇t every time in each iteration in order to guarantee the CFL condition. Then the next iteration starts by updating the biofilm according to the new level set function. These five steps constitute the algorithm used for solving (4.13)-(4.15) for one time iteration.

We started the simulation with a biofilm that has a planar height h_{ini} and perturbation of the form $\varepsilon\cos(kx)$, where ε is the initial height of the perturbation and k is the wave number. From the results summarised in Figure 3.8, if the initial planar height, h_{ini}, is fixed whilst the death rate μ is increased, the dynamics of the interface will change from the situation that the planar expansion happens before the spatial pattern to the situation that the spatial pattern arises first. Simulations were performed with different parameter value μ and a fixed value h_{ini}. We chose 20 rows of grid point from the bottom of the computational domain as the initial planar height h_{ini}. Therefore, the

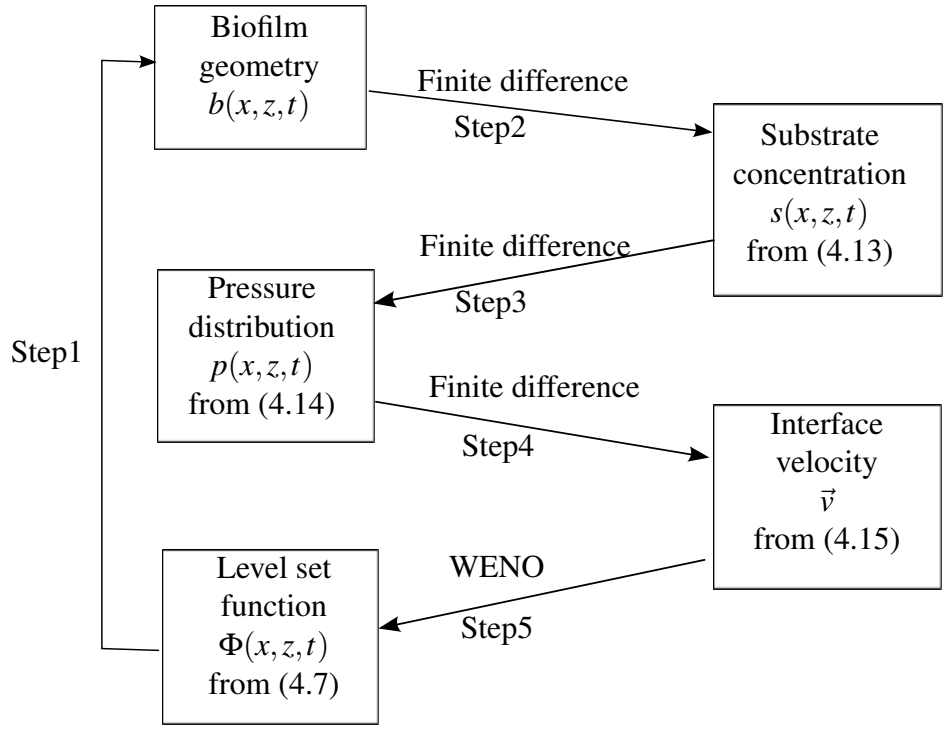

Figure 4.3: General algorithm used to solve the biofilm model (4.13)-(4.16).

value of h_{ini} was correspondingly chosen to be $h_{ini} = 15.6\mu$m. Figure 4.4 represents the case where the interface grows uniformly in the vertical direction at the beginning and the spatial pattern is observable later. This mimics the case where expansion arises first that corresponds to the lower region in Figure 3.8. Figure 4.5 represents the case where the interface destabilises immediately after the biofilm starts to grow. These two sets of simulations suggest that the cell death rate, μ, is one of the key factors that determine what type of interface growth a biofilm can present. Note that the time points of the simulations are not the regular, evenly chosen time steps. This is because in the computational algorithm, the time step varies for each iteration in order to guarantee the stability of the algorithm.

In the case where the increase in depth arises before spatial pattern is observable, we want to use numerical simulations to investigate whether it is the maturity of the biofilm (time) or the depth of a biofilm that triggers the transition from the planar growth to

spatial patterning. A number of simulations were performed with the same parameter values apart from the initial depth h_{ini}. Numerical results suggest that it is not the maturity of the biofilm that triggers the transition because it takes shorter for the transition to occur when initial depth is higher. Moreover, the transition occurs when the average height reaches around the same height when the initial depth was chosen to be different. These observations suggest that, under the same environmental conditions, the initially thin and thick biofilms have approximately the same final height at which spatial pattern occurs. Furthermore, it will take the thin biofilm a longer period for expansion before spatial pattern takes place. Figure 4.7 shows the simulations of biofilm growth with $2/3$ of the initial depth as that shown in Figure 4.6. In Figure 4.6, the spatial pattern starts to be clearly observable between $t = 31.9h$ and $t = 42.87h$ (shown in Figure 4.6(c) and 4.6(d)), while in Figure 4.7, spatial pattern becomes clearly observable between about $t = 82.03h$ and $t = 102.53h$ (shown in Figure 4.7(d) and 4.7(e)). Also, in both of these simulations, the transition occurs when the average height reaches around 40 μm. .

Figure 4.8 shows the results of a simulation with the same parameter values as used in Figure 4.7 and the same initial biofilm depth $h_{ini} = 15.6\mu m$, but with a reduced death rate. We observed that the reduced death rate causes the biofilm to grow to a greater depth before the initiation of pattern formation. Similar simulations using different death rates reveal that the onset of pattern formation is delayed (in the sense of depth) as the cell death rate decreases.

Finally, we consider the effect of the wave number on the spatial pattern formation. In Figure 4.9, the wave number is chosen to be $k = 2$ and in Figure 4.10, the wave number is chosen to be $k = 13$. We observed that in Figure 4.10, the spatial pattern disappeared at the beginning, but it came back after some time with a clearly smaller wavenumber. This is consistent with the analytical result that the dispersion relation $\omega(k,t)$ is bigger if the wave number k is smaller (see Section 3.5.2 in Chapter 3 for detail).

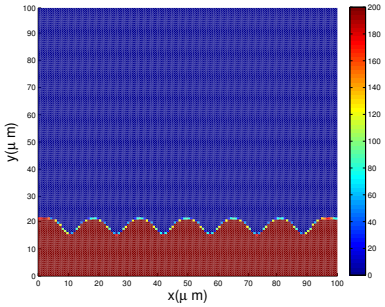

(a) Biomass at $t = 0$ hrs.

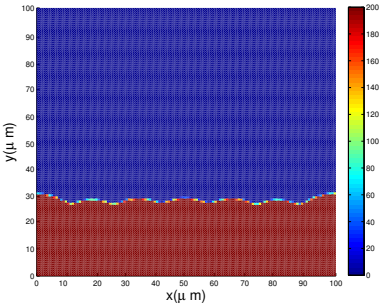

(b) Biomass at $t = 87.09$ hrs.

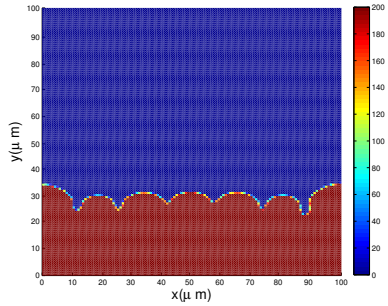

(c) Biomass at $t = 167.19$ hrs.

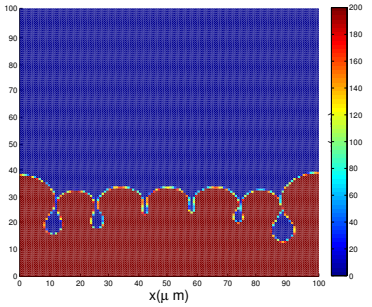

(d) Biomass at $t = 228.65$ hrs.

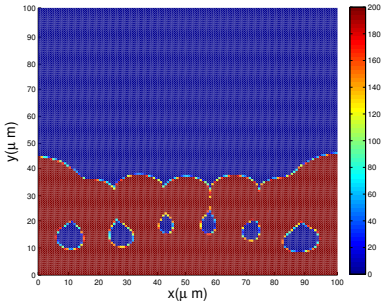

(e) Biomass at $t = 365.09$ hrs.

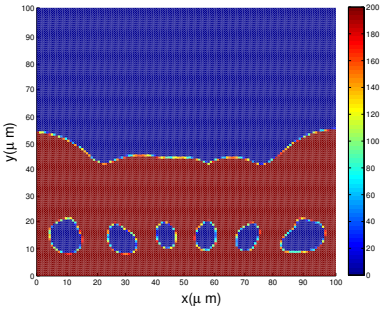

(f) Biomass at $t = 392.56$ hrs.

Figure 4.4: Evolution of the biofilm growth by system (4.13)-(4.15) in 2-D. The initial planar height is chosen to be $h_{ini} = 15.6\mu m$ and the wave number k is chosen to be $k = 7$. The bacterial death rate over Darcy's coefficient is chosen as $\frac{\mu}{\lambda} = 2.46h^{-1}$. The vertical expansion cane observed before spatial pattern grows.

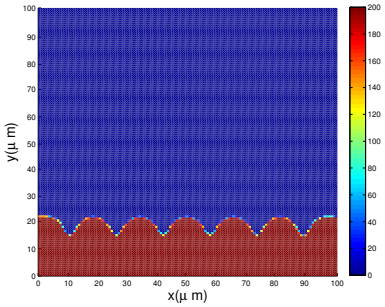

(a) Biomass at $t = 0$ hrs.

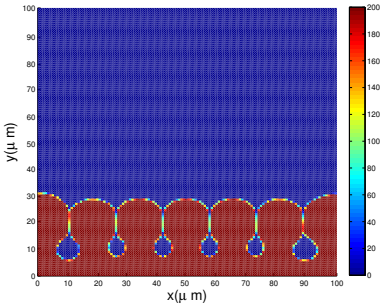

(b) Biomass at $t = 182.52$ hrs.

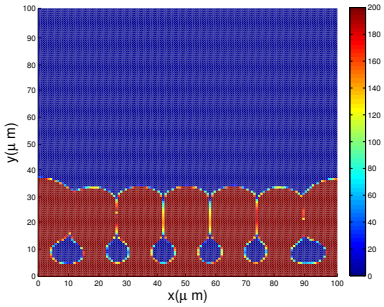

(c) Biomass at $t = 291.96$ hrs.

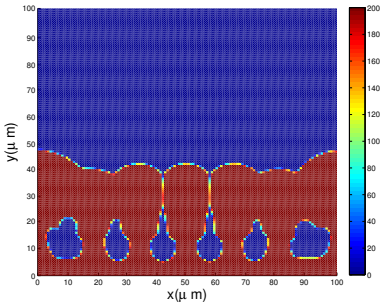

(d) Biomass at $t = 481.88$ hrs.

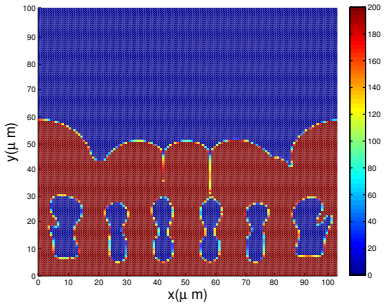

(e) Biomass at $t = 698.89$ hrs.

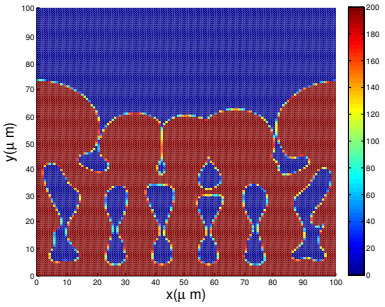

(f) Biomass at $t = 956.1$ hrs.

Figure 4.5: Evolution of the biofilm growth by system (4.13)-(4.15) in 2-D. The initial planar height is chosen to be $h_{ini} = 15.6\mu m$ and the wave number k is chosen to be $k = 7$. The bacterial death rate over Darcy's coefficient is chosen as $\frac{\mu}{\lambda} = 2.47h^{-1}$. The growth of the spatial pattern can be observed from $t = 0$.

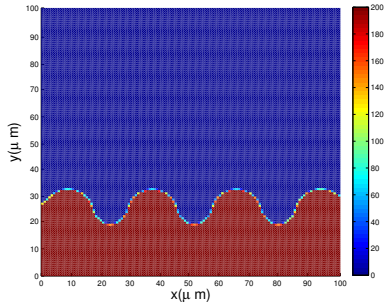

(a) Biomass at $t = 0$ hrs.

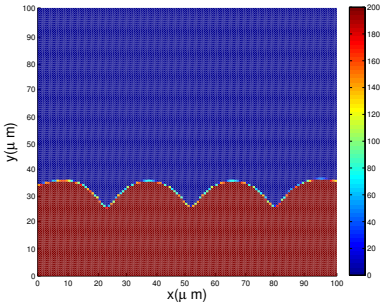

(b) Biomass at $t = 15.63$ hrs.

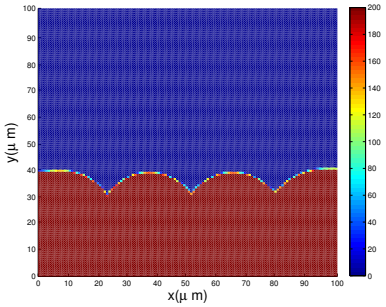

(c) Biomass at $t = 31.9$ hrs.

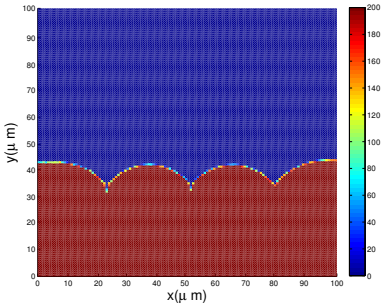

(d) Biomass at $t = 42.87$ hrs.

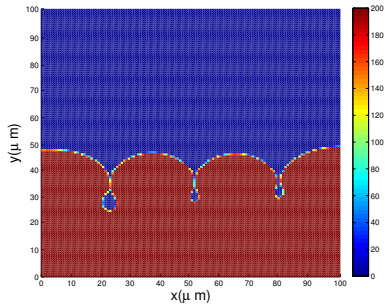

(e) Biomass at $t = 79.6$ hrs.

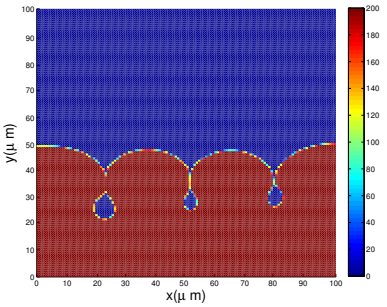

(f) Biomass at $t = 86.24$ hrs.

Figure 4.6: Evolution of the biofilm growth by system (4.13)-(4.15) in 2-D. The initial planar height is chosen to be $h_{ini} = 23.4\mu m$, and the wave number k is chosen to be $k = 4$. The bacterial death rate over Darcy's coefficient is chosen as $\frac{\mu}{\lambda} = 2.45h^{-1}$ such that initially the growth of planar depth is dominant before spatial pattern growth becomes dominant at later time.

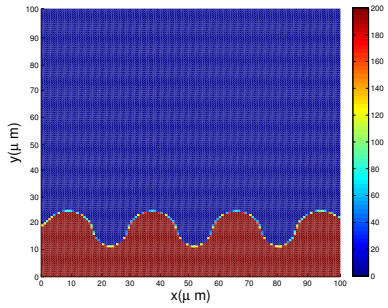

(a) Biomass at $t = 0$ hrs.

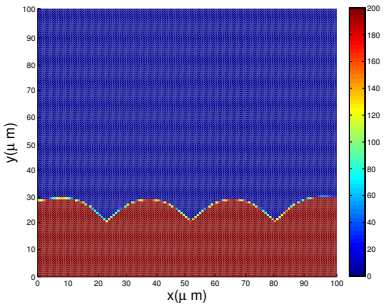

(b) Biomass at $t = 24.77$ hrs.

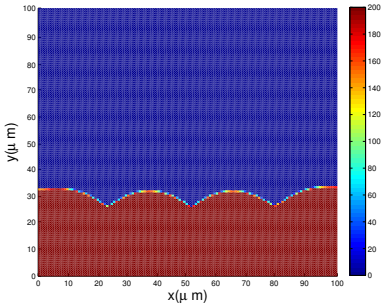

(c) Biomass at $t = 39.24$ hrs.

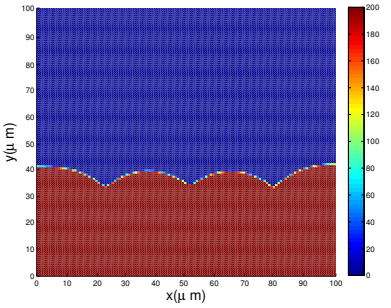

(d) Biomass at $t = 82.03$ hrs.

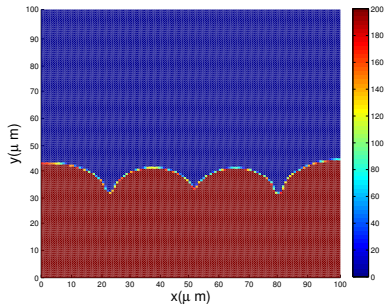

(e) Biomass at $t = 102.53$ hrs.

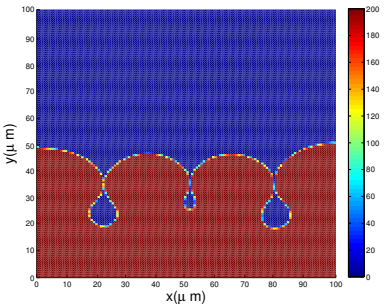

(f) Biomass at $t = 146.82$ hrs.

Figure 4.7: Evolution of the biofilm growth by system (4.13)-(4.15) in 2-D. The initial planar height is chosen to be $h_{ini} = 15.6\mu m$, which is $2/3$ of the initial height used in Figure 4.6, and the wave number k is chosen to be $k = 4$. The bacterial death rate over Darcy's coefficient is chosen as $\frac{\mu}{\lambda} = 2.45h^{-1}$ such that initially the growth of planar depth is dominant before spatial pattern growth becomes dominant at later time.

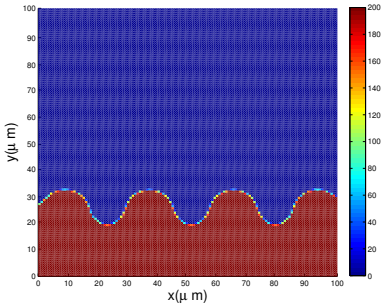

(a) Biomass at $t = 0$ hrs.

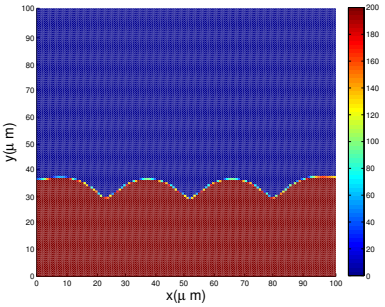

(b) Biomass at $t = 16.01$ hrs.

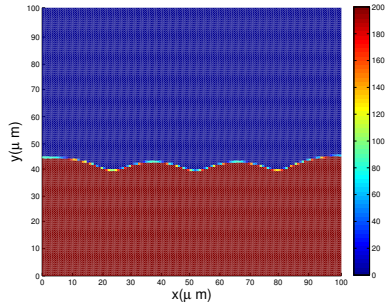

(c) Biomass at $t = 34.11$ hrs.

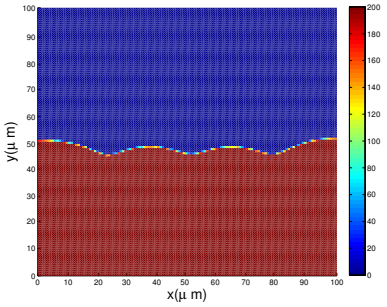

(d) Biomass at $t = 59.92$ hrs.

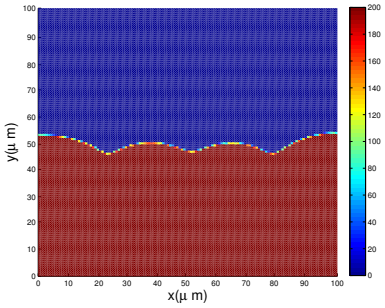

(e) Biomass at $t = 72.84$ hrs.

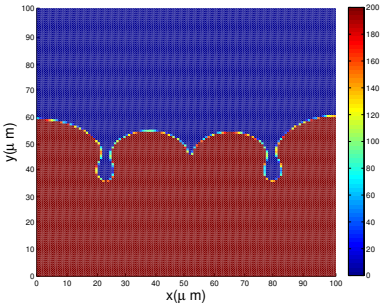

(f) Biomass at $t = 110.06$ hrs.

Figure 4.8: Evolution of the biofilm growth by system (4.13)-(4.15) in 2-D. The initial planar height is chosen to be $h_{ini} = 15.6\mu m$, which is the same as used in Figure 4.7, and the wave number k is chosen to be $k = 4$. The bacterial death rate over Darcy's coefficient is chosen as $\frac{\mu}{\lambda} = 2.43h^{-1}$ which is smaller than that used in Figure 4.7.

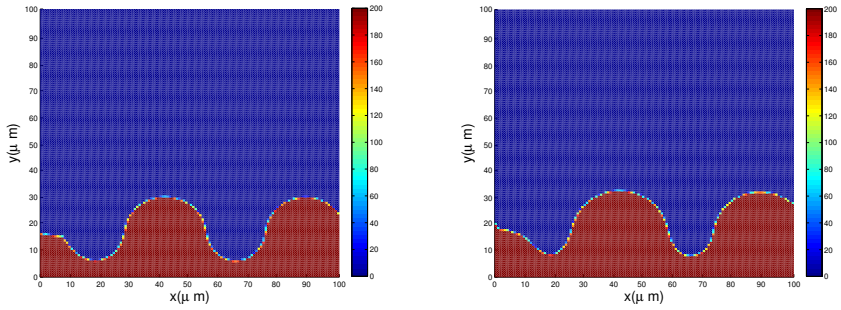

(a) Biomass at $t = 0$ hrs.

(b) Biomass at $t = 15.26$ hrs.

(c) Biomass at $t = 32.55$ hrs.

(d) Biomass at $t = 58.42$ hrs.

Figure 4.9: Simulation of biomass growth of system (4.13) -(4.15) in 2-D with initial biofilm height set as $15.6\mu m$. The bacterial death rate over Darcy's coefficient is chosen as $\frac{\mu}{\lambda} = 2.46h^{-1}$. The wave number is chosen as 2 in the simulation.

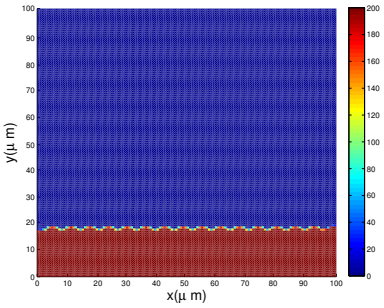

(a) Biomass at $t = 0$ hrs.

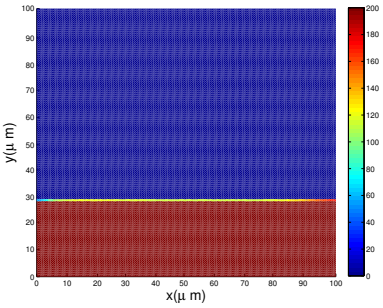

(b) Biomass at $t = 45.44$ hrs.

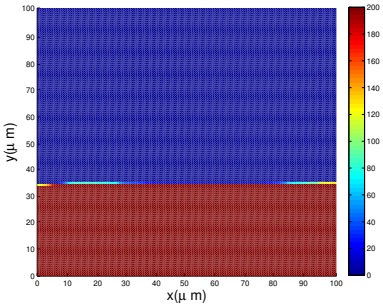

(c) Biomass at $t = 100$ hrs.

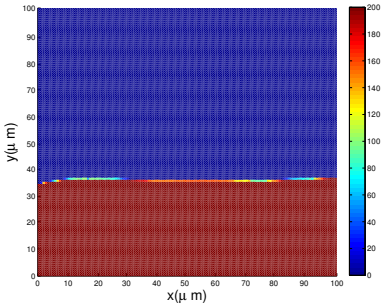

(d) Biomass at $t = 149.23$ hrs.

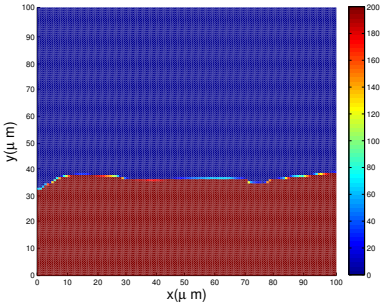

(e) Biomass at $t = 191.18$ hrs.

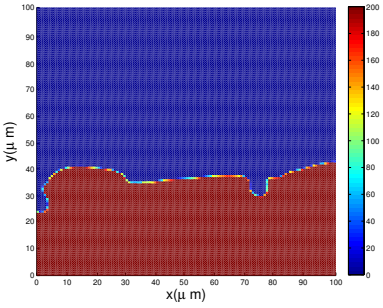

(f) Biomass at $t = 243.79$ hrs.

Figure 4.10: Simulation of biomass growth of system (4.13) -(4.15) in 2-D with initial biofilm height set as $15.6\mu m$. The bacterial death rate over Darcy's coefficient is chosen as $\frac{\mu}{\lambda} = 2.46h^{-1}$. The wave number is chosen as 13 in the simulation.

Chapter 5

Expansion of Biofilm Driven by Osmotic Pressure

5.1 Introduction

It is shown in Chapter 6 that there is a significant difference between the wild-type biofilm and the *eps* mutant in both radial expansion and in vertical growth. Although the radius of the wild-type biofilm and the *bslA* mutant tend to be similar, the rate of growth of their heights are significantly different especially at the early stage of biofilm growth, i.e. before 36 hours. In this chapter, we will use a mathematical model to better understand how these differences of biofilm growth occur. As we will discuss here, an adaptation of the model in [116] is capable of accurately capturing dynamics of the mutants with functional EPS components.

We will first show the general idea of the model and the detail of the model set up will be given in the Appendix 8.1. Then, we will simplify the model by applying the thin-film approximation. With the simplified model, we are able to solve the model

analytically and obtain a relationship to describe how the height of the biofilm changes over time. Finally, we will give our interpretation of the biological difference between different strains observed in the experiment by using the result of the model.

5.2 Model Introduction

The volume fraction is a quantity that was first widely used in the mathematical modelling of chemical systems that involves polymers and solvent [93]. The polymer and solvent system is usually assumed to be a system constituted of a uniform lattice and each lattice entry is occupied by either a solvent molecule or a polymer molecule. Usually, the size of a polymer molecule is much larger than a water molecule, therefore, it is always assumed that each polymer molecule can occupy more than one lattice entry. With the above assumptions, the volume fraction for the polymer molecule is defined as

$$\phi_{poly} = \frac{\text{Total number of lattice entries occupied by polymer molecules}}{\text{Total number of entries in the lattice}}.$$

The definition of the volume fraction can also be rewritten in terms of the number of molecules in the system. If we denote n_s as the number of the solvent molecules and n_p as the number of the polymer molecules in the system, and we also denote $r = \frac{V_p}{V_s}$, where V_p is the volume of each of the polymer molecule while V_s is the volume of each of the solvent molecule, then the volume fraction can be rewritten as

$$\phi_{poly} = \frac{n_p r}{n_s + n_p r}.$$

The volume fraction has a number of advantages in mathematical modelling. First of all, the volume fraction is one way of expressing the composition of a mixture with a dimensionless quantity. Therefore, with the use of volume fraction, it is relatively easy

to compare different components in the system. Secondly, the total volume fraction of all the components in the system sums to one. This allows a system to be written in terms of one less variable. Finally, using the volume fraction will not over/under estimate the fraction. In the polymer-solvent system, there is usually a small number of the polymer molecules and a large number of the solvent molecules. Therefore, if using the mole fraction (number fraction), the value would be very small. Similarly, since the weight of the polymer molecules is always much larger than that of the water molecules, the weight fraction would be very large if used.

More recently, the concept of volume fraction has been adapted to the mathematical modelling of the biological systems that typically involve interaction between cells and liquid in the system along with the hydration dynamics. Wolgemuth et. al. [145] proposed a mathematical model with the use of volume fraction to study the swelling dynamics of polyelectrolyte gels used for drug release. Cogan and Keener [28] stated that there are numerous biological and biotechnological examples where the structure and dynamics of polymer gels regulates the local environment. They derived a model of gel dynamics based on two-phase: the networked polymer and the fluid solvent, with the use of volume fraction. This model of gel dynamics has been widely adapted to study the biofilm structure by treating the biofilm as a mixture of biomaterial consisting of the biomass and the EPS molecules, and solvent consisting of water and substrate[4, 116, 143, 152].

In [116], Seminara et al. reported that, in the first 24 h of biofilm development, mutants lacking the EPS component show a dramatically reduced surface motility (radial expansion) compared to the wild type. They proposed that this difference was due to osmotic stresses generated by secretion of EPS. They further hypothesized that the EPS supports an osmotic pressure balance with the agar, causing swelling of the biofilm through uptake of water. To test this hypothesis, they developed a mathematical model to investigate how the shape of a biofilm would change as a result of balancing osmotic

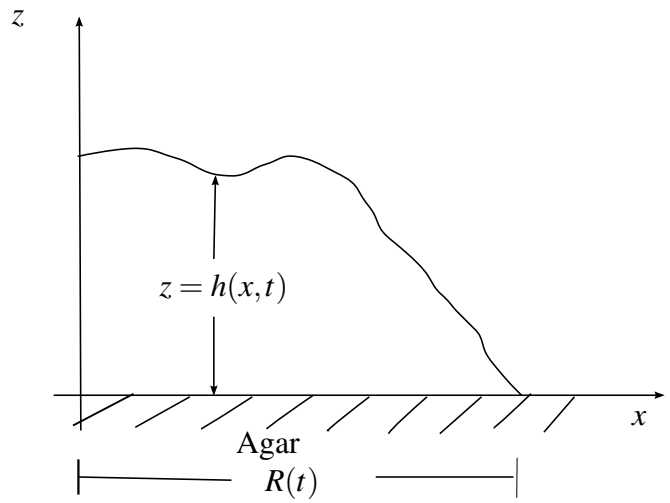

Figure 5.1: Sketch of the geometry of the biofilm that will be modelled in this section. The biofilm grows on the agar surface and is surrounded by air.

pressure gradients due to EPS secretion.

The model considers a biofilm grows on an agar surface and is in contact with air above. The model considers the biofilm in vertical section. The geometry of the model is shown in Figure 5.1. The biofilm region is defined as $[0,R(t)] \times [0,h(x,t)]$ where $R(t)$ is the radius of the biofilm and $h(x,t)$ is the height of the biofilm.

The model in [116] considered the biofilm as a mixture of biomass and water with a biomass volume fraction ϕ and water volume fraction $1-\phi$. When the water volume fraction is in equilibrium with the agar, the biofilm volume fraction is a constant ϕ_∞, so that the osmotic pressure in the biofilm equals that in the agar. As the biomass grows, it consumes water to produce more biomass, creating an osmotic imbalance in the biofilm and therefore uptake of water from the agar takes place. Details of the construction of model are given in the Appendix 8.1. Here, we will describe the general idea behind how the model is set up.

The biomass growth modifies ϕ according to the mass conservation law for both the water and the biomass. The space-time distributions of the velocities for the biomass and the water respectively are determined by minimising the sum of mixing free energy change and dissipation in the biofilm system, including both the biomass and water.

To analyse the mathematical model, Seminara et al. [116] considered small departures from the osmotic balance ϕ_∞, i.e. they expanded the solution as $\phi = \phi_\infty + \varepsilon\phi$. By using the thin-film approximation, the model was further reduced to a single partial differential equation for the biofilm height. Then, they looked for a self-similarity solution of the height equation to obtain a single expression for the biofilm radius and the other expression for the biofilm height. The expression derived for the biofilm radius predicted that the radius is initially constant (swelling stage) but then starts to grow exponentially (expansive stage). The expression for the biofilm height predicted that initially the biofilm steepens without spreading, and later the biofilm undergoes expansion and smoothening. They also found that the transition time between these two phases of biofilm development was determined by a single parameter that was a combination of geometric and material parameters. However, Seminara et al. also stated that the *eps* mutant biofilm cannot effectively generate osmotic pressure. Therefore, they concluded that their model accurately captured the two-phase growth in wild type, but is unable to capture the behavior of the *eps* mutant.

In the experiment described in Chapter 6, we compare the radius and height of the wild type biofilm, *bslA* mutant, which is deficient of the hydrophobic layer surrounding the biofilm surface, and the *eps* mutant, which is deficient of the EPS matrix. We confirmed the experimental results Seminara et al. obtained. We also found that there was difference in both the radius and height development between the wild type biofilm and the *bslA* mutant. Furthermore, we noticed that the morphology of the wild type biofilm and the *bslA* mutant were dramatically different. With these experimental observations as motivation, we wish to investigate the function of the hydrophobic layer that is lacked in the *bslA* mutant. We wish to test whether this hydrophobic layer contributes to water loss or water absorption at the biofilm-air interface.

In this chapter, we will adapt the model proposed by Seminara et al. [116] to test the hypothesis proposed above. We will also modify the boundary conditions used in [116]

as we take different hypotheses into consideration. Details of the model construction and boundary conditions are given in Appendix 8.1.

5.3 Mathematical Analysis

In this section, we will conduct the thin-film analysis following the procedure given in [116]. We wish to obtain an expression to describe how the height of the biofilm changes overtime. The model we will study is given as follows:

$$\phi_t + (\phi u)_x + (\phi v)_z = g\phi; \tag{5.1a}$$

$$u_x + v_z = \left(\frac{(1-\phi)^2}{\zeta} p_x\right)_x + \left(\frac{(1-\phi)^2}{\zeta} p_z\right)_z; \tag{5.1b}$$

$$\mu_b(u_{xx} + u_{zz}) = p_x + E\phi_x; \tag{5.1c}$$

$$\mu_b(v_{xx} + v_{zz}) = p_z + E\phi_z. \tag{5.1d}$$

with the boundary conditions:

$$\mathbf{v}_b = (u,v) = (0,0) \quad \text{at} \quad z = 0, \tag{5.2a}$$

$$u_z = 0 \quad \text{at} \quad z = h(x,t), \tag{5.2b}$$

$$-p + 2\mu_b v_z = -p_{ext} \quad \text{at} \quad z = h(x,t), \tag{5.2c}$$

$$h_t + uh_x = v, \quad \text{at} \quad z = h(x,t). \tag{5.2d}$$

5.3.1 Non-Dimensionalisation

Similar to the model studied in Chapter 3, system (5.1) includes a moving boundary that makes the system difficult to study. Therefore, scaling factors are introduced in

order to simplify the model. Seminara et al. [116] introduced the initial radius of biofilm R_0 and the height of the biofilm $h(x,t)$ as the scaling factors. However, since $h(x,t)$ changes with both space and time, we will instead introduce the initial height of the biofilm h_0 as the scaling factor. By setting

$$z' = \frac{z}{h_0}, x' = \frac{x}{R_0}, H = \frac{h}{h_0}, u' = \frac{u}{gh_0}, v' = \frac{v}{gh_0}, p' = \frac{p}{gh_0^2\zeta}, t' = gt$$

and substituting into system (5.1), the non-dimensional system can be obtained after dropping primes for simplicity:

$$\phi_t + \frac{h_0}{R_0}\frac{\partial(\phi u)}{\partial x} + \frac{\partial(\phi v)}{\partial z} = \phi; \tag{5.3a}$$

$$\frac{h_0}{R_0}\frac{\partial u}{\partial x} + \frac{\partial v}{\partial z} = \left(\frac{h_0}{R_0}\right)^2 \left[(1-\phi)^2 p_x\right]_x + \left[(1-\phi)^2 p_z\right]_z; \tag{5.3b}$$

$$\frac{\mu_b R_0}{\zeta h_0^3}\left[\left(\frac{h_0}{R_0}\right)^2 \frac{\partial^2 u}{\partial x^2} + \frac{\partial^2 u}{\partial z^2}\right] = \frac{\partial p}{\partial x} + \frac{E}{g\zeta h_0^2}\frac{\partial \phi}{\partial x}; \tag{5.3c}$$

$$\frac{\mu_b}{\zeta h_0^2}\left[\left(\frac{h_0}{R_0}\right)^2 \frac{\partial^2 v}{\partial x^2} + \frac{\partial^2 v}{\partial z^2}\right] = \frac{\partial p}{\partial z} + \frac{E}{g\zeta h_0^2}\frac{\partial \phi}{\partial z}. \tag{5.3d}$$

The initial radius of the biofilm is about 2mm as we experimentally showed in Section 6.3 in Chapter 6, while the initial height of the biofilm is less than 60μm as shown in Section 6.4 in Chapter 6. Hence, the ratio $\frac{h_0}{R_0}$ is less than 0.03. Therefore, it is reasonable to assume that $\frac{h_0}{R_0}$ is sufficiently small. Furthermore, it is assumed that the volume fraction of the biomass is at a quasi-steady state. Under these assumptions,

system (5.3) can be approximated by:

$$\phi_z v + \phi v_z = \phi; \tag{5.4a}$$

$$v_z = [(1-\phi)^2 p_{zz} - 2(1-\phi)\phi_z p_z]; \tag{5.4b}$$

$$K_2 u_{zz} = p_x + K_1 \phi_x; \tag{5.4c}$$

$$K_3 v_{zz} = p_z + K_1 \phi_z; \tag{5.4d}$$

where $K_1 = \frac{E}{g\zeta h_0^2}$, $K_2 = \frac{\mu_b R_0}{\zeta h_0^3}$ and $K_3 = \frac{\mu_b}{\zeta h_0^2}$.

Substituting the desired forms of non-dimensional variables into the boundary conditions (5.2) gives the corresponding dimensionless boundary conditions:

$$u = 0; v = 0; \qquad \text{at} \quad z = 0 \tag{5.5a}$$

$$u_z = 0; \qquad \text{at} \quad z = H(x,t) \tag{5.5b}$$

$$-p + 2K_3 v_z = -p^*_{ext}; \qquad \text{at} \quad z = H(x,t) \tag{5.5c}$$

$$H_t + \frac{h_0}{R_0} H_x u = v; \qquad \text{at} \quad z = H(x,t) \tag{5.5d}$$

where $p^*_{ext} = \frac{p_{ext}}{gh_0\zeta}$.

To summarise, system (5.4), together with the boundary conditions (5.5) constitute the dimensionless form of biofilm model studied in this section.

5.3.2 Thin-Film Analysis

The parameter groupings K_1, K_2 and K_3 are defined in terms of the original parameters in the model and the typical values of these parameters collected from literatures are shown in Table 5.1. From this table, it follows that $K_1 = O(10^7)$ while $K_2 = O(1)$ and $K_3 = O(10^{-2})$. Therefore, letting $\varepsilon = K_1^{-1}$, we have $\varepsilon \ll 1$. Therefore, system (5.4) is

Notation	Description	Value/Order	Unit	Reference
μ_b	Viscosity of biofilm	$O(10^2)$	$Pa \cdot s$	[143, 152]
ζ	Water-Network friction	$O(10^{14})$	$Pa \cdot s \cdot m^{-2}$	[143]
h_0	Initial biofilm heigh	$O(10^{-5})$	m	Section 6.4
R_0	Initial biofilm width	$O(10^{-3})$	m	Section 6.3
g	Growth coefficient	$O(10^{-5})$	s^{-1}	[102]
E	Osmotic coefficient	2×10^6	Pa	[143]

Table 5.1: Typical Parameter Value of the Original Model

a scaling problem. Next we seek a solution of the form $f = f_0 + \varepsilon f_1 + O(\varepsilon^2)$, where $f = u(x,z,t), v(x,z,t), \phi(x,z,t), p(x,z,t)$.

Substituting the desired form of solutions into system (5.4) and ignoring the $O(\varepsilon^2)$ terms and higher order terms gives:

$$(\phi_{0,z} + \varepsilon\phi_{1,z})(v_0 + \varepsilon v_1) + (\phi_0 + \varepsilon\phi_1)(v_{0,z} + \varepsilon v_{1,z}) \sim \phi_0 + \varepsilon\phi_1; \tag{5.6a}$$

$$v_{0,z} + \varepsilon v_{1,z} \sim (1 - \phi_0 - \varepsilon\phi_1)^2(p_{0,zz} + \varepsilon p_{1,zz}) - 2(\phi_{0,z} + \varepsilon\phi_{1,z})(p_{0,z} + \varepsilon p_{1,z})(1 - \phi_0 - \varepsilon\phi_1); \tag{5.6b}$$

$$K_2(u_{0,zz} + \varepsilon u_{1,zz}) \sim p_{0,x} + \varepsilon p_{1,x} + \varepsilon^{-1}(\phi_{0,x} + \varepsilon\phi_{1,x}); \tag{5.6c}$$

$$K_3(v_{0,zz} + \varepsilon v_{1,zz}) \sim p_{0,z} + \varepsilon p_{1,z} + \varepsilon^{-1}(\phi_{0,z} + \varepsilon\phi_{1,z}). \tag{5.6d}$$

Equations (5.6c) and (5.6d) imply

$$\phi_{0,x} = \phi_{0,z} = 0. \tag{5.7}$$

Substituting this into (5.6) and letting $\varepsilon \to 0$ yields:

$$\phi_0 v_{0,z} = \phi_0; \tag{5.8a}$$

$$v_{0,z} = (1-\phi_0)^2 p_{0,zz}; \tag{5.8b}$$

$$K_2 u_{0,zz} = p_{0,x} + \phi_{1,x}; \tag{5.8c}$$

$$K_3 v_{0,zz} = p_{0,z} + \phi_{1,z}. \tag{5.8d}$$

Similarly, substituting the desired form of solutions into the boundary conditions (5.5a)-(5.5c) and letting $\varepsilon \to 0$ gives the boundary conditions for the aymptotic solutions to (5.8) as follows:

$$u_0 = 0;\ v_0 = 0; \qquad \text{at} \quad z = 0 \tag{5.9a}$$

$$u_{0,z} = 0; \qquad \text{at} \quad z = H(x,t) \tag{5.9b}$$

$$-p_0 + 2K_3 v_{0,z} = -p^*_{ext}. \quad \text{at} \quad z = H(x,t) \tag{5.9c}$$

Next, we will solve system (5.8) along with the boundary conditions (5.9). According to the assumption that the volume fraction of the biofilm, ϕ, is at a quasi-static state, solving (5.7) gives

$$\phi_0 = \phi_\infty, \tag{5.10}$$

where ϕ_∞ is a constant. Substituting (5.10) into (5.8a) yields $v_{0,z} = 1$ which has solution $v_0(x,z,t) = z + A(x,t)$ where $A(x,t)$ is to be determined by the boundary condition. Substituting this expression for v_0 into (5.9a) gives $A(x,t) = 0$ and hence we have

$$v_0(x,z,t) = z. \tag{5.11}$$

Now, we will solve for $p_0(x,z,t)$ and $\phi_1(x,z,t)$. Substituting solutions (5.10) and (5.11)

into (5.8b), and (5.11) into (5.8d), we obtain

$$(1-\phi_\infty)^2 p_{0,zz} = 1; \tag{5.12a}$$

$$p_{0,z} + \phi_{1,z} = 0. \tag{5.12b}$$

Differentiating (5.12b) with respect to z and substituting (5.12a) in gives

$$\phi_{1,zz} = \frac{-1}{(1-\phi_\infty)^2}. \tag{5.13}$$

Since we only have one boundary condition for p_0 (equation (5.9c)), we will solve equation (5.13) for ϕ_1 and (5.12b) for p_0. Before doing this, the boundary conditions for $\phi_1(x,z,t)$ needs to be specified.

In [116], Seminara et al. claimed that there is little evaporation at the biofilm-air interface for the wild-type biofilm. Hence, they suggested that no-flux boundary conditions should be applied, i.e. the volume fraction of the water should satisfy

$$(1-\phi)\mathbf{v}_w \cdot \mathbf{n} = 0, \tag{5.14}$$

in the dimensional form, where $\mathbf{n}$ is the unit normal at the biofilm-air interface.

Next, we will prove that the no-flux boundary condition is not suitable for the system at equilibrium, i.e. $\phi = \phi_\infty$. According to (8.12b), (5.14) can be rewritten as

$$(1-\phi)(\mathbf{v}_b - \frac{1-\phi}{\zeta}\nabla p) \cdot \mathbf{n} = 0, \tag{5.15}$$

which is equivalent to

$$(1-\phi)(v - \frac{1-\phi}{\zeta} p_z) = 0. \tag{5.16}$$

Substituting the non-dimensional parameters that were listed in Section into (5.16)

yields

$$(1-\phi)[v - K_2(1-\phi)p_z] = 0 \tag{5.17}$$

after dropping primes. Substituting the desired form of solutions into (5.17) and ignoring the $O(\varepsilon)$ terms gives:

$$(1-\phi_0)[v_0 - (1-\phi_0)p_{0,z}] = 0. \tag{5.18}$$

Given that $\phi_0 = \phi_\infty \neq 1$, equation (5.18) implies

$$v_0 - (1-\phi_\infty)p_{0,z} = 0. \tag{5.19}$$

Differentiating the boundary condition (5.9c) with respect to z and applying it to (5.19) gives

$$v_0 - K_3(1-\phi_\infty)v_{0,zz} = 0, \quad \text{at} z = H(x,t). \tag{5.20}$$

The above equation is contradict to equation (5.11). Therefore, the contradiction implies that the no-flux boundary condition is not suitable for the system at equilibrium where the volume fraction of the biomass is a constant.

In order to model the evaporation effect at the biofilm-air interface, we employ an alternative boundary condition to the no-flux boundary condition.

At the biofilm-air interface, we assume that there is no difference in the water volume fraction in the biomass and the air for the wild-type biofilm. Biologically we know that the *bslA* mutant does not have the hydrophobic layer. Therefore, we assume that there is evaporation/absorption of water for the *bslA* mutant at the biofilm-air interface. Hence, we have boundary condition for the volume fraction of the water as follow:

$$(1-\phi)_z(z = h(x,t)) = \alpha^*,$$

where $\alpha^* = 0$ represents wild-type biofilm, $\alpha^* \neq 0$ represents the *bslA* mutant. At this stage, we do not know the sign of α^*. But, notice here, $\alpha^* < 0$ represents the case where water is of higher concentration outside the biofilm, therefore implies that water is absorbed from the air into the biofilm. Similarly, $\alpha^* > 0$ represents the case where water is of lower concentration outside the biofilm, therefore water is lost from the biofilm. $\alpha^* > 0$ means that the water is lost from the biofilm at the biofilm-air interface whilst $\alpha^* < 0$ means that the water is absorbed from the air at the biofilm-air interface. Simply, we have

$$\phi_z(z = h(x,t)) = \alpha, \tag{5.21}$$

where $\alpha = -\alpha^*$. Equation (5.21) in the non-dimensional form is given by

$$\phi_z(z = H(x,t)) = a, \tag{5.22}$$

where $a = h_0\alpha$.

Substituting the assumed form of ϕ into the boundary condition (5.22) yields $\phi_{0,z} + \varepsilon\phi_{1,z} = a$. With (5.7), we have

$$\phi_{1,z}(z = H(x,t)) = b, \tag{5.23}$$

where $b = \frac{a}{\varepsilon}$. It has been suggested in [116] that the biofilm growth changes the water volume fraction in the biofilm and thereby water is absorbed from the biofilm-agar surface to dilute the biofilm concentration, creating a gradient normal to the interface. The osmotic imbalance is determined by the local density and the geometry of the biofilm. It is assumed in [116] that the boundary condition for ϕ_1 at $z = 0$ is given by

$$\phi_{1,z} = \frac{h_0\phi_1}{R_0R(t)}, \qquad \text{at} \quad z = 0. \tag{5.24}$$

This boundary condition implies that at the biofilm-agar interface, the more the local

density of cells is, or the smaller the radius of the biofilm is, the more difference there exists between the biomass volume fraction in the biofilm and in the agar.

Next we will solve for $\phi_1(x,z,t)$ and $p_0(x,z,t)$ with boundary conditions (5.9c), (5.23) and (5.24). Solving (5.13) yields

$$\phi_1(x,z,t) = \frac{-1}{(1-\phi_\infty)^2}\frac{z^2}{2} + B(x,t)z + C(x,t)$$

where $B(x,t)$ and $C(x,t)$ are to be determined by the boundary conditions. Substituting this expression into (5.23) gives $B(x,t) = b + \frac{H(x,t)}{(1-\phi_\infty)^2}$, and substituting into (5.24) yields $C(x,t) = \frac{R_0R(t)}{h_0}[b + \frac{H(x,t)}{(1-\phi_\infty)^2}]$. Hence, we have:

$$\phi_1(x,z,t) = \frac{1}{(1-\phi_\infty)^2}\left[H(x,t)z - \frac{z^2}{2} + \frac{R_0R(t)}{h_0}H(x,t)\right] + b\left[z + \frac{R_0R(t)}{h_0}\right]. \quad (5.25)$$

Differentiating (5.25) with respect to z once and substituting into (5.12b) and integrating once with respect to z yields:

$$p_0(x,z,t) = \frac{-1}{(1-\phi_\infty)^2}\left[H(x,t)z - \frac{z^2}{2} + \frac{R_0R(t)}{h_0}H(x,t)\right] - b\left[z + \frac{R_0R(t)}{h_0}\right] + D(x,t),$$

where $D(x,t)$ needs to be determined by the boundary condition. Substituting $p_0(x,z,t)$ into the boundary condition (5.9c) gives

$$D(x,t) = \frac{1}{(1-\phi_\infty)^2}\left[\frac{H^2(x,t)}{2} + \frac{R_0R(t)}{h_0}H(x,t)\right] + b\left[H(x,t) + \frac{R_0R(t)}{h_0}\right] + 2K_3 + p^*_{ext}.$$

Thus, the solution of p_0 can be rewritten as

$$p_0(x,z,t) = \frac{[H(x,t)-z]^2}{2(1-\phi_\infty)^2} + b\left[H(x,t)-z\right] + p^*_{ext} + 2K_3. \quad (5.26)$$

Finally, we will use the solutions for ϕ_1 and p_0 to solve for $u_0(x,z,t)$ from (5.8c)

with the boundary conditions (5.9a) and (5.9b). Differentiating (5.25) and (5.26) with respect to x and substituting into (5.8c) we obtain

$$K_2 u_{0,zz} = \frac{H_x(x,t)}{(1-\phi_\infty)^2}\left[H(x,t)+\frac{R_0 R(t)}{h_0}\right]+bH_x(x,t).$$

Integrating the above equation twice with respect to z gives

$$u_0(x,z,t) = \left[\frac{1}{K_2(1-\phi_\infty)^2}\left(H(x,t)+\frac{R_0R(t)}{h_0}\right)+\frac{b}{K_2}\right]\frac{H_x(x,t)z^2}{2}+E(x,t)z+F(x,t)$$

and $E(x,t)$ and $F(x,t)$ are constants of integration. Substituting the above solution into the boundary conditions (5.9a) and (5.9b) yields $E(x,t) = -\frac{HH_x}{K_2(1-\phi_\infty)^2}(H+\frac{R_0R(t)}{h_0}) - \frac{b}{K_2}HH_x$ and $F(x,t)=0$. Thus, the horizontal velocity u_0 is given by:

$$u_0(x,z,t) = \left[\frac{1}{K_2(1-\phi_\infty)^2}\left(H(x,t)+\frac{R_0R(t)}{h_0}\right)+\frac{b}{K_2}\right]\left[\frac{z^2}{2}-H(x,t)z\right]H_x(x,t),$$

which can be rewritten as

$$u_0(x,z,t) = \frac{R_0}{h_0}\left[\frac{1}{K_2(1-\phi_\infty)^2}\left(H(x,t)\frac{h_0}{R_0}+R(t)\right)+\frac{h_0 b}{R_0K_2}\right]\left[\frac{z^2}{2}-H(x,t)z\right]H_x(x,t), \tag{5.27}$$

In the thin-film theory, it is a common technique to integrate the continuity equation in the vertical direction to generate an equation for the height of the thin film. In this manner, the continuity equation for the volume fraction of the biomass (5.3a) is integrated in the z direction from $z=0$ to $z=H(x,t)$ to give:

$$\int_0^{H(x,t)}\frac{\partial\phi}{\partial t}dz+\frac{h_0}{R_0}\int_0^{H(x,t)}\frac{\partial(\phi u)}{\partial x}dz+\int_0^{H(x,t)}\frac{\partial(\phi v)}{\partial z}dz=\int_0^{H(x,t)}\phi\, dz. \tag{5.28}$$

Applying the Leibnitz integral rule for variable limits to each integral in the above

equation yields:

$$\int_0^{H(x,t)} \frac{\partial \phi}{\partial t} dz = \frac{\partial}{\partial t}\left[\int_0^{H(x,t)} \phi(x,z,t)dz\right] - \phi(x,H,t)H_t(x,t)$$
$$\int_0^{H(x,t)} \frac{\partial (\phi u)}{\partial x} dz = \frac{\partial}{\partial x}\left(\int_0^{H(x,t)} \phi(x,z,t)u(x,z,t)dz\right) - \phi(x,H,t)u(x,H,t)H_x$$
$$\int_0^{H(x,t)} \frac{\partial (\phi v)}{\partial z} dz = \phi(x,H,t)v(x,H,t) - \phi(x,0,t)v(x,0,t).$$

Substituting the individual terms into (5.28) we can obtain

$$\frac{\partial}{\partial t}\left[\int_0^{H(x,t)} \phi dz\right] + \frac{h_0}{R_0}\frac{\partial}{\partial x}\left(\int_0^{H(x,t)} \phi u dz\right)$$
$$- \phi(x,H,t)\left[\frac{h_0}{R_0}u(x,H,t)H_x + H_t - v(x,H,t)\right] - \phi(x,0,t)v(x,0,t)$$
$$= \int_0^{H(x,t)} \phi dz.$$

The boundary condition (5.5a) and (5.5d) simplify the above integral further to give:

$$\frac{\partial}{\partial t}\left[\int_0^{H(x,t)} \phi(x,z,t)dz\right] + \frac{h_0}{R_0}\frac{\partial}{\partial x}\left(\int_0^{H(x,t)} \phi(x,z,t)u(x,z,t)dz\right) = \int_0^{H(x,t)} \phi(x,z,t)dz. \tag{5.29}$$

Substituting the asymptotic solutions of system (5.4), which are given by(5.10), (5.25), (5.26) and (5.27), into (5.29) gives

$$\phi_\infty \frac{\partial H(x,t)}{\partial t}$$
$$+ \frac{\partial}{\partial x}\int_0^{H(x,t)} \phi_\infty \left[\frac{1}{K_2(1-\phi_\infty)^2}\left(H(x,t)\frac{h_0}{R_0} + R(t)\right) + w\right]\left[\frac{z^2}{2} - H(x,t)z\right]H_x(x,t)dz$$
$$= \phi_\infty H(x,t),$$

where $w = \frac{h_0 b}{R_0 K_2}$. Notice here that the parameter w can be represented by the original parameters as follows: $w = \frac{h_0 a K_1}{R_0 K_2}$ given $b = \frac{a}{\varepsilon}$ where $\varepsilon = K_1^{-1}$, and $K_1 = O(10^7)$. From

Table 5.1, it is clear that although $\frac{h_0}{R_0}$ is less than order $O(10^{-2})$, w is about $10^5 a$. Therefore, w can not be ignored in the equation. With the thin-film assumption that $\frac{h_0}{R_0} \ll 1$, the above equation can be further simplified to

$$\phi_\infty \frac{\partial H(x,t)}{\partial t} + \frac{\partial}{\partial x} \int_0^{H(x,t)} \phi_\infty H_x(x,t) \left[\frac{R(t)}{K_2(1-\phi_\infty)^2} + w \right] \left[\frac{z^2}{2} - H(x,t)z \right] dz = \phi_\infty H(x,t).$$

After simple algebra, the equation for the biofilm height can be obtained as follow:

$$H_t - \left(KR(t) + \frac{w}{3} \right) \left(H^3 H_x \right)_x = H, \tag{5.30}$$

where $K = \frac{1}{3K_2(1-\phi_\infty)^2}$. This is the equation that governs the dynamic of the biofilm height.

5.3.3 Numerical Simulation with Appropriate Expression for $R(t)$

It can be seen from Figure 6.2 in Chapter 6 that the radius of both the wild-type biofilm and the *bslA* mutant biofilm increases approximately linearly over time. Therefore, it is reasonable as the first step to express the dimensional $R(t)$ as

$$R(t) = \beta t + R_0, \tag{5.31}$$

where R_0 is the initial radius of the biofilm that has been used in the non-dimensionalisation. We used a least-square fit of Figure 6.2 in Chapter 6 to determine the linear regression that fits (5.31) where R is the mean radius of both the wild-type biofilm and the *bslA* mutant. With the use of MATLAB, we obtained $\beta = 0.1257$mm/h and $R_0 = 1.86$mm. Non-dimensionalizing (5.31) with the scaling factors used previously and dropping the $'$ for $R'(t)$ and t' gives

$$R(t) = \gamma t + 1, \tag{5.32}$$

where $\gamma = \frac{\beta}{R_0 g}$. With the parameter value for g given in Table 5.1, we can estimate the parameter value γ to be $\gamma = 1.8$. Hence, the equation we will simulate in this section is given by

$$H_t - \left[K(\gamma t + 1) + \frac{w}{3}\right]\left(H^3 H_x\right)_x = H \tag{5.33}$$

Next, we will set the initial condition and boundary condition for equation (5.33). The computational domain for equation (5.33) can be seen in Figure 8.1 in Appendix 8.1. We chose the computational domain for the simulation as $x \in [0, 10]$ since it can be seen from Figure (6.2) in Chapter 6 that the largest radius after 48 hours is no bigger than $R = 9$ mm which corresponds to $R' = 4.8$ in the dimensionless form. Initially, we assume that

$$H(x,0) = \begin{cases} 1 & \text{for} \quad x \leq 1 \\ 0 & \text{for} \quad x > 1 \end{cases} . \tag{5.34}$$

Here, since H is the dimensionless form of the biofilm height, and the scale is chosen to be the initial height of the biofilm, $H = 1$ represents the initial height of biofilm after inoculation. As for the boundary conditions, since we consider the side view of half of the biofilm from the centre, it is reasonable to apply the no-flux boundary condition to equation (5.33), i.e.

$$\left[K(\gamma t + 1) + \frac{w}{3}\right]\left(H^3 H_x\right) = 0 \quad \text{at} \quad x = 0 \quad \text{and} \quad x = 10. \tag{5.35}$$

Next, we will examine two hypotheses regarding the function of the hydrophobic layer that is absent in the *bslA* mutant by comparing the numerical simulations with the experimental data. The first hypothesis states that the biofilm absorbs water from the air with the absence of the hydrophobic layer, while the second hypothesis states that the biofilm loses water into the air with the absence of the hydrophobic layer. As mentioned in (5.21) in Appendix 8.1, in the dimensional model, $\alpha = 0$ represents

the case of wild-type biofilm, $\alpha = -\alpha^* > 0$ represents the case where water is of higher concentration outside the biofilm therefore water is absorbed from the air, and $\alpha = -\alpha^* < 0$ represents the case where water is of lower concentration outside the biofilm therefore water is lost from the biofilm. Accordingly, $w = 0$ represents the case of wild-type, $w > 0$ represents the case where the water is absorbed from the air, and $w < 0$ represents the case where the water is lost from the biofilm.

Equation (5.33) along with the initial condition (5.34) and the boundary condition (5.35) is solved numerically using COMSOL 4.2. The setup of the numerical simulation can be found in Appendix 8.3. The time points chosen in the simulation are $t = 0, 0.25, 0.5, ..., 2$, which are the approximate dimensionless values for the time points taken in the experiment, i.e. corresponding to $t = 0, 6h, 12h, ..., 48h$. Following [116], we chose the parameter $K = 0.4$. Figure 5.2 shows the solution of $H(x,t)$ at $t = 0, 0.25, 0.5, ..., 2$ for different values of w. It can be seen from Figure 5.2(a) that when $w = -1$, initially $H(x,t)$ increases mainly in the vertical direction and then spreads out horizontally at later stage, and $H(x,t)$ reaches around 2.25 folds of the initial height (corresponding dimensional value of $135\mu m$) and radius reaches around 4 folds of the initial radius (corresponding dimensional value of $7.44mm$) of the biofilm at $t = 2$. Similarly, from Figure 5.2(c), when $w = 2$, $H(x,t)$ increases vertically much more slowly but spread out horizontally much faster than the case where $w = -1$. Eventually, $H(x,t)$ reaches around 2 folds of the initial biofilm height (corresponding dimensional value of $120\mu m$) and radius reaches around 4.5 folds of the initial biofilm radius (corresponding dimensional value of $8.73mm$) at $t = 2$.

In the numerical simulations, we define the height of the biofilm to be $H(0,t)$ and the radius of the biofilm to be the first x-coordinate of $H(x,t) = 0$. Figure 5.3 shows how the height of the biofilm and the radius of the biofilm change over time for each of the three cases: $w = -1, 0, 2$. From Figure 5.3(a), in the case $w = -1$ (red), the height of the biofilm initially increases at the same rate compared with the case $w = 0$ (blue).

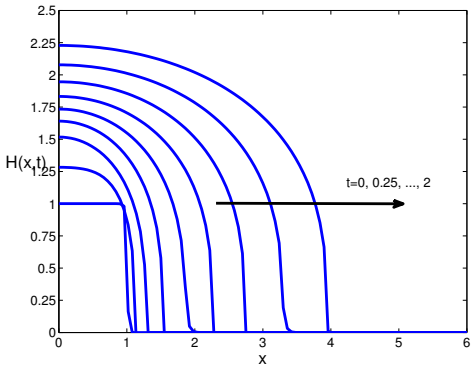

(a) Numerical solution of $H(x,t)$ given $w = -1$.

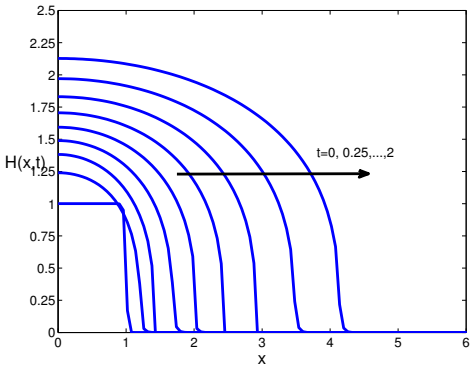

(b) Numerical solution of $H(x,t)$ given $w = 0$.

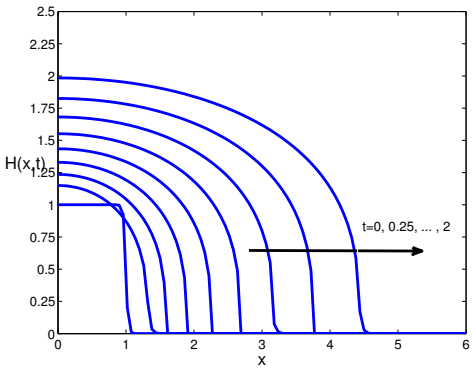

(c) Numerical solution of $H(x,t)$ given $w = 2$.

Figure 5.2: Numerical simulation of $H(x,t)$ from (5.33) with initial condition (5.34) and boundary conditions (5.34), given different values of w at $t = 0, 0.25, 0.5, ..., 2$.

Later on, the height of the biofilm keeps growing, and then the growth slows down at later time. As for the case where $w > 0$ (black), it is clear that the rate at which the biofilm height increases is much slower than that for the case $w = 0$ (blue). From Figure 5.3(b), the radius of the biofilm is largest for w positive and smallest for w negative for all values of time.

Next, we will compare the numerical simulation with the experimental data for the wild-type biofilm in terms of development of both the height and the radius over time, to examine the validation of the model predictions. Since we were not able to measure the height or the radius of the wild-type biofilm at $t = 0h$ in the experiment, we can use

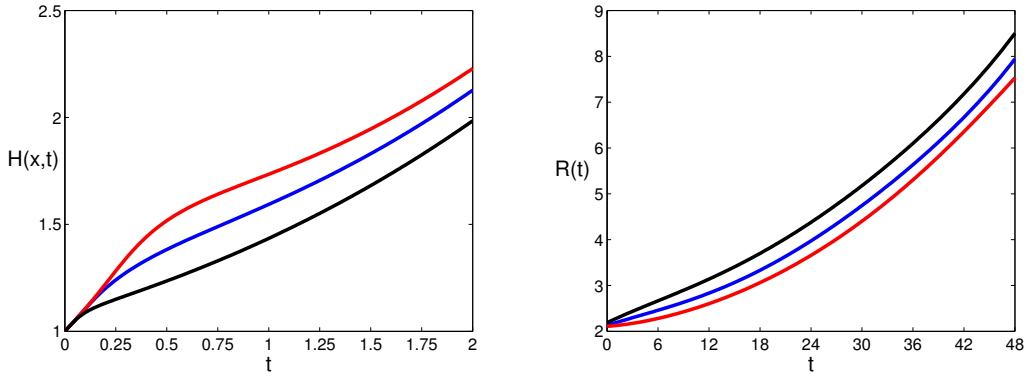

(a) Height of the biofilm over time given $w = -1, 0, 2$.

(b) Radius of the biofilm over time given $w = -1, 0, 2$.

Figure 5.3: Numerical simulation of the development of the height and radius of the biofilm over time given $w = -1$ (red), $w = 0$ (blue), $w = 2$ (black).

the ratio of the height at $t = 48h$ and at $t = 12h$ and the ratio of the radius at $t = 48h$ and at $t = 6h$ to examine the validation of the model prediction in terms of the height.

As can be seen from Figure 6.10 in Chapter 6, the average height of the wild-type biofilm increases from around $120\mu m$ to around $170\mu m$ from $t = 12h$ to $t = 48h$. Therefore the ratio of the change in height is around 1.4. In the numerical simulation for the wild-type, which corresponds to the case where $w = 0$ shown in Figure 5.2(b), the ratio between the height of the biofilm at $t = 2$ (the top plot) and $t = 0.5$ (third plot from the bottom) is $\frac{2.1}{1.375} \approx 1.5$. Similarly, as can be seen from Figure 6.2 in Chapter 6, the average radius of the wild-type biofilm increases from around $2.4mm$ to $7mm$ from $t = 6h$ to $t = 48h$. Therefore, the ratio of the change in the radius is approximately 2.91. In the numerical simulation shown in Figure 5.2(b), the ratio between the radius of the wild-type biofilm at $t = 2$ (the top plot) and $t = 0.25$ (the second plot from the bottom) is $\frac{4.1}{1.4} \approx 2.9$. Hence, our simulation of the development of the height and radius of the wild-type biofilm are in agreement with our experimental data.

Next, we will compare the difference between the numerical simulations for $w = 0$ and $w \neq 0$ to the difference between the height and radius of the wild-type biofilm and the

bslA mutant from the experimental data, to investigate the two hypotheses regarding the function of the hydrophobic layer that is absent in the *bslA* mutant. Reading from Figure 6.10 in Chapter 6, the height of the *bslA* mutant is smaller than that of the wild-type at $t = 12h$, and the height of the *bslA* mutant catches up with that of the wild-type at the later stage of biofilm growth. Comparing the solution of $H(0,t)$ at the early stage for $w < 0$ and $w > 0$ with that for $w = 0$ in Figure 5.3(a), it is clear that the height for the case $w > 0$ at the early stage grows more slowly than that for $w = 0$, while the height for the case $w < 0$ at the early stage grows faster than that for $w = 0$. Therefore, the case where $w > 0$ fits to the observed features of the height difference between the *bslA* and the wild-type biofilm.

We plotted the solution of $H(x,t)$ at $t = 2$ for a range of values of w in Figure 5.4. It is clear that as w increases, the value of $H(0,t)$ decreases whilst the radius increases. It is clear from Figure 6.2 that the radius of the *bslA* mutant is slightly greater than that of the wild-type at all the chosen time points, and especially at $t = 48h$. From Figure 6.10, at $t = 48h$, the height of the *bslA* mutant is close to, but slightly smaller than that of the wild-type. These observed changes match the observed features in the simulations on increasing w. Therefore, comparisons between the experimental data and the numerical simulations implies that $w > 0$ for the *bslA* mutant, i.e. the *bslA* mutant biofilm absorbs water from the air.

5.4 Conclusion

In this chapter, we used a mathematical model to investigate a hypothesis regarding the function of the hydrophobic layer shown to coat wild-type biofilms [64]. This layer is missing in the *bslA* mutant. We hypothesised that the lack of the hydrophobic layer would help the biofilm either absorb water from the environment or lose water to the

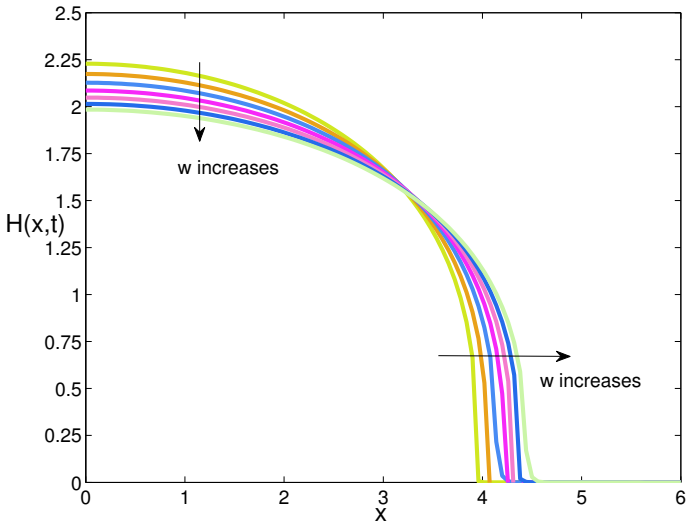

Figure 5.4: Numerical simulation of $H(x,t)$ from (5.33) with initial condition (5.34) and boundary conditions (5.34), given different values of w at $t = 2$.

environment.

With a thin-film approximation applied to the four-equation system for the biomass (water) volume fraction, we were able to reduce the system to a single equation that describes the change of the biofilm height as a function of time and radial distance from the centre. We then compared the simulated height profiles for each of these two hypotheses with the experimental results obtained for the height growth over time for the *bslA* mutant. The complex details of the difference between the development of the height of the wild-type biofilm and the *bslA* mutant are not captured in the numerical simulation. However, from the comparison between these two strains at the beginning and end of the period of biofilm growth, we can still conclude that the hypothesis that the biofilm without the hydrophobic layer is able to absorb water from the air at the biofilm-air interface is preferred. Therefore, this result implies that the hydrophobic layer limits water intake from the surrounding environment.

This result is in line with a recent experiment conducted by Hobley et. al. [64]. In that experiment, both the wild-type biofilm and the *bslA* mutant were grown on the surface

of the MSgg agar. After the complex morphology had formed, five-microlitre droplets of water were placed on the surface of complex colonies and allowed to equilibrate for 5 min before photography. The *bslA* mutant colony was shown to be subject to wetting by the water droplet while the wild-type colony was not. Our model suggests that this difference in wetting between these two strains is due to the ability of the *bslA* mutant to absorb water from the environment.

In Chapter 2, we proposed that the drying of the EPS matrix would cause the contraction of the biofilm and thereby cause the wrinkling pattern formation of the developed biofilm. We further suggest that the ability of the *bslA* mutant of absorption of water from the air might slow down or even eliminate the drying procedure of the biofilm and hence this could also be the reason why the *bslA* mutant exhibits the almost flat morphology compared to the wild-type biofilm where a wrinkling pattern formation can be observed (Figure 6.1 in Chater 6).

Chapter 6

Experimental Methods and Results

6.1 Introduction

In this chapter, we will show all the experimental work that we have done, giving details of the materials, methods and the results. We group all of the experimental work together here which we have referred to throughout this thesis.

We aimed to investigate functional property of the *bslA* mutant and therefore the functional property of the hydrophobic layer that is deficient in the *bslA* mutant. Two specific questions will be investigated deeply in this chapter. First of all, we wish to know whether the *bslA* mutant has the EPS matrix in the biofilm or not. The second question is at what stage of the biofilm development, the *bslA* mutant has effect on.

We first examine how the radius of the biofilms change with time and compare the radius of different strains. Subsequently we focus on the measurement of the biofilm height of the three different strains that we study using both microscopic analysis and statistical techniques. We compare the biofilm height as well as the contact angle at the biofilm edge, among the wild-type and the two mutants.

6.2 General Methods for the Preparation of Strains

The species that was used in the experiments was *Bacillus subtilis*, which is a Gram-positive soil bacterium. *B. subtilis* has proven highly amenable to genetic manipulation, and has become widely adopted as a model organism for laboratory studies [42, 87]. We examined the complex structure of the colonies on the surface of an agar plate. Each colony is a representation of a biofilm. The experiments were conducted for the wild-type cells and for two mutant strains: *eps* mutant and *bslA* mutant that are impaired in extracellular polymeric substance (EPS) production and hydrophobic layer production respectively. The wild-type strain refers to the phenotype of the typical form of *B. subtilis* as it occurs in nature. EPS is considered to be one of the main components of the biofilm [20, 19, 74]. The *eps* deleted mutation is no longer able to produce the extracellular polysaccharides in the biofilm. One of the other important components identified in the biofilm matrix is the protein called BslA [64]. It forms an elastic film at the interfaces of the biofilms that is responsible for the hydrophobicity of the biofilms. The *bslA* deleted mutation is no longer able to secrete the film-forming protein therefore no hydrophobic layer is presented on the surface of the biofilm. All the strains used in this experiments were the ones harbouring the *gfp* coding region under the control of an IPTG inducible promoter. Under the biofilm-forming conditions, fluorescence generated allows for the visualization of the biofilms by microscopy.

The *Bacillus subtilis* strains used in these experiments are detailed in Table 6.1. All the strains were streaked from -80°C freezer stocks onto 1.5% agar Lysogeny broth (LB) agar plates and incubated at 37°C overnight. The next morning, an isolated colony was transferred into 3mL LB medium and incubated on a shaker at 37°C and 220rmp for 3 hours.

After incubation, a drop of 1.5μL of cells was spotted onto a square of 1.5% agar that was attached on a microscope slide and contained minimal salts glycerol glutamate

(MSgg) medium [17] with 0.5% glycerol, 0.5% glutamate and metal mix that is made by $2mM$ $MgCl_2$, $700\mu M$ $CaCl_2$, $50\mu M$ $MnCl_2$, $50\mu M$ $FeCl_3$, $1\mu M$ $ZnCl_2$ and $2\mu M$ thiamine. Each slide was prepared as follows. An MSgg agar plate was cut into squares of 2cm$\times$2cm. The agar square was mounted on a standard microscope slide with adhesive. Each slide was stored in an empty petri dish that was covered with a damp tissue on the bottom. After the droplets of bacteria dried, the sample was transferred to a humidified incubator and kept at 30°C until required.

Strain	Genotype	Source
NRS1473	3610 *sacA*::$P_{hy-spank}$-*gfpmut2 (kan)*	NSWLab
NRS3799	3610 *epsA-O*::*tet sacA*::$P_{hy-spank}$-*gfpmut2 (kan)*	NSWLab
NRS3812	3610 *bslA*::*cat sacA*::$P_{hy-spank}$-*gfpmut2 (kan)*	NSWLab

Table 6.1: Full list of strains used in this study.

Time-lapse imaging of the development of the biofilm height was performed using a DeltaVision Core wide-field microscope mounted on an Olympus inverted stand with an Olympus $\times$10 lens and CoolSNAPHQ camera with differential interference contrast (DIC) and fluorescence optics. For each experiment, 12 independent fields, each containing the edge of the biofilm, were manually identified. Data sets (1024 by 1024 pixels with 1-by-1 binning and z-sections of between 12 and 20 spaced by size between $8\mu m$ and $12.5\mu m$) were acquired every 6 hours for up to 48 hours and were stored in the microscope control software (softWoRx). Green fluorescent protein (GFP) was imaged using a 100-W Mercury lamp and a fluorescein isothiocyanate (FITC) filter set (excitation [EX] wavelength, $490/20$ nm; emission [EM] wavelength, $528/38$ nm) with an exposure time of between 0.1s and 0.5s. Post acquisition data sets were rendered and analysed using OMERO software (http://openmicroscopy.org).

6.3 Radius Measurement

In this section, we will give details of how we examined the radius of the biofilm over time. We first describe the method we used to analyse the data which was obtained from the experimental images. Then we will discuss the results and implementation of the radius measurement.

6.3.1 Methods for Data Analysis

The 2-D image analysis was conducted using the OMERO platform [2] and custom scripts written in MATLAB via the OMERO Application Programming Interface (API). First, we obtained the light intensity of all the points in the entire image via API and stored the light intensity as a 2-D matrix in MATLAB. Then, we used the scripts written in MATLAB to carry out the image analysis. Details of the MATLAB script can be found in Appendix 8.2.

After storing the light intensity of the experimental images as a 2-D matrix in MATLAB, we used Otsu's method [100] to set the threshold of the light intensity that distinguishes the biofilm and the background of the image. We supposed that the size of the image in terms of the number of pixels is $M \times N$ and then assumed threshold of the light intensity was I^*. Categorising all the light intensities of the image into foreground where the light intensity satisfies $I > I^*$ and background where the light intensity satisfies $I < I^*$, some statistical terms were obtained as follows:

Group	Number of points	Weight	Mean	Variance
Foreground	N_0	$\omega_0 = \frac{N_0}{M \times N}$	μ_0	$(\mu - \mu_0)^2$
Background	N_1	$\omega_1 = \frac{N_1}{M \times N}$	μ_1	$(\mu - \mu_1)^2$

where $\mu_0(\mu_1)$ was the mean of the light intensity of all the points in the foreground

(background) and μ was the mean of the light intensity of the entire image, and $N_0 + N_1 = M \times N$. Notice here, all of the statistical terms were related to the threshold light intensity I^*. If we defined the weighted sum of variances of the two classes as

$$\sigma^2 = \omega_0(\mu - \mu_0)^2 + \omega_1(\mu - \mu_1)^2$$

then the aim of the Otsu's method was to minimise σ^2 by varying the value of I^*.

Having obtained the threshold I^* that minimises σ^2, we counted the number of the points that lay in the range of the light intensity for the biofilm (i.e. the points in the foreground). Given the size of the rectangular image with dimensions and the total pixel number of the entire image, we obtained the area of the biofilm region. Assuming that the biofilm was of a circular shape, we calculated the radius of the biofilm using the formula $R = \sqrt{S/\pi}$, where S was the calculated area of the biofilm.

6.3.2 Results

Seminara et al. [116] have conducted experiments to measure the radius of the wild-type biofilm and the *eps* mutant biofilm from time 0 to 30 hours. They found that the radius of the *eps* mutant was always smaller than that of the wild-type biofilm. They commented on the importance of EPS for biofilm spreading and suggested that the EPS concentration causes an increase in the osmotic pressure, causing swelling of the biofilm through uptake of water from the agar. In our experiments we also observed that the radius of the *eps* mutant was significantly smaller than that of the wild-type (shown in Figure 6.1). We also included the *bslA* mutant in our experiments and we observed that the radius of the *eps* mutant was significantly smaller than that of the wild-type biofilm, whilst *bslA* mutant colony displayed a very slight expansion in colony size that was not statistically distinct from the wild-type biofilm, see Figure

6.1.

The results were obtained in the following way. In our experiment, we compared the colony expansion of the wild-type, *eps* mutant and *bslA* mutant. For each of the three strains, we grew three colonies, and with the method discussed in Section 6.2, the radial growth rate was obtained by averaging over 3 colonies for each of the three strains wild-type, *bslA* mutant and *eps*, Figure 6.2. The error bars shown in Figure 6.2 indicate the standard error which is defined as

$$\mathrm{SD} = \frac{\sigma}{\sqrt{n}}, \tag{6.1}$$

where σ is the standard derivation of the data and n is the sample size.

These observations agree well with the experimental data obtained by Seminara et al. [116]. It suggests that the production of EPS itself could function to enhance colony spreading. Since the colony size of the *bslA* mutant is only slightly bigger than that of the wild-type, it suggests that the lack of the hydrophobic layer on the surface of the biofilm is not a key determining factor for the biofilm expansion but the hydrophobic layer may help the expansion slightly. By comparing the radius growth of these three strains, we suggest that the expansion of the *bslA* mutant is enhanced and we further suggest that the EPS matrix could be presented in the *bslA* mutant.

The other result that we obtained from this experiment was that the morphology of the biofilm differed between the wild-type biofilm, *eps* mutant and the *bslA* mutant. This difference of morphology among different strains has been observed previously. Our result confirmed the observed difference. As can be seen from Figure 6.1, the wrinkling pattern started to form in the middle of the wild-type biofilm at 24 hours, and later on, the spatial pattern expands to the edge of the biofilm. As for the *bslA* mutant, no wrinkling pattern formation was observed. However, small dotty pattern

was presented by the *bslA* mutant. For the *eps* mutant, the biofilm presented a flat and disc-like shape without any spatial pattern. This observation suggests that both the EPS matrix and the hydrophobic layer are important factors in determining the pattern formation of the biofilm. This result is consistent with previous findings [29, 39, 83].

6.4 Height Analysis

In this section, we give details of how we measured the height of the biofilm over time, and compare the edge for the wild-type biofilm, *eps* mutant and *bslA* mutant. We first describe the method we used to analyse the data which was obtained from the experimental images. Then we will discuss the result and implementation of the height measurement.

6.4.1 Image Setting Procedure

The preparation of the colony for this experiment is identical to that described in Section 6.2.

Samples were imaged every 6 hours after being transferred using a Delta Vision microscope with a $10\times$ Olympus objective and SoftWoRX software. Rather than focusing on the entire colony, the field of view was the edge of each colony. We took images at the right, left, top and bottom edges of the colony as shown in Figure 6.3. The total number of pixels of the region of interest was 2048×1024 for both the right and left edges and 1024×2048 for both the top and bottom edges.

We took a series of Z-sections, where the variation in Z corresponds to the variation in height of the biofilm over the field. We increased Z in increments of size ΔZ, where larger Z corresponded to focusing on part of the biofilm that was further away from the

microscope, and therefore a thinner part of the biofilm.

Then as we increased Z, we focused on thinner parts of the biofilm until the whole field became out of focus at which point we had passed the thinnest part (the edge) of the biofilm. Figure 6.4 shows an example of different focusing regions corresponding to different Z-sections when Z changes with a constant distance $\Delta Z = 10\mu$m. Since we knew that in the background region, which is shown in black in Figure 6.4, the height of the biofilm was zero, the thickness of the biofilm that was in focus in each Z-section could be calculated by adding an appropriate multiple of ΔZ related to the value of Z when the background was in focus.

The details of the image setting procedure are as follows. The extreme Z-sections are defined as: where part of the field became in focus for the first time, and where the entire field became out of focus for the first time, as we increased the value of Z, and then we denote these Z-values by Z_0 and Z_1 respectively. For example in the experiment shown in Figure 6.4, we set $Z_0 = 3$ and $Z_1 = 14$. Therefore, for each Z-section between Z_0 and Z_1, there is a region of the field that is in focus. If the field was taken at either the right or left edge of the biofilm then this region spanned from top to bottom of the field and it was the x-coordinates of this region that we were interested in (see for example Figure 6.4). Specifically, we took the x-coordinate in terms of pixel number of the boundary closer to the background of the region in focus, for example the right boundary of the red boxes shown in Figure 6.4 and recorded this coordinate as x_i. We did this for each Z-section between Z_0 and Z_1 and the x-coordinates for all the largest extreme boundary points of focus regions were stored in one vector which was of length n where $n = Z_1 - Z_0$. Therefore, each Z-section was in focus in the interval $(1, x_1), (x_1 + 1, x_2), ..., (x_n + 1, 2048)$. Then we denoted the centre point of each interval as p_i and stored them in a vector by $\vec{P} = (p_1, p_2, ..., p_{n+1})$. Therefore, x_i were related

to p_i in the following way:

$$
\begin{aligned}
&p_1 = (x_1 - 1)/2; \\
&p_i = (x_i - x_{i-1} - 1)/2; \quad \text{for} \quad i = 2, 3, ..., n; \\
&p_n = (2048 - x_n)/2.
\end{aligned}
$$

Example of $\vec{P}$ and $\vec{X}$ can be found in Figure 6.5. A similar process was carried out for fields at the top and bottom edges of the biofilm, but here we took y-coordinates instead of x-coordinates. Hence we had a set of x-coordinates for which the corresponding biofilm height could be calculated as an appropriate multiple of ΔZ. We stored the height values in a vector $\vec{H}$.

In the next section, we will explain how we use the height data that we have obtained at discrete points, $\vec{X}$, to obtain the height profile of the entire field.

6.4.2 Methods of Data Analysis

The images were stored in OMERO [2] and the image analysis was performed with scripts written in MATLAB via the OMERO Application Programming Interface (API). In OMERO, API can obtain the light intensity of an image. In this section, we will discuss how we map the light intensity of the image to the biofilm height by using the data acquired in the previous section.

For each field of view, the light intensity of the entire image for each Z-section from Z_0 to Z_1 was downloaded into MATLAB. For each Z-section, we considered the light intensity along a straight line through the centre of the image. For the fields at left and right edges of a biofilm, we stored the light intensity line $y = 512$ whilst we considered

the intensity along the vertical line $x = 512$ for the top and bottom edges, shown by the red lines cross the centre of the images of the edge in Figure 6.3. An example of a line along which we considered the light intensity at the right edge and the corresponding light intensity profile is shown in Figure 6.5. Therefore, we obtained n light intensity profiles which were denoted by $I_k(x)$ where $k = 1, 2, ..., n+1$ and x was from 1 to 2048.

Next, we generated one light intensity profile that took all the Z-sections into account by a weighted average of the $n+1$ light intensity profiles, $I_k(x)$. We called this overall light intensity the weighted light intensity and denoted it by $I(x)$. We defined the weighted light intensity in the following way. In the following, let $x_i : x_j$ denote sequence $x_i, x_i + 1, ..., x_j$. For the x-coordinates from $1 : x_1$, we defined

$$I(1 : x_1) = I_1(1 : x_1).$$

For intervals $x_i + 1 : x_{i+1}$ where $i = 1, 2, ..., n-1$, we defined

$$I(x_i + 1 : x_{i+1}) = 0.7I_i(x_i + 1 : x_{i+1}) + 0.15I_{i-1}(x_i + 1 : x_{i+1}) + 0.15I_{1+i}(x_i + 1 : x_{i+1}).$$

For the interval $x_n + 1 : 2048$, we defined the weighted light intensity to be

$$I(x_n + 1 : 2048) = I_{z_1 - 1}(x_n + 1 : 2048).$$

Other weighting parameters have been tested and the result did not show significant difference from the weighting parameter we used here, i.e. $0.7, 0.15, 0.15$.

A schematic illustration of the weighting method is shown in the line profile of Figure 6.6. It shows the individual light intensity profiles for a sample with three Z-sections, the blue profile corresponding to the light intensity on the Z_0 section, the red profile corresponding to that of the $Z_0 + 1 = Z_1 - 1$ section and the black profile corresponding to that of the Z_1 section. For the left region in Figure 6.6, i.e. $x = 1 : 500$, light intensity

profile I_{Z_0} was used as the weighted light intensity. For the middle part of Figure 6.6, i.e. $x = 501 : 1500$, all of the three light intensity profiles were used and we used the weighting formulae as follow:

$$I = 0.15I_{z_0} + 0.7I_{z_0+1} + 0.15I_{z_1}.$$

For the right region, i.e. $x = 1501 : 2048$, light intensity profile of I_{Z_1} was used as the weighted light intensity.

Next, we will show the details of how to use the light intensity profile to determine the height of the biofilm. It has been suggested that the light intensity is proportional to the total number of the GFP molecules presented in the biofilm and the number of GFP is proportional to the number of cells [51, 82]. We also assumed that the biofilm height is proportional to the number of cells. Therefore, it was reasonable to map the light intensity to the height of the biofilm by a linear mapping of the form

$$h(x) = \alpha I(x) \tag{6.2}$$

where α was the parameter to be determined by the data in the vectors $\vec{P}$ and $\vec{H}$. By substituting the entries in $\vec{P}$ into the weighted light intensity $I(x)$, we obtained the weighted light intensity at points of known height. We denoted this by $I(p_1), I(p_2), ..., I(p_{n+1})$. Then we used every value of $I(p_1), I(p_2), ..., I(p_{n+1})$ where we knew the corresponding height $\vec{H}$ from a Z-section to calculate the least-squared value of α. We then used this value of α as the mapping parameter in equation (6.2). We could then use (6.2) to calculate $h(x)$ for all values of x, i.e. to obtain the height profile for all the edges for every colony.

Next, a statistical test was conducted to compare the three strains with use of MATLAB. We divided the height profile into two parts: the biofilm height, where the height

profile obtained does not change significantly along the x-direction, and the leading edge where the height profile decreases as x increases. We compared the mean height and the mean slope of the leading edge of wild-type biofilm and *bslA* mutant, and wild-type biofilm and *eps* mutant. The null hypothesis for each test was chosen to be that the mean of the measurements were equal for each pair. We assumed that the samples for each strain were normally distributed. However, since there was no evidence to show that the variances of each pair were equal, we applied Welch's t-test in the statistical analysis [22]. If we denote the mean of the sample in each pair to be $\bar{x_1}$ and $\bar{x_2}$, the number of samples for each pair to be n_1 and n_2, and the standard deviations to be s_1^2 and s_2^2, then the Welch's t-test uses t statistic:

$$t = \frac{\bar{x_1} - \bar{x_2}}{\sqrt{\frac{s_1^2}{n_1} + \frac{s_2^2}{n_2}}},$$

which is calculated for mean heights in the biofilm height region for the pair of wild-type biofilm and *eps* mutant and the pair of wild-type biofilm and *bslA* mutant, and also calculated for the mean slope in the leading edge for both of these two pairs.

6.4.3 Results

Figure 6.7 shows the height profile plot for each strain at different time points. The black profile is the mean of the height profile and the green shading shows the standard error. In order to illustrate the fitness of our mapping method, we also plotted the points from the $\vec{P}$ and corresponding $\vec{H}$ vectors along with the mean of the height profile of the corresponding strain. Figure 6.8 shows the comparison of the data collected and the mean of the fitted height profile at all the time points. Our mapping method fitted the raw data very well.

A comparison of the mean of the height profile for the wild-type biofilm and *bslA*

mutant, wild-type biofilm and *eps* mutant at all the time points is shown in Figure 6.9. It is clear that at $t = 12$ hours, the height of the wild-type biofilm is greater than that of both the *bslA* mutant and the *eps* mutant. And for the leading edge, the slope of the wild-type biofilm is similar to that of the *bslA* mutant but smaller than that of the *eps* mutant. After $t = 42$ hours, the mean height of the wild-type biofilm is almost the same as that of the *bslA* mutant but greater than that of the *eps* mutant, and the slope of wild-type biofilm is also similar to that of the *bslA* mutant but greater than that of the *eps* mutant.

The average height over the biofilm height region and the standard error over time for each strain is shown in Figure 6.10. The discussion of this development of the biofilm height can be found in Chapter 5.

The Welch's *t*-test using the value of t given in the previous section has been applied to both the height and the slope of the leading edge of the wild-type biofilm and *bslA* mutant, and the wild-type biofilm and *eps* mutant. The predominated significant level was chosen to be 5%. The alternative hypothesis used were chosen to be one-tailed, two-tailed for different time points and different strains according to the experimental observation. The result of the statistical test of the biofilm height is shown in the Table 6.2, and the result of the statistical test of the slope of the leading edge is shown in Table 6.3.

Height c. f. wild-type							
Time	12hrs	18hrs	24hrs	30hrs	36hrs	42hrs	48hrs
bslA mutant	$<$	$>$	$>$	$<$	$<$	$=$	$=$
eps mutant	$<$	$<$	$<$	$<$	$<$	$<$	$<$

Table 6.2: The statistical result of the comparison of the biofilm height between the wild-type biofilm and the mutants at different time point with significant level 5%.

By comparing the mutants with the wild-type biofilm in terms of both the height and the slope of the leading edge, two conclusions can be drawn regarding to the function of the hydrophobic layer and the EPS matrix. It was known that the hydrophobic

Slope c. f. wild-type							
Time	12hrs	18hrs	24hrs	30hrs	36hrs	42hrs	48hrs
bslA mutant	$=$	$<$	$<$	$<$	$<$	$=$	$=$
eps mutant	$>$	$<$	$<$	$<$	$<$	$<$	$<$

Table 6.3: The statistical result of the comparison of the slope of the leading edge between the wild-type biofilm and the mutants at different time point with significant level 5%.

layer, which is defected in the *bslA* mutant, is functional in the mature biofilm, as it is non-wetting [64]. From our experimental result, we suggest that the hydrophobic layer might have a particular influence in the biofilm spreading in the vertical direction at the early stage of the biofilm growth, i.e. up until 36 hours. However, the EPS matrix, which is defected in the *eps* mutant, might affect the biofilm during the whole process of the biofilm growth. Also, from Figure 6.10, the difference in the height of the biofilm between the *bslA* mutant and the *eps* mutant differed significantly, and the height of both the wild-type biofilm and the *bslA* mutant were greater than that of the *eps* mutant. Hence, we also suggest that the EPS matrix should be present in the *bslA* mutant.

6.5 Conclusion

In this chapter, we showed the experimental work that we have conducted. We aimed to investigate whether the *bslA* mutant synthesised a functional exopolysaccharides used in the biofilm matrix or not, and at what stage the *bslA* mutation impacted the biofilm development.

We first examined how the radius of the biofilms change with time and compared the radius of different strains. We found that the radius of the *eps* mutant is significantly smaller than that of both the wild-type biofilm and the *bslA* mutant, whist *bslA* mutant displayed a very slight enhancement in colony size that was not statistically distinct

from the wild-type biofilm. We conclude that the production of the EPS matrix could function to enhance colony spreading, and the lack of the hydrophobic layer on the surface of the biofilm, which is defected in the *bslA* mutant, is not a key determining factor for the biofilm expansion. Our experimental results also confirmed the observed difference in the morphology between wild-type, *eps* mutant and the *bslA* mutant.

We then measured the height of the biofilm over time, and compared the edge of the wild-type biofilm, *eps* mutant and *bslA* mutant. We developed a new way to measure the biofilm height by mapping the light intensity to the height of the biofilm. By comparing the height and the slope at the leading edge of the biofilm at the edge, we found that the hydrophobic layer has a particular influence in the biofilm spreading in the vertical direction up until 36 hours, whilst the EPS matrix, which is defected in the *eps* mutant might affect the biofilm during the whole process of the biofilm growth.

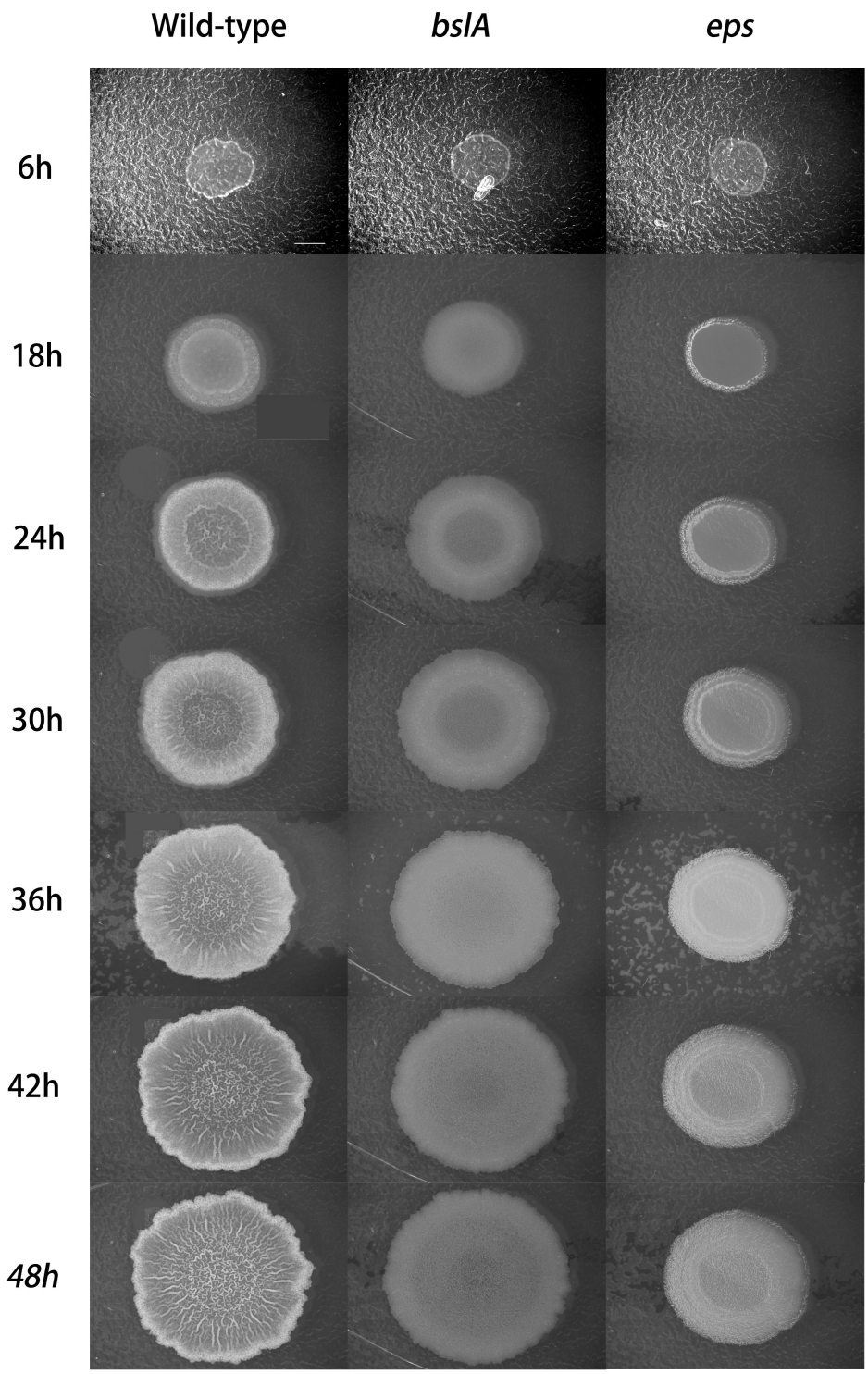

Figure 6.1: Top view of *B. subtilis* biofilm morphology and expansion on MSgg agar plates at different time points for wild-type strain (left column), the *bslA* mutant (middle column), and the *eps* mutant (right column). Scale bar in the top-left image indicates 2.5mm. This set of images is a representative of images collected from 12 biological replicates.

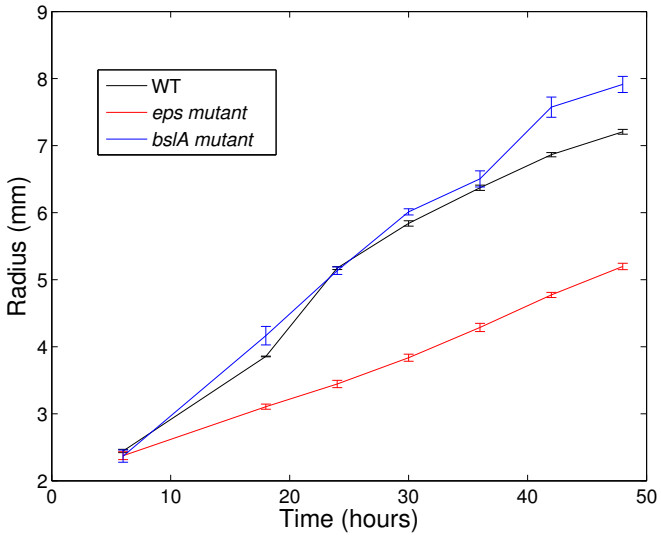

Figure 6.2: Radial growth of the three strains: WT, *bslA* mutant and *eps* mutant on MSgg agar plates. The error plot indicated the standard error generated from 3 samples of each strain.

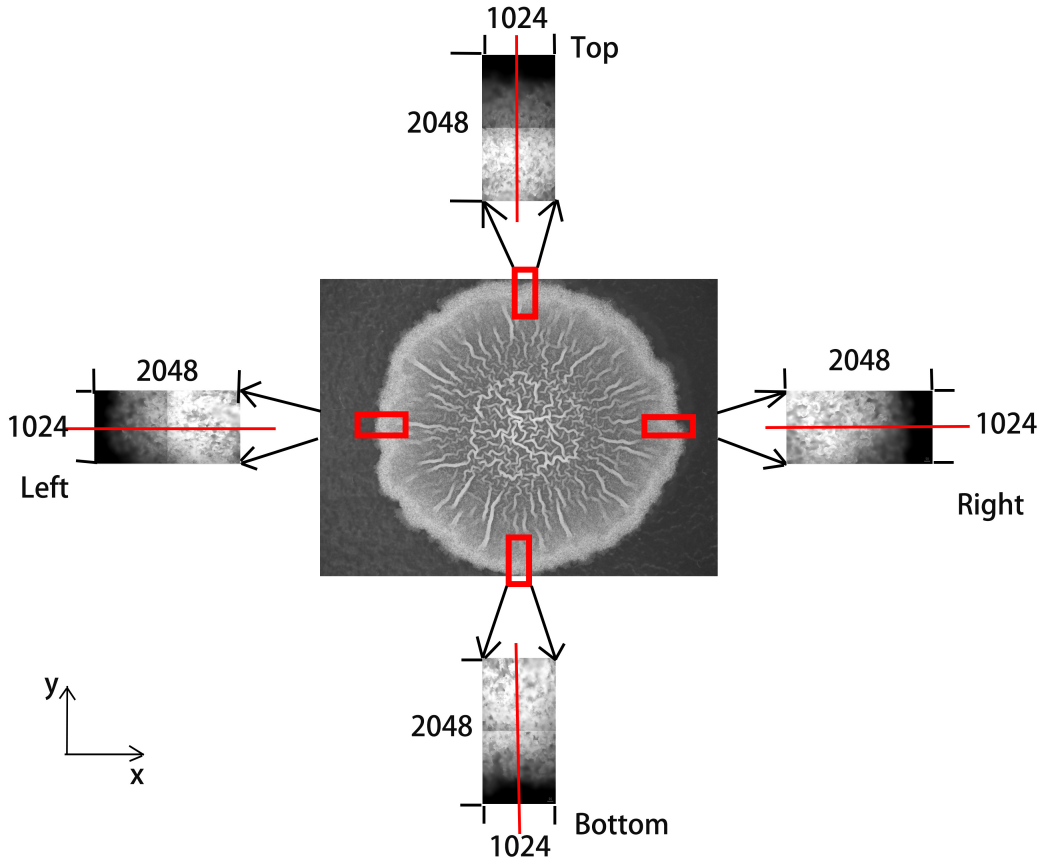

Figure 6.3: The middle image is the top view image of the wild-type biofilm after 42 hours. The red rectangles indicate the regions of interest in the height measurement experiment. The four smaller images are the images of the corresponding edges of the biofilm with the name we referred in the text and the size in terms of pixel number. The red line across the centre of the edges are the line profiles we used in the experiment.

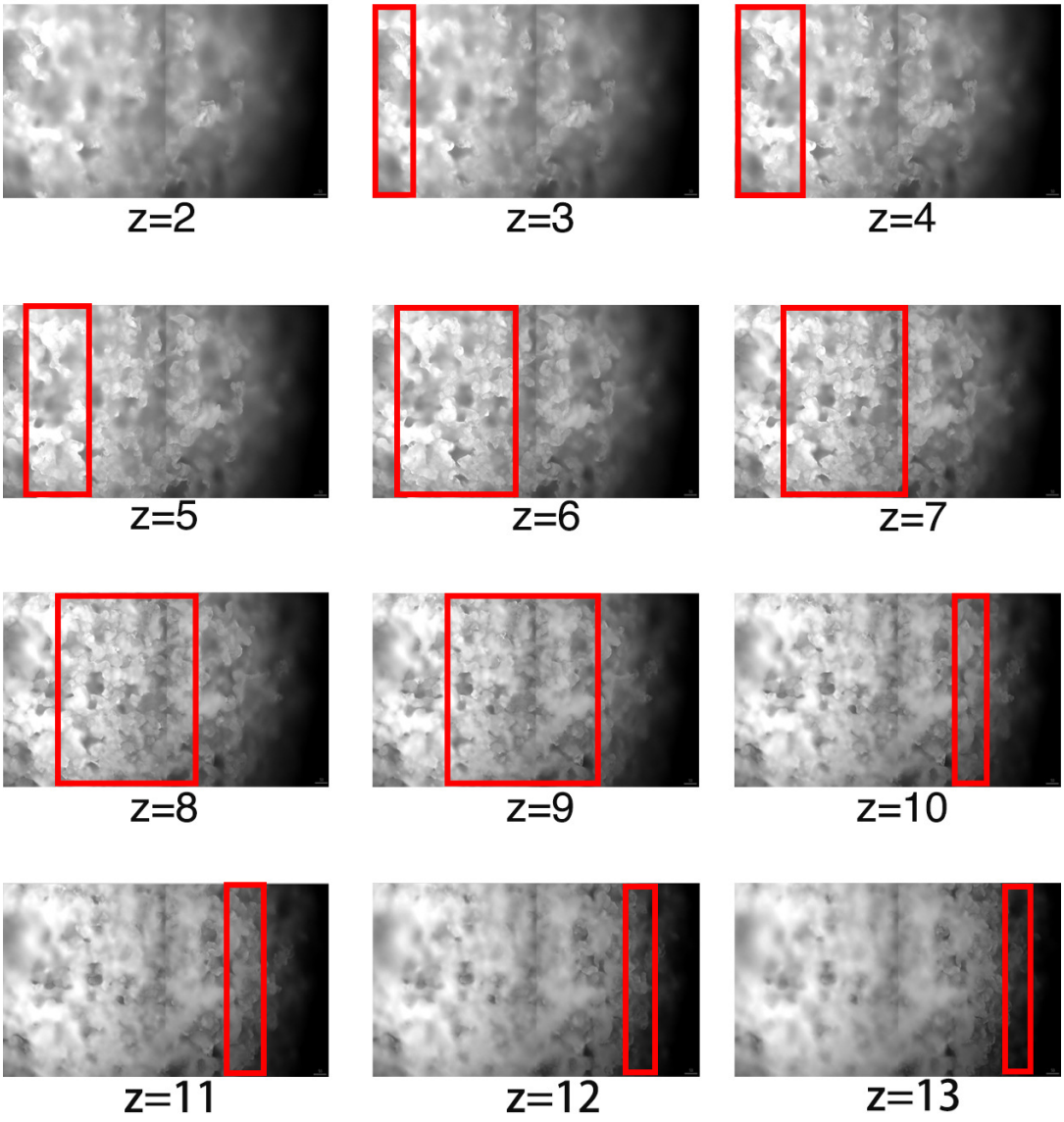

Figure 6.4: Snapshots of the field when the Z- section is moving from $Z = 2$ to $Z = 13$ with the section height $\Delta Z = 10\mu$m. The field is the right edge of the wild-type biofilm at $t = 24h$. The red rectangle highlights the region which is in focus with the corresponding Z-section.

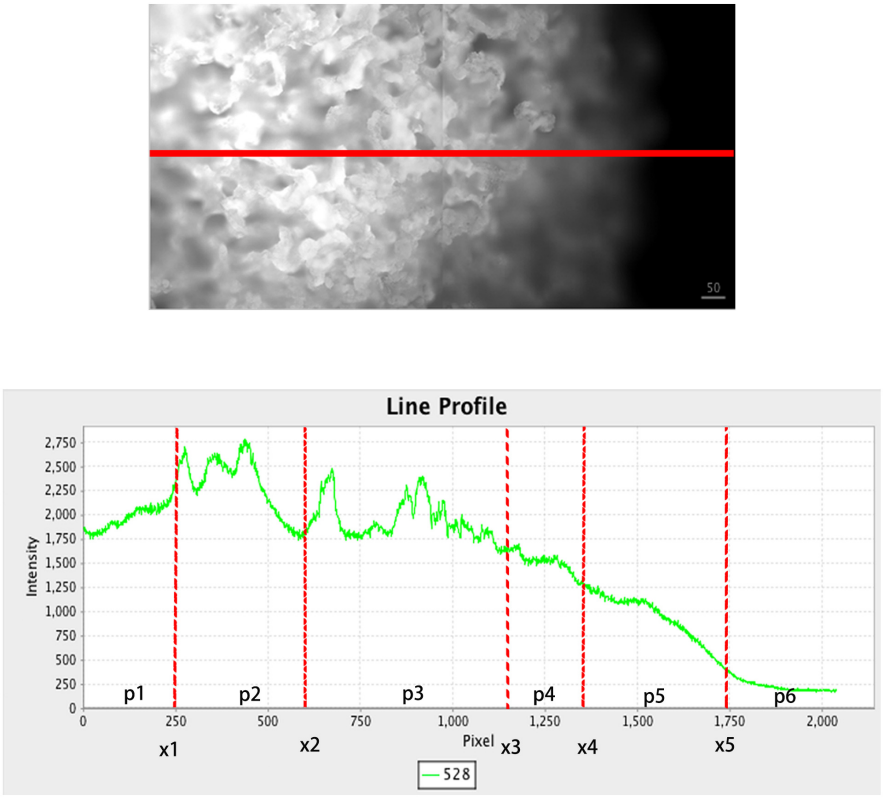

Figure 6.5: The upper image shows the field of view of the right edge of wild-type biofilm at $t = 24h$. The red line indicates the region of interest the light intensity of which is used in the analysis. The line profile in the lower image shows the light intensity of the region of interest. The red circles are the schematic sample light intensity which divide the entire line into several intervals shown by the dashed red lines.

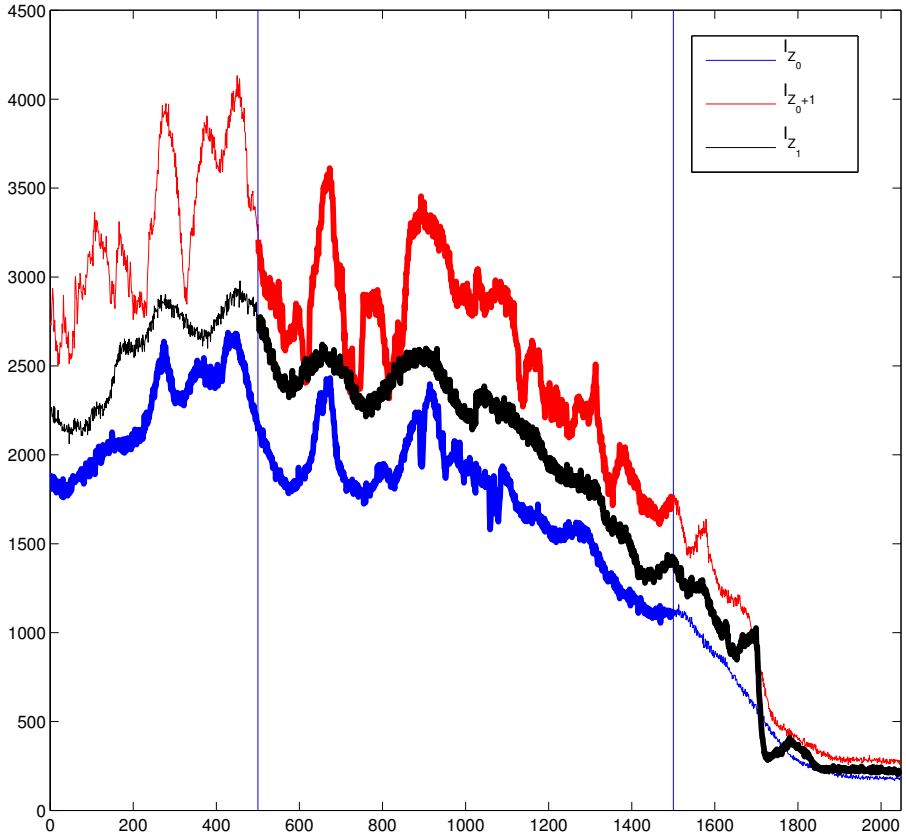

Figure 6.6: Schematic illustration of how to generate the weighted light intensity from the light intensity profile for each Z-section. The thicker part of each light profile represents the data used to calculate the weighted light intensity for the corresponding region.

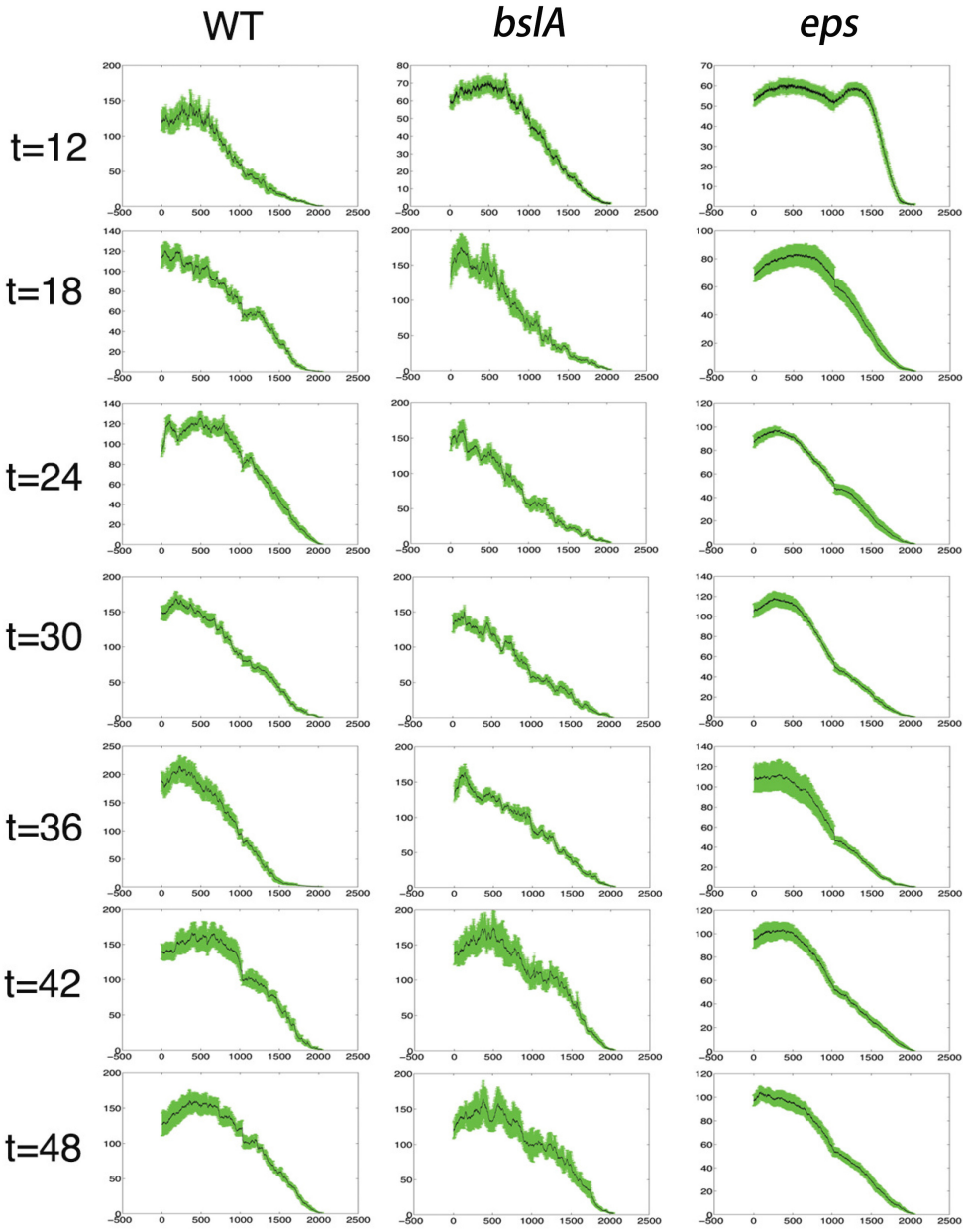

Figure 6.7: The height profile of each strain at different time points. The height profile is generated by averaging the four edges of each colony for three colonies for each strain. The mean height profile is shown by the black curve and the standard error is shown by the green shading.

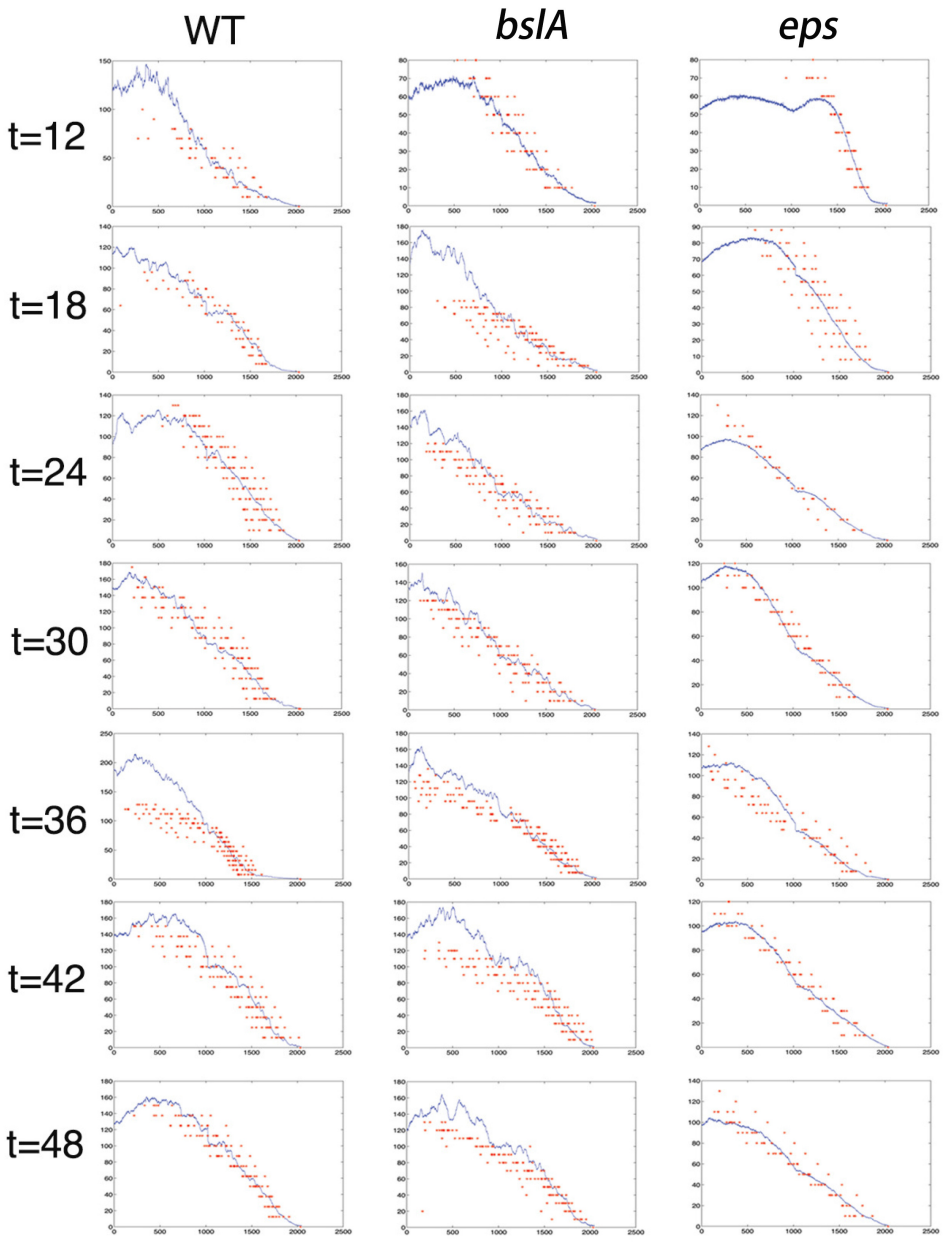

Figure 6.8: Comparison of the raw data collected from the Z-section (shown in red dots) and the mapped mean height profile for each strain at different time points.

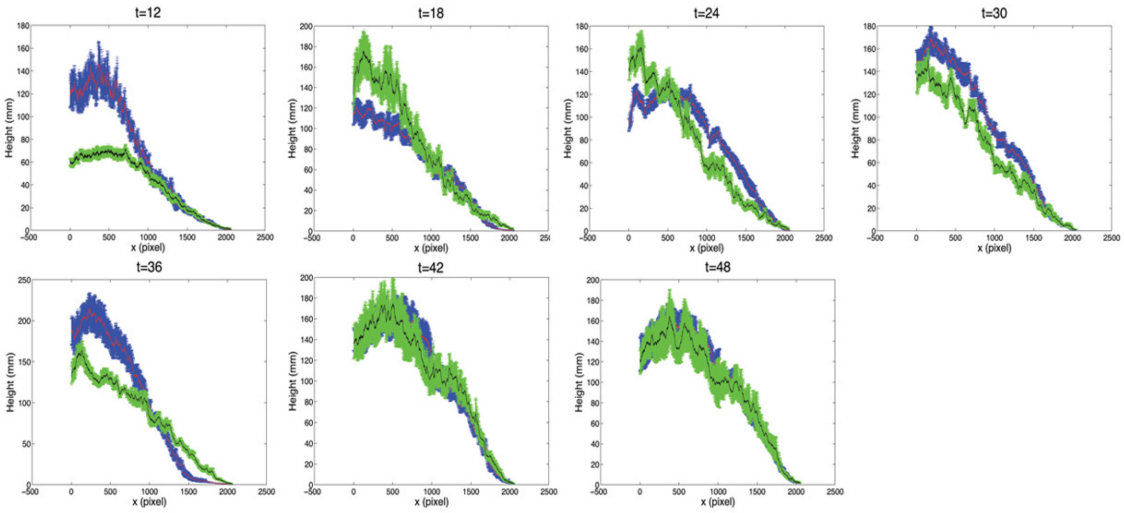

(a) Comparison of the height profile between the wild-type and the *bslA* mutant.

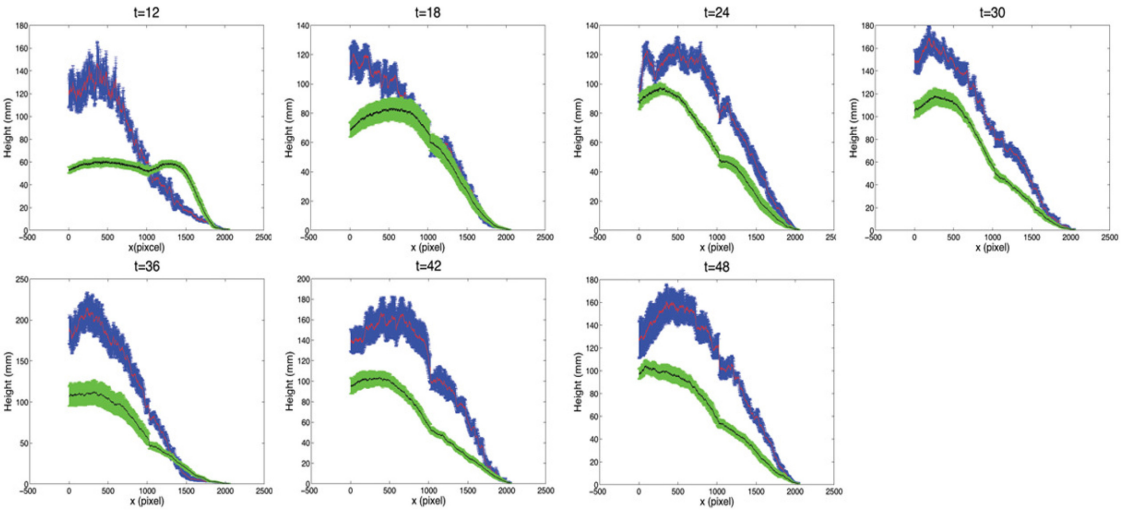

(b) Comparison of the height profile between the wild-type biofilm and the *eps* mutant.

Figure 6.9: Comparison of the height profile between the wild-type biofilm and *bslA* mutant (Figure 6.9(a)), the wild-type and the *eps* mutant (Figure 6.9(b)) at different time points. The mean of the height of the wild-type biofilm is shown by the red curve and blue shading is the standard error. The mean of the height of the mutants is shown by the black curve and the green shading is the standard error.

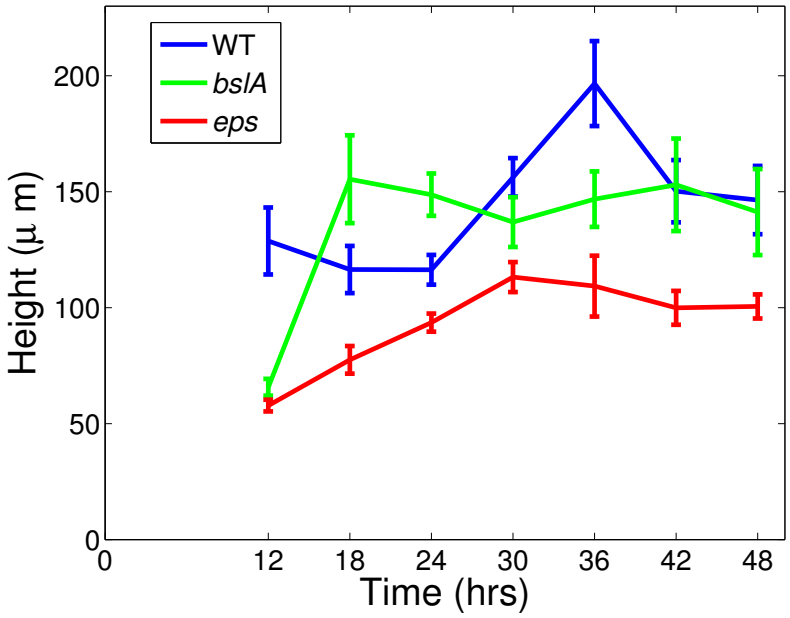

Figure 6.10: Growth of the biofilm height at the edge overtime for each strain. Data plotted is the average height and the error bar indicates the standard error.

Chapter 7

Conclusions and Future Work

7.1 Conclusions and Discussion

In this thesis we presented a combination of mathematical modelling and experimental observations in order to study and better understand the development of bacterial biofilm. To do this, we have taken a continuum modelling approach and studied three hypotheses relating to the mechanisms of biofilm development and how the heterogeneous structure of biofilms form. The first hypothesis was that the EPS matrix drives the heterogeneous structure of the biofilm by interacting with the bacterial cells. The second hypothesis was that the development of the biofilm is driven by the pressure caused by cell growth and division. In this case, the EPS matrix was assumed to be a porous medium, since the EPS matrix usually exhibits a void honeycomb structure. The third hypothesis considered in this thesis was that the development of the biofilm is dependent on osmotic pressure. In this case, an increase in EPS concentration causes an increase in osmotic pressure, resulting in swelling of the biofilm through uptake of water from the agar as well as from the air. To motivate and inform this modelling, we also conducted a series of laboratory experiments to measure the radius and the height

of the biofilm of different strains over time.

In Chapter 2, we studied a minimal model to investigate the effect of the EPS matrix on biofilm expansion and subsequent structure. We introduced a new reaction-diffusion system consisting of two PDE equations to describe the cell density and the EPS concentration. Our first aim was to study whether the presence of the EPS matrix affects the biofilm expansion or not. Our second aim was to ascertain whether the interaction between the movement of the EPS molecules and cell movement results in the spatial pattern that can be observed in experiments?

We first studied whether the EPS matrix affects the spreading speed of the biofilm by seeking a travelling wave solution of the model. Results of the travelling wave analysis showed that the minimum speed of the spreading of the biofilm depends on the rate of cell diffusion and net cell growth rate. Interestingly, our analysis predicts that the spreading speed is independent of the concentration of the EPS matrix. In conclusion, we think that this result demonstrates that the reaction-diffusion approach is not valid for the study of the biofilm expansion.

Next, we applied stability analysis in the angular direction to study pattern formation with two different hypotheses regarding the possible effects of the EPS matrix. The first hypothesis stated that cells move up gradient of EPS concentration by haptotaxis, while the second hypothesis stated that the EPS matrix itself contracts the biofilm system (e.g. when the agar dries out). We found that a spatial pattern can occur under both of these two hypotheses. Therefore, we suggest that spatial pattern of the biofilm may occur as a result of the interaction between the movement of the EPS molecules and the movement of the cells.

In Chapter 3, we digressed from the cell-EPS interaction to explore the mathematics of the model that hypothesised that the expansion of the biofilm is caused by the

cell growth. We followed paper [37] that used Darcy's law to model the cell movement which is related to the cell growth and division. The substrate concentration is modelled by a reaction diffusion equation. Our aim was to investigate whether the heterogeneous structure of the biofilm could arise from the net cell growth only, without the influence of cell diffusion and other external effects.

We first analysed the mathematical model that includes cell growth without any loss of cells. The analytical results showed that the heterogeneous structure on the biofilm interface could be obtained with the mechanism that the cell movement is caused by cell growth and division.

Then we extended model in [37] to include the loss of cells in order to examine the effect of cell loss on the structure of the biofilm. Planar solution analysis identified the factors that determine the average depth of the biofilm and the time that is required before interface heterogeneity starts to form. Therefore we predict that the average depth of a more viscous biofilm should be higher than the average depth of a less viscous biofilm. Also, the result of the 1-D planar analysis predicted that a more viscous biofilm will spend a longer time in planar height development before the possibility of interface heterogeneity arises. Therefore we deduce that one of the possible roles of the EPS matrix, which controls the viscosity of the biofilm, is to control both the depth of the biofilm and the heterogeneity of the growing surface. These factors may have advantages in different environmental conditions.

Results of the interface instability analysis showed that the cell death introduced another term in the dispersion relation. Therefore, we predict that at the early stage of biofilm growth, bacterial death stabilises the planar interface, whereas at the mature stage of biofilm growth, cell death destabilises the planar interface. By comparing the velocity of the planar interface and that of the perturbed height, we were able to classify different dynamics of the interface pattern in terms of the death rate. By increasing the

death rate, we could obtain three different patterns ranging from 'expansion first and pattern later', to 'pattern occurs immediately', to 'decaying biofilm'. All of these analytical results were numerically explored in Chapter 4. Numerical results are related to statements discussed above.

In Chapter 5, we employed the mathematical modelling approach proposed by Seminara et al. [116]. We used this approach to investigate the hypotheses regarding the function of the hydrophobic layer that is absent in the *bslA* mutant *B. subtilis*. We hypothesised that the lack of the hydrophobic layer could either help the biofilm absorb water from the environment or lose water to the environment. Using a thin-film approximation, we were able to reduce the full model to a single equation that describes the change of the biofilm height over time. This change of different biofilm height over time is experimentally measured in Chapter 6. Based on the experimental observation discussed in Chapter 6, we compared the wild-type strain and the *bslA* mutant at the beginning and end of biofilm growth, and made a comparison of the simulated height profiles in the absence of the hydrophobic layer. This allows us to conclude that the hypothesis stating that water can be absorbed from the environment.

In Chapter 6, we presented the results from a series of laboratory experiments, which we conducted to investigate the difference between the wild-type *B. subtilis* biofilm and two mutant strains, the *eps* mutant and the *bslA* mutant. These experiments allowed us to better understand the function of these key components, and the effect they have on growth and development of the biofilm.

We collected data on the radius and height of the wild-type, *eps* mutant and *bslA* mutant of *B. subtilis* every 6 hours after inoculation. Using image analysis, we observed that the wild-type colony displayed a very slight reduction in colony size that was not statistically distinct from the *bslA* mutant. However, the size of the *eps* mutant was dramatically smaller than that of the wild-type and *bslA* mutant. These observations

suggest that the lack of the hydrophobic layer on the surface of the biofilm, i.e. *bslA* mutant, is not a key limiting factor in biofilm radial expansion. On the contrary, the observations do suggest that the production of the EPS matrix could function to enhance colony radial expansion.

We also developed a method to measure the height of the colony by mapping the light intensity to the height profile. We first observed that the height of the wild-type remained the same before 24 hours and increased after 24 hours. Using statistical analysis, we observed that, the height of the *eps* mutant is always smaller compared to the height of the wild-type. However, compared to the height of the wild-type, the height of the *bslA* mutant is smaller at $t = 12$ hours, but increases to be greater than that of the wild-type after 18 hours. Later on, the wild-type catches up to be comparable with the *bslA* mutant after around 36 hours. Therefore, we conclude that the hydrophobic layer which is deleted in the *bslA* mutant may have a significant effect on early stage biofilm development.

In this thesis, we have used different mathematical techniques combined with a series of experiments to study the hypotheses regarding growth and development of bacterial biofilms. Each modelling technique focused on a particular mechanism, which we propose to be responsible for the radial expansion, spatial pattern formation, or control of depth of biofilm. We have been able to better understand the interaction between the EPS matrix and cell movement, the role of cell death, and the effects of the hydrophobic layer at different stages of biofilm development. The models we have developed are generic and therefore results hold for a wide range of bacterial biofilms. However, specific results regarding the biofilms of wild-type and mutant species of *B. subtilus* were obtained by comparison to our experimental data.

7.2 Future Work

In this thesis, we have investigated hypotheses regarding how the biofilm expands and how a heterogeneous structure of biofilm may arise. However, there are still many unanswered questions in the mathematical modelling of biofilms, especially in the effort of incorporating further relevant physical, chemical, biological and ecological processes occurring at various time and length scales.

7.2.1 EPS Production Influenced by Quorum Sensing

As mentioned in Chapter 1, quorum sensing has been considered to play a critical role on biofilm pattern formation. Specially, it has been suggested that the amount of EPS production per cell might be influenced by quorum sensing [112]. Therefore, it would be interesting to include the quorum sensing processes in the mathematical model proposed in Chapter 2. This could be accomplished by introducing an evolution equation for the AHL molecules, which are the key components in the quorum sensing process produced by the cells. The diffusion of AHL can be assumed to be similar to that for the cell density. As for the equation of the cell density, we might need two equations for a down regulated QS population that produces low EPS and the up regulated QS population that produces more EPS. These two populations could switch to each other depending on the local AHL concentration.

7.2.2 Stochastic Darcy's Law

In Chapter 3, we assumed that the porous medium constructed by the EPS matrix was uniform, therefore we applied the Darcy's law to the system with a constant Darcy parameter. However, as can be seen from the experimental image of the biofilm, the heterogeneous structure of the biofilm may result in an inconsistent EPS matrix. Hence, in order to be more realistic, it may be better to apply a stochastic Darcy's law to the system. This could be accomplished by using a stochastic permeability parameter in the Darcy's law equation, i.e.

$$\mathbf{u} = -\lambda(\eta(t,\mathbf{x}))\nabla p,$$

where the permeability parameter $\lambda(\eta(t,\mathbf{x}))$ has a noise parameter η that is dependent on both the time and the position. Hence, equation (3.7) becomes

$$\nabla[\lambda(\eta(t,\mathbf{x}))\nabla p] = -g(s).$$

However, this stochastic system requires the improvement on the fast advancing computing technology that was used in Chapter 4.

7.2.3 Model with Fluid Flow over the Biofilm

In Chapter3, we assumed that the aqueous environment above the biofilm is static. However, fluid flow could potentially be a significant factor in determining biofilm architecture [40]. It could assist the growth by maintaining the substrate supply via advection. Therefore, the role of fluid flow can be viewed as an important factor in determining biofilm growth.

The model in Chapter 3 could be extended by including fluid flow in the aqueous

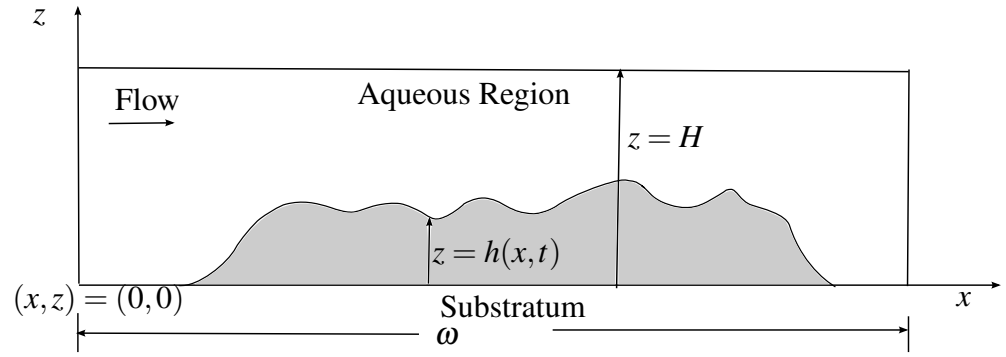

Figure 7.1: Schematic of biofilm, indication the orientation of axes. The substrate is introduced via influx from the left boundary of the domain.

region. Therefore, the effect of fluid flow on the distribution of substrate and the heterogeneous structure of the biofilm could be studied.

The new model would focus on biofilm growth after a sufficiently high cell density is reached. Hence, the bacterial cell density inside the biofilm can be taken as constant. Similar to the model constructed in Chapter 3, the biofilm thickness is considered to be dependent on only the x-direction. Two regions are separated by the biofilm height $h(x,t) > 0$, as shown in Figure 7.1: the biofilm region $0 < z < h(x,t)$ and the aqueous region $h(x,t) < z < H$, where H is the height of the conduit. The computational domain could be chosen to be an open subdomain with length w and the entire biofilm is growing within the domain, existing within a longer conduit.

The fluid could reasonably be assumed to be an incompressible Newtonian fluid with constant viscosity. Since the height of the slab is always much smaller than the length of it, the gravity of the fluid flow in the slab can be assumed to have no influence on the flow movement. Therefore, the body force of the fluid flow can be neglected. Suitable evolution equations for the fluid flow could be of the form:

$$\rho\left(\frac{\partial \mathbf{u}}{\partial t} + \mathbf{u}\cdot\nabla\mathbf{u}\right) = -\nabla p + \mu\nabla^2\mathbf{u}; \tag{7.1a}$$

$$\nabla\cdot\mathbf{u} = 0, \tag{7.1b}$$

where ρ and μ are the density and the viscosity of the fluid, respectively. The substrate concentration $s(x,z,t)$ in the aqueous region is governed by

$$s_t = D_1 \nabla^2 s - \nabla \cdot (\mathbf{u} s), \tag{7.2}$$

where the convective contribution to the transport of substrate in the aqueous region is controlled by the flow velocity vector $\mathbf{u} \equiv (u,v)$.

In the biofilm region, the substrate diffuses and is consumed by cell growth. In addition, it is reasonable to assume that the biofilm is sufficiently stiff that the fluid velocity can be considered negligible in the biofilm region [40], i.e. $\mathbf{u} \equiv \mathbf{0}$ for $0 < z < h(x,t)$. Therefore, the rate of change of substrate concentration is given by

$$s_t = D_2 \nabla^2 s - \alpha s, \tag{7.3}$$

where α is the substrate consumption rate that is proportional to the constant biomass density.

Following the model construction in Chapter 3, the growth driven pressure, $f(x,z,t)$, could be of the form:

$$\lambda \nabla^2 f = -Y \alpha s + d, \tag{7.4}$$

where λ is the coefficient defined as the ratio of permeability of the porous medium over the product of medium viscosity and porosity, Y represents the yield rate of the biofilm growth, and d is the bacterial cell death rate.

At the bottom of the biofilm, the vertical velocity of cell movement is set to be zero. Hence, the boundary condition for the growth driven pressure $f(x,z,t)$ at the base of the biofilm is given by

$$f_z(z=0) = 0. \tag{7.5}$$

For the same reason, the flux of substrate $s(x,z,t)$ across the boundary is set to be zero at the base of the biofilm, i.e.

$$s_z(z=0)=0. \tag{7.6}$$

A no-slip boundary condition to the fluid flow at the base of the biofilm. Therefore, we have

$$\mathbf{u}(z=0)=0. \tag{7.7}$$

At the top of the domain under consideration, i.e. $z=H$, no loss of substrate is assumed across the top boundary, i.e.

$$s_z(z=H)=0. \tag{7.8}$$

A no-slip boundary condition is applied to the fluid flow, i.e.

$$\mathbf{u}(z=H)=0. \tag{7.9}$$

At the biofilm interface, i.e. $z=h(x,t)$, the boundary conditions are given the same as used in Chapter 3.

The flow is assumed to come from the left boundary of the computational domain. It is assumed to follow *Poiseuille Flow*, where the flow is driven by the pressure difference at the end of the channel. Therefore, the boundary conditions for the pressure which determines the fluid flow are:

$$p(x=0)=p_0,\ p(x=w)=p_1, \tag{7.10}$$

and additionally, we require $p_0 > p_1$ in order to generate the fluid flow from left to right in the domain. The substrate concentration is assumed to be in the fluid upstream

of the biofilm, i.e.

$$s(x=0) = s_0. \tag{7.11}$$

On the right boundary where the fluid flow leaves the domain, we can apply an open boundary condition, i.e. $s_x = 0$, to the substrate concentration $s(x,z,t)$. Thus, the substrate concentration across the right boundary is considered to be uniform in the x-direction. This assumes that the right boundary is sufficiently 'down stream' of the biofilm.

With the level-set method described in Chapter 4, the model with fluid flow can be solved numerically. Figures 7.2(a) and 7.2(b) show surface plots of the level-set function $\phi(x,z,t)$, which indicates the biofilm region for $\phi < 0.5$ and the aqueous region for $\phi > 0.5$, at $t = 0$ and $t = 10$ respectively. Two observations can be obtained from the simulations. First of all, it is clear that the closer the biofilm is to the substrate inflow, the faster the biofilm grows. Secondly, by comparing the initial location of the colonies with their location at $t = 10$, it is also clear that the colonies shift to the right, i.e. in the direction of fluid flow, due to the velocity from the fluid flow. These early results provide a glimpse into possible future applications of the fluid flow model for the biofilm development.

7.2.4 Modelling the osmotic effect of the EPS matrix

There are also many unanswered questions generated by the work presented in Chapter 6 that are of great interest. First and foremost, by combining the experimental observation with the mathematical model, we have suggested that the lack of the hydrophobic layer helps the biofilm absorb water from the environment. The mathematical model we used in Chapter 5 was suitable for the strains that are able to produce EPS matrix to take in water from the agar, i.e. both the wild-type biofilm and the *bslA* mutant.

Therefore, we did not take into account the *eps* mutant in the model. It has been suggested that in the absence of osmotic forces, the EPS mutant may spread owing to an alternative mechanism based on cell-cell contact and called 'sliding'. It would be of great interest to construct a mathematical model to describe the spreading of the *eps* mutant and therefore we would better understand the function of the EPS matrix in the biofilm.

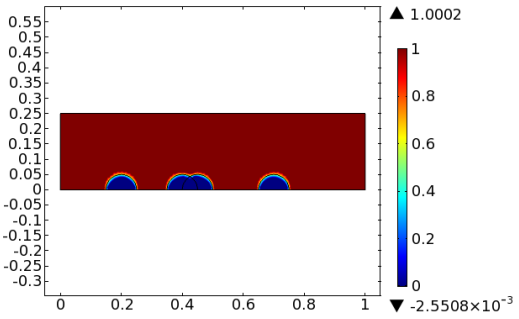

(a) Biomass at $t = 0$.

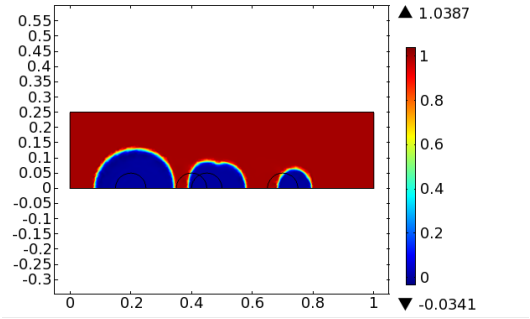

(b) Biomass at $t = 10$.

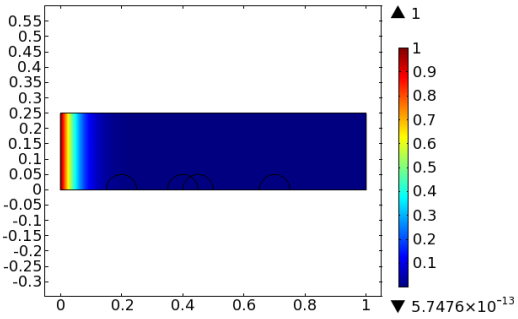

(c) Substrate concentration at $t = 0$.

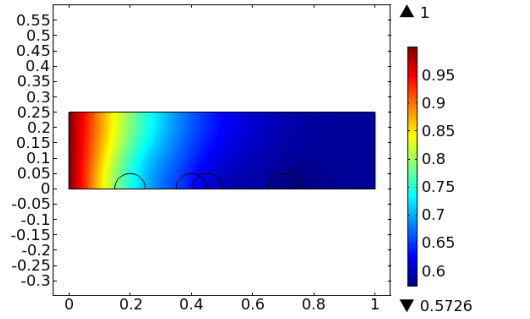

(d) Substrate concentration at $t = 10$.

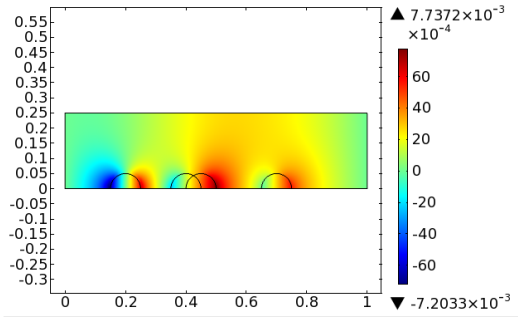

(e) Horizontal velocity of the cell at $t = 1$.

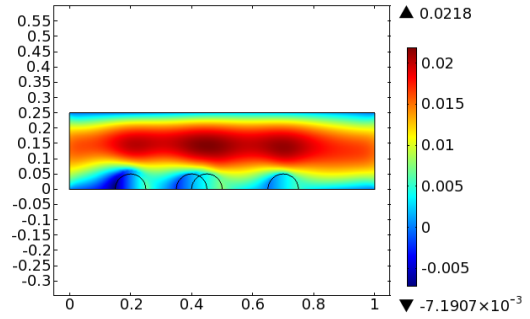

(f) Net horizontal velocity of the cell at $t = 1$.

Figure 7.2: Growth of randomly distributed semi-curcular shaped colonies with the effect of fluid flow. The surface plots of the level set function ϕ (Figure 7.2(a) and 7.2(b)) at $t = 0$ and $t = 10$ respectively show the growth of the colonies. The distribution of the substrate concentration is plotted in Figure 7.2(c) and 7.2(d) for $t = 0$ and $t = 10$ respectively. The surface plots of the horizontal velocity of the biofilm at $t = 1$, which is caused by growth, is shown in Figure 7.2(e). The net horizontal velocity of the biofilm at $t = 11$ is also plotted in 7.2(f). The black circles indicate the initial location of the colonies.

Chapter 8

Appendix

8.1 Appendix for Chapter 5

8.1.1 Governing Equations

The model considers a biofilm grows on an agar surface and is in contact with air above. The model considers the biofilm in vertical section. The geometry of the model is shown in Figure 8.1. The biofilm region is defined as $[0,R(t)] \times [0,h(x,t)]$ where $R(t)$ is the radius of the biofilm and $h(x,t)$ is the height of the biofilm.

The model considers the biofilm as a two component system of a mixture of biomass and water. Osmotic pressure is maintained within the biofilm as a result of the EPS matrix. The volume fraction of the biomass is denoted as $\phi(x,z,t)$ where $0 \leq \phi(x,z,t) \leq 1$, and thus the volume fraction of water is defined as $1-\phi(x,z,t)$. The biomass is assumed to grow at a constant rate g. Also it is assumed that the biomass can be convected by the biomass network. Therefore, according to the mass conservation law, the

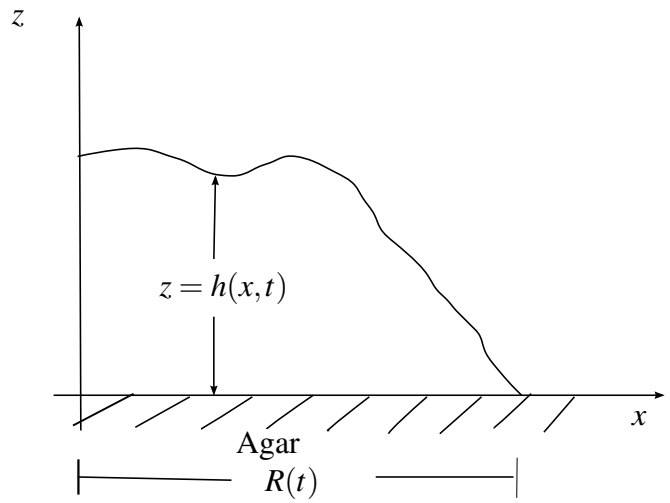

Figure 8.1: Sketch of the geometry of the biofilm that will be modelled in this section. The biofilm grows on the agar surface and is surrounded by air.

governing equation for the biomass volume fraction is:

$$\frac{\partial \phi}{\partial t} + \nabla \cdot (\phi \mathbf{v}_b) = g\phi, \tag{8.1}$$

where $\mathbf{v}_b$ is the velocity of the biomass network. Similarly, water is consumed by the biomass growth. Also, water is convected by the water velocity $\mathbf{v}_w$. Therefore, the water volume fraction satisfies

$$\frac{\partial (1-\phi)}{\partial t} + \nabla \cdot ((1-\phi)\mathbf{v}_w) = -g\phi. \tag{8.2}$$

It follows from (8.1) and (8.2) that

$$\nabla \cdot (\phi \mathbf{v}_b + (1-\phi)\mathbf{v}_w) = 0. \tag{8.3}$$

Next, expressions for $\mathbf{v}_b$ and $\mathbf{v}_w$ will be determined by minimizing the sum of free energy change and dissipation of the biofilm system. The detail of this approach can be found in [38, 78]. The sum is referred to as the *Rayleighian*. The dissipation is caused

by the relative motion between the biomass and water. Therefore, the dissipation function can be written as

$$W = \int \zeta(\mathbf{v}_b - \mathbf{v}_w)^2 dV, \tag{8.4}$$

where ζ is the friction coefficient [38, 52] which is defined as

$$\zeta = \mu_w \xi^{-2}, \tag{8.5}$$

where μ_w is the viscosity of water and ξ is the average distance between particles, i.e. cell-cell, or water molecule-water molecule, or cell-water molecule. The integral region dV refers only to a 2-D region in x and z.

The free energy change in the general situation consists of two terms: mixing free energy F_{mix} and elastic free energy F_{el} which is caused by the conformational entropy of the cells. The mixing free energy is defined as

$$f_{mix} = \int f(\phi(r)) dV$$

where $f(\phi)$ is the free energy per unit volume. Therefore, the change of the mixing free energy with time is given by

$$F'_{mix} = \int \frac{\partial f}{\partial \phi} \frac{\partial \phi}{\partial t} dV.$$

Substituting (8.1) into the above equation yields

$$F'_{mix} = \int \frac{\partial f}{\partial \phi} \left[-\nabla \cdot (\phi \mathbf{v}_b) + g\phi \right] dV. \tag{8.6}$$

By definition, the change of the elastic free energy is given by

$$F'_{el} = \int \sigma_b \cdot \nabla \mathbf{v}_b dV \tag{8.7}$$

where σ_b is the stress tensor of the biomass. Combining the dissipation (8.4), the change of the mixing free energy (8.6) and the elastic free energy (8.7) yields the expression of the Rayleighian, denoted as R, as follow:

$$R = \int \left[\frac{1}{2}\zeta(\mathbf{v}_b - \mathbf{v}_w)^2 - \frac{\partial f}{\partial \phi}(\nabla \cdot (\phi \mathbf{v}_b) - g\phi) + \sigma_b \cdot \nabla \mathbf{v}_b \right] dV. \tag{8.8}$$

The velocities must also satisfy the incompressible condition, (8.3). Hence, an additional restriction needs to be added to the Rayleighian when minimizing. Therefore, using the method of Lagrange multipliers to include the restriction, the Rayleighian to be minimized is given by

$$R = \int [\frac{1}{2}\zeta(\mathbf{v}_b - \mathbf{v}_w)^2 - \frac{\partial f}{\partial \phi}(\nabla \cdot (\phi \mathbf{v}_b) - g\phi) + \sigma_b \cdot \nabla \mathbf{v}_b - p(\nabla \cdot (\mathbf{v}_b \phi + \mathbf{v}_w(1-\phi))] dV, \tag{8.9}$$

where $p(x,z,t)$ is the pressure driven by the motion of both the biomass and water.

Next, (8.9) will be minimized by differentiating with respect to both $\mathbf{v}_b$ and $\mathbf{v}_w$. Taking differentiation of the second term of (8.9) with respect to $\mathbf{v}_b$ as an example, we have:

$$\frac{\partial}{\partial \mathbf{v}_b}\left[\int -\frac{\partial f}{\partial \phi}(\nabla \cdot (\phi \mathbf{v}_b) - g\phi) dV \right] = -\frac{\partial}{\partial \mathbf{v}_b}\left[\int \frac{\partial f}{\partial \phi}(\nabla \cdot (\phi \mathbf{v}_b)) dV \right]. \tag{8.10}$$

Applying the Divergence Theorem to the integral on the right hand side of the above equation yields

$$\int \frac{\partial f}{\partial \phi}(\nabla \cdot (\phi \mathbf{v}_b)) dV = \int \frac{\partial f}{\partial \phi}(\phi \mathbf{v}_b) \cdot dS - \int (\phi \mathbf{v}_b) \cdot \nabla \frac{\partial f}{\partial \phi} dV$$

where dS is the boundary of the 2-D domain dV. According to the no-slip boundary condition which will be given later in this section, the first term on the right hand side

of the above equation is reduced to zero, leading to

$$\int \frac{\partial f}{\partial \phi}(\nabla \cdot (\phi \mathbf{v}_b))dV = -\int (\phi \mathbf{v}_b) \cdot \nabla \frac{\partial f}{\partial \phi} dV.$$

Therefore, substituting the above equation into the right hand side of equation (8.10) and differentiating with respect to $\mathbf{v}_b$, equation (8.10) can be simplified to

$$\frac{\partial}{\partial \mathbf{v}_b}\left[\int -\frac{\partial f}{\partial \phi}(\nabla \cdot (\phi \mathbf{v}_b) - g\phi)dV\right] = \int \phi \nabla \frac{\partial f}{\partial \phi} dV.$$

Following similar procedures, it can be shown that:

$$\frac{\partial R}{\partial \mathbf{v}_b} = \int [\zeta(\mathbf{v}_b - \mathbf{v}_w) + \phi \nabla(\frac{\partial f}{\partial \phi}) + \phi \nabla p - \nabla \cdot \sigma_b]dV;$$
$$\frac{\partial R}{\partial \mathbf{v}_w} = \int [\zeta(\mathbf{v}_w - \mathbf{v}_b) + (1-\phi)\nabla p]dV.$$

To minimise R, we set both these expressions equal to zero. Then, since the 2-D domain is arbitrary, then in order for the integrals to be zero, we must have:

$$\zeta(\mathbf{v}_b - \mathbf{v}_w) + \phi \nabla(\frac{\partial f}{\partial \phi}) + \phi \nabla p - \nabla \cdot \sigma_b = 0 \tag{8.12a}$$

$$\zeta(\mathbf{v}_w - \mathbf{v}_b) + (1-\phi)\nabla p = 0. \tag{8.12b}$$

We note that osmotic pressure, Ψ is given by

$$\Psi = \phi \frac{\partial f}{\partial \phi} - f,$$

and therefore the second term on the left hand side of (8.12a) is equal to

$$\nabla \Psi = \phi \nabla \frac{\partial f}{\partial \phi}.$$

Additionally, the stress tensor of the biomass is given by $\sigma_b = \mu_b(\nabla \mathbf{v}_b + \nabla \mathbf{v}_b^T)$. Therefore, equation (8.12a) can be rewritten as

$$\zeta(\mathbf{v}_b - \mathbf{v}_w) + \nabla\Psi + \phi\nabla p - \mu_b\nabla^2\mathbf{v}_b = 0 \tag{8.13}$$

Equations (8.1), (8.3), (8.12b) and (8.13) constitute the full system to be studied in this section. Adding equation (8.13) and (8.12b) yields

$$\mu_b\nabla^2\mathbf{v}_b = \nabla(p + \Psi). \tag{8.14}$$

Substituting (8.12b) into (8.3) to eliminate $\mathbf{v}_w$ gives

$$\nabla \cdot \mathbf{v}_b = \nabla\left[\frac{(1-\phi)^2}{\zeta}\nabla p\right]. \tag{8.15}$$

In this way, the system can be further reduced to a three-equation system given by (8.1), (8.14) and (8.15).

The osmotic pressure Ψ is assumed to be a linear function of the volume fraction of the biomass, i.e. $\Psi(\phi) = E\phi$ for some constant E. We will now explicitly write the three equation system in terms of the coordinates x and z. To do this, we define the coordinates of $\mathbf{v}_b$ as $\mathbf{v}_b = (u, v)$. Then system (8.1), (8.14) and (8.15) becomes:

$$\phi_t + (\phi u)_x + (\phi v)_z = g\phi; \tag{8.16a}$$

$$u_x + v_z = \left(\frac{(1-\phi)^2}{\zeta}p_x\right)_x + \left(\frac{(1-\phi)^2}{\zeta}p_z\right)_z; \tag{8.16b}$$

$$\mu_b(u_{xx} + u_{zz}) = p_x + E\phi_x; \tag{8.16c}$$

$$\mu_b(v_{xx} + v_{zz}) = p_z + E\phi_z. \tag{8.16d}$$

8.1.2 Boundary Conditions

Next, we will give details of how the boundary conditions are derived for the system. The model considers a biofilm growing on the surface of agar. During the time course of typical experiments, cells do not penetrate into the agar. However, the agar is relatively stiff and hence cells do not glide over the surface. Therefore, a no-slip boundary condition for the velocity of the biomass is assumed at the biofilm-agar interface, i.e.

$$\mathbf{v}_b = (u, v) = (0, 0) \qquad \text{at} \quad z = 0. \tag{8.17}$$

The biofilm-air interface can be treated as a fluid-fluid interface. The velocity fields in both the biofilm and the air are continuous across this interface, i.e. all components of the velocity of the biomass are equal to the corresponding components of the velocity of the air at the biofilm-air interface $z = h(x,t)$. If we denote the velocity of the air region $z > h(x,t)$ as $\mathbf{v}_a \equiv (u^a, v^a)$, then the boundary conditions at the biofilm-air interface is $\mathbf{v}_a = \mathbf{v}_b$, which we write in component form

$$\begin{aligned} \mathbf{v_a} \cdot \mathbf{x} &= \mathbf{v_b} \cdot \mathbf{x}; \qquad \text{Tangent to the interface,} \\ \mathbf{v_a} \cdot \mathbf{n} &= \mathbf{v_b} \cdot \mathbf{n}; \qquad \text{Normal to the interface,} \end{aligned}$$

where $\mathbf{x}$ is the unit tangent vector to the biofilm-air interface, while $\mathbf{n}$ is the unit normal vector. If we denote $\mathbf{T}$ to be the stress tensor in the biomass and also denote $\hat{\mathbf{T}}$ to be the stress tensor in the air which have the form

$$\mathbf{T} = -p\mathbf{I} + \mu_b[\nabla \mathbf{v}_b + (\nabla \mathbf{v}_b)^T] \tag{8.18a}$$

$$\hat{\mathbf{T}} = -p_a\mathbf{I} + \mu_a[\nabla \mathbf{v}_a + (\nabla \mathbf{v}_a)^T] \tag{8.18b}$$

where $\mathbf{I}$ is the identity matrix, p is the pressure of the biomass, p_a is the pressure of

the air at the biofilm-air interface, μ_a is the viscosity of the air and μ_b is the viscosity of the biofilm. Then from the force balance equation detailed in [79, 80], the stress balance equation for the biomass and air can be derived as

$$\mathbf{n}\cdot\mathbf{T}-\mathbf{n}\cdot\hat{\mathbf{T}}=\sigma\mathbf{n}\nabla\cdot\mathbf{n}-\nabla\sigma, \tag{8.19}$$

where σ represents the interfacial stress tensor that depends on the temperature and the components of the interface. It is assumed that both the temperature and the components of the interface are uniform leading to a constant value of σ.

Both the normal and the tangential stress must be balanced at the biofilm-air interface. Each component will now be considered in turn. Taking the scalar product of the unit tangent vector $\mathbf{x}$ and the equation (8.19) yields the tangential stress balance equation at the interface as follows:

$$\mathbf{n}\cdot\mathbf{T}\cdot\mathbf{x}-\mathbf{n}\cdot\hat{\mathbf{T}}\cdot\mathbf{x}=\nabla\sigma\cdot\mathbf{x}. \tag{8.20}$$

Since the interfacial stress tensor σ is assumed to be a constant, the right side of equation (8.20) equals zero. It is also reasonable to assume that there is no force existing in the tangential direction at the biofilm-air interface, therefore the tangential component of the pressure in both the biomass and the air becomes zero. Thus, substituting the definition of $\mathbf{T}$ and $\hat{\mathbf{T}}$ from (8.18) into (8.20) yields

$$\mu_b\frac{\partial u}{\partial z}=\mu_a\frac{\partial u^a}{\partial z}.$$

It is obvious that $\mu_a \ll \mu_b$, therefore we can simplify and approximate this equation to give:

$$\frac{\partial u}{\partial z}=0 \qquad \text{at } z=h(x,t). \tag{8.21}$$

Similarly, taking the scalar product of the unit normal vector **n** and the equation (8.19) yields

$$\mathbf{n}\cdot\mathbf{T}\cdot\mathbf{n}-\mathbf{n}\cdot\hat{\mathbf{T}}\cdot\mathbf{n}=\sigma(\nabla\cdot\mathbf{n}). \tag{8.22}$$

The right hand side of (8.22) represents the force that is responsible for the creation of the curvature of the interface. The shape of the biofilm-air interface is distorted by this force. For simplicity, the shape distortion of the biofilm-air interface is assumed to be very small, therefore this force is assumed to zero. Substituting (8.18) into (8.22) and setting the RHS to zero gives

$$-p+2\mu_b v_z-(-p_a+2\mu_a v_z^a)=0.$$

Then assuming that p_a is constant and $\mu_a \ll 1$, the above equation can be simplified to

$$-p+2\mu_b v_z=-p_{ext} \qquad \text{at} \quad z=h(x,t), \tag{8.23}$$

where $p_{ext}=-p_a$ represents the external force that acts on the biofilm-air interface.

On the biofilm-air interface $z=h(x,t)$, we have $z-h(x,t)=0$. Therefore, taking the substantial derivative (for details see [125]) of this equation gives

$$\frac{D(z-h(x,t))}{Dt}=0,$$

and this can be rewritten as

$$\frac{\partial(z-h(x,t))}{\partial t}+u\frac{\partial(z-h(x,t))}{\partial x}+v\frac{\partial(z-h(x,t))}{\partial z}=0,$$

which simplifies to

$$h_t+uh_x=v, \text{ at } z=h(x,t). \tag{8.24}$$

As a summary, equation (8.17), (8.21), (8.23), (8.24) and (5.21) constitute the boundary conditions for the system (8.16).

8.2 MATLAB Files

8.2.1 'cross_diffusion_pde' Program

Program that uses the PDEPE solver to solve system (2.20) in 1-D and plots the result. Similar program is also used to solve system (5.33) and plot the solution.

```
function []=cross_diffusion_pde()
m=0;
xmax=50;
tmax=100;
xstep=1000;
tstep=20;
x=linspace(0,xmax,xstep);
t=linspace(0,tmax,tstep);

%parameters
global d1;
global d3;
global d4;
global rho;
global delta;
global beta;
global alpha;

%Para that generates instability
delta=20;
beta=0.2;
```

```
rho=0.01;
d1=0.1;
alpha=0.005;
d3=0.1;
d4=0.5;

% delta=20;
% beta=0.2;
% rho=0.01;
% d1=1;
% alpha=0.01;
% d3=0.1;
% d4=0.5;
sol=pdepe(m,@cross_diffusion_model,@cross_diffusion_initial,
    @cross_diffusion_bc,x,t);
u=sol(:,:,1);
v=sol(:,:,2);
plot(x,u)

clc;
%-------------------------------------------------------
function [c,f,s]=cross_diffusion_model(x,t,u,DuDx)
%function components
global d1;
global d3;
global d4;
global rho;
global delta;
global beta;
global alpha;
c=[1;1];
f=[d1*DuDx(1)+alpha*u(1)*DuDx(2);d3*u(2)*DuDx(1)+d4*DuDx(2)];
s=[rho*u(1)*(delta-u(1)); beta*u(1)^2-u(1)*u(2)];
```

```
%-----------------------------------------------------
function value=cross_diffusion_initial(x)
%a=rand(1,length(x));
u0=exp(-x^2);
v0=0;
value=[u0;v0];
%-----------------------------------------------------
function [pl,ql,pr,qr]=cross_diffusion_bc(xl,ul,xr,ur,t)
pl=[0;0];
ql=[1;1];
pr=[0;0];
qr=[1;1];
```

8.2.2 'cross_tw_velocity' Program

Program that uses the PDEPE solver to solve system (2.20) in 1-D and compute the travelling wave speed, with varied parameter values .

```
function cross_tw_velocity
m=0;
xmax=500;
tmax=100;
xstep=1000;
tstep=60;
x=linspace(0,xmax,xstep);
t=linspace(0,tmax,tstep);
dt=tmax/(tstep-1);

%set parameter value
%l=10;%l is the no. of parameters tried
%
% % %-------------------------------------------------------------
```

```
% %delta
% para_ini=10;
% d_para=1;
% para=para_ini:d_para:20;
%
% % %-----------------------------------------------------------------
% % %rho
% para_ini=0.01;
% d_para=0.001;
% para=para_ini:d_para:0.03;

% % %-----------------------------------------------------------------
% %beta
% para_ini=0.15;
% d_para=0.001;
% para=para_ini:d_para:0.3;

% %-----------------------------------------------------------------
%d1
para_ini=0.1;
d_para=0.1;
para=para_ini:d_para:5;

global alpha;
global delta;
global rho;
global beta;
global d1;
global d3;
global d4;

alpha=0;
```

```
d3=0.5;
d4=1;
v=zeros(1,length(para));
for i=1:length(para)
%     d1=1;
%     delta=para(i);
%     rho=0.01;
%     beta=0.2;

%     d1=1;
%     delta=20;
%     rho=para(i);
%     beta=0.2;

%     d1=1;
%     delta=20;
%     rho=0.01;
%     beta=para(i);

    d1=para(i);
    delta=20;
    beta=0.2;
    rho=0.01;

    sol=pdepe(m,@cross_diffusion_model,@cross_diffusion_initial,
       @cross_diffusion_bc,x,t);
    b=sol(:,:,1);%cell density
    w=0;

    dist=zeros(1,tstep-w);
    velocity=zeros(1,tstep-w-1);
    for j=(w+1):tstep
        ind=max(find(b(j,:)>1e-2));
```

```
        dist(j-w)=x(ind);
    end

    for j=1:(tstep-w-1)
        velocity(j)=(dist(j+1)-dist(j))/dt;
    end

    v(i)=mean(velocity);
end
figure
plot(para,v);
hold on

%-----------------------------------------------
function [c,f,s]=cross_diffusion_model(x,t,u,DuDx)
%function components
global d1;
global d3;
global d4;
global rho;
global delta;
global beta;
global alpha;
c=[1;1];
f=[d1*DuDx(1)+alpha*u(1)*DuDx(2);d3*u(2)*DuDx(1)+d4*DuDx(2)];
s=[rho*u(1)*(delta-u(1)); beta*u(1)^2-u(1)*u(2)];
%-----------------------------------------------
function value=cross_diffusion_initial(x)
u0=exp(-x^2);
v0=0;
value=[u0;v0];
%-----------------------------------------------
function [pl,ql,pr,qr]=cross_diffusion_bc(xl,ul,xr,ur,t)
```

```
pl=[0;0];
ql=[1;1];
pr=[0;0];
qr=[1;1];
```

8.2.3 'height_speed_plot' Program

Program that uses the ODE45 solver to solve system (3.79) with different initial value. It also compares the two approximations with the numerical simulation.

```
function []=height_speed_plot()
global K;
global G;
global mu;
global L;
global h0;
global g;

K=8;
G=4;
mu=0.05;
L=2;
g=sqrt(G);
h0=0.01;%h0*g determines the approximation

%-----------------------------------------------
%exact solution
[t,y1]=ode45(@hexact,[0,100],h0);
u1=(K.*tanh(g.*y1))./(g.*(g*L.*tanh(g.*y1)+K))-mu.*y1;
figure;
plot(y1,u1);
hold on;
```

```
%-----------------------------------------------
%appr solution with tanh=1
[t,y2]=ode45(@hlarge,[0,100],h0);
u2=K/(g*(g*L+K))-mu.*y2;
plot(y2,u2,'r.');
hold on;

%-----------------------------------------------
%appr solution with tanh(x)=x
[t,y3]=ode45(@hsmall,[0,100],h0);
u3=K.*y3./(G*L.*y3+K)-mu.*y3;
plot(y3,u3,'k.');
hold on;

title(['Velocity plot against height with h0=',num2str(h0)],'
    fontsize',24);
xlabel('Height','fontsize',18);
ylabel('Velocity','fontsize',18);
legend('Exact solution','Appr solution with tanh=1','Appr solution
    with tanhx=x');

%-----------------------------------------------
function dhdt=hexact(t,h)
global K;
global mu;
global L;
global g;
global G;
dhdt=(K*tanh(g*h))/(g*(g*L*tanh(g*h)+K))-mu*h;
%-----------------------------------------------
function dhdt=hlarge(t,h)
global K;
```

```
global mu;
global L;
global g;
global G;
dhdt=K/(g*(g*L+K))-mu*h;
%-----------------------------------------------
function dhdt=hsmall(t,h)
global K;
global mu;
global L;
global g;
global G;
dhdt=K*h/(G*L*h+K)-mu*h;
```

8.2.4 'radius_calculator' Program

Program that uses the otsu solver to calculate the radius of the biofilm at different time.

```
function radius=radius_calculator(imageId,tvalue)
client=loadOmero('nightshade.openmicroscopy.org.uk');
session=client.createSession('laoshenlee','3giphonen96');

%-----------------------------------------------
radius=zeros(1,tvalue);
L=otsu(imageId);

for i=1:tvalue
    k=0;
    plane=getPlane(session,imageId,0,0,i-1);
    a=size(plane);
    n=a(1);
    m=a(2);
    for j=1:n
```

```
        for u=1:m
            if plane(j,u)>L
                k=k+1;
            end
        end
    end
    ratio=k/(m*n);
    area1=2.5^2*274.64*367.24/(45.51^2);
    area=area1*ratio;
    R=sqrt(area/pi);
    radius(1,i)=R;
end
```

8.2.5 'height_calculation' Program

Program that maps the light intensity to the height of the biofilm. It first obtains the light intensity of the biofilm. Then it calculates the weighted light intensity according to the method described in 6.4.2.

```
function height=height_calculation(imageId,z0,zn,interval,
    sample_height,m,n,indicator)
%indicator is: 1--top  2--bottom  3--left  4--right

%interval is chosen to be the outer bound of the focus region
    including the
%right edge as the last term
%the first term in the interval is non-zero and the last term is the
     width
%of the domain

%z0 and zn are chosen to be the first focus one and the last focus
    one
```

```
%no. of smaple height is from z0 to zn-1

%m is the no. of pixels in the width of the image
%n is the no. of pixels in the height of the image

%l=m/1024;
k=zn-z0+1;
x_pix=round(interval/660*1024);

light=weight_transfer(imageId,z0,k,x_pix,m,n,indicator);
height=mapping_linear(light,sample_height,k,x_pix);

figure;
plot(1:max(m,n),height)

function light=weight_transfer(imageId,z0,k,x_pix,m,n,indicator)

%find the focused region coresponding to z stack and transform to
    pixel

a=max(m,n);
light=zeros(1,a);

plane=zeros(k,n,m);%plane is used to store the light intensity for
    the useful stacks

a=max(m,n);
line=zeros(k,a);%line is used to store the light intensity cross the
     centre of the useful
%stacks

%connect to omero and get the light profile through the centre of
    each
```

```
%stack
client=loadOmero('nightshade.openmicroscopy.org.uk');
session=client.createSession('laoshenlee','3giphonen96');
images=getImages(session,imageId);

if indicator==4
    for i=1:k
        plane(i,:,:)=getPlane(session,images,z0-2+i,0,0);
    end

    for i=1:k
        line(i,:)=plane(i,512,:);
    end

elseif indicator==3
    for i=1:k
        plane(i,:,:)=getPlane(session,images,z0-2+i,0,0);
    end

    for i=1:k
        for j=1:m
            line(i,j)=plane(i,512,m+1-j);
        end
    end
elseif indicator==2
    for i=1:k
        plane(i,:,:)=getPlane(session,images,z0-2+i,0,0);
    end

    for i=1:k
        line(i,:)=plane(i,:,512);
    end
```

```
elseif indicator==1
    for i=1:k
        plane(i,:,:)=getPlane(session,images,z0-2+i,0,0);
    end

    for i=1:k
        for j=1:a
            line(i,j)=plane(i,a+1-j,512);
        end
    end
end

%weigh the light intensity
light(1:x_pix(1))=line(1,1:x_pix(1));
for i=2:k-1
    light(x_pix(i-1):x_pix(i))=0.7*line(i,x_pix(i-1):x_pix(i))+...
        0.15*line(i-1,x_pix(i-1):x_pix(i))+...
        0.15*line(i+1,x_pix(i-1):x_pix(i));
end
light(x_pix(k-1):a)=line(k,x_pix(k-1):a);

light_min=min(light);
light=light-light_min;

client.closeSession();

function height=mapping_linear(weighted_light,sample_height,k,x_pix)
sample_light=zeros(1,k-1);

%calculate the parameter value
for i=1:k-1
    sample_light(i)=weighted_light(x_pix(i));
end
y=sample_height;
```

```
x=sample_light;
p=polyfit(x,y',1);

height=p(1)*weighted_light+p(2);
```

8.3 COMSOL Multiphysics Settings

8.3.1 Fluid Flow Setting

Given below are general mesh and solver setting used in COMSOL setup when solving system (7.1) to (7.4). Settings were the same for all simulations with the obvious exception of initial conditions and parameter value, both of which can be set up by following COMSOL documentation.

1. Modules Used
    - Navier-Stokes equation: 'Laminar flow (spf)' (incompressible)
    - Substrate equation: 'Transport of Diluted Species (chds)' (convection)
    - Growth pressure equation: 'PDE (g)'
    - Level set equation: 'Level set (ls)'
2. Boundary Condition Types Used
    - No-slip: 'Wall'
    - Inflow: 'Inlet'(pressure, no viscous stress)
    - Outflow: 'Outlet' (pressure, no viscous stress)
    - No-slip for substrate: 'No flux'
    - Substrate inflow: 'Inflow'

- Substrate outflow: ‘Open boundary’
- Boundary conditions for F: ‘Zero flux’
- No-slip for the level-set variable: ‘No flow’
- Boundary conditions for the level-set variable at the end: ‘Inlet’

3. Mesh setting
    - Sequence Type: ‘Physics-controlled mesh’
    - Element size: ‘Fine’
4. Time-Dependent Solver
    - Absolute Tolerance
        - Global method: ‘Scaled’
    - Time Stepping
        - Method: ‘BDF’
        - Maximum BDF order: 2
        - Minimum BDF order: 1
    - Output
        - Store time-derivatives: ‘On’
        - Store solution out-of-core: ‘On’
    - Advanced
        - Error estimation: ‘Inclued algebraic’
        - Matrix Symmetry: ‘Automatic’

Bibliography

[1] K. A. Adal and B. M. Farr. Central venous catheter-related infections: a review. *Nutrition*, 12(3):208–213, 1996.

[2] C. Allan. Omero: Flexible, model-driven data management for experimental biology. *Nat Methods*, 9(3):245–253, 2012.

[3] G. Almogy, L. Stone, and N. Ben-Tal. Multi-stage regulation, akey to reliable adaptive biochemical pathways. *Journal of Biophysics*, 81:3016–3028, 2001.

[4] E. Alpkvist and I. Klapper. A multidimensional multispecies continuum model for heterogeneous biofilm development. *Bulletin of mathematical biology*, 69:765–789, 2007.

[5] K. Anguige, J. R. King, and J. P. Ward. A multi-phase mathematical model of quorum sensing in a maturing *Pseudomonas aerugunosa* biofilm. *Mathematical Biosciences*, 203(2):240–276, 2006.

[6] L. K. Archibald and R. P. Gaynes. Hospital acquired infections in the united states: the importance of interhospital comparisons. *Nosocomial Infection*, 11(2):245–255, 1997.

[7] S. Asakura and H. Honda. Two-state model for bacterial chemoreceptor proteins: The role of multiple methylation. *Journal of Mathematical Biology*, 176:349–367, 1984.

[8] M. Asallya, M. Kittisopikul, P. Ruéd, Y. Du, Z. Hu, T. Çag!atay, A.B. Robinson, H. Lu, J. Garcia-Ojalvod, and G.M. Süel. Localized cell death focuses mechanical forces during 3d patterning in a biofilm. *PNAS*, 109(46):18891–18896, 2012.

[9] M. M. Baum, A. Kainovic, T. O'Keeffe, R. Pandita, K. McDonald, S. Wu, and P. Webster. Characterization of structures in biofilms formed by a pseudomonas fluorescens isolated from soil. *Microbiology*, 9(103), 2009.

[10] C. R. Bell, M. Brylinsky, and P. Johnson-Green, editors. *Multidimensional modelling of biofilm structure*. Atlantic Canada Society for Microbial Ecology, 1999.

[11] E. Ben-Jacob, I. Cohen, I. Golding, and Y. Kozlovsky. *Modelling branching and chiral colonial patterning of lubracting bacteria*, pages 211–254. Springer-Verlag, 2001.

[12] E. Ben-Jacob, I. Cohen, and D. Gutnick. Cooperative organization of bacterial colonies: From genotype to morphotype. *Annual Review of Microbiology*, (52):779–806, 1998.

[13] E. Ben-Jacob, I. Cohen, O. Shochet, A. Czirok, and T. Vicsek. Cooperative formation of chiral patterns during growth of bacterial colonies. *Physical Review Letters*, 15(75):2899–2902, 1995.

[14] E. Ben-Jacob, H. Shmueli, O. Shochet, and A.Tenenbaum. Adaptive self-organization during growth of bacterial colonies. *Physica A*, (187):378–424, 1992.

[15] E. Ben-Jacob, O. Shochet, A. Tenenbaum, I. Cohen, A. Czirok, and T. Vicsek. Generic modeling of cooperative growth patterns in bacterial colonies. *Nature*, (368):46–49, 1994.

[16] I. B. Bischofs, J. A. Hug, A. W. Liu, D. M. Worf, and A. P. Arkin. Complexity in bacterial cell-cell communication: quorum signal integration and subpopulation signaling in the *Bacillus subtilis* phosphorelay. *PNAS*, 106:6459–6464, 2009.

[17] S. S. Branda, J. E. González-Pastor, S. Ben-Yehuda, R. Losick, and R. Kolter. Fruiting body formation by *Bacillus subtilis*. *PNAS*, 98(20):11621–11626, 2001.

[18] S. S. Branda, J. E. González-Pastor, E. Dervyn, S. D. Ehrlich, R. Losick, and R. Kolter. Genes involved in formation of structured multicellular communities by bacillus subtilis. *Journal of Bacteriology*, 186(12):3970–3979, 2004.

[19] S. S. Branda, A. Vik, L. Friedman, and R. Kolter. Biofilms: the matrix revisited. *TRENDS in Microbiology*, 13(1):20–26, 2005.

[20] S.S. Branda, F. Chu, DB. Kearns, R. Losick, and R. Kolter. A major protein component of the *Bacillus subtilis* biofilm matrix. *Molecular Microbiology*, 59(4):1229–1238, 2006.

[21] A. Bridier, D.L. Coq, F. Dubois-Brissonnet, V. Thomas, S. Aymerich, and R. Briandet. The spatial architecture of *Bacillus subtilis* biofilms deciphered using a surface-associated model and in situ imaging. *PLoS one*, 6(1), 2011.

[22] D. Brown and P. Rothery. *Models in biology: mathematics, statistics and computing*. John Wiley and Sons, 1994.

[23] V. Caselles, F. Catte, T. Coll, and F. Dibos. A geometric model for active contours in image processing. *Numerical Mathematics*, 66:1–33, 1993.

[24] Y. Chai, F. Chu, R. Kolter, and R. Losick. Biastability and biofilm formation in *Bacillus subtilis* biofilm matrix. *Molecular Microbiology*, 59:1229–1238, 2008.

[25] H. T. Chang and B. E. Rittmann. Mathematical modelling of biofilm on activated carbon. *Environmental science technology*, 21:273–280, 1987.

[26] D.L. Chopp. Computing minimal surfaces via level set curvature flow. *Journal of computational physics*, 106:77–91, 1993.

[27] N. G. Cogan. Effect of persister formation on bacterial response to dosing. *Journal of Theoretical Biology*, 238:694–703, 2006.

[28] N.G. Cogan and J.P. Keener. Channel formation in gels. *SIAM J. Appl. Math*, 65(6):1839–1854, 2005.

[29] J. W. Costerton, Z. Lewandowski, D. E. Caldwell, D. R. Korber, and H. M. Lappin-Scott. Microbial biofilms. *Annual Review of Microbiology*, 49:711–745, 1995.

[30] A.B. Cunningham, W.G. Characklis, F. Abedeen, and D. Crawford. Influence of biofilm accumulation on porous media hydrodynamics. *Environmental science technology*, 25:1305–1311, 1991.

[31] M. E. Davey and G.A. O'Toole. Microbial biofilms: from ecology to molecular genetics. *Microbiology and molecular biology reviews*, 64(4):847–867, 2000.

[32] D. De-Beer, P. Stoodley, F. Roe, and Z. Lewandowski. Effects of biofilm structrue on oxygen distribution and mass-transport. *Biotechnology and bioengineering*, 43(11):1131–1138, 1994.

[33] M. Dichinson and A. L. Bisno. Infections associated with prosthetic devices: clinical considerations. *International Journal of Artificial Organs*, 16(749-754), 1993.

[34] R. Dillon and L. Fauci. Microscale model of bacterial and biofilm dynamics in porous media. *Biotechnology and bioengineering*, 68(5):536–547, 2000.

[35] R. Dillon, L. Fauci, A. Fogelson, and D. Gaver. Modelling biofilm processes using the immersed boundary method. *Journal of computational physics*, 129(1):57–73, 1996.

[36] J. Dockery and J. Keener. A mathematical model for quorum sensing in *Pseudomonas aeruginosa*. *Bulletin of mathematical biology*, 00:1–22, 2000.

[37] J. Dockery and I. Klapper. Finger formation in biofilm layers. *SIAM J. Appl. Math*, 62(3):853–869, 2001.

[38] M. Doi and A. Onuki. Dynamic coupling between stress and composition in polymer solutions and blends. *J. Phys. 2 France*, 2(8):1631–1656, 1992.

[39] R. M. Donlan. Biofilms: Microbial life on surfaces. *Emerging infectious diseases*, 8(9):881–890, 2002.

[40] R. Duddu, D.L. Chopp, and B. Moran. A two-dimensional continuum model of biofilm growth incorporating fluid flow and shear stress based detachment. *Biotechnology and bioengeering*, 103(1):92–104, 2009.

[41] F. A. L. Dullien. *Porous Media: Fluid Transport and Pore Structure*. Academic Press, 1992.

[42] A. M. Earl, R. Losick, and R. Kolter. Ecology and genomics of bacillus subtilis. *Trends in microbiology*, 16(6):269–275, 2008.

[43] H. J. Eberl. A deterministic continuum model for the formation of eps in heterogeneous biofilm architectures. 2004.

[44] H. J. Eberl, D. F. Parker, and M. C. M. Loosdrecht. A new deterministic spatio-temporal continnum model for biofilm development. *Journal of Theoretical medicine*, 3:161–175, 2001.

[45] H. J. Eberl and R. Sudarsan. Exposure of biofilms to slow flow fields: The convective contribution to growth and disinfection. *Theoretical biology*, 253:788–807, 2008.

[46] H.C. Flemming and J. Wingender. The biofilm matrix. *Nature Review Microbiol*, 8:623–633, 2010.

[47] H.C. Flemming, J. Wingender, and M. C. Griegbe. *Physico-chemical properties of biofilms.*, pages 18–34. Harwood Academic Publishers, 2000.

[48] M. R. Frederick, C. Kuttler, K. A. Hense, and H. J. Eberl. A mathematical model of quorum sensing regulated eps production in biofilm communities. *Theoretical biology and medical modelling*, 8(8), 2011.

[49] H. Fujikawa. Diversity of the growth patterns of *Bacillus subtilis* colonies on agar plates. *FEMS microbiology ecology*, 13(3):159–168, 1994.

[50] H. Fujikawa and M. Matsushita. Fractal growth of bacillus subtilis on agar plates. *J.Phys.Soc.Jap*, 58:3875–3878, 1989.

[51] A. Furtado and R. Henry. Measurement of green fluorescent protein concentration in single cells by image analysis. *Analytical Biochemistry*, 310:84–92, 2002.

[52] P.de Gennes. *Scaling concepts in polymer physics*. Cornell University, 1979.

[53] A. L. Gillen. *The genesis of germs: the origin of diseases and the coming plagues*. New leaf publishing group, 2007.

[54] A. Goldbeter and D. Koshland. Simple molecular model for sensing and adaptation based on receptor modification with application to bacterial chemotaxis. *Journal of Molecular Biology*, 161(395-416), 1982.

[55] I. Golding, Y. Kozlovsky, I. Cohen, and E. Ben-Jacob. Studies of bacterial branching growth using reaction-diffusion models for colonial development. *Physica A*, (260):510–554, 1998.

[56] A. B. Goryachev, D. J. Toh, and T. Lee. Systems analysis of a quorum sensing network: Design constraints imposed by the functional requirements, network topology and kinetic constants. *BioSystems*, 83:178–187, 2006.

[57] W. Gujer and O. Wanner. *Modeling mixed population biofilms*. Wiley, New York, 1990.

[58] L. Hall-Stoodley and P. Stoodley. Evolving concepts in biofilm infections. *Cell Microbiology*, 11:1034–1043, 2009.

[59] R.M. Harshey. Bacterial motility on a surface: many ways to a common goal. *Annu. Rev. Microbiol*, 57:249–273, 2003.

[60] A. Harten, B. Engquist, S. Osher, and S. Chakravarthy. Uniformly high-order accurate essentially non-oscillatory schemes iii. *Journal of computational physics*, 71:231–303, 1987.

[61] D. Hauri and J. Ross. A model of excitation and adaptation in bacterial chemotaxis. *Journal of Biophysics*, (708-722), 68.

[62] D. Hekmat, M. Stephan, R. Bauer, A. Feuchitinger, and D. Vortmeyer. Modelling of multispecies biofilm population dynamics in a trickle-bed bioreactor used for waste gas treatment. *Procee Biochemistry*, 41:1409–1416, 2006.

[63] J. W. Hickman, D. F. Tifrea, and C. S. Harwood. A chemosensory system that regulates biofilm formation through modulation of cyclic diguanylate levels. *PNAS*, 102(40):14422–14427, 2005.

[64] L. Hobley, A. Ostrowski, F. V. Rao, K. M. Bromley, M. Porter, A. R. Prescott, C. E. MacPhee, D. M. F. van Aalten, and N. R. Stanley-Wall. Bsla is a self-assembling bacterial hydrophobin that coats the *Bacillus subtilis* biofilm. *PNAS*, 110(33):13600–13605, 2013.

[65] S. Jabbari, J. T. Heap, and J. R. King. Mathematical modelling of the sporulation-initiation network in *Bacillus subtilis* revealing the dual role of the putative quorum-sensing signal molecule phra. *Bulletin of mathematical biology*, (73):181–211, 2011.

[66] S. James, P. Nilsson, G. James, S. Kjelleberg, and T. Fagertrom. Luminescence conctrol in the marine bacterium *Vibrio fischeri*: An analysis of the dynamics of *lux* regulation. *Journal of Molecular Biology*, 296:1127–1137, 2000.

[67] J. W. Jeong, J. Snay, and M. M. Ataai. A mathematical model for examining growth and sporulation processes of *Bacillus subtilis*. *Biotechnology and bioengeering*, 35:160–184, 1990.

[68] H. De Jong, J. Geiselmann, G. Batt, C. Hernandez, and M. Page. Qualitative simulation of the initiation of sporulation in *Bacillus subtilis*. *Bulletin of mathematical biology*, 66:261–299, 2004.

[69] D.B. Kearns, F. Chu, S.S. Branda, R. Kolter, and R. Losick. A master regulator for biofilm formation by *Bacillus subtilis*. *Molecular Microbiology*, 55(3):739–749, 2005.

[70] W. Kim, M. Schollmeyer, M. Nimtz, V. Wray, and K. Geider. Genetics of biosynthesis and structure of the capsular exopolysaccharide from the asian pear pathogen erwinia pyrifoliae. *Microbiology*, 148(4015-4024), 2002.

[71] I. Klapper and J. Dockery. Mathematical description of microbial biofilms. *SIAM Review*, 53(2):221–265, 2010.

[72] I. Klapper, C. J. Rupp, R. Cargo, B. Purvedorj, and P. Stoodley. Viscoelastic fluid description of bacterial biofilm material properties. *Biotechnology and bioengineering*, 80(3), 2002.

[73] K. Kobayashi and M. Iwano. Bsla(yuab) forms a hydrophobic layer on the surface of *Bacillus subtilis* biofilms. *Molecular Microbiology*, 85(1):51–66, 2012.

[74] K. Kobayashi and M. Iwano. Bsla(yuab) forms a hydrophobic layer on the surface of *Bacillus subtilis* biofilms. *Molecular Microbiology*, 85(1):51–66, 2012.

[75] Y. Kozlovsky, I. Cohen, I. Golding, and E. Ben-Jacob. Lubricating bacteria model for branching growth of bacterial colonies. *Physical Review E*, 59(6):7025–7035, 1999.

[76] J. Kreft, C. Picioreanu, J. W. T. Wipenny, and M. C. M. Loosdrecht. Individual-based modelling of biofilms. *Microbiology*, 147:2897–2912, 2001.

[77] J.U. Kreft and J.W. Wimpenny. Effect of eps on biofilm structure and function as revealed by an inidvidual-based model of biofilm growth. *Water Science of Technology*, 43(6):135–141, 2001.

[78] L. D. Landau and E. M. Lifshitz. *Course of theoretical physics vol V – Statistical physics*. Elsevier, Oxford, Uk, 1980.

[79] E. Lauga, M.P. Brenner, and H.A. Stone. *Microfluidics: The No-Slip Boundary Condition*. Springer, 2005.

[80] L. G. Leal. *Laminar flow and convective transport processes: scaling principles and symptotic analysis*. Butterworth-Heinemann, 1992.

[81] A. Leeuwenhoek. *Part of a letter from Mr Antony van Leeuwenhoek, concerning the worms in sheeps livers, gnats, and animalcula in the excrements of frogs*, volume 22. Philosophical transactions, 1753.

[82] J. H. J. Leveau and S. E. Lindow. Predictive and interpretive simulation of green fluorescent protein expression in reporter bacteria. *Journal of Bacteriology*, 183(23):6752–6762, 2001.

[83] Z. Lewandowski. *Biofilms: recent advances in their study and control*, pages 1–17. Harwood Academic Publishers, 2000.

[84] Ulf W. Liebal, Thomas Millat, Imke G. de Jong, Oscar P. Kuipers, Uwe Volker, and Olaf Wolkenhauer. How mathematical modelling elucidates signalling in *Bacillus subtilis*. *Molecular Microbiology*, 77(5):1083–1095, 2010.

[85] X.D. Liu, S. Osher, and T. Chan. Weighted essentially non-oscillatory schemes. *Journal of computational physics*, 126:202–212, 1996.

[86] D. López, H. Vlamakis, and R. Kolter. Biofilms. *Cold Spring Harbor Perspectives in Biology*, 2010.

[87] B. Macek, I. Mijakovic, J. V. Olsen, F. Gnad, C. Kumar, P. R. Jensen, and M. Mann. The serine/threonine/tyrosine phosphoproteome of the model bacterium bacillus subtilis. *Molecular and Cellular Proteomics*, 6:697–707, 2007.

[88] R. Malladi and J.A.Sethian. Image processing via level set curvature flow. *PNAS*, 92:7046–7050, 1995.

[89] V. L. Marlow, M. Porter, L. Hobley, T. B. Kiley, R. Swedlow, F. A. Davidson, and N. R. Staley-Wall. Phosphorylated degu manipulates cell fate differentiation in the *Bacillus subtilis* biofilm. *Journal of Bacteriology*, 196(1):16–27, 2014.

[90] F. Matsushita, F. Hiramatsu, N. Kobayashi, T. Ozawa, Y. Yamazaki, and T. Matsuyama. Colony formation in bacteria: experiments and modeling. *Biofilms*, 1:305–317, 2004.

[91] M. Matsushita and H. Fujikawa. Diffusion-limited growth in bacterial colony formation. *Physica A*, 168:498–506, 1990.

[92] M. Matsushita, J. Wakita, H. Itoh, K. Watanabe, T. Arai, T. Matsuyama, H. Sakaguchi, and M. Mimura. Formation of colony patterns by a bacterial cell population. *Physica A*, 274:190–199, 1999.

[93] A. D. McNaught and A. Wilkinson. *International Union of Pure and Applied Chemistry: Compendium of Chemical Terminology*. IUPAC, 1997.

[94] B. Mello, L. Shaw, and Y. Tu. Effects of receptor interaction in bacterial chemotaxis. *Journal of Biophysics*, 87:1578–1595, 2004.

[95] M. Mimura, H. Sakaguchi, and M. Matsushita. Reaction-diffusion modelling of bacterial colony patterns. *Physica A*, 282:283–303, 2000.

[96] M. Morohashi, Y. Ohashi, S. Tani, K. Ishii, M. Itaya, H. Nanamiya, F. Kawamura, M. Tomita, and T. Soga. Model-based definition of population heterogeneity and its effects on metabolism in sporulation *Bacillus subtilis*. *Journal of Biochemistry*, 142:183–191, 2007.

[97] S. Osher and R. Fedkiw. *Level set methods and dynamic implicit surfaces*. Springer, 2003.

[98] G. O'Toole, H.B. Kaplan, and R. Kolter. Biofilm formation as microbial development. *Annu Review of Microbiology*, 54:49–79, 2000.

[99] G. O'Toole and R. Kolter. The initiation of biofilm formation in *Pseudomonas fluorescens* wcs365 proceeds via multiple, convergent signalling pathways: a genetic analysis. *Molecular Microbiology*, 28(3):449–461, 1998.

[100] N. Otsu. A threshold selection method from gray-level histograms. *IEEE Transaction on Systems, Man and Cybernetics*, 9(1):62–66, 1979.

[101] C. Picioreanu, J-U. Kreft, and M.C. van Loosdrecht. Particle-based multidimensional multispecies biofilm model. *Applied and environmental microbiology*, 70(5):3024–3040, 2004.

[102] C. Picioreanu, M.C.van Loosdrecht, and J.J.Heijnen. A theoretical study on the effect of surface roughness on mass transport and transformation in biofilms. *Biotechnol. Bioeng*, 68:355–369, 2000.

[103] C. Picioreanu, M. van Loosdrecht, and J. J. Heijnen. Two-dimensional model of biofilm detachment caused by internl stress from liquid flow. *Biotechnology and bioengineering*, 72(2):205–218, 2001.

[104] C. Picioreanu, M.C. van Loosdrecht, and J. J. Heijnen. Mathematical modeling of biofilm structure with a hybrid differential-discrete cellular automaton approach. *Biotechnology and bioengineering*, 58(1):101–116, 1998.

[105] G. Pizarro, D. Griffeath, and D. R. Noguera. Quantitative cellular automaton model for biofilms. *Journal of Environmental Engineering*, 127(9), 2001.

[106] W.H. Press, B.P. Flannery, S.A. Teukollsky, and W.T. Vetterling. *Numerical recipes in C: the art of scientific computing.* Cambridge University Press, Cambridge., 1997.

[107] C. Rao and G. Ordal. The molecular basis of excitation and adaptation during chemotactic sensory transduction in bacteria. *Contributions to Microbiology*, 16:33–64, 2009.

[108] C. V. Rao, J. R. Kirby, and A. P. Arkin. Design and diversity in bacterial chemotaxis: a comparative study in *Escherichia coli* and *Bacillus subtilis*. *PLoS Biology*, 2(2):239–252, 2004.

[109] I. G. Ron, I. Golding, B. Lifsitz-Mercer, and E. Ben-Jacob. Bursts of sectors in

expanding bacterial colonies as a possible model for tumor growth and metastases. *Physica A*, 320:485–496, 2003.

[110] E. Rosenbrand. *Modelling biofilm distribution and its effect on two-phase flow in porous media*. PhD thesis, Delft University of Technology, March 2010.

[111] P.A. Sackinger, P.R. Schunk, and R.R. Rao. A newton-raphson pseudo-solid domain mapping technique for free and moving boundary problems: A finite element implementation. *Journal of computational physics*, 125(1):83–103, 1996.

[112] Y. Sakuraki and R. Kolter. Quorum-sensing regulation of the biofilm matrix genes (pel) of *Pseudomonas aeruginosa*. *Journal of Bacteriology*, 189(14):5383–5386, 2007.

[113] D. Schultz, P. G. Wolynes, E. Ben-Jacob, and J. N. Onuchic. Deciding fate in adverse times: Sporulation and competence in *Bacillus subtilis*. *PNAS*, 106(50):21027–21034, 2009.

[114] D. J. Schwab, A. Baetica, and P. Mehta. Dynamical quorum-sensing in oscillators coupled through an external medium. *PhysicaD*, 241(21):1782–1788, 2012.

[115] L. Segel and A. Goldbeter. A mechanism for exact sensory adaptation based on receptor modification. *Journal of Theoretical Biology*, 120:151–179, 1986.

[116] A. Seminara, T.E. Angelini, J.N. Wilking, H. Vlamakis, S. Ebrahim, R. Kolter, D.A. Weitz, and M.P. Brenner. Osmotic spreading of bacillus subtilis biofilms driven by an extracellular matrix. *PNAS*, 109(4):1116–1121, 2012.

[117] J.A. Sethian. *Level set methods and fast marching methods: Evolving Interfaces in Computational Geometry, Fluid Mechanics, Computer Vision, and Materials Science*. Cambridge University Press, 1999.

[118] J.A. Sethian and P. Smereka. Level set methods for fluid interfaces. *Annu Review of fluid mechanics*, 35:341–372, 2003.

[119] C.W. Shu and S. Osher. Efficient implementation of essentially non-oscillatory shock capturing schemes. *Journal of computational physics*, 77:439–471, 1988.

[120] C.W. Shu and S. Osher. Efficient implementation of essentially non-oscillatory shock capturing schemes ii. *Journal of computational physics*, 83:32–78, 1989.

[121] P. Stoodley, D. De-Beer, and Z. Lewandowski. Liquid flow in biofilm systems. *Applied and environmental microbiology*, 60(8):2711–2716, 1994.

[122] P. Stoodley, S. Yang, H. Lappin-Scott, and Z. Lewandowski. Relationship between mass transfer coefficient and liquid flow velocity in heterogenous biofilms using microelectrodes and confocal microscopy. *Biotechnology and bioengeering*, 56(6):681–688, 1997.

[123] I.W. Sutherland. Biofilm exopolysaccharides: a strong and sticky framework. *Microbiology*, (147):3–9, 2001.

[124] T. Takaishi, M. Mimura, and Y. Nishiura. Pattern formation in coupled reaction-diffusion systems. *Japan Journal of Industrial and Applied Mathematics*, 12:385–424, 1995.

[125] D.J. Tritton. *Physical Fluid Dynamics*. Oxford science publications, 1988.

[126] U. Trottenberg, C. Oosterlee, and A. Schuller. *Multigrid*. Academic Press, 2001.

[127] L. Tsimring, H. Levine, I. Aranson, E. Ben-Jacob, I. Cohen, O. Shochet, and W. N. Reynolds. Aggregation patterns in stressed bacteria. *Physical Review Letters*, 75:1859–1862, 1995.

[128] R.C. Tyson. Pattern formation by *E.coli*-mathematical and numerical investigation of a biological phenomenon, 1996.

[129] R.C. Tyson, S.R. Lubkin, and J.D.Murray. A minimal mechanism for bacterial pattern formation. *Proc. R. Soc. Lond.B*, 266(299-304), 1998.

[130] R.C. Tyson, S.R. Lubkin, and J.D.Murray. Model and analysis of chemotactic bacterial patterns in liquid medium. *J. Math.Biol*, 38:359–375, 1999.

[131] E. Ullner, A. Koseska, J. Kurths, E. Volkov, H. Kants, and J. Garcia-Ojava. Multistability of synthetic genetic networks with repressive cell-to-cell communication. *Physical Review E*, 78(031904), 2008.

[132] USGS. Environmental health-toxic substances. *http://toxics.usgs.gov/photo_gallery/metals_variation.html*.

[133] M. C. M. van Loosdrecht, J. Heijnen, and H. Eberl. Mathematical modelling of biofilm structure. *Journal of general and moleclar microbiology*, 81:245–256, 2002.

[134] H. A. Videla and L. K. Herrera. Microbiologically influenced corrosion: looking to the future. *Interenational Microbiolofy*, 8:169–180, 2005.

[135] H. Vlamakis, C. Aguilar, R. Losick, and R. Kolter. Control of cell fate by the formation of an architecturally complex bacterial community. *Genens and Dev*, 22:945–953, 2008.

[136] C. A. Voigt, D. M. Worf, and A. P. Arkin. The *Bacillus subtilis sin* operon: an evolvable network motif. *Genetics*, 169:1187–1202, 2005.

[137] J. P. Ward, J. R. King, and A. J. Koerber. Mathematical modelling of quorum sensing in bacteria. *Journal of Mathematics Applied Medicine and Biology*, 18:263–292, 2001.

[138] J.P. Ward and J.R. King. Thin-film modelling of biofilm growth and quorum sensing. *Journal of Eng Math*, 73:71–92, 2012.

[139] S. Whitaker. Diffusion and dispersion in porous media. *American Institute of Chemical Engineers*, 13(3):420–427, 1967.

[140] J. Wimpenny, W. Manz, and U. Szewzyk. Heterogeneity in biofilms. *FEMS microbiology reviews*, 24:661–671, 2000.

[141] J. W. T. Wimpenny and Ric Colasanti. A unifying hypothesis for the structure of microbial biofilms based on cellular automaton models. *FEMS microbiology ecology*, 22:1–16, 1997.

[142] J. Wingender and T.R. Neu. What are bacterial extracellular polymeric substances. pages 1–19, 1999.

[143] H. F. Winstanley, M. Chapwanya, M. J. McGuinness, and A. C. Fowler. A polymer solvent model of biofilm growth. *Proceeding of the royal society A*, 467:1449–1467, 2010.

[144] T. A. Witten and L. M. Sander. Diffusion-limited aggregation, a kinetic critical phenomenon. *Physical Review Letters*, 47(19):1400–1403, 1981.

[145] C. W. Wolgemuth, A. Mogilner, and G. Oster. The hydration dynamics of polyelectrolyte gels with applications to cell motility and dryg delivery. *European Biophysics Journal*, 33:146–158, 2003.

[146] J. B. Xavier, M. K. de Kreuk, C. Picioreanu, and M. C. M. van Loosdrecht. Multi-scale inidividual-based model of microbial and bioconversion dynamics in aerobic granular sludge. *Environmental science technology*, 41(18):6410–6417, 2007.

[147] J.B. Xavier, E.M. Garcia, and K.R. Foster. Social evolution of spatial patterns in bacterial biofilms: When conflict drives disorder. *The American Naturalist*, 174(1):1–12, 2009.

[148] J.B. Xavier, C. Picioreanu, and M.C. van Loosdrecht. A framework for multidimensional modelling of activity and structure of multispecies biofilms. *Environmental microbiology*, 7(8):1085–1103, 2005.

[149] J.B. Xavier, C. Picioreanu, and M.C. van Loosdrecht. A general description of detachment for multidimensional modelling of biofilms. *Biotechnology and bioengeering*, 6(91):651–669, 2005.

[150] N. Yildirim and M. C. Machey. Feedback regulation in the lactose operon: A mathematical modelling study and comparison with experimental data. *Biophsical Journal*, 84:2841–2851, 2003.

[151] N. Zelver. What are biofilms? *http://www.biofilm.montana.edu/node/2390*.

[152] T. Zhang, N.G. Cogan, and Q. Wang. Phase field models for biofilms. *SIAM J. Appl. Math*, 69(3):641–669, 2008.